Universidad de Jaén

Escuela de Doctorado

TESIS DOCTORAL

●

CRACK TIP FIELDS CHARACTERISATION ON NON-PLANAR SURFACES EMPLOYING A DIFFERENTIAL GEOMETRY APPROACH AND 3D DIGITAL IMAGE CORRELATION. EXPERIMENTAL AND NUMERICAL STUDY

CARACTERIZACIÓN DE CAMPOS EN LAS INMEDIACIONES DEL VÉRTICE DE GRIETA EN SUPERFICIES NO PLANAS UTILIZANDO GEOMETRÍA DIFERENCIAL Y CORRELACIÓN DIGITAL DE IMÁGENES 3D. ESTUDIO EXPERIMENTAL Y NUMÉRICO

PRESENTADA POR:
ALONSO CAMACHO REYES

DIRIGIDA POR:
FRANCISCO ALBERTO DÍAZ GARRIDO
JOSÉ MANUEL VASCO OLMO

JAÉN, 17 DE OCTUBRE DE 2022

ISBN XXXXXXX

Agradecimientos

En primer lugar, me gustaría agradecer a mis directores de tesis, Francisco Díaz y José Manuel Vasco, por su constante ayuda y confianza depositada durante la realización de la tesis. A mis compañeros Luis, Elías, Ángel y Juan Antonio. Por su ayuda y amistad durante toda esta etapa. Me gustaría, además, hacer especial mención a nuestro director común, Francisco Díaz. Quien ha conseguido crear un grupo de gran valor personal y profesional. Gracias a todos, porque con vuestro trabajo y dedicación habéis creado un grupo extraordinario.

También, al resto de compañeros del Departamento de Ingeniería Mecánica y Minera de Universidad de Jaén por su amable acogida.

To Professor Fernando Antunes for his help and advice during my research stay in the Mechanical Engineering Department of the University of Coimbra. Your teachings and principles were key to achieving my goals. Thank you for your supervision and closeness.

To Diogo and Edmundo and all the rest of the people of the Mechanical Engineering Department of the University of Coimbra who made my stay easier.

To Professor Neil James from the University of Plymouth to whom I have to acknowledge his enriching suggestions and advice during my PhD studies. His extensive experience was key to my PhD education.

A mis padres, Alonso y Juani, que han hecho todo lo que estaba en sus manos para que hoy este aquí. Sin ellos, no sería quien soy. A mis hermanos, Fernando y Pedro, y a mis cuñadas Puri e Inma que de una forma u otra han sido participes.

A mi abuela Marina, que desde allá donde esté, siempre ha soplado para orientarme en la dirección correcta.

Y como no, a Alicia, que con su constante apoyo y compresión hizo más sencillo este camino.

Resumen

En este trabajo se desarrolla una metodología para la caracterización de los campos en las inmediaciones del vértice de grietas a fatiga contenidas en superficies no planas (curvas) con curvatura Gaussiana nula en condiciones de tensión plana. El objetivo es combinar un modelo analítico para la descripción de los campos en el vértice de grieta, modificándolo previamente mediante el empleo de conceptos de geometría diferencial para considerar el efecto de curvatura, con alguna técnica óptica adecuada para la medición de los campos de desplazamientos tridimensionales para llevar a cabo la caracterización de los campos en las inmediaciones del vértice de la grieta y, de esta forma, determinar los parámetros que gobiernan los campos en las inmediaciones del vértice. Esta metodología se ha validado utilizando probetas cilíndricas huecas de pared delgada que contienen una grieta circunferencial para dos materiales distintos, acero inoxidable austenítico 304L y aleación de aluminio 2024-T3. Para la medición experimental de los campos de desplazamientos alrededor del vértice de grieta se ha empleado la técnica de correlación digital de imágenes 3D (DIC-3D), mientras que para la descripción de los campos en las inmediaciones del vértice de grieta se ha empleado el modelo basado en las series de expansión de Williams, modificado mediante geometría diferencial, tal y como se ha comentado anteriormente. Adicionalmente, se ha empleado el análisis mediante elementos finitos para proporcionar aquella información necesaria para la validación del método que no puede medirse experimentalmente mediante correlación digital de imágenes y proporcionar, de esta forma, información complementaria para una validación más completa. Asimismo, se ha realizado una comparación entre los campos obtenidos de forma experimental y los obtenidos numéricamente utilizando una técnica de descomposición de imágenes que permite comparar todo el campo circundante al vértice de grieta más allá del análisis de un único parámetro como es el factor de intensidad de tensiones para modo de carga I K_I. Otro punto importante abordado en este trabajo es el proceso de ajuste matemático llevado a cabo sobre los datos experimentales para la determinación de los parámetros que gobiernan la caracterización de los campos en el vértice de grieta. Así, se ha desarrollado un novedoso método de ajuste basado en optimización, combinando un algoritmo genético junto con un método determinístico, evitando, de esta forma, soluciones

iniciales mal condicionadas y asegurando la convergencia a un mínimo global con un coste computacional relativamente bajo. Dicho método de cálculo de parámetros gobernantes del campo en el vértice se ha validado utilizando un modelo más avanzado a los puramente elásticos como es el modelo CJP para así poner a prueba la metodología y llevarla al límite.

Los resultados muestran que los campos existentes alrededor del vértice de una grieta propagada por fatiga en una superficie no plana pueden caracterizarse perfectamente utilizando el método propuesto basado en geometría diferencial, proporcionando buenos resultados para los factores de intensidad de tensiones (<5% con respecto a las soluciones teóricas), los parámetros de calidad del ajuste (<0,5%), así como en términos de correspondencia entre los campos numéricos y experimentales (coeficientes de correlación superiores al 97%).

Con respecto al algoritmo para el cálculo de los parámetros que caracterizan la singularidad delante del vértice de la grieta, los resultados muestran que, para modelos complejos no puramente elásticos de caracterización de los campos como es el modelo CJP, la metodología desarrollada es más una necesidad que una mejora ya que ligeras desviaciones en parámetros como la localización del vértice de grieta puede inducir errores considerablemente altos en dichos parámetros. Por tanto, una metodología de cálculo robusta, precisa y fácilmente automatizable ha sido desarrollada y validada.

Abstract

In this work, a novel methodology for the characterisation of crack tip fields on non-planar (curved-shape) and zero Gaussian curvature cracked surfaces under plane stress conditions has been developed. The objective is to combine an analytical crack tip field model, previously modified employing differential geometry concepts to consider the curvature effect, and a suitable optical technique providing the 3D displacement fields surrounding the crack tip in order to characterise the crack tip fields and infer the parameters governing them. This approach is validated using hollow thin wall cylindrical samples containing a circumferential crack in two different materials, namely austenitic stainless steel 304L and aluminium alloy 2024-T3. 3D digital image correlation has been employed to measure the crack tip displacement fields and Williams' expansion series model (previously modified using differential geometry) was chosen to infer the crack tip parameters by employing different terms in the expansion series. Finite element analysis has been also employed to provide necessary information to validate the methodology that cannot be measured via digital experimental correlation and also provide complementary information for an integral validation. In addition, a comprehensive comparison between the experimental and numerical fields has been performed using an image comparison technique which allows comparing the whole crack tip field beyond the analysis of a single crack tip parameter i.e. K_I. Other important point addressed in this work is the fitting process for the determination of the crack tip parameters from the analysis of the experimental data. A novel hybrid optimisation-based fitting approach is developed by combining a genetic algorithm together with a deterministic method and hence, avoiding ill-conditioned initial solutions and ensuring the convergence to a global minimum with relatively low computational cost.

Results show that the crack tip fields on a cracked non-planar surface can be perfectly characterised using the proposed differential geometry-based approach providing well results for opening mode stress intensity factors (<5% regarding theoretical solutions), fitting quality parameters (<0.5%) as well as in terms of the agreement between numerical and experimental fields (correlation coefficients >98%).

Regarding the algorithm for determining the crack tip singularity parameters, results show that the algorithm is a necessity rather than an improvement especially in the case of more complex non-purely elastic models as the CJP model since slight deviations in some parameters as the crack tip location could lead to high errors in the calculation process of the crack tip parameters. Thus, a robust, accurate and easily automatable methodology has been developed and validated.

Nomenclature

Variables sorted as appear in the text

$\sigma_x, \sigma_y, \tau_{xy}$	Plane stress tensor
K_I	Opening mode stress intensity factor
K_{II}	In-plane shear mode stress intensity factor
σ_{0x}	Non-singular stress along the crack growth direction
r, θ	Polar coordinates
u_x, u_y, u_z	Displacement fields
G	Shear modulus
ν	Poisson's coefficient
κ	Function depending on Poisson's coefficient
p	Williams sum index
a_p	Mode I Williams' series coefficient
b_p	Mode II Williams' series coefficient
A, B, C, E, F	Coefficients of the CJP crack tip field model
j	Imaginary unit
z	Complex variable
K_F	opening mode stress intensity factor in the CJP model
K_R	retardation stress intensity factor in the CJP model
K_S	shear stress intensity factor in the CJP model
σ_{0y}	Non-singular stress along the crack opening direction
ΔK_{CJP}	effective stress intensity factor range by the CJP model
ξ, η	Parametrisation parameters
Q	Arbitrary point for Frenet-Serret trihedral definition
$\vec{\rho}(x, y, z)$	Position vector

$\vec{T}, \vec{B}, \vec{N}$	Frenet-Serret trihedral components
x', y'	Curve coordinates on the unwrapped surface
$\overrightarrow{e_x}, \overrightarrow{e_y}, \overrightarrow{e_z},$	Unity vectors along Cartesian directions
ξ_0, η_0	Lower integration limits for arc-lengths calculation
S_y	Yield stress 0.2%
ϵ_f	Elongation at failure
$\boldsymbol{\sigma}'$	Deviatory stress tensor
$\boldsymbol{X}$	Back-stress tensor
Y	Flow stress
σ_0, Q, b	Voce law parameters
$\bar{\epsilon}$	Equivalent plastic strain
C', D', Q'	Chaboche law parameters
$\dot{\boldsymbol{X}}$	Back-stress rate
$\dot{\boldsymbol{\epsilon}}$	Plastic strain rate
X_0, ϵ_0	Initial values at the beginning of each half-cycle
χ	Variable indicating loading or unloading
E'	Young modulus
K', n'	Ramberg-Osgood law parameters
u_T, u_B, u_N	Displacement fields along Frenet-Serret directions
r', θ'	Polar coordinates on the unwrapped plane
T_i, B_i, N_i	Components of the Frenet-Serret vectors with $i = x, y, z$
z_n	Out-of-unwrapped-plane coordinate
r_p	Dugdale plastic radius
$x_{SD}^{min}, x_{SD}^{max}, y_{SD}^{min}, y_{SD}^{max}$	Crack tip search domain bounds
f	Objective function
$\Delta x, \Delta y$	Crack tip coordinates
u_{x0}, u_{y0}, R_{xy}	Parameters modelling the rigid body motion
R_c, θ_c, z_c	Cylindrical coordinates
P	Applied load
t	Specimen thickness
W	Specimen width
a	Crack length
R	Cylindrical pipe mean radius
γ	Angle subtended by the crack
$I(i,j)$	Intensity matrix

f_i	Intensity of each Tchebichef moment
$\widetilde{T}_i$	Tchebichef polynomial shape descriptor
d	Euclidean distance between computed crack tip locations
d/a	Normalised Euclidean distance between crack tip locations
t_{GA}	Genetic algorithm optimisation time
t_{IP}	Interior-Point algorithm optimisation time
t_T	Total optimisation time
z_c/z_{max}	Normalised cylinder half-length
$\Delta K_I^{95\%}$	Stress intensity factor confidence intervals range
γ/π	Normalised crack length

Contents

Table of contents

Tabla de contenidos

List of Figures

List of Tables

1.Introduction

1.1. Introduction, motivation and objectives

Fatigue cracks are the main source of failures in in-service mechanical components. It is estimated that around 90% of failures are due to fatigue processes [1]. In this scenario, the challenge for engineers is to reduce, or at least, predict these fatigue fails to avoid, for instance, production problems or more seriously, human safety problems. Thus, the way forward consists of a better understanding of fatigue cracks and their behaviour during crack growth allowing not only to achieve safety guarantees but optimising design and manufacturing processes and hence, reducing economical costs and environmental impact. The vertiginous technological development that happened during the last decades has allowed the development of better, non-invasive and robust experimental optical techniques for assessing problems related to fatigue crack growth. Since the 80s, many works have been conducted where optical techniques have been combined with analytical crack tip field models to study and analyse the structural integrity in mechanical elements and to try to improve a better understanding of the mechanisms governing fatigue crack growth. Some of the topics investigated by using full-field optical techniques are the experimental determination of stress intensity factors [2–5], the experimental evaluation of plasticity induced crack shielding [6–11], the experimental evaluation of the effect on fatigue crack growth due to the application of overloads [12–14] or the experimental estimation of the plastic zone at the crack tip [15–17], among others. Although many methodologies have been developed in the last decades, there are some unresolved, unclear or improvable issues that should be assessed [9,18–24]. The present work addresses the crack tip field characterisation issue in non-planar surfaces (curved-shape) which is a topic poorly studied by researchers and thus, not existing much information about it in the literature. Therefore, in this thesis, an experimental-theoretical formulation to extend crack tip field models to the analysis of non-planar cracked surfaces under plane stress conditions is developed by modifying the original formulation of the crack tip field models for flat samples by using differential geometry. The objective is to determine crack tip parameters via a suitable optical experimental technique such as 3D digital image correlation

(DIC-3D) together with the theoretical description of the crack tip fields either for the analysis of complex geometry industrial components or for research purposes. In addition, finite element analysis is also included to provide that crack tip field information that cannot be measured via optical experimental techniques such as through-thickness information or full stress tensor data. Beyond the experimental extension of crack tip field models to the analysis of non-planar surfaces, the fitting process for determining crack tip singularity parameters from experimentally measured data is fully addressed and analysed, which is a critical aspect. The objective is to develop a robust and automatic methodology for the determination of the crack tip parameters by combing a crack tip field model with a suitable experimental optical technique to provide crack tip field data. This approach arises mainly due to the sensitivity of some crack tip field models [7,25] to the initially chosen position of the crack tip when the characterising parameters are inferred from experimental data. To avoid user-supplied crack tip position providing inaccurate fitting results, this variable is included in the mathematical fitting turning the problem into a highly non-linear problem. According to this, the mathematical problem is addressed using a hybrid optimisation approach based on the combination of a heuristic and a non-initial solution required method (Genetic Algorithm) [26] and a deterministic Newton-type one (Interior-Point Method) [27].

1.2. Scope of the thesis

The main objective of the current thesis is the development of a novel methodology to characterise crack tip fields on non flat surfaces by combining the use of digital image correlation in 3D together with the modification of a crack tip field model for flat samples by using differential geometry. According to this, the thesis has been organised into 8 chapters. Thus, in this first Chapter, the objectives and the motivation of the work have been detailed. The rest of the chapters are briefly described below.

In Chapter 2, fundamentals and theory are described. First, the three crack tip field models employed in this work are described. These models are Irwin-Westergaard's approach, Williams' expansion series and the CJP model, by Christopher, James and Patterson. Next, some differential geometry fundamentals that are necessary to develop the extension of the 2D crack tip field models to the analysis of non-planar surfaces are described. Moreover, the two optimisation algorithms employed for the estimation of the crack tip characterising parameters from experimental data are described and in last, the fundamentals of the experimental full-field optical technique employed in this thesis, digital image correlation, are detailed.

Chapter 3 is a literature review where three topics are addressed. Firstly, the damage tolerance approach for fatigue assessment and the contribution of experimental optical techniques on the

study and investigation of this topic. Secondly, the experimental characterisation of crack tip fields on non-planar elements by employing 2D flat models is reviewed. Finally, the mathematical fitting approaches for inferring the parameters characterising crack tip fields from experimental data are addressed.

In Chapter 4, the experimental work and the numerical modelling are described. Regarding the experimental campaign, two kinds of fatigue testing are detailed both in CT specimens and in hollow cylindrical specimens using 2D and 3D Digital Image Correlation, respectively. Next, two numerical models replicating the fatigue testing on the cylindrical pipe specimens are described.

In Chapter 5, the different methodologies are detailed. First, the extended formulation of crack tip field models to the analysis of non-flat cracked elements based on differential geometry is described. Secondly, the procedure for determining the crack tip parameters either from experimental or numerical data is detailed. Thirdly, experimental correlations to validate the experimental results are described, and finally, the Image Decomposition technique for the full-field comparison of the experimental and numerical displacements maps is described.

Results are presented and discussed in Chapter 6. Results are organised in two sections. In the first one, the improved methodology for determining the crack tip characterising parameters and the crack tip location is validated. In the second section, the proposed method for the calculation of the crack tip parameters on non-flat cracked elements is experimentally validated and compared with numerical data and theoretical correlations.

Finally, in Chapter 7, the conclusions of the thesis are described and in Chapter 8, different possible future works deriving from the ideas or results reported in this work are detailed and briefly discussed.

1E. Introducción

1.1E. Introducción, motivación y objetivos

Las grietas por fatiga son el principal origen de los fallos que se producen en componentes mecánicos en servicio. Se estima que en torno al 90% de los fallos en componentes mecánicos son debidos al proceso de fatiga [1]. En este escenario, la misión del ingeniero es reducir o, al menos, predecir dichos fallos para evitar entre otros, problemas de producción o algo más serio, como es poner en riesgo la vida de las personas. De esta forma, el camino a seguir comienza por un mejor entendimiento de las grietas por fatiga, así como su comportamiento durante el crecimiento de éstas, y no solo para conseguir los requerimientos de seguridad, sino para optimizar diseños y procesos de fabricación que permitirían, además, reducir costes e impacto medioambiental. El vertiginoso desarrollo tecnológico acontecido en las últimas décadas ha permitido desarrollar mejores y robustas técnicas ópticas experimentales non invasivas que han dado pie analizar problemas asociados al crecimiento de grieta por fatiga. Desde los años 80 se han llevado a cabo una inmensa cantidad de trabajos en los cuales se han combinado determinadas técnicas ópticas de campo completo con modelos analíticos para la descripción de campos en las inmediaciones del vértice de grieta para estudiar y analizar la integridad estructural de elementos mecánicos y así, proporcionar un mejor entendimiento en los mecanismos que gobiernan el crecimiento de grieta por fatiga. Como ejemplos, algunos de estos tópicos son, la determinación experimental de los factores de intensidad de tensiones [2–5], la evaluación experimental del efecto de shielding inducido por plasticidad [6–11], el efecto de las sobrecargas en el crecimiento de grieta a fatiga [12–14] o la determinación experimental de la zona plástica circundante al vértice [15–17], entre otros. Aunque una gran cantidad de metodologías y trabajos han sido desarrollados en estas últimas décadas, aún existen ciertas cuestiones no totalmente claras, sin resolver o que presentan ciertos aspectos presumiblemente mejorables [9,18–24]. Este trabajo aborda la caracterización de campos en las inmediaciones del vértice de grieta en superficies no planas (de forma curva) el cual es un tema escasamente abordado hasta la fecha por los investigadores y del que no existe mucha información en la literatura actual. Por lo tanto, en la

presente tesis se desarrolla una metodología teórico-experimental basada en geometría diferencial para extender el uso de los modelos planos de caracterización de campos a superficies curvas agrietadas en condiciones de tensión plana. El objetivo es combinar alguna técnica óptica experimental adecuada, como correlación digital de imágenes 3D (DIC-3D), con la formulación extendida que se propone de dichos modelos para bien, analizar componentes industriales complejos o bien para fines de investigación. Además, se incluye el análisis por elementos finitos para proporcionar aquella información que no puede obtener mediante técnicas ópticas experimental como los campos dentro del elemento (a través del espesor) así como los tensores de tensión o deformación completos. Adicionalmente, el proceso matemático de ajuste para la obtención de los parámetros gobernantes de la singularidad en el vértice es analizado, el cual es un aspecto crítico para la determinación de estos. El objetivo es desarrollar una metodología robusta y automática para obtener dichos parámetros combinando campos experimentales con modelos analíticos de descripción de campos. Esta metodología surge principalmente debido a la alta sensibilidad de algunos modelos analíticos a la posición del vértice de grieta seleccionada durante el proceso de cálculo [7,25]. Así, para evitar valores de posición del vértice manualmente seleccionados, los cuales pueden inducir a resultados erróneos, esta variable se incluye en el proceso de ajuste matemático transformando el problema matemático en un problema de ajuste altamente no lineal. Por lo tanto, se propone abordar el problema utilizando un método híbrido de optimización basado en la combinación de un método heurístico que no requiere solución inicial (Algoritmo Genético) [26] con otro método determinístico de tipo Newton (Método de Punto Interior) [27].

1.2E. Alcance de la tesis

El objetivo principal de la presente tesis es el desarrollo de una metodología novedosa para caracterizar los campos en las inmediaciones del vértice de grieta en superficies curvas combinando Correlación Digital de Imágenes 3D junto con un modelo de caracterización de los campos circundantes al vértice previamente modificado utilizando geometría diferencial. De acuerdo con esto, la tesis se ha organizado en 8 capítulos. Así, en este primer capítulo se han detallado los objetivos y la motivación del trabajo. A continuación, se describen brevemente el resto de los capítulos.

En el Capítulo 2, se describen los fundamentos y los aspectos teóricos. En primer lugar, se describen los tres modelos de caracterización de campos en el vértice empleados en este trabajo. Estos modelos son, el de Irwin basado en las ecuaciones de Westergaard, las series de expansión de Williams y el modelo de Christopher, James y Patterson, conocido como modelo CJP. A continuación, se describen los fundamentos de geometría diferencial necesarios para desarrollar la extensión de los modelos planos bidimensionales al análisis de superficies no planas. Además,

se describen los dos algoritmos de optimización empleados para la estimación de los parámetros de caracterización de la singularidad en el vértice de grieta a partir de datos experimentales y, por último, se detallan los fundamentos de la técnica óptica experimental de campo completo empleada en esta tesis, Correlación Digital de Imágenes.

En el capítulo 3 se realiza una revisión bibliográfica en la que se abordan a grandes rasgos tres temas. En primer lugar, el método de tolerancia al daño (damage-tolerance approach) para la evaluación de fatiga y la contribución de las técnicas ópticas experimentales en el estudio e investigación de este tema. En segundo lugar, se revisa la caracterización experimental de los campos en la vecindad del vértice de grieta en elementos no planos mediante el empleo de modelos planos bidimensionales. Por último, se abordan los métodos de ajuste matemático para estimar los parámetros que caracterizan la singularidad a partir de los datos experimentales.

En el capítulo 4 se describe el trabajo experimental y el modelado numérico. En cuanto a la campaña experimental, se detallan dos tipos de ensayos a fatiga, tanto en probetas CT como en probetas cilíndricas huecas utilizando Correlación Digital de Imágenes 2D y 3D, respectivamente. A continuación, se describen dos modelos numéricos de elementos finitos que reproducen los ensayos de fatiga en las probetas cilíndricas.

En el capítulo 5, se detallan las diferentes metodologías. En primer lugar, se describe la formulación extendida de los modelos de campos en el vértice de grieta al análisis de elementos agrietados no planos basada en geometría diferencial. En segundo lugar, se detalla el procedimiento para determinar los parámetros de la singularidad en el vértice a partir de datos experimentales o numéricos. En tercer lugar, se describen las correlaciones empíricas utilizadas para validar los resultados experimentales y, por último, se describe la técnica de descomposición de imágenes para la comparación completa de los mapas de desplazamiento experimentales y numéricos.

Los resultados son presentados y discutidos en el capítulo 6. Dichos resultados se organizan en dos secciones. En la primera, se valida la metodología mejorada para determinar los parámetros de caracterización de la singularidad en el vértice y la localización del mismo. En la segunda sección, se valida experimentalmente el método propuesto para el cálculo de los parámetros gobernantes en el vértice en elementos fracturados no planos y se realizan comparaciones tanto con datos numéricos como con correlaciones teóricas.

Finalmente, en el capítulo 7, se describen las conclusiones de la tesis y en el capítulo 8, se detallan y discuten brevemente diferentes posibles trabajos futuros derivados de las ideas o resultados reportados en este trabajo.

2.Fundamentals and theory

Chapter 2 covers those necessary fundamentals and theoretical aspects which layout the basis of the present work. First, the three employed mathematical crack tip fields' models are described. Next, those differential geometry aspects necessary for developing the proposed approach are presented. Subsequently, the employed mathematical optimisation algorithms are described and in last, the fundamentals of the used experimental optical technique, digital image correlation, are presented.

2.1. Mathematical description of the crack tip fields

In the following epigraphs, the mathematical models employed in the course of this investigation for the characterisation of the crack tip fields are described.

2.1.1. Irwin-Westergaard's approach

Based on Westergaard's stress function [28] for describing the linear and elastic stress fields surrounding a crack on an infinite plate, Irwin [29] established that the crack tip singularity is governed by two parameters representing the stress intensity and a non-singular stress along the crack growth direction (T-stress). Hence, according to this model, the stress tensor near the crack tip is given by equation 1.

$$\begin{Bmatrix}\sigma_x\\ \sigma_y\\ \tau_{xy}\end{Bmatrix} = \frac{K_I}{\sqrt{2\pi r}}\begin{Bmatrix}\cos\frac{\theta}{2}\left(1-\sin\frac{\theta}{2}\sin\frac{3\theta}{2}\right)\\ \cos\frac{\theta}{2}\left(1+\sin\frac{\theta}{2}\sin\frac{3\theta}{2}\right)\\ \sin\frac{\theta}{2}\cos\frac{3\theta}{2}\end{Bmatrix} + \frac{K_{II}}{\sqrt{2\pi r}}\begin{Bmatrix}-\sin\frac{\theta}{2}\left(2+\cos\frac{\theta}{2}\cos\frac{3\theta}{2}\right)\\ \sin\frac{\theta}{2}\cos\frac{\theta}{2}\sin\frac{3\theta}{2}\\ \cos\frac{\theta}{2}\left(1-\sin\frac{\theta}{2}\sin\frac{3\theta}{2}\right)\end{Bmatrix} + \begin{Bmatrix}\sigma_{0x}\\ 0\\ 0\end{Bmatrix} \quad (1)$$

Where σ_x, σ_y and τ_{xy} are the components of the plane stress tensor in the neighbourhood of the crack tip, r and θ are a set of polar coordinates referred to the crack tip (see Figure 1). K_I and K_{II} are the stress intensity factors for fracture mode I (opening mode stress intensity factor) and mode II (in-plane shear mode stress intensity factor), respectively, and σ_{0x} is the non-singular stress

along the crack growth direction. In addition, the displacement fields on the crack plane are given by equation 2.

$$\begin{Bmatrix} u_x \\ u_y \end{Bmatrix} = \frac{K_I}{2G}\sqrt{\frac{r}{2\pi}}\begin{Bmatrix} \cos\frac{\theta}{2}\left(\kappa - 1 + 2\sin^2\frac{\theta}{2}\right) \\ \sin\frac{\theta}{2}\left(\kappa + 1 - 2\cos^2\frac{\theta}{2}\right) \end{Bmatrix} + \frac{K_{II}}{2G}\sqrt{\frac{r}{2\pi}}\begin{Bmatrix} \sin\frac{\theta}{2}\left(\kappa + 1 + 2\cos^2\frac{\theta}{2}\right) \\ \cos\frac{\theta}{2}\left(\kappa - 1 - 2\sin^2\frac{\theta}{2}\right) \end{Bmatrix} + \frac{\sigma_{0x}}{8G}\begin{Bmatrix} (\kappa+1)\cos\theta \\ (\kappa-3)\sin\theta \end{Bmatrix} \tag{2}$$

Here u_x and u_y are the components of the plane displacement field, G is the shear modulus and κ is $\frac{3-\nu}{1+\nu}$ for plane stress or $3-4\nu$ for plane strain, and ν is the Poisson's ratio of the material.

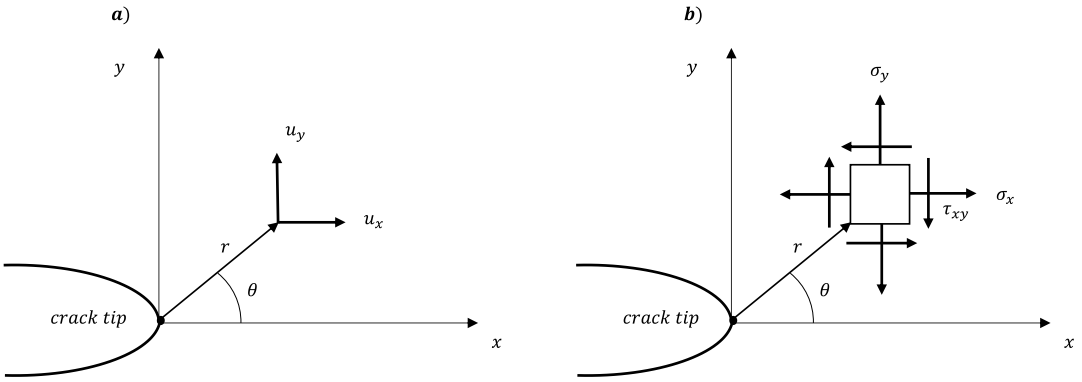

Figure 1: a) Displacement field components and b) stress tensor components for a point surrounding the crack tip in terms of the polar coordinates.

2.1.2. Williams' expansion series

Williams [30] described the linear and elastic stress fields surrounding a crack as a mathematical series governed by different coefficients. The stress tensor according to Williams is given by equation 3.

$$\begin{Bmatrix} \sigma_x \\ \sigma_y \\ \tau_{xy} \end{Bmatrix} = \sum_{p=1}^{\infty}\frac{p}{2}a_p r^{\frac{p-2}{2}}\begin{Bmatrix} \left(2+(-1)^p+\frac{p}{2}\right)\cos\left(\frac{p}{2}-1\right)\theta - \left(\frac{p}{2}-1\right)\cos\left(\frac{p}{2}-3\right)\theta \\ \left(2-(-1)^p-\frac{p}{2}\right)\cos\left(\frac{p}{2}-1\right)\theta + \left(\frac{p}{2}-1\right)\cos\left(\frac{p}{2}-3\right)\theta \\ -\left((-1)^p+\frac{p}{2}\right)\sin\left(\frac{p}{2}-1\right)\theta + \left(\frac{p}{2}-1\right)\sin\left(\frac{p}{2}-3\right)\theta \end{Bmatrix} - \sum_{p=1}^{\infty}\frac{p}{2}b_p r^{\frac{p-2}{2}}\begin{Bmatrix} \left(2-(-1)^p+\frac{p}{2}\right)\sin\left(\frac{p}{2}-1\right)\theta - \left(\frac{p}{2}-1\right)\sin\left(\frac{p}{2}-3\right)\theta \\ \left(2+(-1)^p-\frac{p}{2}\right)\sin\left(\frac{p}{2}-1\right)\theta + \left(\frac{p}{2}-1\right)\sin\left(\frac{p}{2}-3\right)\theta \\ -\left((-1)^p-\frac{p}{2}\right)\cos\left(\frac{p}{2}-1\right)\theta - \left(\frac{p}{2}-1\right)\cos\left(\frac{p}{2}-3\right)\theta \end{Bmatrix} \tag{3}$$

Where p is a sum index, a_p are the coefficients related to fracture mode I ($K_I = \sqrt{2\pi}\,a_1$) and b_p are the coefficients related to fracture mode II ($K_{II} = \sqrt{2\pi}\,b_1$). The T-stress is determined from the second coefficient for mode I term ($\sigma_{0x} = 4a_2$). In a similar way, the displacement fields are given by equation 4

$$\begin{Bmatrix} u_x \\ u_y \end{Bmatrix} = \sum_{p=1}^{\infty} \frac{r^{\frac{p}{2}}}{2G} a_p \begin{Bmatrix} \left(\kappa + \frac{p}{2} + (-1)^p\right)\cos\frac{p\theta}{2} - \frac{p}{2}\cos\frac{(p-4)\theta}{2} \\ \left(\kappa - \frac{p}{2} - (-1)^p\right)\sin\frac{p\theta}{2} + \frac{p}{2}\sin\frac{(p-4)\theta}{2} \end{Bmatrix} + \sum_{p=1}^{\infty} \frac{r^{\frac{p}{2}}}{2G} b_p \begin{Bmatrix} -\left(\kappa + \frac{p}{2} - (-1)^p\right)\sin\frac{p\theta}{2} + \frac{p}{2}\sin\frac{(p-4)\theta}{2} \\ \left(\kappa - \frac{p}{2} + (-1)^p\right)\cos\frac{p\theta}{2} - \frac{p}{2}\cos\frac{(p-4)\theta}{2} \end{Bmatrix} \quad (4)$$

Williams' model is a generalisation of Irwin-Westergaard's approach. In other words, Irwin-Westergaard's model is a particular case of Williams' model when the two first series terms are employed to describe the crack tip fields. Actually, higher-order terms are negligible when a zone within the singularity zone is described and the crack tip plasticity no longer affects the elastic field.

2.1.3. Christopher, James and Patterson model

The model developed by Christopher, James and Patterson, known as the CJP model [6,7,31], is a linear and elastic crack tip field model considering the influence of the plastic enclave on the global elastic field. The CJP model is based on the Nurse and Patterson formulation [3,32] for describing Muskhelishvili's complex potential functions [33] as Fourier series. This linear and elastic model is able to reproduce any shielding effect on the K-field by considering the effect of the plasticity-induced crack wake contact and the compatibility-induced strains at the elastoplastic boundary. According to the CJP model, crack tip stress fields are characterised by five coefficients as follows:

$$\begin{Bmatrix} \sigma_x \\ \sigma_y \\ \tau_{xy} \end{Bmatrix} = \frac{1}{\sqrt{r}} \begin{Bmatrix} -\frac{1}{2}(A + 4B + 8E)\cos\frac{\theta}{2} - \frac{1}{2}B\cos\frac{5\theta}{2} - \frac{1}{2}E\left(\ln r\left(\cos\frac{5\theta}{2} + 3\cos\frac{\theta}{2}\right) + \theta\left(\sin\frac{5\theta}{2} + 3\sin\frac{\theta}{2}\right)\right) \\ \frac{1}{2}(A - 4B - 8E)\cos\frac{\theta}{2} + \frac{1}{2}B\cos\frac{5\theta}{2} + \frac{1}{2}E\left(\ln r\left(\cos\frac{5\theta}{2} - 5\cos\frac{\theta}{2}\right) + \theta\left(\sin\frac{5\theta}{2} - 5\sin\frac{\theta}{2}\right)\right) \\ \frac{1}{2}\left(A\sin\frac{\theta}{2} + B\sin\frac{5\theta}{2}\right) - E\sin\theta\left(\ln r\cos\frac{3\theta}{2} + \theta\sin\frac{3\theta}{2}\right) \end{Bmatrix} + \begin{Bmatrix} C \\ F \\ 0 \end{Bmatrix} \quad (5)$$

Where A, B, C, E and F are the coefficients governing the stress singularity field. The displacement fields are given by equation 6

$$2G(u_x + u_y j) = \kappa\left[-2(B+2E)z^{\frac{1}{2}} + 4Ez^{\frac{1}{2}} - 2Ez^{\frac{1}{2}}\ln(z) - \frac{C-F}{4}z\right] - z\left[-(B+2E)\bar{z}^{\frac{-1}{2}} - E\bar{z}^{\frac{-1}{2}}\overline{\ln(z)} - \frac{C-F}{4}\right] - \left[A\bar{z}^{\frac{1}{2}} + E\bar{z}^{\frac{1}{2}}\overline{\ln(z)} - 2E\bar{z}^{\frac{1}{2}} + \frac{C+F}{2}\bar{z}\right] \quad (6)$$

Where j is the imaginary unit and z is a complex variable $z = r(cos\theta + j\sin\theta)$. These five coefficients define three stress intensity factors and two non-singular stresses as shown in equations 7, 8, 9, 10 and 11. K_F corresponds to the equivalent mode I stress intensity factor, K_R, known as the retardation stress intensity factor, is related to the shielding effect, and K_S is the shear stress intensity factor. σ_{0x} and σ_{0y} represent the non-singular stresses along the crack growth and the crack opening directions, respectively.

$$K_F = \sqrt{\frac{\pi}{2}}(A - 3B - 8E) \quad (7)$$

$$K_R = -\pi\sqrt{\frac{\pi}{2}}E \quad (8)$$

$$K_S = \sqrt{\frac{\pi}{2}}(A + B) \quad (9)$$

$$\sigma_{0x} = -C \quad (10)$$

$$\sigma_{0y} = -F \quad (11)$$

According to some authors [13,34], the effective stress intensity factor range accounting for the shielding effect is obtained through the combination of ΔK_F and ΔK_R as displayed in equation 12.

$$\Delta K_{CJP} = \left(K_{F,max} \pm K_{R,max}\right) - \left(K_{F,min} \pm K_{R,min}\right) = \Delta K_F \pm \Delta K_R \quad (12)$$

Here operator Δ indicates the range during a loading cycle. Positives signs in K_R imply crack growth acceleration ($K_F + |K_R|$) and negative signs crack growth retardation ($K_F - |K_R|$).

2.2. Differential geometry fundamentals

If a non-planar surface is under consideration, this can be parametrised in terms of two parameters ξ and η that represent two orthogonal directions. If a point over the surface Q is located through a position vector $\vec{\rho}(x, y, z)$ referring to an arbitrary coordinate system in the space, the Frenet-Serret trihedral [35], which is compound by three orthogonal vectors called tangential, binormal and normal, can be defined in that point.

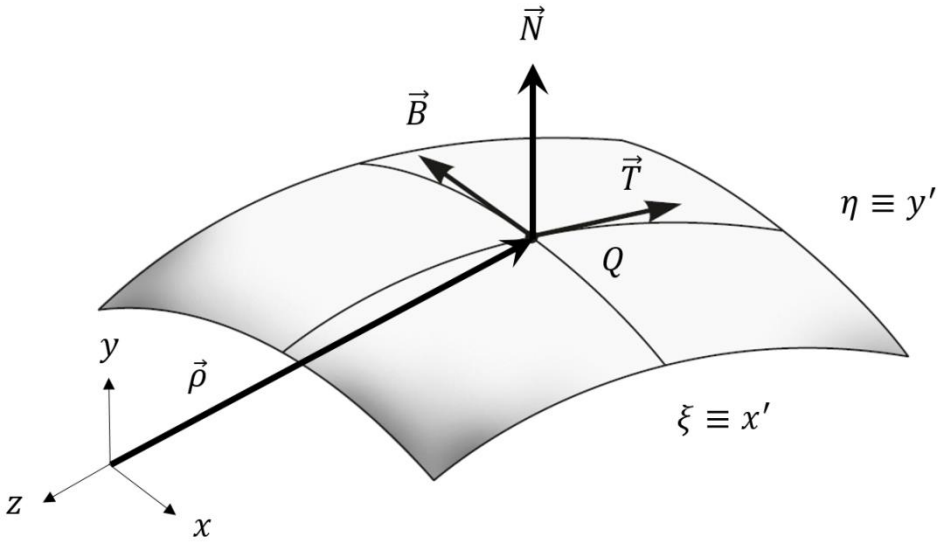

Figure 2: Frenet-Serret trihedral in a point Q of a curve surface [35].

These three unity vectors are calculated through the position vector of the surface points and the parametrisation directions as shown in equations 13, 14 and 15. The curve coordinates are calculated by integrating the modulus of the tangential and binormal vectors as shown in equations 16 and 17.

$$\vec{T} = \frac{\frac{\partial \vec{\rho}}{\partial \xi}}{\left\|\frac{\partial \vec{\rho}}{\partial \xi}\right\|} = \frac{\frac{\partial x}{\partial \xi}\overrightarrow{e_x} + \frac{\partial y}{\partial \xi}\overrightarrow{e_y} + \frac{\partial z}{\partial \xi}\overrightarrow{e_z}}{\sqrt{\left(\frac{\partial x}{\partial \xi}\right)^2 + \left(\frac{\partial y}{\partial \xi}\right)^2 + \left(\frac{\partial z}{\partial \xi}\right)^2}} \tag{13}$$

$$\vec{B} = \frac{\frac{\partial \vec{\rho}}{\partial \eta}}{\left\|\frac{\partial \vec{\rho}}{\partial \eta}\right\|} = \frac{\frac{\partial x}{\partial \eta}\overrightarrow{e_x} + \frac{\partial y}{\partial \eta}\overrightarrow{e_y} + \frac{\partial z}{\partial \eta}\overrightarrow{e_z}}{\sqrt{\left(\frac{\partial x}{\partial \eta}\right)^2 + \left(\frac{\partial y}{\partial \eta}\right)^2 + \left(\frac{\partial z}{\partial \eta}\right)^2}} \tag{14}$$

$$\vec{N} = \frac{\frac{\partial \vec{\rho}}{\partial \xi}}{\left\|\frac{\partial \vec{\rho}}{\partial \xi}\right\|} \times \frac{\frac{\partial \vec{\rho}}{\partial \eta}}{\left\|\frac{\partial \vec{\rho}}{\partial \eta}\right\|} \tag{15}$$

$$x' = \int_{\xi_0}^{\xi} \sqrt{\left(\frac{\partial x}{\partial \xi}\right)^2 + \left(\frac{\partial y}{\partial \xi}\right)^2 + \left(\frac{\partial z}{\partial \xi}\right)^2}\, d\xi \tag{16}$$

$$y' = \int_{\eta_0}^{\eta} \sqrt{\left(\frac{\partial x}{\partial \eta}\right)^2 + \left(\frac{\partial y}{\partial \eta}\right)^2 + \left(\frac{\partial z}{\partial \eta}\right)^2}\, d\eta \tag{17}$$

Where $\vec{T}$ is the tangential vector, $\vec{B}$ is the binormal vector and $\vec{N}$ is the normal vector. e_x, e_y and e_z are the unitary components of a vector in a Cartesian coordinate system and $\times$ is the operator cross product. Double verticals bars denote the operator norm (Euclidean distance), $x'$and y' are the arc-length coordinates and ξ_0 and η_0 are the lower integration limits for curve coordinates calculation.

2.3. Multi-dimensional non-linear optimisation algorithms

In this epigraph, the two optimisation algorithms employed to determine the crack tip characterising parameters from experimental data are briefly described.

2.3.1. Interior-Point methods for nonlinear optimisation

Barrier methods or Interior-Point (IP) algorithms as employed in non-linear optimisation [27,36–39] are deterministic and gradient-based methods used in non-linear optimisation problems involving constraints. As reported by some authors [40], these kinds of algorithms are recognised as the most appropriate for large-scale optimisation problems. Originally, IP algorithms arose as alternative methods to the Dantzig-Simplex method [41] for linear optimisation problems involving a high number of unknowns (large linear optimisation problems). IP algorithms ensure a fast and proper convergence provided that a well-conditioned initial solution is given. The objective is to transform the inequality constrained optimisation problem into an equality-constrained problem that is easier to solve. Thus, a logarithm term (barrier term) is included in the objective function modelling the removed inequality constrains and turning the problem into a penalty or barrier problem. Hence, by applying the first-order optimality conditions (Karush-Kuhn-Tucker) [42] to the penalty equality-constrained problem, a nonlinear equation system is obtained that can be solved via Newton's method [40].

2.3.2. Genetic algorithms for non-linear optimisation

Genetic algorithms (GA) [26] as used in mathematical optimisation are heuristic, direct search, constrained or unconstrained, and zero-order methods based on concepts derived from Darwinian species evolution theory. In general, these kinds of algorithms operate following a "survival process" as follows. An initial population (set of stochastically generated initial solutions) is created and the "population individuals" are evaluated through a fitness function (objective function) to determine their 'survival' value. According to evolutionary theory, the fittest progenitors must produce the fittest subsequent generation. Thus, the best individuals in the population, according to their fitness value, are selected to create a new and improved generation by replacing the least fit individuals. A better solution is then generated by combining the best progenitors through crossover and mutation operations. This process is repeated through subsequent generations until a solution is found that satisfies the fitness function to the desired accuracy. In mathematical optimisation, GAs are employed in highly nonlinear problems to find global minima. This kind of algorithm is computationally expensive since they usually require a large number of iterations. However, these methods are the only ones that can ensure that a global minimum solution is found. Their advantage is that they do not require accurate initial solutions due to their stochastic and evolutionary nature, compared with other deterministic methods where

a well-chosen initial solution is required to achieve a global minimum. GA techniques are often used in conjunction with a second technique to find local minima; this is useful when several global minima have similar values.

2.3.3. Hybrid approach. Combining deterministic and heuristic algorithms

As described in previous sections, deterministic methods need well-conditioned initial solutions to ensure the convergence to an optimum value. In addition, heuristic and non-initial solution required algorithms as GAs are the only one able to find optimum values but a high computational cost is required. Hence, the most effective way of addressing this kind of problems is by combining both methods and hence, obtaining a hybrid optimisation approach. Thus, the optimisation process starts using a GA, which does not require any initial solution and avoid convergence risks when this variable is user-supplied. After a certain number of iterations when the solution is relatively closer to the optimum, the IP algorithm starts to iterate employing the last one solution generated by the GA. In this way, the disadvantages of both techniques are removed since initial solutions are avoided due to the use of GA and computational cost are considerably reduced since IP method achieves a fast solution ensuring the convergence to a global minima.

2.4. Digital image correlation

Digital image correlation (DIC) [43] is an experimental technique for in-plane and out-of-plane displacement measurements on a solid surface. In contrast with single-point measurement, DIC is a full-field and non-invasive optical technique which allows measuring the displacement fields without possible apparatus influence on the measurement. First image correlation attempts to measure the displacement field on an element arose in the 80s with the pioneering works of Peters et al [44], Sutton et al [45,46], Anderson et al [47] and Chu et al [48]. Nowadays, DIC is a well-established technique commonly used in both research works and industrial applications. Today, many commercial systems can be found on the market [49]. Moreover, DIC has had a positive impact on fatigue and fracture research fields and it has underpinned many works (detailed in Chapter 3) providing a better understanding of fatigue and fracture issues such as crack tip governing parameters, crack closure or crack tip plasticity influence among many others.

DIC calculates the displacement field by comparing a sequence of images referred to a reference image representing the unloaded or the zero state. Thus, the displacement field is determined through the differences between both loaded and unloaded images. The comparison between both images is done by splitting the image into facets that are compared with the same facets in the unloaded state allowing obtaining the displacement of each facet (see Figure 3). The matching

between deformed and not deformed facets is achieved through generating stochastic patterns allowing the same facet to be recognised in both images univocally. The stochastic patterns are usually generated by painting the solid with a black speckle over a white background (or reciprocal depending on the case). In some cases depending on the spatial resolution as well as the material surface roughness, it is not necessary to apply paint layers since the material surface could provide stochastic patterns. Some typical speckle patterns are shown in Figure 4

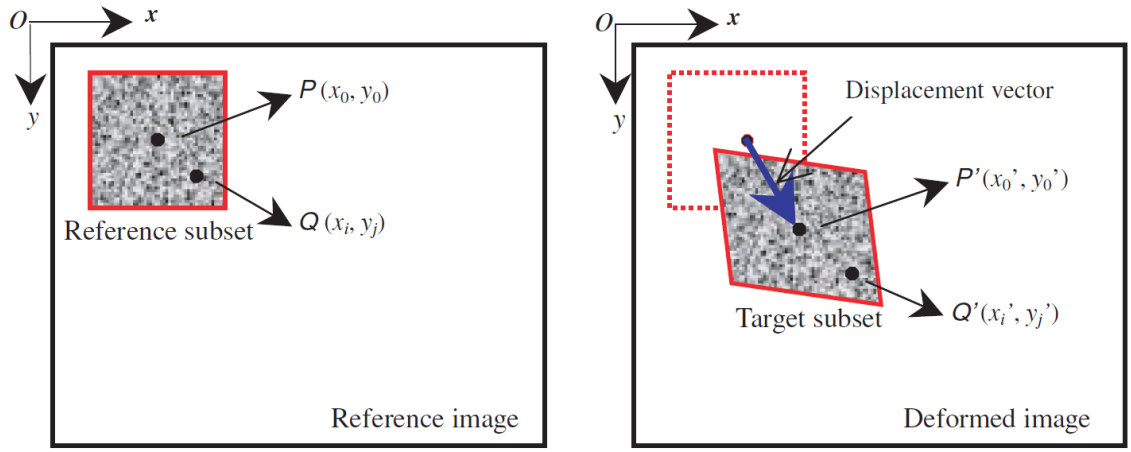

Figure 3: Example of subset on reference and deformed images for image matching [50]

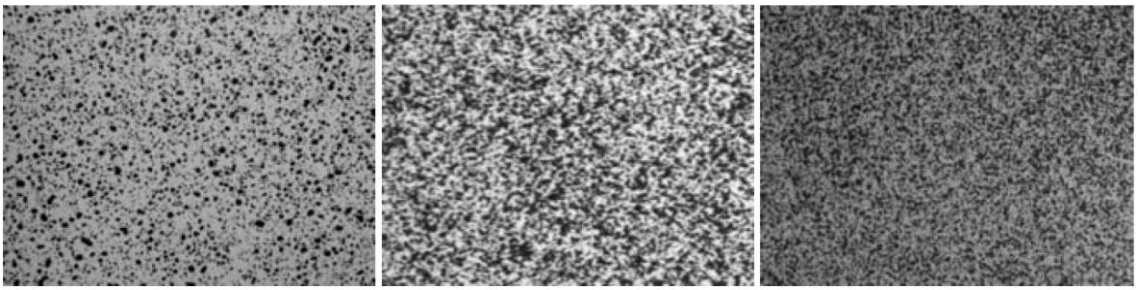

Figure 4: Examples of typical speckle patterns [43]

DIC facets matching is done and quantified by defining a correlation criterion. Especially, two criteria are the most popular, the cross-correlation (CC) and the sum-squares differences (SSD) approaches. Based on previous criteria, two kinds of approaches can be derived normalising (NCC and ZNCC) or zero normalising (NSSD or ZNSSD) the previous functions. According to Pan et al [50]; zero normalised type criteria provided better matching results since avoiding illumination problems such as linear scale and the intensity offset. In fact, commercial DIC algorithms usually employ some of these criteria by default.

As mentioned above, DIC can be used to obtain in-plane and also out-of-plane measurements. For in-plane measurements, the two-dimensional version, known as 2D-DIC, is usually employed. In this case, a single-camera system is enough to obtain the plane displacement field. A typical set-up for 2D-DIC is shown in Figure 5. As shown in this Figure, for a correct two-

dimensional measurement, the camera sensor must be placed coplanar with the measurement plane. Thus, the sensor optical axis must be perpendicular to the specimen/solid surface. Otherwise, measurement results would not be correct since the out-of-plane motion could be captured as an in-plane motion and hence, introducing a significant measurement error. Another important point is the specimen thickness variation during the loading process. When a plane solid is vertically loaded, two deformations appear due to Poisson's effect. One of them occurs in the horizontal axis and the other in the out-of-plane direction (thickness reduction if traction or thickness increment if compression). The thickness reduction leads to a motion which could be interpreted as an in-plane horizontal motion and hence, modifying the displacement measurement. Although some authors have proved that this effect can be removed by employing telecentric lenses [51], 2D-DIC measurements still require accurate setup configurations to avoid these kinds of problems.

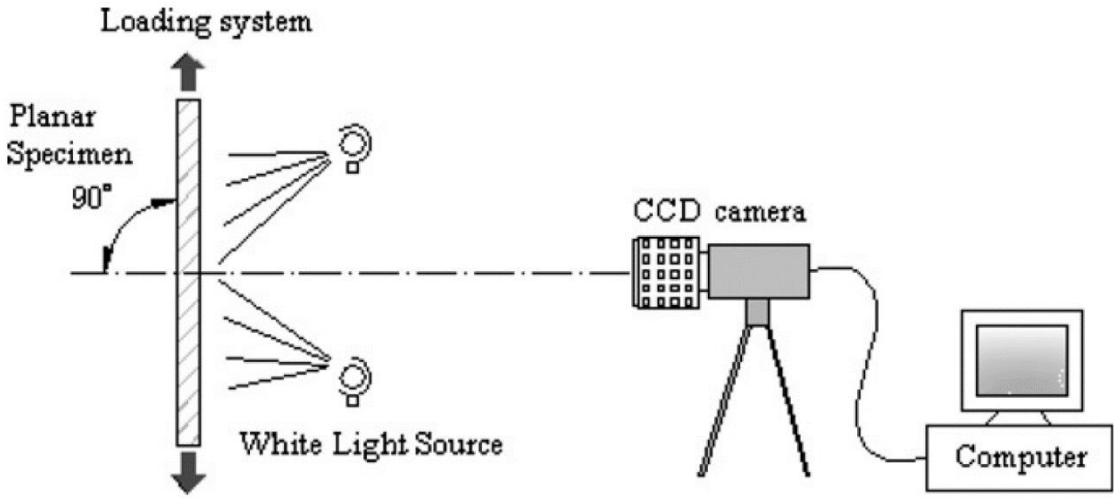

Figure 5: Typical single-camera set-up for 2D-DIC measurements [50]

The three-dimensional DIC version, known as 3D-DIC, allows obtaining the three displacement field components on a surface. Three-dimensional displacement measurements require stereoscopic vision systems comprising at least two cameras to detect depth changes (out of each sensors plane motions). Thus, the first step for carrying out a 3D-DIC is to locate both cameras referred to a coordinate system (commonly called in handbooks as world-coordinate system) for subsequently images matching and displacements calculation. This spatial calibration process is done through a calibration grid or target whose dimensions and features are previously known to calculate the relative position between the cameras and the world coordinate system. Figure 6 shows a schematic representation of a two-camera stereoscopic vision system during the calibration process. Figure 7 shows images for the calibration process for a two-camera stereoscopic system.

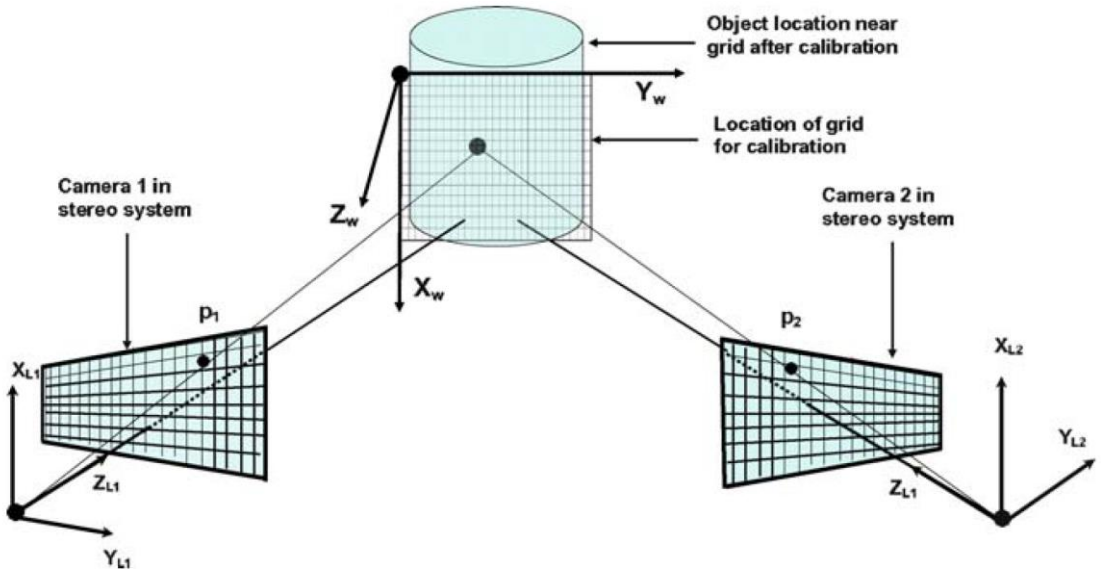

Figure 6: Schematic representation of a stereoscopic system during calibration process [43]

Figure 7: Images from a two-camera stereoscopic system during spatial calibration showing the calibration grid [52]

The calibration process is a very relevant aspect during DIC measurements since all possible motions in the spatial directions (either rotations or displacements) should be captured in order to ensure correct calibration. Otherwise, if a specimen movement occurs in any direction, which would not have been considered during the calibration, displacement data in that direction could not be significant since there could be an important measurement error.

3.Literature review

In this Section, three main points are addressed. First, an introduction describing the role of crack tip characterising parameters on fatigue crack growth (damage-tolerance fatigue approach) and the impact of experimental optical techniques on this topic. Secondly, the characterisation of crack tip fields and characterising parameters on non-planar surfaces employing optical experimental techniques. Finally, the mathematical fitting approaches for determining crack tip parameters from experimental data available in the literature thus far are discussed.

3.1. Crack tip characterising parameters and their role on fatigue crack growth

Commonly, three kinds of approaches are established in the literature to address fatigue issues. The stress-life, the strain-life and the damage-tolerance approaches [53]. Since the 60s, the damage-tolerance approach, which is based on Fracture Mechanics theory, has been one of the most popular methods for assessing components susceptible to fatigue crack failures. Especially in aircraft and marine structures as a consequence of the terrible fails occurred in the mid-20 century [54,55]. In 1961, Paris et al [56] established that the fatigue crack growth rate can be characterised by the stress intensity factor range at constant amplitude loading cycle under small scale yielding conditions. Thus, Paris et al. [57] demonstrated that fracture mechanics was a useful tool for characterising crack growth by fatigue through their power law that relates the fatigue crack growth rate da/dN with the stress intensity factor range ΔK. Although his work was initially received with much criticism by the scientific community, since Paris' contribution other fatigue crack growth laws have been developed based on the stress intensity as characterising parameter and including other parameters also influencing the fatigue crack growth rate as the fracture toughness, the stress ratio or the fatigue threshold [58–61]. Some years later, Elber [62,63] observed that a fatigue crack can close prematurely even under a fully tension cycle load due to the plastic deformation left in the wake of the fatigue crack tip. Therefore, this premature contact between the crack flanks caused a reduction in the apparent driving force for fatigue advance.

This phenomenon is known as plasticity-induced crack closure and allowed Elber to postulate that crack closure decreased the fatigue crack growth rate, redefying the original Paris equation by replacing the nominal range by the effective range due to the crack closure effect (better defined as plasticity-induced crack tip shielding since arising from the effects of the plastic enclave) [62–64]. Of particular note, other empirical laws have been developed based on the Paris idea but replacing the stress intensity factor by elastoplastic-based parameters such as J-integral [65–68], the crack opening displacement (COD) [69] or more recently the plastic range of the crack tip opening displacement ($\Delta CTOD_p$) [70–73].

Since parameters governing the singularity field are considered crack driving forces for fatigue advance according to the fatigue damage-tolerance approach, their experimental determination supposes a relevant point for assessing fatigue crack growth mechanisms. A common and effective way to determine the crack tip parameters from experimental data is by combining the crack tip field data obtained by using an optical technique with a mathematical model for describing the crack tip fields [3,6,7,25,28,30,31,33]. Until the work reported by Sanford and Dally [74], the crack tip parameters were calculated using single, double or triple-points methods [75–79]. Sanford and Dally proposed a multi-point approach for determining the stress intensity factors using digital-photoelasticity data [80] that allows calculating these values robustly. This work by Sanford and Dally together with the vertiginous development of other potential full-field optical techniques such as digital image correlation [43] or thermoelastic stress analysis [81] underpinned a large number of research works trying to improve the understanding of the mechanisms driving fatigue crack growth from the calculation and analysis of those parameters characterising the crack tip fields. Some of these works are described below. Nurse and Patterson [3,82] employed Muskhelishvili's approach [33] to determine mixed-mode stress intensity factors from digital photoelasticity data on a turbine disk. Diaz et al. [83,84] calculated the stress intensity factor ranges from thermoelastic data using Nurse and Patterson Muskhelishvili-based approach [33]. In these works, beyond the methodology for the assessment of the crack tip thermoelastic data, the authors noted that thermoelastic stress analysis (TSA) was able to reproduce the effective stress intensity range due to crack closure since TSA provided the linear and elastic response of the analysed component. Some studies where crack tip data by DIC were used for this purpose are the works reported by Lopez-Crespo et al. [85,86] using Nurse and Patterson Muskhelishvili-based approach [33]; the work by Du et al. [87], where an aircraft structure component was evaluated trough last described Lopez-Crespo's methodology; the works by Vasco-Olmo et al. [8,15], where different crack tip field models were employed to assess crack tip shielding phenomenon; the work by Gonzales et al. [12], where they used a linear J-integral approach in conjunction with Williams' expansion series model [30]; the work by Yang et al. [34], who defined a new effective crack driving force based on the CJP model crack tip parameters, as well

as the work by Diaz et al. [88], that combines TSA and DIC for determining the effective stress intensity factor range. Note that although the earliest method developed by Sanford and Dally was conceived as an experimental data-based method, some authors have also developed methodologies to determine the parameters characterising crack tip fields by analysing numerical data obtained by the finite element method [89].

3.2. Crack tip fields characterisation on non-planar surfaces

One of the major limitations of the above-described crack tip field models is that are formulated for a flat cracked element under plane stress or strain conditions. This fact limits the models' applicability since curve-shaped elements cannot be assessed via the above-described method. Thus, for instance, complex geometry industrial components, as well as cylindrical specimens commonly used for fatigue testing, are not within the scope of those methodologies. Nonetheless, some authors have tried to determine crack tip parameters on non-flat surfaces by employing the original formulation of the crack tip field models for flat components in combination with 3D or 2D-DIC but assuming some limiting hypotheses [24,90–94]. Clear examples which cover these hypotheses can be found in the works reported by Vormwald et al. [24] and Mokhtarishirazabad et al. [94]. Vormwald et al. inferred the mixed-mode (I+II+III) stress intensity factors on a hollow cylinder (Figure 8) from 3D-DIC data employing Irwin-Westergaard' approach [28,29]. They assumed that the curvature effect is negligible when a high magnification lens is employed. In addition, because of this hypothesis, they considered that the crack growth direction is perfectly straight although the crack grew circumferentially. This last implies that the component of the displacement field along the crack growth direction was not correctly modelled since as the crack grows, that direction changes. In the work conducted by Mokhtarishirazabad et al., the authors calculated the stress intensity factor on a cylindrical surface (Figure 9) employing 2D-DIC data and an ultra-high magnification lens (microscope type). In this work, due to the lens magnification, the element curvature could be neglected during the analysis; however, the major limitation of this approach lies in the existence of a plastic zone surrounding the crack tip. Hence, if the magnification is highly increased, only the plastically deformed area could be captured and linear elastic crack-tip field models would no longer be applicable to the analysis of this area.

As exposed, there is not much information, works or methodologies for the calculation of crack tip parameters through combining mathematical models describing the crack tip fields and experimental optical techniques and hence, a limitation on analysing fatigue cracks on curved-shape elements. As reported in Chapter 1, the main aim of the present thesis is to develop a

methodology for extending the use of crack tip field models for flat components to non-planar surfaces and thus taking a first step in analysing these kinds of elements.

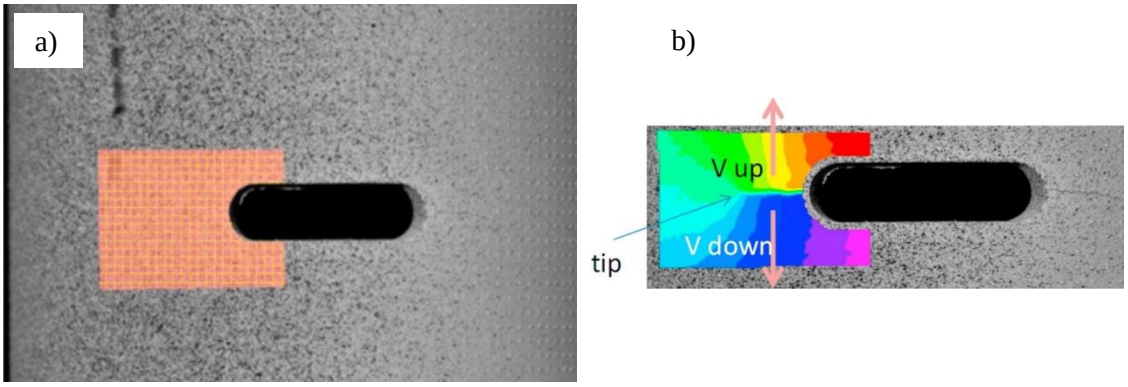

Figure 8: Hollow cylinder under mixed mode fatigue loading of the work of Vormwald et al. [24]. a) Interest region surrounding the crack tip and b) axial displacement map on the cylinder surface

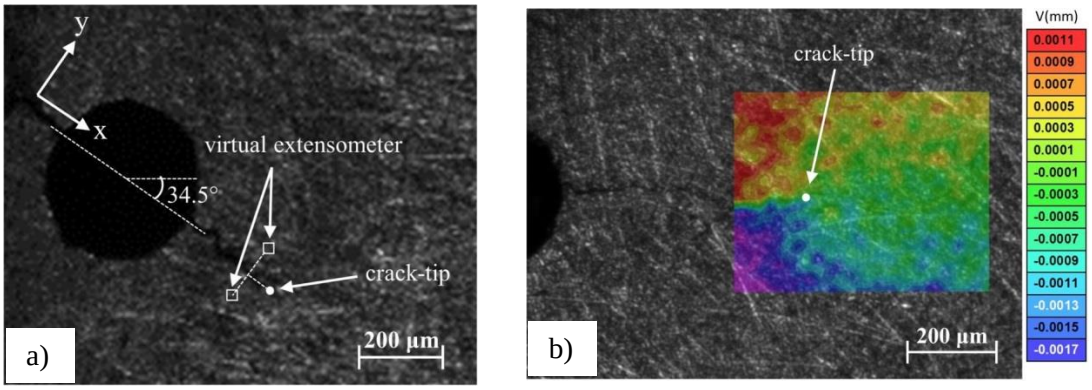

Figure 9: High-resolution crack tip images from Mokhtarishirazabad et al. [94]. a) Figure showing the fatigue-growing crack and its orientation due to the biaxial load and b) axial displacement map surrounding the crack tip

3.3. Fitting approaches for crack tip parameters determination from experimental data

A relevant aspect when crack tip parameters are inferred from experimental data is how the mathematical fitting is performed. Depending on the data nature as well as what variables are considered as fitting unknowns, the mathematical problem can be linear, where analytical exact methods are enough, or non-linear and therefore the use of numerical methods are required, for which well-chosen initial solutions must be established to ensure the convergence. When isochromatic data is under analysis, the fitting problem is non-linear without depending on what variables are considered for fitting. This is because isochromatic data are related to Mohr's circle and quadratic operators are involved in the mathematical fitting expression. Sanford and Dally [2,74] addressed the problem by employing Newton's method to iteratively solve a non-linear equations system. Nurse and Patterson [32] used the previous described Sanford approach based on Newton's method, however they noted that the crack tip position was an important variable

when a set of data points was collected since the crack tip field models are formulated with the crack tip as the coordinate origin. Moreover, other approaches based on mathematical optimisation can be found in the literature, for example, in the works conducted by Christopher et al [6,7]. When crack tip thermoelastic data is used and the crack tip location is not included as unknown, the mathematical fitting problem remains linear and a suitable matrix factorisation is enough to determine crack tip parameters. For example, the work conducted by Tomlinson et al [4] who determined mixed mode stress intensity factors (I+II) via linear least square fitting. In the works published by Diaz et al. [83,84], the authors considered the crack tip location as unknown to avoid errors when this variable is user-supplied. Since a non-linear fitting problem was obtained, the authors employed an optimisation-based approach for stress intensity factor determination using Nelder and Mead Down-Hill Simplex heuristic method [95,96]. Nonetheless, when mean stress terms are included in the thermoelastic equation as in the formulation by Palumbo et al. [97], the problem cannot be addressed linearly since the existence of quadratic terms in the fitting equation implies solving a non-linear fitting problem although the crack tip is not included as unknown. Similarly to Diaz et al. [83,84], Palumbo et al. solved the non-linear problem through Nelder and Mead's algorithm [95,96]. As with TSA data, inferring crack tip parameters from DIC data only requires a suitable matrix factorisation if the crack tip coordinates are not included in the mathematical fitting problem. Some examples of that linear approach where crack tip data is manually collected can be found in following works [8,34,85,86,98,99]. Nonetheless, some authors have developed methodologies for solving the fitting problem considering the crack tip location as unknown to avoid problems when it is user-supplied as well as know its location on the displacement maps for any purpose. Yoneyama et al [100] proposed to use Newton's method for determining both Williams' model coefficients and the crack position. In this work, to avoid an ill-conditioned initial solution, the authors used empirical correlations for generating an initial solution. Zanganeh et al [101] also employing Williams' model to perform a comparison among different optimisation algorithms such as a full-Newton gradient-based (trust-region reflective), a quasi-Newton gradient-based (Sequential Quadratic Programming) and three heuristic-based as Nelder and Mead's [95,96], a Pattern Search method [102] and a Genetic Algorithm [26]. They used an initial linear fitting by guessing an initial crack tip location on the displacement map to avoid a user-made initial solution based on empirical correlations. Figure 10 shows a comparison between those algorithms using artificial (theoretically obtained) fields. Yang et al [103] proposed to employ the Levenberg-Marquardt algorithm [104] to determine the CJP model coefficients. Yang et al. dealt with the initial solution problem as Zanganeh et al. by making an initial linear fitting in order to avoid a bad-chosen initial solution.

Algorithm	Ideal crack-tip location		Found crack-tip location		Searching range around point A	Error %	
	x (mm)	*y* (mm)	*x* (mm)	*y* (mm)		*x*	*y*
Trust-region reflective Newton	1	0.5	0	0	(−1.5,1.5), (−1.5,1.5)	−100	−100
SQP, Quasi-Newton, line-search	1	0.5	0.7901	0.2696	(−1.5,1.5), (−1.5,1.5)	−20.99	−46.08
Simplex	1	0.5	1	0.5	Unconstrained	0	0
Pattern Search	1	0.5	1	0.5	(−1.5,1.5), (−1.5,1.5)	0	0
GA	1	0.5	0.9991	0.4992	(−1.5,1.5), (−1.5,1.5)	−0.09	−0.16

SQP, sequential quadratic programming.

Figure 10: Comparison between different algorithms for crack tip calculation carried out by Zanganeh et al [101]

However, the above-described methodologies show certain problems. As reported by Vasco-Olmo [105], some models such as the CJP are very sensitive to the crack tip location. In fact, a one-pixel error during crack tip selection can induct a very high error in fitted crack tip parameters. Thus, to avoid crack tip position user-supplied values that provide not accurate crack tip characterising parameters values, the crack tip location should be considered as a fitting variable and hence obtaining a nonlinear mathematical problem. Even though there are some approaches to address these kinds of problems, these methodologies present some limitations. For instance, the approach developed by Yoneyama et al. [100] for constructing the initial solution requires knowing previously some numerical or theoretical stress intensity factor value in order to ensure a well-chosen initial solution and hence, the convergence to the real solution. Thus, Yoneyama's method is effective for simple geometries or specimens where empirical correlations are available and it can lose effectiveness when a complex or no standard geometry is under consideration and therefore the stress intensity factors cannot be previously known. Those approaches developed by Zanganeh et al. [101] and Yang et al. [103] avoid generating an initial solution by making an initial linear fitting to extract crack tip parameters values. However, if the employed model is clearly sensitive to the crack tip position, initially obtained parameters would not be accurate and therefore, an ill-conditioned initial solution could be obtained. Hence, according to all these reasons, it is necessary to improve these approaches and hence, to develop a more robust methodology for the estimation of the crack tip parameters from experimental full-field crack tip data.

4.Apparatus and methods

This Section is divided into 2 main parts, the experimental work and the numerical modelling. The experimental work covers two kind of fatigue testing, fatigue testing on a flat and standard specimen (CT-specimen) using 2D-DIC and the second one on thin-walled cylindrical specimens using 3D-DIC. Subsequently, the numerical modelling for replicating the experimental tests on the different cylindrical specimens are described.

4.1. Experimental testing

Different fatigue crack growth tests have been conduted in order to validate both the proposed fitting algorithm for the crack tip parameters determination as well as the extended formulation of the crack tip field models for the analysis of non-planar cracked surfaces under plane stress conditions. To validate the proposed fitting algorithm a fatigue crack growth test was performed in a Compact-Tension specimen made of commercially pure titanium employing 2D-DIC. The extended formulation to non-planar surfaces was validated by testing two cylindrical pipes made of 304L stainless steel and 2024-T3 aluminium alloy using 3D-DIC.

4.1.1. Fatigue crack growth tests on Compact-Tension specimen employing 2D digital image correlation

A Compact-Tension (CT) specimen made of commercially pure titanium Grade 2 was tested under a sinusoidal constant amplitude loading. Specimen dimensions are shown in Figure 11a. Material mechanical properties and chemical composition are shown in Tables 1 and 2, respectively. A stress ratio value of 0.6 was chosen to avoid any closure influence [15] and a maximum load of 750 N was applied to be significantly higher than the fatigue threshold value [15]. The fatigue test was conducted on an Electropuls E3000 electrodynamic machine at the frequency of 10 Hz. To perform DIC processing, one side of the specimen surface was sprayed with a stochastically black speckle pattern over a white background as shown in Figure 11b. The other specimen side was polished to improve the crack propagation visualisation during testing.

Table 1: Mechanical properties for commercially pure titanium Grade 2

Parameter	Young modulus (GPa)	Ultimate tensile strength (MPa)	Yield stress (MPa)	Elongation at failure (%)	Poisson's coefficient
Value	105	448	390	20	0.33

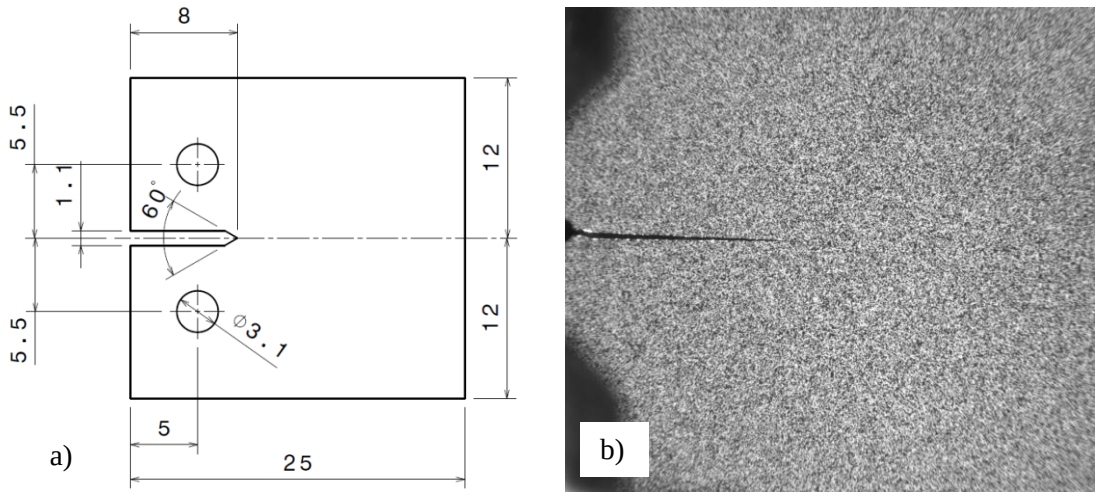

Figure 11: a) CT-specimen dimensions and b) speckle image

Thus, a system comprising two charge-coupled device (CCD) cameras was employed for 2D DIC image acquisition and crack length monitoring. The experimental setup is shown in Figure 12. A Marlin F-146B/C with a 2-Mpixel resolution was employed for DIC measurements and a DANTEC dynamics 2-Mpixel resolution was employed for crack tracking. To increase the spatial resolution around the crack tip, both cameras were fitted with macro-zoom lenses model MLH-10X EO. Thus, a spatial resolution of 13.7 μm/pixel was achieved for DIC images. In addition, a fibre optic light was employed to achieve a uniform illumination improving DIC images.

Table 2: Chemical composition (wt%) of commercially pure titanium Grade 2

Element (wt %)	Fe	C	N	O	H	Ti
Specification	<0.20	≤0.08	≤0.05	≤0.20	≤0.015	Balance
Specimen	0.10	0.01	<0.01	0.12	0.002	Balance

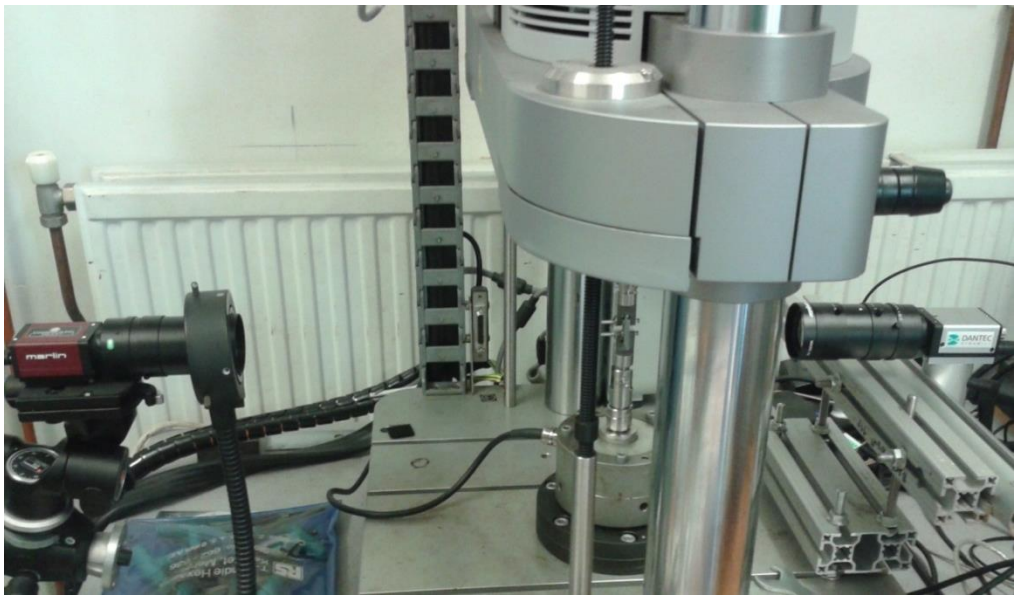

Figure 12: Experimental set-up for CT specimen fatigue testing

Data acquisition was made by pausing the fatigue test and acquiring a loading cycle with a loading increment of 25 N between the maximum and minimum loading cycle values (450-750 N) together with a reference image at 10 N representing the unloading state. The load value of the reference image was chosen in order to avoid any rigid body motion that could occur when the specimen is unloaded. This process was repeated for different crack lengths by controlling its propagation using the second camera.

DIC processing was made using the commercially VIC-2D software provided by Correlated Solutions Inc. A 25-pixel subset size and a 1-pixel step were employed in order to achieve full resolution displacement maps. Figure 13 shows vertical and displacement maps at the maximum load for a crack length of 9.4 mm obtained with the 2D-DIC algorithm

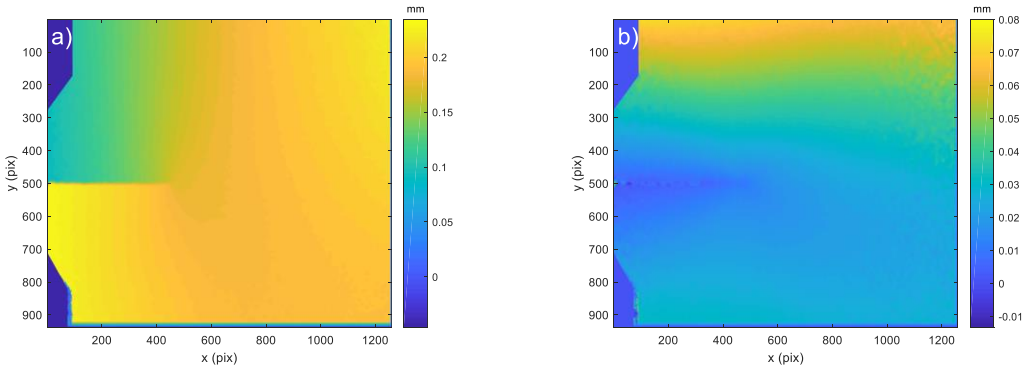

Figure 13: a) Vertical and b) horizontal displacement maps for a crack length of 9.4 mm at the maximum load of 750 N

4.1.2. Fatigue crack growth tests on cylindrical pipes employing 3D digital image correlation

To validate the proposed approach for cracked curve surfaces, cylindrical thin-wall pipes were cyclically tested under constant amplitude loading. Specimens design was made according to ASTM E606 standard [106] that provides suitable dimensions relationships for fatigue testing. Two different materials were chosen for fatigue testing, austenitic stainless steel (SS304L) and an aluminium alloy (AA2024-T3). Chemical compositions and mechanical properties provided by the manufacturer are shown in Tables 3 and 4, respectively. These materials were chosen as they were representative of certain industrial applications such as chemical, marine and food industries, in the case of the SS304L, and for aircraft and transport structures as in the case of the AA2024-T3.

Table 3: Chemical composition of both alloys (wt %)

304L	0.02 C	0.39 Si	1.37 Mn	0.001 S	0.029 P	8.01 Ni	18.15 Cr	
2024-T3	3.8 Cu	0.1 Cr	0.3 Mn	0.5 Fe	1.2 Mg	0.5 Si	0.15 Ti	0.25 Zn

Table 4: Mechanical properties of the alloys

Mechanical property	**Units**	**SS304L**	**AA2024-T3**
Young modulus	GPa	197	73.1
Poisson's ratio	Dimensionless	0.33	0.33
Yield stress	MPa	312	355
Ultimate tensile stress	MPa	646	483
Elongation at failure	%	53	18

Both specimens were manufactured with a length of 203.2 mm and a thickness of 2.11 mm. To suit the commercially available material, a diameter of 26.7 mm was chosen for the SS304L and 25.4 mm for the AA2024-T3. For a correct gripping during testing, SS304L specimen ends were machined to 25.4 mm. An initial notch was generated for both specimens allowing the crack to grow in both holes. The notch consists of a through-thickness 1.5 mm drill and two 0.1 mm sawn slots (using EDM technology) in the circumferential direction at both holes sides as shown in Figure 14. If the notch length (1.7 mm) is normalised by employing the outer pipe perimeter, a value of 1.5% is obtained. The reason for manufacturing a tiny notch is to avoid the effect of the residual stresses due to the manufacturing process on the crack tip field and thus avoiding modifying stress intensity values.

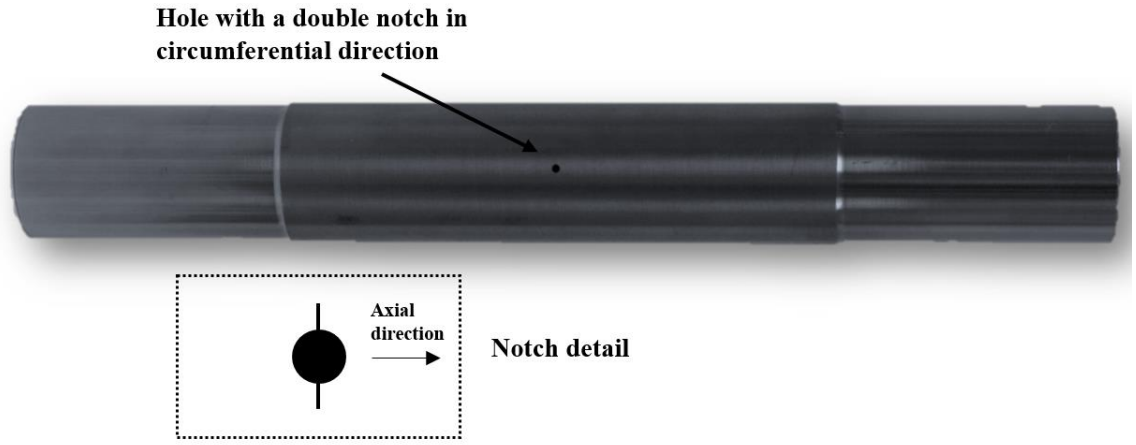

Figure 14: SS304L specimen used during fatigue experiments

Fatigue testing was carried out on a servohydraulic machine MTS Landmark 370.10 with a loading capacity of 100 kN. For both aluminium and stainless steel specimens, a stress ratio of 0.525 was chosen to avoid any closure influence during fatigue crack growth [107,108]. The maximum load of the loading cycle was chosen in order to reach the fatigue threshold value. Thus, 33% of the equivalent yield stress load was considered for the stainless steel [108] and 20% for the aluminium alloy [107]. To measure the displacement fields with 3D-DIC, a stereoscopic vision system comprising three 5-Mpixel CCD cameras was employed (model Stingray F504) allowing the whole measurement of the crack path and the surrounding field (see Figure 15). The displacement fields were measured for different crack lengths to assess methodology validity within a crack length range. The experimental setup for fatigue testing is shown in Figure 15. To increase the spatial resolution surrounding the crack tip, three macro-zoom lenses were fitted to each camera (model MLH-10X EO). To obtain suitable measurements on cylindrical specimens, it was required closer lens apertures to allow focusing beyond the sensor plane. Hence, closer apertures require external illumination sources in order to achieve an enough and uniform illumination. Thus, a dual-point fibre optic light source was employed to illuminate both specimen sides as shown in Figure 15. The speckle pattern for images matching in both specimens was generated by spraying black paint over a white background and employing an airbrush to achieve DIC facets recognition. Figure 16a shows a speckle image from one camera showing also the fatigue crack during the test.

The calibration of the stereoscopic vision system was carried out by employing a calibration grid comprising 9x9 dots 2-mm spaced (as shown in Figure 16b). A peer cameras calibration was performed and thus generating two measurement domains (left and centre cameras and centre and right cameras). As reported in Chapter 2, spatial calibration during 3D-DIC measurements is a relevant and critical point. Therefore, calibration was done by considering all possible specimen

movements as displacements and rotations in any spatial axis and thus, acquiring images for those cases. For that calibration, an average spatial resolution of 0.022 mm/pixel was achieved.

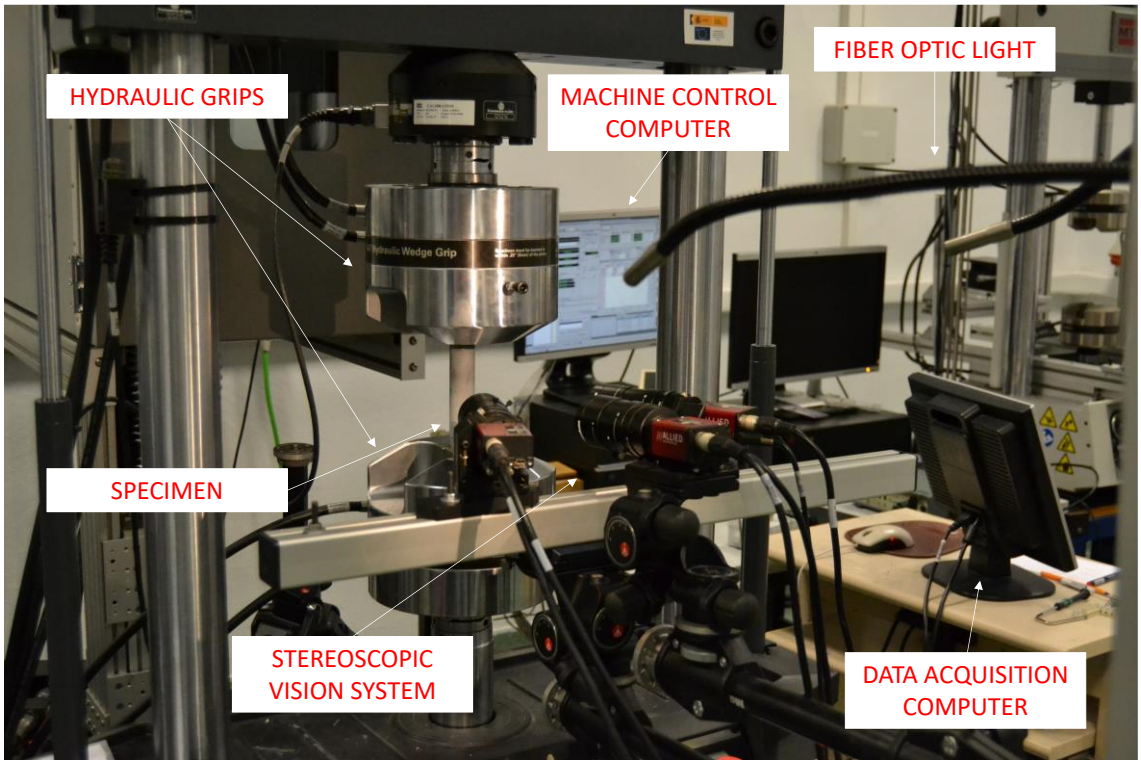

Figure 15: Experimental setup for cylindrical specimens testing.

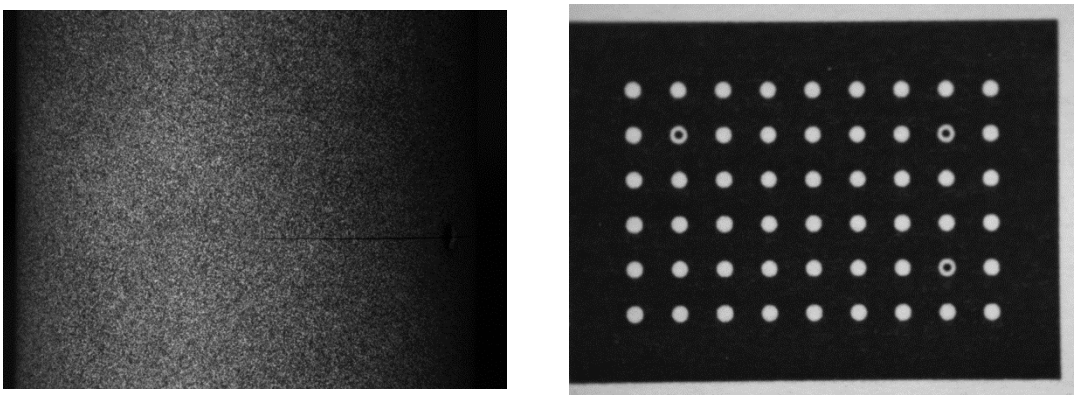

Figure 16: a) Speckle image during SS304L specimen testing and b) calibration grid

DIC processing was performed using the commercial software 3D-VIC provided by Correlated Solutions Inc. A subset facet size of 29 pixels and a 1-pixel step were used for DIC processing and it was found as reliable values to obtain a good resolution in the displacement maps.

It is important to note that crack growth shape was different for each material. For the aluminium alloy, two cracks emanated from both holes as shown in Figure 17a. However, for the stainless steel specimen, the crack emanated circumferentially from only one side as shown in Figure 17b.

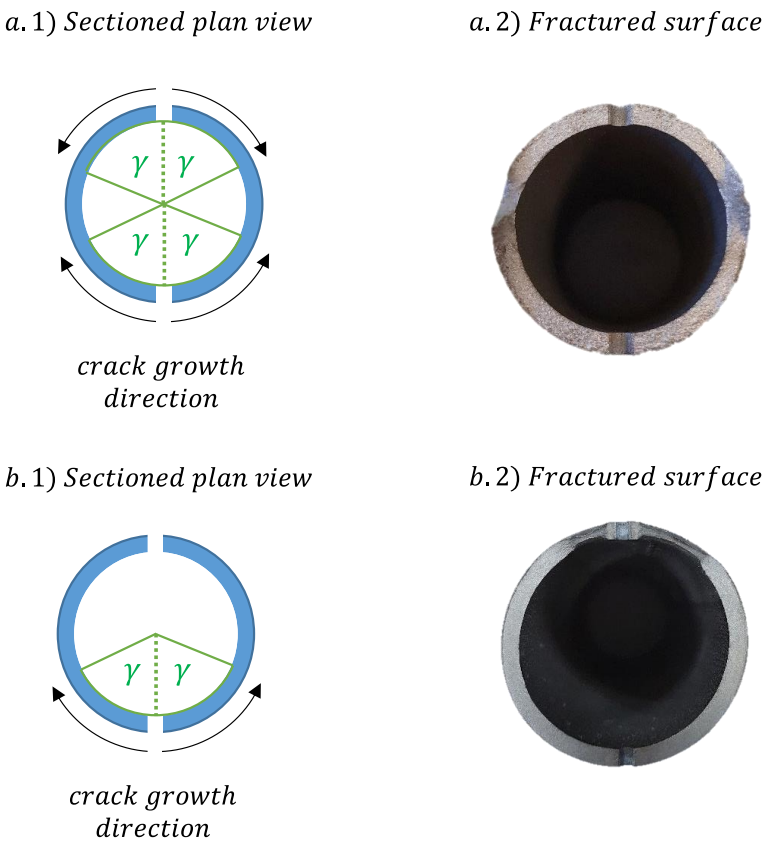

Figure 17: Crack growth shapes. a) and b) refer to aluminium alloy and stainless steel, respectively and 1) and 2) refer to the schematic graph showing the crack angle definition and specimen after fatigue failure, respectively.

These two different crack topologies allow a more comprehensive validation of the methodology since two different cases can be assessed.

4.2. Numerical modelling

Two numerical models were built in ABAQUS replicating fatigue tests on cylindrical specimens and thus allowing a comparison with experimental data as well as providing information to validate the proposed approach that cannot be measured using 3D-DIC.

4.2.1. Stainless steel specimen numerical modelling

Due to the employed specimen geometry and the crack growth shape, there is symmetry between two planes (radial-tangential and radial-axial). In addition, cylinder ends can be removed since their effect on the crack tip fields is fully negligible. Moreover, according to the Saint-Venant principle, the axial load can be relocated below the ends. Hence, computational cost can be reduced by modelling only a part of the specimen as shown in Figure 18a.

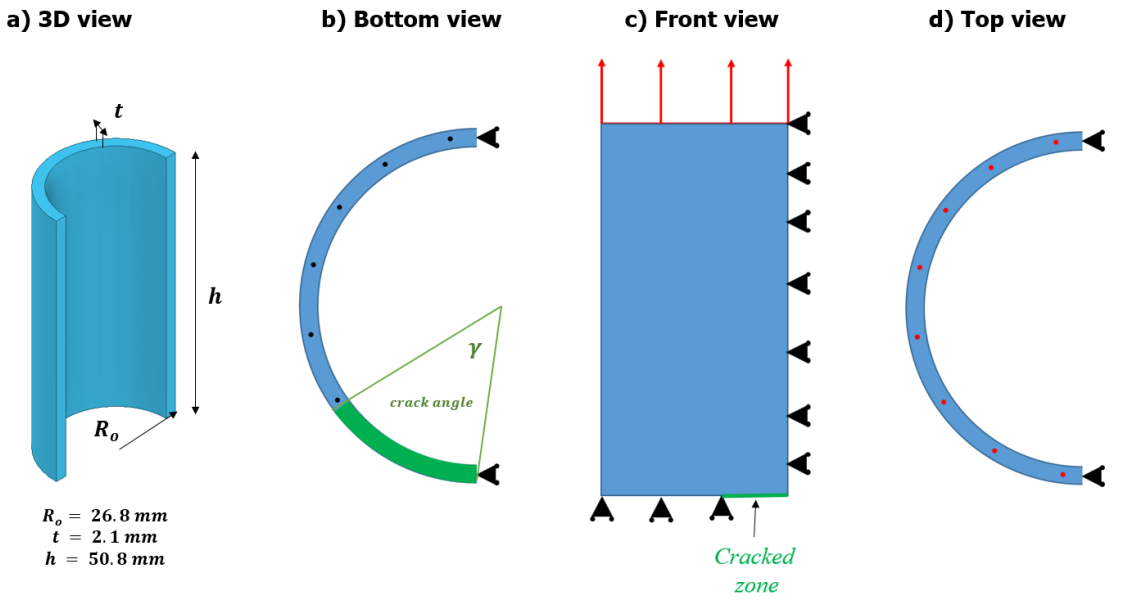

Figure 18: Numerical model, geometry, boundary conditions and loads for the SS304L specimen. a) 3D view, b) bottom view, c) front view and d) top view. The black points indicate the boundary condition applied and the red points the applied load

Symmetry conditions were modelled by constraining the displacement along the normal directions of the symmetry planes as shown in Figure 18. The external axial load was modelled as a uniform pressure load calculated as the ratio between the external axial load and the annulus area applied on the top of the model. The crack was modelled as the green unconstrained zone shown in Figure 18b. Through-thickness holes were not modelled since those act as initial notch and therefore, they were considered as part of the crack. In addition, residual stresses due to the manufacturing process should disappear as the crack grows and for larger cracks than the initial notch, results should be comparable since there would be no residual stresses effect on the crack tip field. Load variation over time was modelled as a sinusoidal load at the same test frequency (10 Hz) and at the same stress ratio (0.525). Regarding wave shape frequency, since no transient or time-dependent phenomena are considered, the value is not significant for the numerical simulation and its value was chosen in order to define a time domain.

The elastoplastic behaviour of the 304L stainless steel was modelled through the generalised Hooke's law for the elastic behaviour and the von Mises criterion together with a combined kinematic-isotropic hardening model for the plastic behaviour. The yield surface according to the von Mises criterion is given by the following expression.

$$\sqrt{\frac{3}{2}(\boldsymbol{\sigma}' - \boldsymbol{X}) : (\boldsymbol{\sigma}' - \boldsymbol{X})} - Y \leq 0 \tag{18}$$

Where $\boldsymbol{\sigma}'$ is the deviatory Cauchy stress tensor, $\boldsymbol{X}$ is the back-stress tensor and Y is the flow stress. The combined evolution of Y and $\boldsymbol{X}$ with plastic deformation is described by Voce isotropic [109] and Chaboche kinematic hardening laws [110] according to the following expressions:

$$Y = \sigma_0 + Q'[1 - \exp(-b\bar{\varepsilon})] \quad (19)$$

$$\dot{\boldsymbol{X}} = \frac{2}{3}C'\dot{\boldsymbol{\varepsilon}} - D'\boldsymbol{X}\dot{\bar{\varepsilon}} \quad (20)$$

Where σ_0, Q' and b are material parameters of the Voce law, $\bar{\varepsilon}$ is the equivalent plastic strain; C' and D' are material parameters of the Chaboche law, $\dot{\boldsymbol{X}}$ is the back-stress rate, $\dot{\boldsymbol{\varepsilon}}$ and $\dot{\bar{\varepsilon}}$ are respectively the plastic strain rate and the equivalent plastic strain rate. In the case of uniaxial cyclic loading, integration of Equation 20 leads to:

$$X = \chi C' + (X_0 - \chi C')\exp\left(-\chi D'(\varepsilon - \varepsilon_0)\right) \quad (21)$$

Where X_0 and ε_0 are the values of X and ε at the beginning of each half cycle, where $\chi = \pm 1$ during loading and unloading, respectively. Material parameters were obtained fitting the model to cyclic stress-strain loops obtained in low-cycle fatigue tests [111]. Materials parameters are shown in Table 3

Table 5: Parameters for the combined hardening of the material [111]

$\boldsymbol{C'}$ $(\boldsymbol{GPa})$	$\boldsymbol{D'}$	$\boldsymbol{Q'}$ $(\boldsymbol{MPa})$	$\boldsymbol{b}$
528	300	87	9

The discretisation of the computational domain was done by employing 3D quadratic hexahedral elements (twenty-node elements). Two regions were created to reduce the computational cost, as shown in Figure 19. To reduce mesh transitions, which can conduct to distorted elements and in consequence, not accurate results, both parts were "glued" by imposing a displacement constraint in the boundary between both parts (tie constraint). This constraint imposes the same displacements in both parts being the refined zone the master and the non-refined zone the slave. The refined zone at the model bottom consists of a ¼ of a cylinder with a height of 25% of the cylinder half-height. This height was previously determined in order to capture enough singularity data for the larger simulated crack lengths. In addition, the size of the finite elements used in the refined zone was 0.1× 0.1× 0.21 mm^3 (length × height × depth). Although lower element sizes have been used in literature [73,112], for the purpose of the present work this size was enough since no plastic parameters or near crack tip phenomena were analysed, which require the modelling of high gradients. Thus, in the refined zone the total number of elements and nodes were 258690 and 1112367, respectively. The coarse zone was modelled employing 11180 nodes and 285 elements with a size of 2.2×2.2×2.1 mm^3.

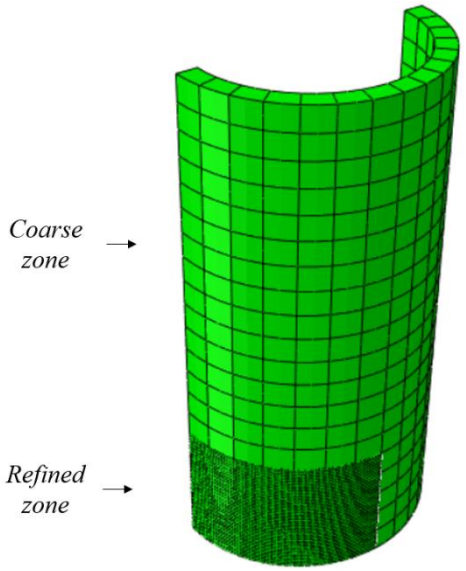

Figure 19: Computational domain for 304L specimen. Coarse and refined meshes

Fatigue crack growth was modelled by employing the node release method and assuming a constant fatigue crack growth rate [111,113]. Thus, every three loading cycles, were, through-thickness nodes were released thus causing the crack growth [112]. The number of cycles until the next node was released was chosen in order to complete the cyclic plasticity loop [111,113]. The range of the crack lengths simulated was from 5 to 60 degrees (in terms of the crack angle defined in Figure 17). It is important to remark that the nodes were released as a straight line along the radial direction and thus, a straight crack front was modelled.

4.2.2. Aluminium specimen numerical modelling

The numerical modelling of this specimen is similar to the above-described modelling for the stainless steel specimen. However, there are three different features because of the crack growth shape and the material that make it different the geometry, the constitutive equations and the computational domain. Due to the crack growth shape in the aluminium specimen, where cracks emanated from both holes, an additional symmetry plane was found and therefore, a more simplified geometry (45º annulus) can be modelled as shown in Figure 20a. As explained for the stainless steel modelling, symmetry conditions were modelled by constraining the normal displacement in the symmetrical areas and the load as a uniform pressure at the top of the body as shown in Figure 20.

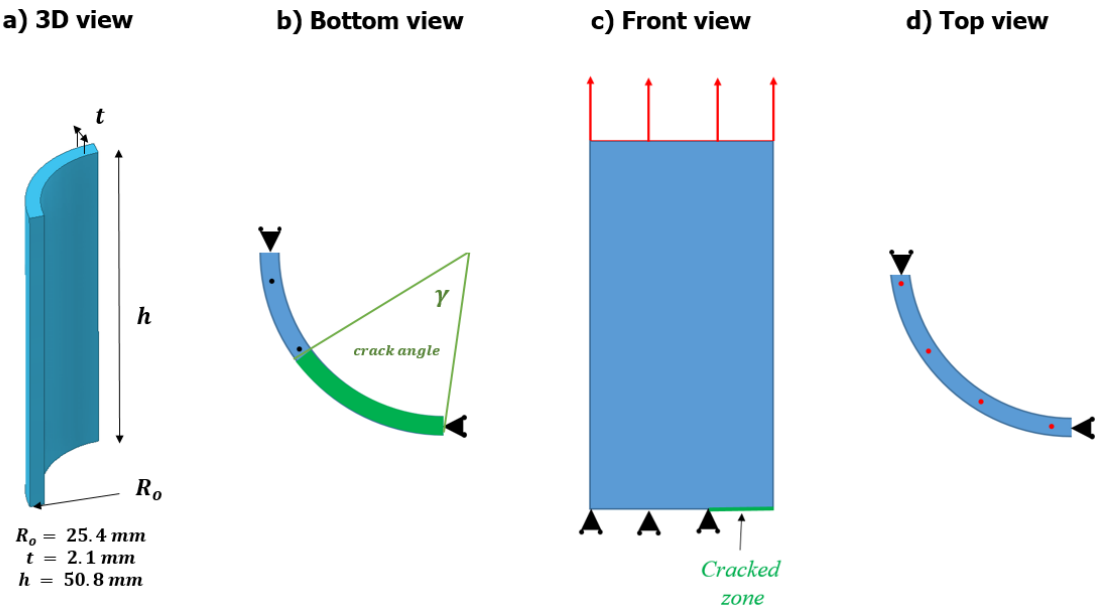

Figure 20: Numerical model, geometry, boundary conditions and loads for AA2024-T3 Aluminium specimen. a) 3D view b) bottom view c) front view and d) top view. The black points indicate the boundary condition applied and the red points the applied load

The weak hardening of this material allows modelling the hardening as isotropic or kinematic not founding differences in numerical results when any rule is used [112]. Concretely, the ratio between the hardening and elastic modulus is 0.003 being significantly lower than the limit of 0.03 established by some authors [112]. Thus, an isotropic hardening rule was used. The material yielding is described through a Ramberg-Osgood law [114] as indicated in the following expression.

$$\epsilon = \frac{\sigma}{E'} + (\frac{\sigma}{K'})^{n'} \quad (22)$$

Where K' and n' are the Ramberg-Osgood laws parameters whose values are 685 MPa and 13.7, respectively [112].

The computational domain was also constructed with quadratic hexahedral elements to improve the results accurate. In this case, since the geometry and the interest area are geometrically simpler, mesh transitions are easily addressed and hence avoiding model constraints between two different parts and meshes as in the stainless steel specimen. The interest area surrounding the crack tip was built using elements with dimensions 0.1×0.1×0.2 mm (length × width× thickness) and the zone far from the crack tip using vast elements with dimensions 1.6×0.1×0.2 mm (length × width× thickness) to reduce the computational cost. Thus, 100672 elements and 430288 nodes were generated.

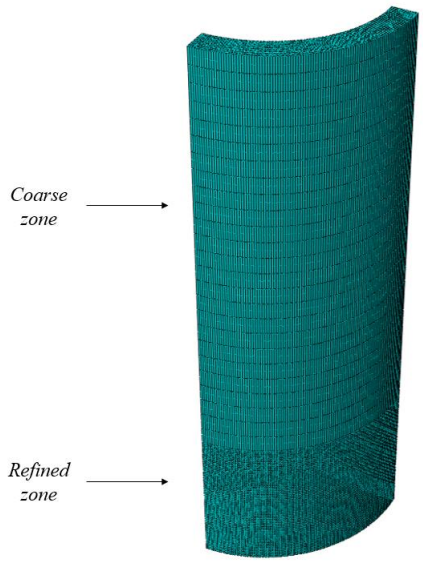

Figure 21: Computational domain for AA2024-T3 specimen numerical simulation

5.Methodologies

In this Chapter, several methodologies are reported and explained. First, the extended formulation of crack tip fields models based on differential geometry is detailed. Secondly, the methodology for crack tip characterising parameters determination for both numerical and experimental fields are described. Thirdly, empirical correlations for stress intensity factors calculation are shown. Subsequently, the Image Decomposition technique for comparing crack tip fields and in last, an alternative method for estimating the crack tip location based on the analysis of vertical displacements maps is described.

5.1. Extended formulation of the crack tip field models to the analysis of non-planar and developable surfaces under plane stress conditions

As previously stated, the objective of this thesis is to combine differential geometry concepts with two-dimensional crack tip field models for flat components and a suitable technique providing 3D displacement fields to characterise the crack tip fields on a non-planar cracked surface. This formulation considers that the cracked surface is under plane stress conditions and the surface is developable (zero Gaussian curvature). According to this, the surface can be flattened onto a plane without distortion. It is assumed that the normal direction to the surface is a principal direction with zero stress. For simplicity, a cylindrical surface containing a central circumferential crack is considered for the methodology development as shown in Figure 22a. The surface is parametrised by considering the crack growth direction as ξ and the crack opening direction under tensile loading as η, which correspond to the circumferential and the axial cylinder directions, respectively.

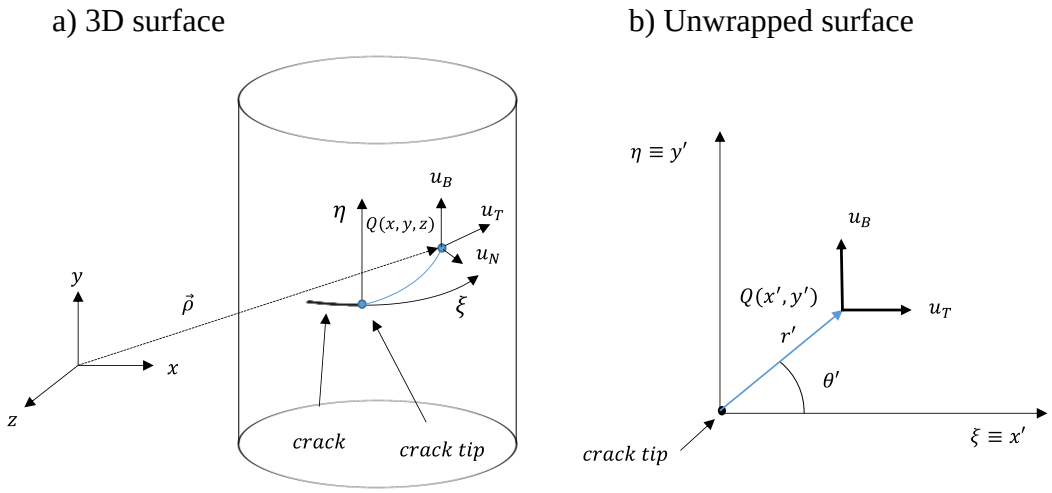

Figure 22: Figure to illustrate the analogy with flat models. a) Cracked surface and b) the equivalent system on the unwrapped plane.

Let consider a point Q located on the surface through a position vector $\vec{\rho}$ referred to an arbitrary system in the space. Moreover, the Cartesian components of the displacement field at that point are known. The Frenet-Serret trihedral can be calculated in terms of the parametrisation directions and the coordinates of the point Q as described in equations 13, 14 and 15. Thus, at each point, the displacement fields expressed in the Frenet-Serret directions can be calculated through the Cartesian displacement fields and Frenet-Serret vectors as follows:

$$u_T = \vec{u} \cdot \vec{T} = \left(u_x \cdot \overrightarrow{e_x} + u_y \cdot \overrightarrow{e_y} + u_z \cdot \overrightarrow{e_z}\right) \cdot \left(T_x \cdot \overrightarrow{e_x} + T_y \cdot \overrightarrow{e_y} + T_z \cdot \overrightarrow{e_z}\right) \quad (18)$$

$$u_B = \vec{u} \cdot \vec{B} = \left(u_x \cdot \overrightarrow{e_x} + u_y \cdot \overrightarrow{e_y} + u_z \cdot \overrightarrow{e_z}\right) \cdot \left(B_x \cdot \overrightarrow{e_x} + B_y \cdot \overrightarrow{e_y} + B_z \cdot \overrightarrow{e_z}\right) \quad (19)$$

$$u_N = \vec{u} \cdot \vec{N} = \left(u_x \cdot \overrightarrow{e_x} + u_y \cdot \overrightarrow{e_y} + u_z \cdot \overrightarrow{e_z}\right) \cdot \left(N_x \cdot \overrightarrow{e_x} + N_y \cdot \overrightarrow{e_y} + N_z \cdot \overrightarrow{e_z}\right) \quad (20)$$

Where u_T is the tangential component of the displacement field, u_B is the binormal component of the displacement field, u_N is the normal component of the displacement field and T_i, B_i and N_i with $i = x, y, z$ are the components of each Frenet-Serret vector.

If the surface is unwrapped as shown in Figure 22b, point Q is located through the curve coordinates x' and y' or the polar coordinates on the unwrapped plane r' and θ'. Thus, the crack growth direction coincides with the tangential direction and the crack opening direction with the binormal direction. Hence, as indicated in equation 21, a 2D crack tip field model (Williams' model is considered as example) can be reformulated in the unwrapped plane by replacing Cartesian plane components of the displacement fields with the tangential and binormal components and the Cartesian coordinates by the curve coordinates. Under plane stress conditions, the out-of-unwrapped-plane component is given by equation 22.

$$\begin{Bmatrix} u_T \\ u_B \end{Bmatrix} = \sum_{p=1}^{\infty} \frac{r'^{\frac{p}{2}}}{2G} a_p \begin{Bmatrix} \left(\kappa + \frac{p}{2} + (-1)^p\right) cos\frac{p\theta'}{2} - \frac{p}{2} cos\frac{(p-4)\theta'}{2} \\ \left(\kappa - \frac{p}{2} - (-1)^p\right) sin\frac{p\theta'}{2} + \frac{p}{2} sin\frac{(p-4)\theta'}{2} \end{Bmatrix} \quad (21)$$

$$u_N = -2z_n \frac{G(1+\nu)}{\nu}(\sigma_T + \sigma_B) \quad (22)$$

In the above expression, z_n represents the out-of-plane coordinate and σ_T and σ_B the normal stresses along the tangential and binormal directions, respectively.

Hence, from the experimentally measured 3D displacement fields, crack tip characterising parameters can be determined from the binormal and tangential components of the displacement fields and their coordinates onto the unwrapped plane. As example, Figure 23 shows the binormal and tangential components of the displacement fields obtained from the experimentally measured 3D crack tip displacement fields and by applying equations 18 and 19 to perform the geometrical transformation for the stainless steel specimen with a normalised crack length of 0.2377, corresponding to a 19.7 mm crack.

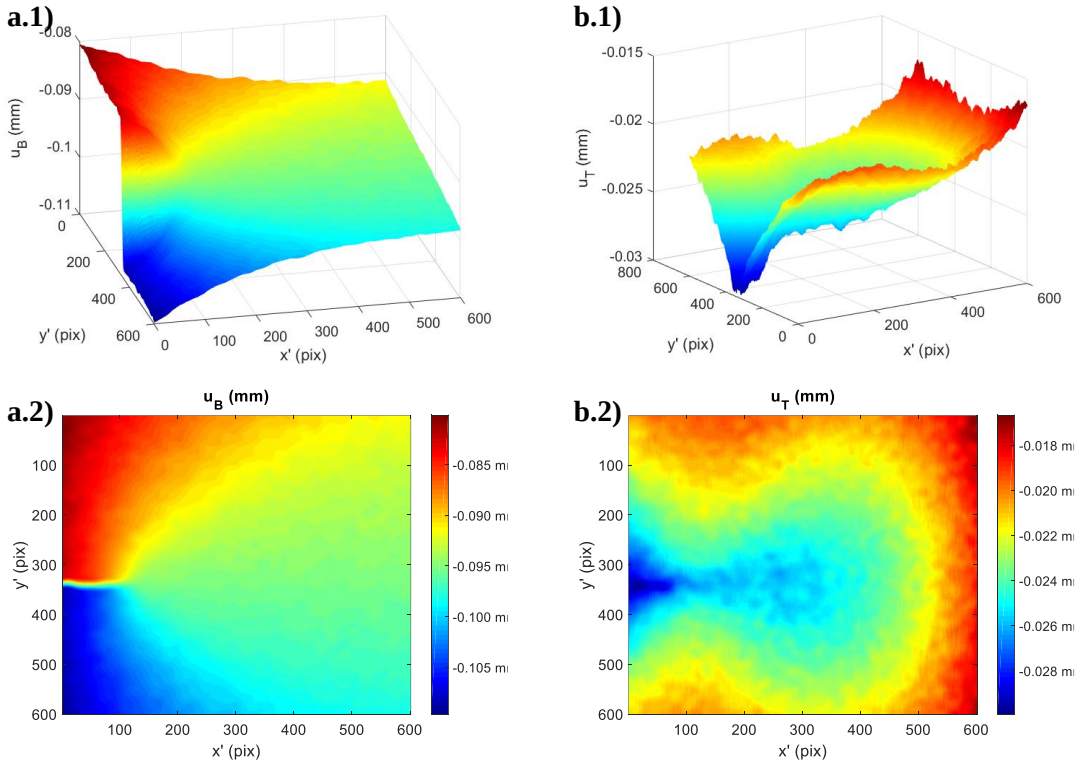

Figure 23: Binormal and tangential components of the displacement fields surrounding the crack tip for a crack length of 19.7 mm (0.2377 in terms of the normalised crack length). a and b indicate binormal and tangential component, respectively and 1 and 2 surface and map view, respectively.

5.2. Crack tip parameters calculation from surrounding crack tip displacement data

In this section, the methodologies for determining the parameters characterising the singularity around the crack tip from the analysis of experimental or numerical data are described. For experimental data, an improved hybrid optimisation-based approach is developed to determine the crack tip parameters from the plane displacement fields. This experimental methodology for crack tip characterising parameters calculation is explained and developed in the next section using 2D displacement fields on a flat specimen (CT) and subsequently extrapolated to cylindrical specimens in Section 6. For numerical data, a different approach consisting in the analysis of the axial displacement behind the crack tip and the axial stress ahead of the crack tip was used. Thus, a different approach to the experimental was used to provide crack tip parameters and hence make the validation stronger.

5.2.1. Calculation from experimental data. Optimisation-based hybrid approach

Once the displacement fields have been obtained, the crack tip parameters are calculated by analysing displacement data surrounding the crack tip. Thus, the first step in this methodology is to extract displacement data to perform the mathematical fitting. From both horizontal and vertical displacement maps, an annular-shaped mesh was generated as shown in Figure 24 in order to avoid the inclusion of plastic data nearest the crack tip into the mathematical fitting algorithm since analysed models are based on linear elastic differential equations as well as extract the singularity zone ahead of the crack tip.

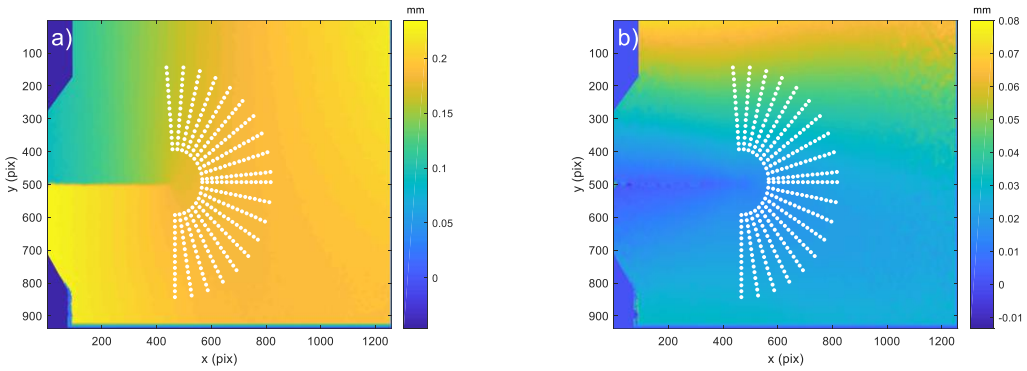

Figure 24: Annular mesh for fitting data extraction superimposed over a) vertical displacement map and b) horizontal displacement map. Maps from the 2D-DIC test on CT specimen for a crack length of 9.4 mm

The inner radius was calculated using the Dugdale plastic radius approximation [115] given by equation 23. Dugdale approximation was chosen rather than other equations as Irwin's expression

[116] since the radius defined by Dugdale provides a conservative value and hence, ensures that no plastic data is included in the collection area.

$$r_p = \frac{\pi}{8}\left(\frac{K_I}{S_y}\right)^2 \tag{23}$$

The outer radius was chosen in order to capture the singularity zone avoiding the area affected by the edge of the specimen. This area can be easily recognised on the vertical displacement map by analysing the orientation of displacement contours (tilted displacement contours imply edge effect) [107]. Regarding points distribution, a sweep angle of 180º was chosen to ensure capturing significantly singularity data. Mesh lines were equally distributed using an angle between lines of 10º and 15 points per line equally spaced (linear distribution). Thus, a collection of 300 points was employed for fitting at each analysed crack length and providing a significant amount of data points. The mesh centre should be placed at the crack tip since crack tip field models are referred to the crack tip. However, an accurate location of the crack tip is not easily determined visually from displacement maps. Hence, to avoid user-supplied errors in that variable, the crack tip location was included as a fitting variable and therefore, turning the problem into a non-linear fitting problem. Thus, the mesh centre was placed at any point close to the crack tip to ensure capturing singularity data without dependence on that variable beyond the collected points. The inclusion of the crack tip as a variable is a further step forwards the automation of the process for crack tip parameters determination for different crack lengths. In this way, the location of the meshes for singularity data extraction can be determined by taking an approximate crack length measurement from DIC images and hence, avoiding repetitive user inputs of such variable.

Once the fitting area has been defined and points extracted, the mathematical fitting problem can be defined. Since the inclusion of the crack tip leads to solving a non-linear and multivariable problem, an optimisation approach was employed. Thus, an objective function was defined through the norm of the difference between the theoretical expression of the chosen model and the collected data as shown in expression 24. To reduce computational costs and therefore, calculation time, the crack tip position was enclosed within a confidence region. This is due to the crack tip position is not easy to find in displacement maps but can be easily enclosed as shown in Figure 25. Those bounds enclosing the crack tip were generated from the coordinate of the mesh centre and defining an offset distance. The offset distance was chosen as 10% percent of crack length (region height and width 20% of the crack length). Thus, these bounds, shown in Figure 25 ($x_{SD}^{min}, x_{SD}^{max}, y_{SD}^{min}, y_{SD}^{max}$), were calculated either adding or subtracting that offset to the mesh centre. The inclusion of those bounds leads to adding two inequality constraints to the optimisation problem as shown in expression 24.

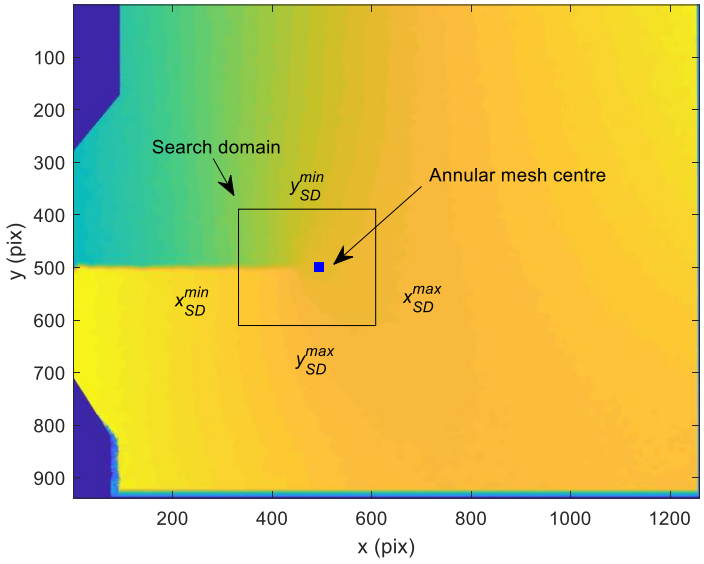

Figure 25: Search domain for enclosing the crack tip superimposed over the vertical displacement map. Displacement map from 2D-DIC fatigue test on CT specimen for a crack length of 9.4 mm

$$\begin{aligned} & & f\left(\Delta x, \Delta y, u_{x0}, u_{y0}, R_{xy}, crack\ tip\ parameters\right) & \\ & \min & = \left\| \left(u_x + ju_y\right)_{th} - \left(u_x + ju_y\right)_{exp} \right\| & \\ & subject\ to & x_{SD}^{min} < \Delta x < x_{SD}^{max} & (24) \\ & & y_{SD}^{min} < \Delta y < y_{SD}^{max} & \\ & & all\ other\ variables\ not\ sign\ constrained & \end{aligned}$$

As shown in expression 24, many variables are involved in the optimisation problem (five variables modelling the rigid body motion, the vertical and horizontal displacements along with the in-plane rotation, and the crack tip position plus the crack tip parameters). Thus, the size of the problem depends on the number of crack tip parameters used to describe the crack tip singularity. However, at least eight variables are involved since the most simple crack tip field description (Irwin-Westergaard approach) implies three additional variables (K_I, K_{II} and σ_{0x}). For the CJP model, eleven variables would be involved in the optimisation problem while for Williams' model the number of variables would depend on the employed number of terms according to: $5 + 2p - 1$.

Hence, for any model, a large number of variables are involved in the fitting problem presenting some problems from the mathematical point of view. The first and probably the most critical issue is the initial solution due to the non-linear nature of the problem. To achieve a global minimum, a well-chosen or conditioned initial solution must be generated. For a simple model as the Irwin-Westergaard approach and if the analysed geometry is a standard specimen or a simple geometry body, a well-conditioned initial solution might be provided by employing empirical correlations since the crack tip parameters can be estimated via those correlations and the other parameters

supplied by the user within reasonable limits. However, if any shielding effect affects to the global stress field, these parameters could take quite different values regarding the nominal and thus providing an ill-conditioned initial solution. For other models, generating a well-conditioned initial solution could be quite complex and therefore leading to local minima. For instance, for the CJP model, the shielding effect involved in coefficients A, B and E could be hard or impossible to estimate and the same for the high-order terms of Williams' series, which can appear depending on the influence of the crack tip plasticity as well as the analysed area. The second issue corresponds to the size of the optimisation problem since conventionally optimisation algorithms (Nelder-Mead, Trust-Reflective Region or Sequential Quadratic Programming) usually present certain problems when the number of variables involved is very large.

For those reasons, a hybrid optimisation approach combining a heuristic and non-initial solution required method together with a Newton-type deterministic one was employed for the determination of the crack tip parameters, improving the fitting process. A genetic algorithm was initially used to run the optimisation process since these methods do not require initial solutions and they are the only ones that are able to guarantee that global minima are achieved. When a close to the optimum solution was found (cumulative relative error of approximately 15%), this solution is then passed to the deterministic one, Interior-Point Algorithm, to refine the solution and reduce computational times since GA employs much time to refine the solution. The optimisation scheme is shown in Figure 26

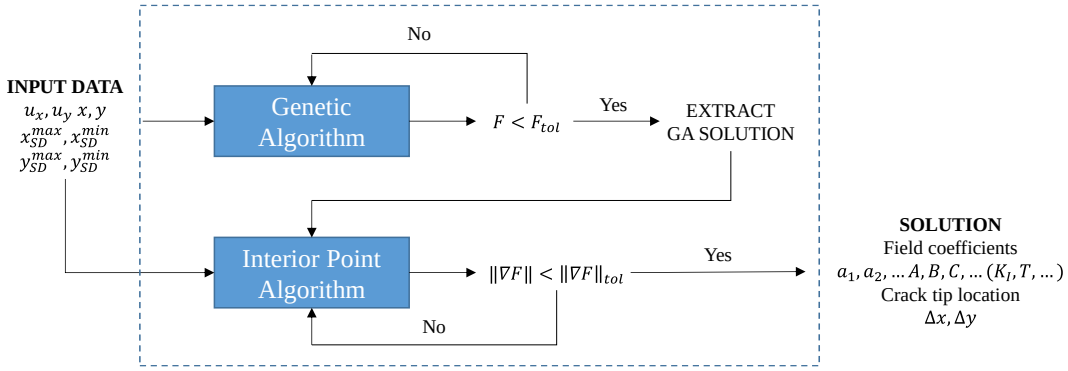

Figure 26: Optimisation scheme

As shown in Figure 26, the inputs are the displacement field data and its coordinates (annular mesh points), which is extracted using the crack length to define mesh parameters, as well as the search domain bounds, which also depend on the crack length. Thus, as all inputs are referred to this variable, the procedure is easily automatable. As shown in the optimisation scheme, the Interior-Point algorithm is controlled by the gradient norm of the objective function (optimisation change in gradient) and thus allowing checking found minima during the algorithm course.

Regarding GA features, due to the heuristic nature of this kind of algorithm, there are some values depending on the optimisation problem and must be previously established by the user (trial and error approach) to ensure proper operation. A population of 250 individuals was chosen according to the number of variables involved in the problem. The initial population was stochastically generated through a Gaussian distribution between two upper and lower limits depending on if the variable is constrained or unconstrained. For constrained variables, inputs established bounds were used and for unconstrained variables values within the range [-10, 10]. At the end of each iteration, the population individuals were sorted according to their rank instead of their fitness value since sometimes very similar fitness values could lead to errors during the sorting stage. Once individuals have been sorted, an elitism level of 5% was chosen (individuals surviving this selection and are included in the next generation). The 70% of the next generation was created through the crossover operator by employing a linear combination between best parents weighted according to their fitness values. Hence, the rest of the population was generated through the mutation operator in compliance with the defined constraints.

For the Interior-Point Algorithm, a quasi-Newton approach and trust-region approach was implemented [38]. Commonly, a full-Newton approach provides better results in terms of computational time but due to the size of the objective function, the gradient, which involves one additional function per variable and constraint, can be large and not tractable. In addition, if the Hessian matrix is also required, a matrix comprising as many rows and columns as variables and constraints would be difficult to manage. Thus, the inclusion of first order and second order derivatives or only the first order derivatives and addressing the Hessian matrix using finite differences requires large computational times only to include these derivatives in the mathematical problem. Hence, first-order derivatives were calculated using the second-order finite difference formulation (central derivative) to reduce discretisation errors and improve the accuracy of the results. The Hessian matrix was computed using the Broyden-Fletcher-Goldfarb-Shanno (BFGS) algorithm [117–119]. To solve each subproblem, a conjugate gradient trust-region approach was used instead of any line search method that could lead to any local minimum.

5.2.2. Calculation from numerical data

Unlike the crack tip parameters determination using experimental data, the numerically crack tip parameters determination is not as complicated since for example avoids locating the crack tip, which is well known and defined in a node, and does not present noisy as interpolation functions give well-shaped displacements, stresses or strains distributions, depending on the order of those polynomials functions. Thus, the process to determine the crack tip parameters from numerical data is not as complex as the experimental determination. From numerical data, the stress intensity factors were calculated from both displacements and stresses in order to provide two kinds of

values to give an exhaustive validation of these parameters. Thus, the axial displacement behind the crack tip and the axial stress ahead of the crack tip along the crack growth (tangential) direction were used to estimate stress intensity factors. Figure 27 shows these profiles for the numerical simulation in the stainless steel specimen.

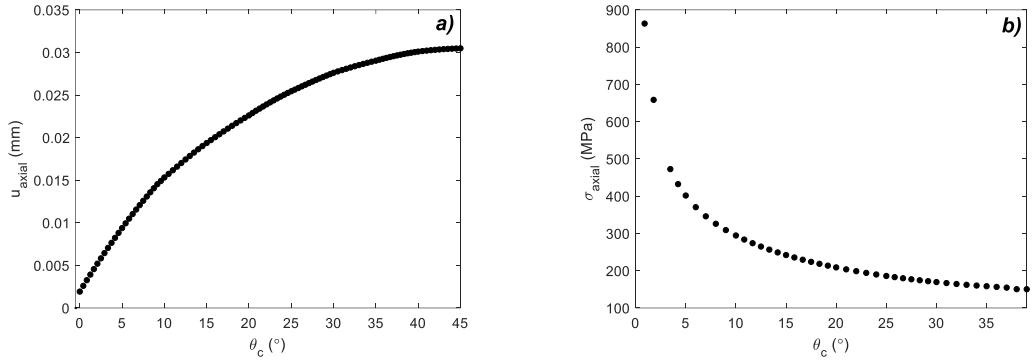

Figure 27: a) Axial displacement profile behind the crack tip and b) axial stress profile ahead of the crack tip both along the crack growth direction. Results from the numerical simulation of the stainless steel specimen at the maximum load for a normalised crack length of 0.225.

From the displacement and stress profiles, stress intensity factors were determined by fitting the simplified to these cases Irwin-Westergaard equations ($\theta = 180°$ and $\theta = 0°$, respectively). The vertical displacement behind the crack tip and the vertical stress ahead of the crack tip along the crack growth direction according to the Irwin-Westergaard approach are indicated in equations 25 and 26

$$u_y = \frac{K_I}{2G}\sqrt{\frac{r}{2\pi}}(\kappa + 1) + u_{y0} \tag{25}$$

$$\sigma_y = \frac{K_I}{\sqrt{2\pi r}} + \sigma_{0y} \tag{26}$$

To avoid the inclusion of plastic data in fitting data, the Von-Mises stress was used to remove nearest the crack tip plastic data. As the crack tip is previously known, the mathematical fitting problem remains linear and once elastic data has been extracted, both stress intensity factors were calculated by solving a linear equations system employing a suitable matrix factorisation. The fitting quality was assessed via Pearson's correlation coefficient between the numerical and the fitted data.

5.3. Standard functions for stress intensity factor determination

Empirical correlations were used to compare the stress intensity factors values obtained experimentally. Three empirical correlations were employed in this work depending on the geometry tested as well as crack growth shapes.

For a CT-specimen, the stress intensity factor under pure mode I is given by ASTM E647 correlation [120] as shown in equation 27

$$K_I = \frac{P}{t\sqrt{W}} \frac{2+\frac{a}{W}}{\left(1-\frac{a}{W}\right)^{\frac{3}{2}}} \left[0.886 + 4.64\left(\frac{a}{W}\right) - 13.32\left(\frac{a}{W}\right)^2 + 14.72\left(\frac{a}{W}\right)^3 - 5.6\left(\frac{a}{W}\right)^4\right] \quad (27)$$

Where t is the specimen thickness, P is the applied load, W is the specimen width and a is the crack length.

For a cylindrical thin wall pipe containing a circumferential crack under tensile load, the mode I stress intensity factor is given by Tada's correlation [121] based on Sanders' elasticity analysis on thin walled cylindrical geometries [122,123]. However, as the crack growth shape is different for both cylindrical specimens, two different correlations were employed. For the case where the crack emanated from only one hole, as in the stainless steel specimen as shown in Figure 17a, the stress intensity factor is given by equation 28 [121]. For the case where the crack emanated from both holes, as in the case of the aluminium alloy specimen as shown in Figure 17b, the nominal stress intensity factor is given by equation 29 [121].

$$K_I = \frac{P}{2\pi R t}\sqrt{R}\left(\frac{\sqrt{2}}{\left(\frac{t}{R\sqrt{12(1-\nu^2)}}\right)^{\frac{1}{2}}}\right)^{\frac{1}{2}}\left(\gamma + \frac{1-\gamma\cdot\cos\gamma}{2\cot\gamma + \sqrt{2}\cot\left(\frac{\pi-\gamma}{\sqrt{2}}\right)}\right) \quad (28)$$

$$K_I = \sqrt{\frac{\tan\gamma}{\gamma}}\frac{P}{2\pi R t}\sqrt{\pi R\gamma} \quad (29)$$

Where R is the mean radius of the cylindrical pipe and γ is the half-crack angle defined in Figure 17. For the stainless steel specimen, the normalised crack length was defined as γ/π and for the aluminium specimen as $2\gamma/\pi$ (angle subtended by the crack divided by the angle subtended by the initial ligament).

5.4. Image decomposition technique for comparing experimental and numerical results

The comparison between full-field numerical and experimental data, as in validating numerical results using experimental data, is not a straightforward procedure. Point-by-point comparisons are not usually possible due to the different coordinates of both numerical and experimental points. Even though numerical data is generated at the same points as experimental data, any rotation or displacement in the experimental coordinate system could lead to an error during the

comparison. Furthermore, point-by-point comparisons sometimes are not easy to interpret or to find a suitable quantitative global parameter to carry out the comparison.

Orthogonal polynomials as the Tchebichef type [124–126] allow extracting field features without depending on the coordinate system as well as the orientation of that coordinate system. Thus, if a displacement, stress or strain map is considered as an image whose pixels have a certain intensity, those maps can be decomposed in an intensity matrix as shown in equation 30 [126–128]

$$I(i,j) = \sum_{i=1}^{N} f_i \widetilde{T}_i(i,j) \tag{30}$$

Where I is an intensity matrix, f_i is the intensity of each Tchebichef moment and $\widetilde{T}_i$ is the shape descriptor of each Tchebichef polynomial. N is the number of shape descriptors which is chosen in order to properly model the displacement, strain or stress map [129].

Thus, this formulation allows, for a comprehensive data comparison, removing orientation effects and, for both in terms of the non-dimensional reconstructed maps as well as in terms of the shape descriptors, allowing checking also differences between same-order shape descriptors that may be attributed to the same physical effect on both numerical and experimental fields.

As example, Figure 28 and Figure 29 show numerical and experimental crack tip fields obtained via FEA and DIC, respectively, to be compared for the stainless steel and the aluminium alloy for normalised crack lengths of 0.27 and 0.47, respectively. As the crack tip field is symmetrical respect to the mid-cylinder-plane (radial-tangential plane containing the crack), only one part was compared as shown in that Figure.

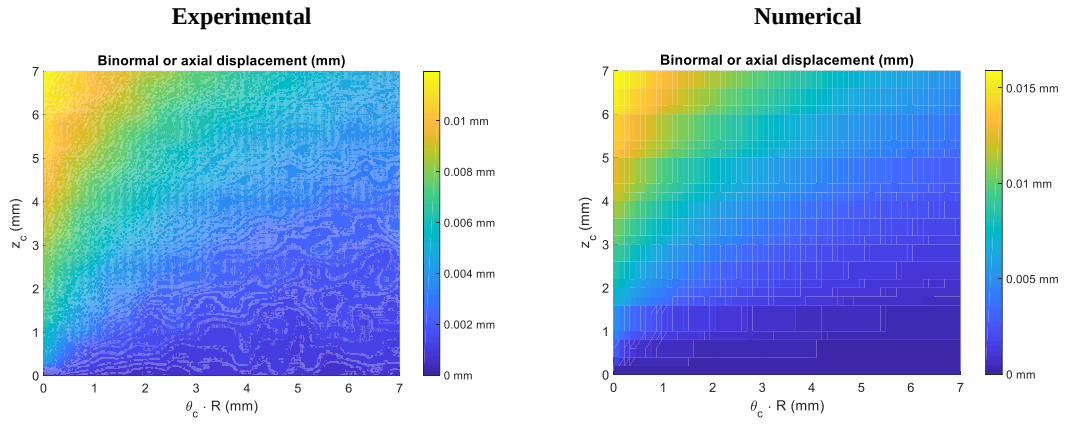

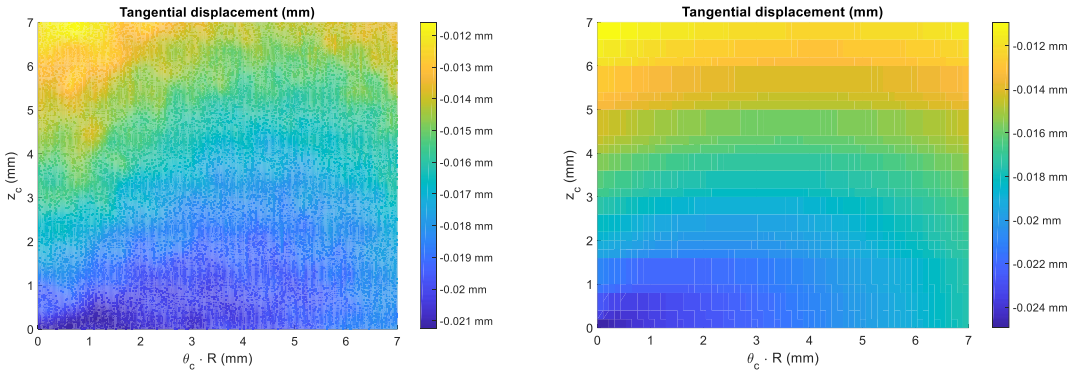

Figure 28: Example, in SS304L, of experimental and numerical displacement fields to perform the comparison using Image Decomposition technique for a normalised crack length of 0.27.

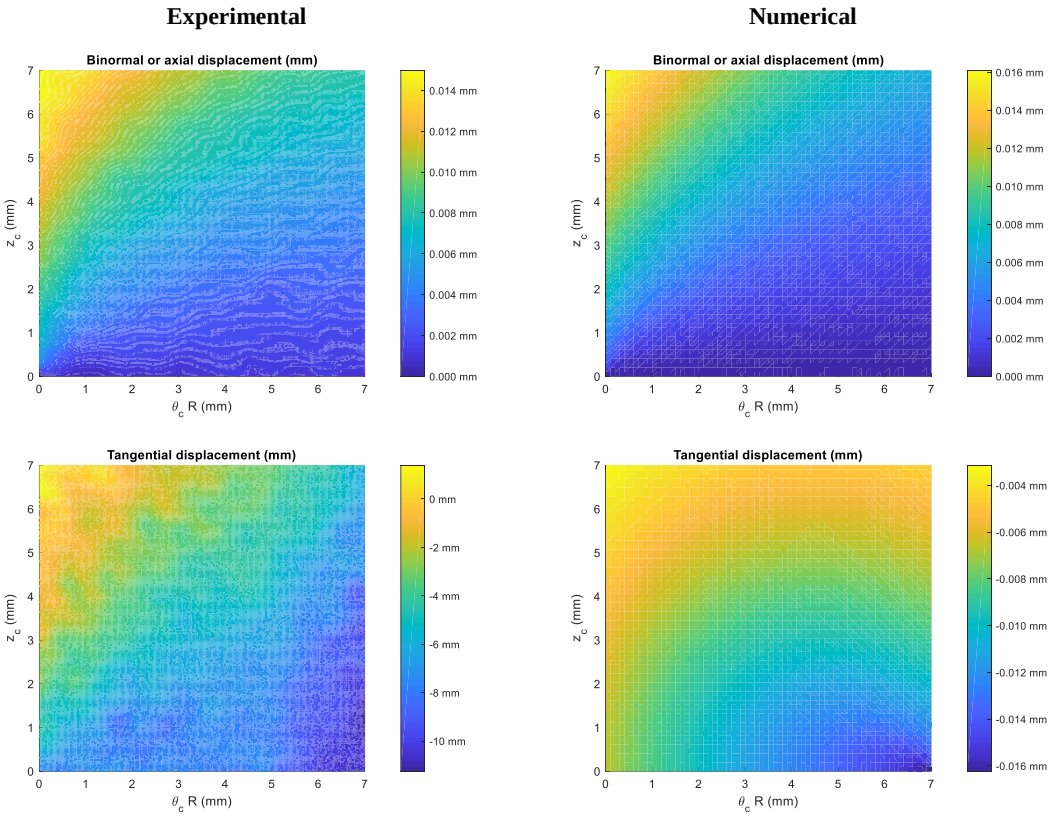

Figure 29: Example, in AA2024-T3, of experimental and numerical displacement fields to perform the comparison using Image Decomposition technique for a normalised crack length of 0.47.

Regarding the image decomposition procedure, 20 shape descriptors were employed for all the analysed cases providing a correlation value higher than 97%, being this value considered enough to accurately reproduce the original fields [129].

5.5. Alternative method for estimating the crack tip location based on the analysis of crack opening direction displacement maps

To check optimised crack tip positions using the above-described hybrid approach, an alternative method providing an estimation of the crack of the crack position is necessary. Thus, the method reported by Vasco-Olmo et al. [130], originally used to determine the crack tip opening displacement, was employed. This method analysed the vertical or crack opening direction displacement maps to find the inflection point occurred at the crack tip because of the discontinuity. Although it can be found in the literature similar methods based on the same idea, i.e. Breitbarth et al. [131,132], this method was chosen since it provides accurate solutions and avoids mathematical fitting stages which are not usually easily addressable since involve the use of hyperbolic trigonometric functions.

The first step is to establish a confidence region enclosing the crack tip in order to extract vertical displacement profiles along the crack opening direction. If these vertical profiles are plotted, Figure 30a is obtained. As shown in this Figure, there is a zone where all the profiles intersect among them. This point can considered as y-coordinate of the crack tip location on the displacement map. The second step is to extract the y-coordinate as well as the displacement value at that point. Once the y-coordinate was established, a vertical displacement profile at the extracted y-coordinate is plotted along the crack growth direction as shown in Figure 30b. If a line of value the above extracted displacement in Figure 30a is also plotted in Figure 30b, the intersection between this line and the displacement profile along the crack growth direction provides the x-coordinate of the crack tip.

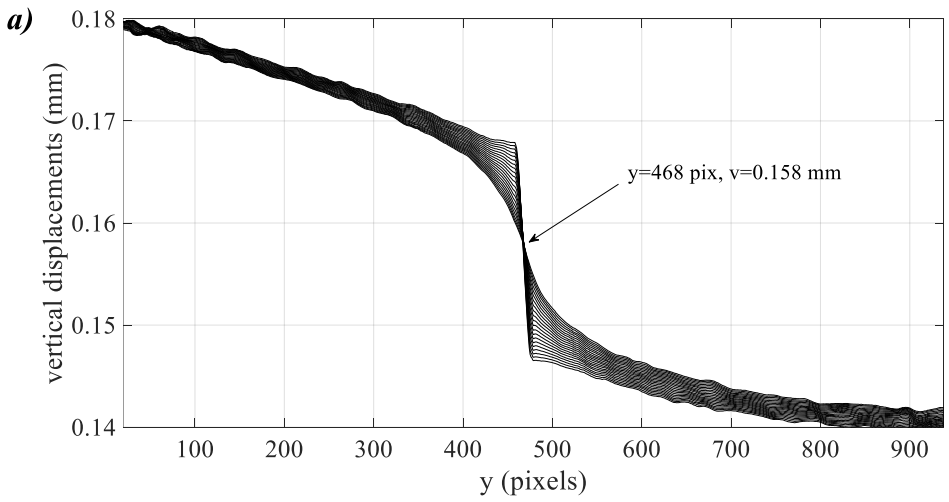

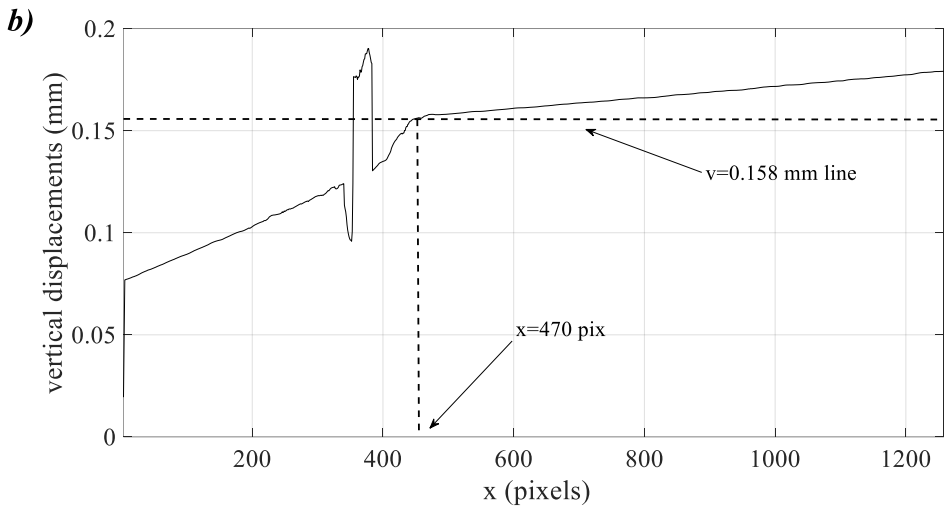

Figure 30: Figure to show the methodology for estimating the crack tip location from vertical displacement maps. a) Set of vertical displacement profiles surrounding the crack tip along the crack opening direction and b) vertical displacement profile for the chosen crack tip y coordinate along the crack growth direction [72]

6.Results and discussion

In this Chapter, results are divided in two main parts. First, the validation of the proposed methodology for crack tip parameters calculation from experimental data is displayed. Thus, a convergence analysis is firstly done and secondly a verification of the calculated characterising parameters and the crack tip locations. In the second part, the validation of the proposed methodology for characterising crack tip fields on non-planar surfaces is displayed. First, the plane stress condition is checked. Subsequently, the methodology is experimentally validated through the comparison of experimental stress intensity factors and the surrounding elastic field with theoretical values. In last, a comparison between numerical and experimental SIFs and crack tip displacements fields is done.

6.1. Improved hybrid approach for crack tip parameters determination from experimental data

The proposed improved methodology for the crack tip parameters determination from experimental data is firstly analysed and validated using displacement fields experimentally obtained in the CT-specimen fatigue testing described in Section 4.1.1. In the following Sections (6.1.1 and 6.1.2), a convergence analysis is performed to analyse the algorithm features as well as a validation of results by comparing both crack tip governing parameters and the crack tip location. The CJP model is chosen to validate this hybrid approach for several reasons. First, a high number of variables are involved in the mathematical fitting problem and some of them are related to plasticity-induced crack shielding effect, whose mathematical modelling is more complex than Williams' model, which is based on polynomials series. Secondly, the CJP model, which is a Muskhelishvili-type model, is very sensitive to the crack tip position initially chosen for the data point collection around the crack tip as reported in Chapter 3. Hence, using this model is a way to test the proposed fitting algorithm and push it to the limit. The validation was performed by analysing crack tip displacement fields obtained at the maximum load (750 N) for

different and representative crack lengths, from 3.47 up to 9.4 mm (0.17 and 0.47 in terms of the normalised crack length).

6.1.1. Convergence analysis

To study the convergence features of the proposed algorithm, an illustrative crack length of 7.75 mm (0.38 in terms of the normalised crack length) was chosen, as a typical example of the results obtained for any other crack length. Figure 31 shows the variation in some parameters during the optimisation process.

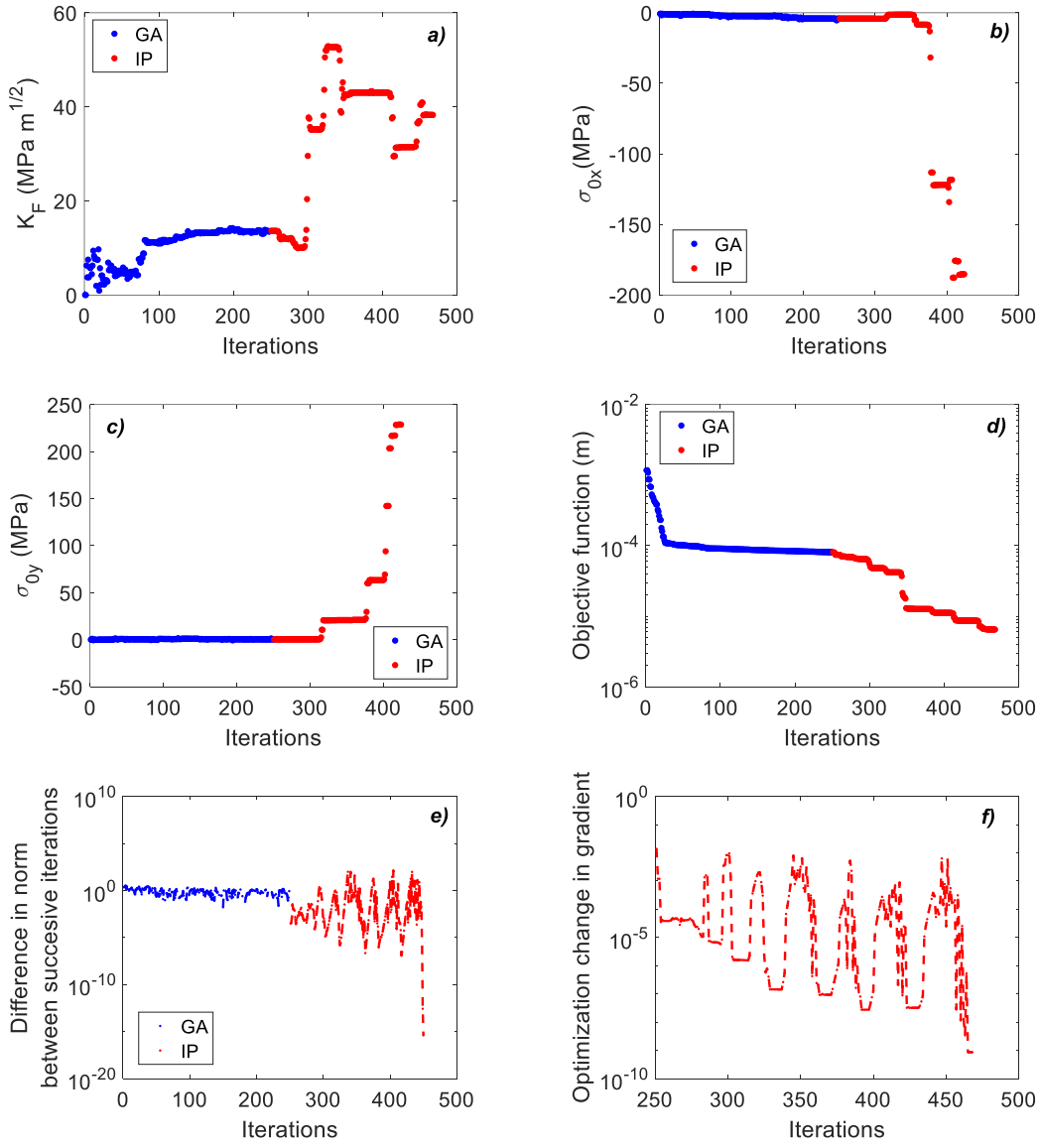

Figure 31: Variations observed in some specific parameters during the optimisation process. a) Opening mode stress intensity factor of the CJP model, b) Non-singular stress along the crack growth direction, c) Non-singular stress along the crack opening direction, d) Fitness or objective function, e) Norm of the difference between solutions at successive iterations and f) optimisation change in gradient (norm of the objective function gradient). Blue points indicate GA iterations and red points IP algorithm iterations. Crack length of 7.75 mm (0.38 in terms of the normalised crack length)

The optimisation change in gradient shown in Figure 31f clearly illustrates the complexity of the optimisation problem since several local minima were found during the algorithm course until reach the global minimum. At these local minima, the crack tip parameters (stress intensity factor and non-singular stresses shown in a, b and c) do not represent the final solution.

For example, for the case of the opening mode stress intensity factor (K_F), shown in Figure 31a, either very low or very high values were found. Moreover, the variation in non-singular stresses between successive iterations is poorly significant since those values hold close to zero until the global minimum starts to be reached at around 350 iterations. The evolution in the objective function, presented in Figure 31d, shows two decreasing regions. The first decrease occurs at around 50 iterations while the GA is running and the second immediately after the IP algorithm starts at around 330 iterations. The first decrease and its subsequent stabilisation are due to GA can provide a well-conditioned initial solution fairly quickly but find some difficulties to refine the solution. The second steep decline during the IP algorithm course coincides with the region where the crack tip parameters approach their final and optimum values. Figure 31e shows the norm between successive solutions. As observed, this parameter experiences an abrupt change (from 10^{-1} to 10^{-16}) when the final solution was achieved. This observation together with the abrupt variation in the optimisation change in gradient as well as the slightest errors in terms of K_F clearly supports the conclusion of the exposed methodology can obtain an optimum value and hence, highlights the ability and powerful of this methodology.

The sensitivity of the stress intensity factor and non-singular stresses to the crack tip position is reflected in Figure 32 and Figure 33 which show the variation of those crack tip parameters with the Euclidean distance to the crack tip during the algorithm course.

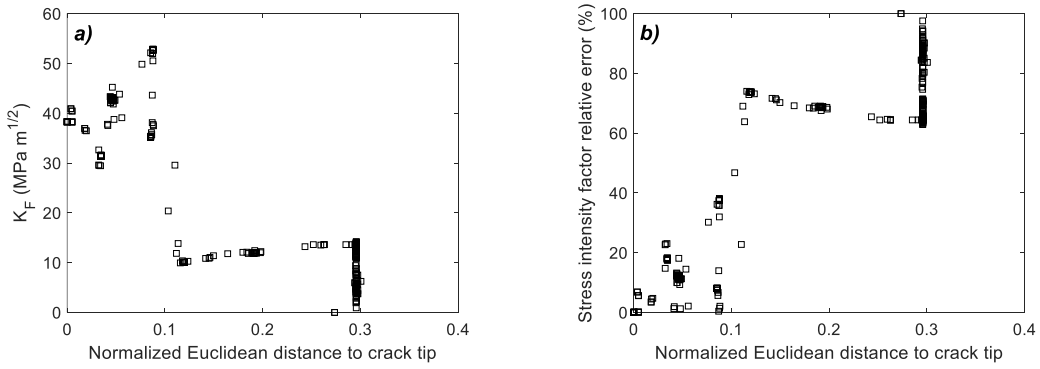

Figure 32: Variation in the CJP model SIF with the normalised Euclidean distance to the crack tip using the crack length. Crack length of 7.75 mm. a) Stress intensity factor and b) Relative error in terms of the stress intensity factor

As observed in Figure 32, the opening mode SIF presents differences of around 20% even though the normalised distance to the optimised crack tip location is lower than 5%. If a 5% error criterion is chosen, only normalised distances lower than 2% provide accurate results in terms of that

variable. A similar trend is observed in Figure 33 for the non-singular stresses. However, in this case, the sensitivity of these variables is higher than for the stress intensity factor since for normalised distances of around 1%, errors of around 10% were found.

These results reported in Figure 32 and Figure 33 illustrate the sensitivity of some crack tip field models to the crack tip location and once again justify the necessity of the proposed methodology for the calculation of the crack tip characterising parameters from experimental data. Moreover, the crack tip position sensitivity when the CJP model is used also demonstrates the ability of this model for capturing local plasticity influences on the global elastic field due to the effect of the plastic enclave generated as the crack grows.

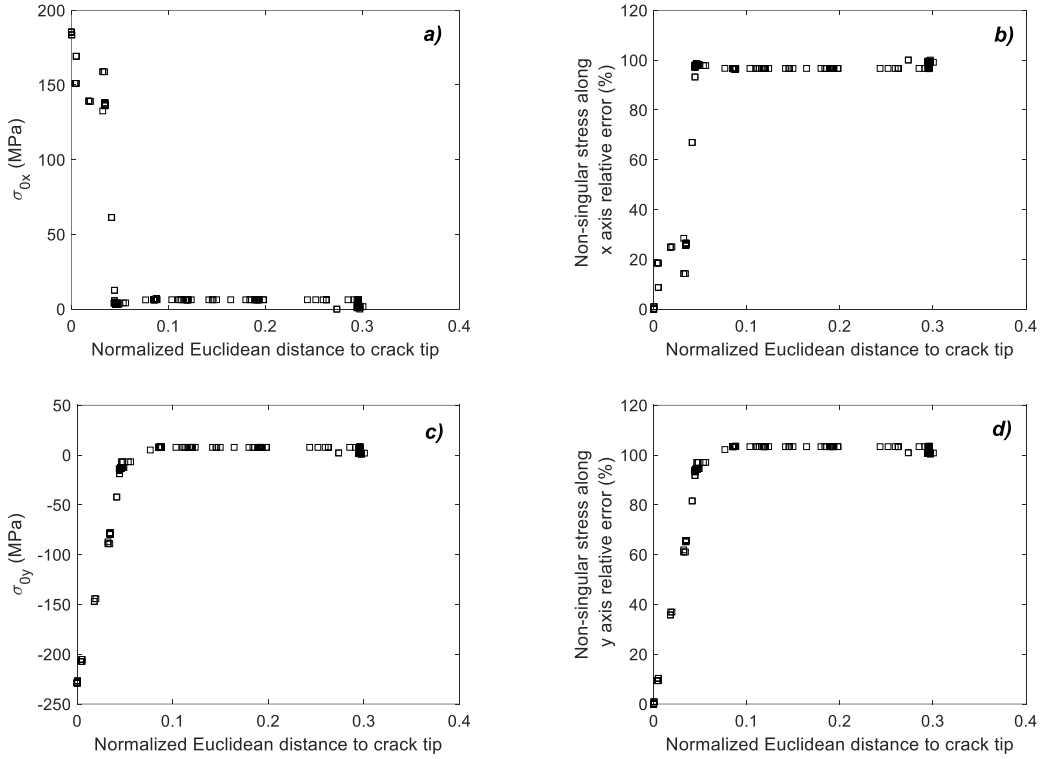

Figure 33: Variation in non-singular stresses with the normalised Euclidean distance to the crack tip using the crack length. Crack length of 7.75 mm. a) and b) non-singular stress along the crack growth direction and relative error in terms of this variable, respectively and c) and d) non-singular stress along the crack opening direction and relative error in terms of each variable, respectively.

To conclude the convergence analysis, the path followed by the crack tip as well as the crack tip coordinates during the algorithm course are analysed. Figure 34 shows the path followed by the optimised crack tip location during the algorithm course superimposed on a cracked specimen speckle image. As shown in this Figure, the crack path tries to border the surrounding crack tip area rather than to reach the optimum value via a straight line. Thus, the algorithm try to find adjacent points until coordinates of the crack tip are closer to the optimum when first, a pseudo-vertical straight way and then a quasi-horizontal straight way was chosen. Figure 35 shows the normalised crack tip coordinates, as the difference between the coordinate at each iteration and

the optimum achieved and divided by the crack length, during the algorithm course. This Figure also highlights the fact reported in the previous Figure. As shown in Figure 35a, the x coordinate descends faster than the y coordinate (Figure 35b) until reaching a closer to the crack tip position when the highest descend was found.

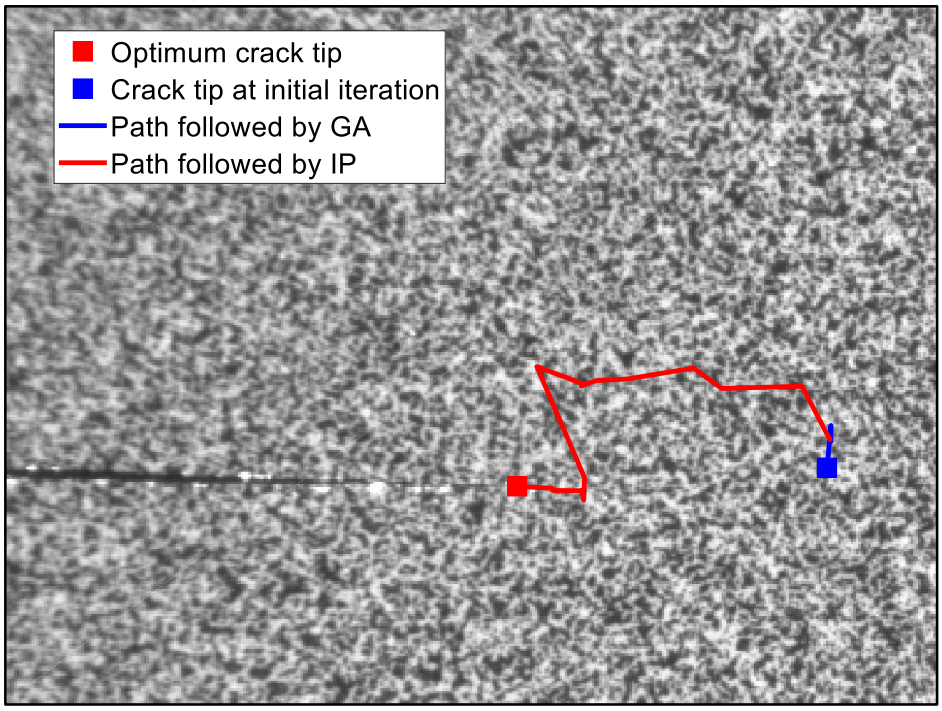

Figure 34: Path followed by the crack tip during the optimisation process superimposed over a speckle image showing the crack. Crack length of 7.75 mm. Blue indicates GA iterations and red refers to IP algorithm iterations

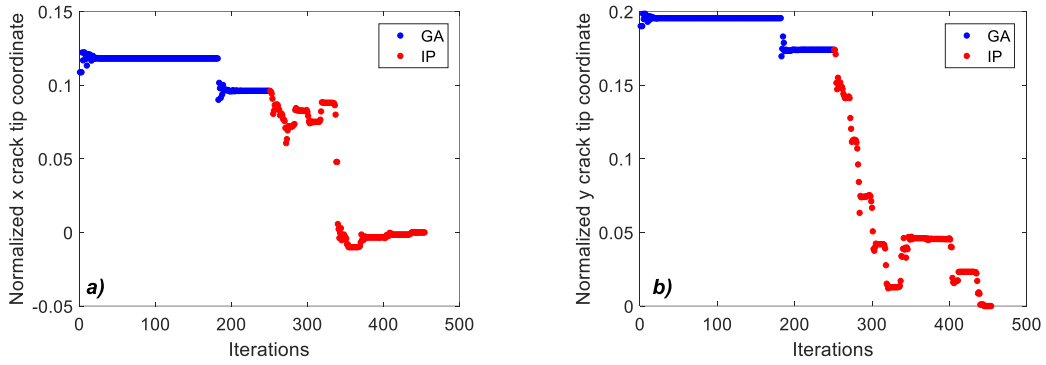

Figure 35: Evolution of the crack tip normalised coordinates using the crack length during the algorithm course for a crack length of 7.75 mm. a) x coordinate and b) y coordinate. Zero value corresponds to the optimum

6.1.2. Results validation

The crack tip characterising parameters (stress intensity factors and non-singular stresses) and the crack tip locations were determined for different crack lengths within the range 3.4 mm and 9.4 mm (0.17 and 0.47 expressed in terms of the normalised crack length). The obtained results for the different analysed crack lengths are detailed in Table 6. To check the validity of the results,

opening mode SIFs were compared with the solution provided by ASTM E647 standard [120] as shown in Figure 36. As shown, both stress intensity factors take similar values and trends, highlighting a high level of agreement between both the CJP model and the nominal stress intensity factors. Moreover, if the average relative difference is calculated, a value of 2.63% is obtained (see last column in Table 6). The obtained results also agree with results previously reported by other authors [105,133,134].

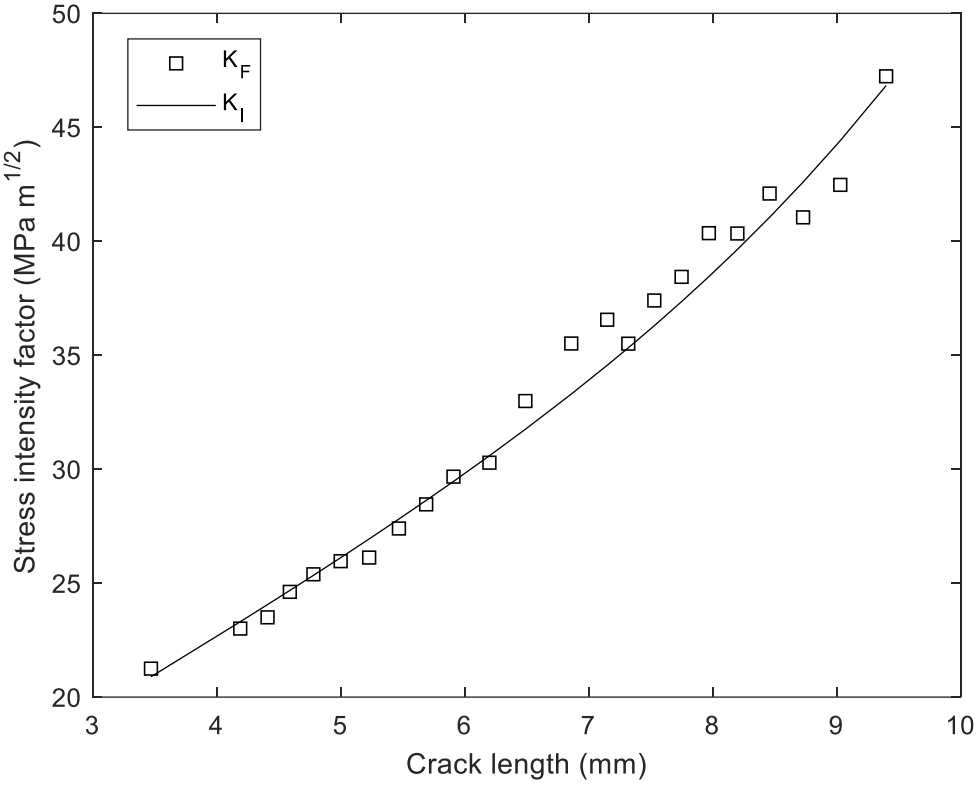

Figure 36: CJP model opening model stress intensity factor and theoretical stress intensity factor from ASTM standard against the crack length.

The validation of the crack position was done by comparing optimised crack tip locations with those determined by employing the alternative approach described in Section 5.5. Both optimised and alternatively determined crack tip locations are reported in Table 6. A good level of agreement was found between both values providing an average relative error around 1.25% and a maximum of 2.65%. Figure 37 shows the relative error between both determined crack tip positions against the crack length. As displayed in this Figure, the higher differences were found for crack lengths between 3 mm and5.5 mm (0.15-0.275 in terms of the normalised crack length) and then immediately descends to constant values around 0.75%. This difference between shorter and larger crack lengths can be explained through the stress intensity which enhances as the crack grows and therefore, displacements maps are less noisy than for the shorter crack lengths which provide better crack tip location values. In addition, notch manufacturing residuals stress might

also affect the surrounding crack tip for shorter crack lengths. To illustrate the agreement between both values, Figure 38 shows both obtained crack tip locations superimposed on a specimen speckle image at the maximum load and for the higher crack length to improve the visualisation and to compare with the visualised crack path on that image.

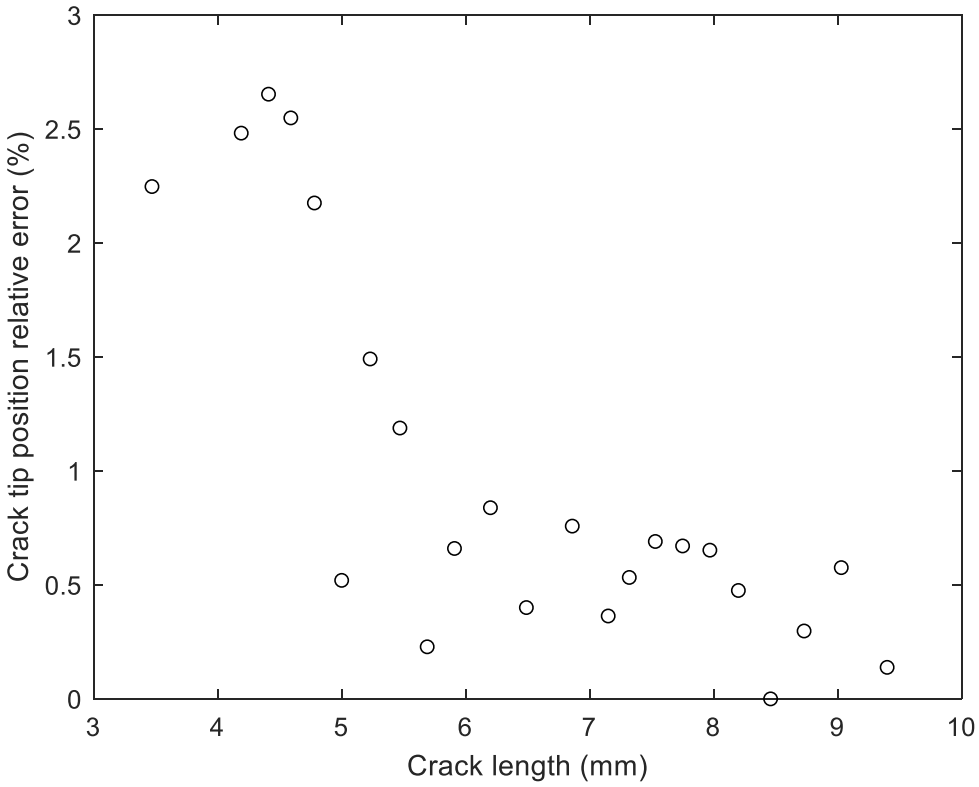

Figure 37: Crack tip position relative error against the crack length

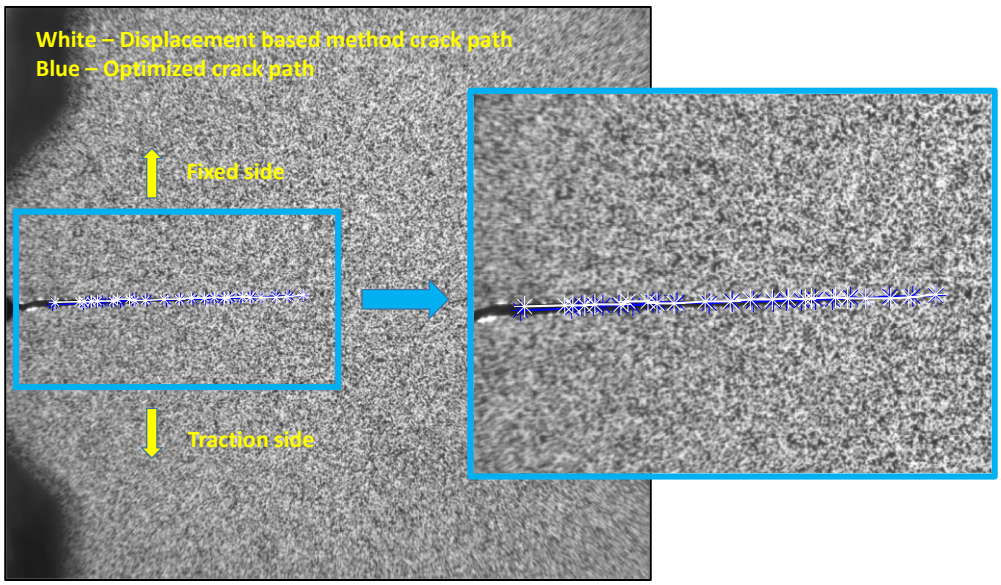

Figure 38: Optimised and calculated from vertical displacement maps crack paths superimposed on a specimen speckle image for the higher crack length 9.4 mm

Table 6: Comparison between crack tip locations and mode I stress intensity factors obtained by the different approaches for the different analysed crack lengths

	Optimised Technique		Vertical Displacement Technique							
a mm	Δx pix	Δy pix	Δx pix	Δy Pix	d pix	d μm	d/a (%)	K_F MPa $m^{1/2}$	K_I MPa $m^{1/2}$	SIFs error (%)
3.47	56	486	60	482	5.66	73.0	2.24	21.25	20.89	1.71
4.19	107	484	100	481	7.62	99.0	2.48	23.01	23.31	1.29
4.41	117	481	108	481	9.00	117	2.65	23.50	24.06	2.32
4.59	129	481	120	481	9.00	117	2.54	24.62	24.68	0.25
4.78	138	481	130	480	8.06	104	2.17	25.39	25.34	0.19
5.00	154	481	156	480	2.24	29.0	0.52	25.96	26.12	0.59
5.23	168	481	163	477	6.40	83.2	1.49	26.12	26.94	3.03
5.47	188	478	183	477	5.10	66.2	1.18	27.40	27.81	1.49
5.69	193	478	192	479	1.41	18.3	0.22	28.46	28.63	0.61
5.91	212	478	209	479	3.16	41.1	0.65	29.67	29.46	0.71
6.20	244	479	240	477	4.47	58.1	0.83	30.28	30.59	1.00
6.49	267	477	265	477	2.00	26.0	0.40	32.99	31.75	3.90
6.86	288	477	285	475	3.61	46.7	0.75	35.51	33.29	6.67
7.15	308	477	307	475	2.24	29.0	0.36	36.56	34.56	5.79
7.32	321	476	323	474	2.83	36.7	0.53	35.51	35.32	0.52
7.53	336	476	340	475	4.12	53.6	0.69	37.40	36.30	3.04
7.75	350	475	346	474	4.12	53.6	0.67	38.44	37.35	2.90
7.97	367	475	370	473	3.61	46.8	0.65	40.36	38.45	4.96
8.20	385	473	382	474	3.16	41.1	0.47	40.34	39.64	1.77
8.46	400	474	400	474	0.00	0.00	0.00	42.10	41.05	2.54
8.73	424	472	425	474	2.24	29.0	0.29	41.05	42.60	3.63
9.03	447	472	443	473	4.12	53.6	0.57	42.47	44.41	4.37
9.4	470	471	470	470	1.00	13.0	0.13	47.24	46.83	0.87
	Average values				4.14	50				2.35

Optimised non-singular stresses against the crack length (σ_{0x} and σ_{0y}) are plotted in Figure 39. Expected results were obtained since for the non-singular stress along the crack growth direction, negative sign values were found due to the lateral specimen contraction due to Poisson's effect. For the non-singular stress along the crack opening direction, positive sign values were found which are related to the applied traction load. It is significant the almost identical trend presented for both parameters. First points, show disagreement regarding to the other points which present better-defined trend and it might be attributed to the effect of the residuals stresses during the notch manufacturing process as well as the transition between fatigue crack growth stages (I-II) where the expected T-stress value could be higher [135].

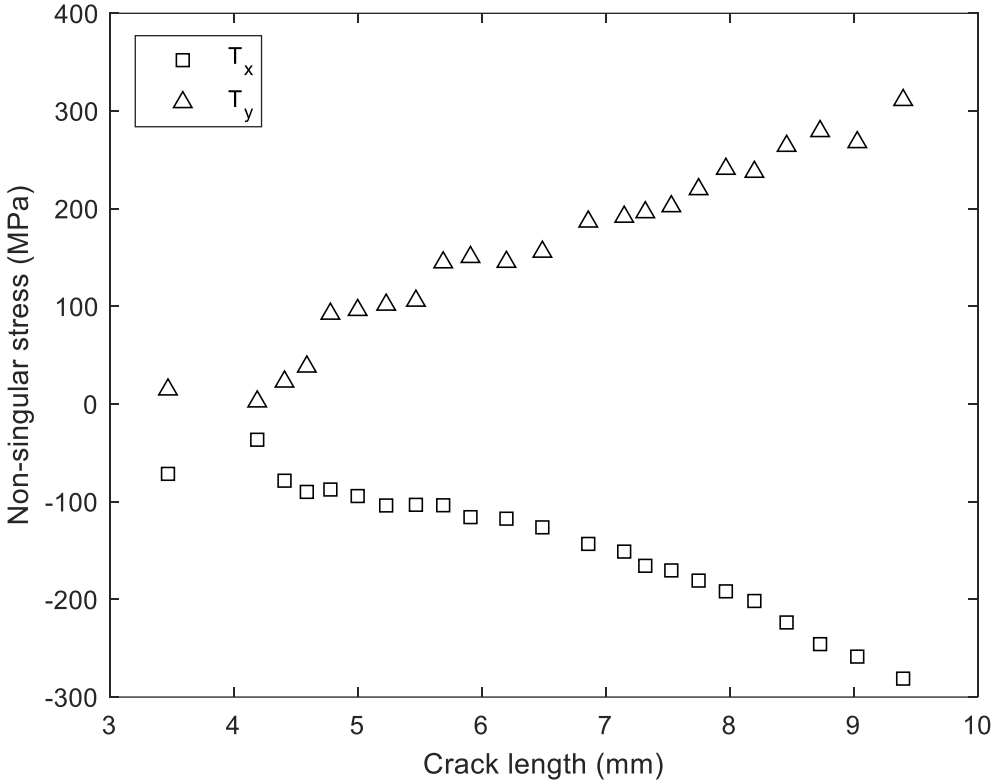

Figure 39: Non-singular stresses along the crack growth (σ_{0x}) and crack opening (σ_{0y}) directions for different crack lengths

To conclude this part, Table 7 shows all obtained stress intensity factors and non-singular stresses, crack tip locations as well as computation times employed by each algorithm. Regarding K_R and K_S parameters, both values increase in negative sign as the crack grows because of the increasing crack tip plasticity and hence enhances the effect of the plastic enclave on the surrounding K-field. In addition, the trend of the obtained values agrees with previously reported results [15,34,99] for the same alloy and therefore provides an additional validation of the proposed characterisation algorithm. Computation times for all cases are around 1 minute with the GA taking around 92% of the total optimisation time. Thus, reasonable times were obtained by the algorithm in contrast to other approaches [101,103]. As shown in Table 7, the fitness function value increases with the crack length. This increasing might be attributed to a loss of fitting quality as the crack grows due to any plasticity effect. However, results in terms of stress intensity factors, non-singular stresses as well as crack tip locations refute this last statement, and the increasing of that value could mainly corresponds to the increase of the stress intensity which implies higher displacement values and hence increments in the objective function values.

Table 7: Optimised characterising parameters, crack tip locations, fitness functions and computation times for the different analysed crack lengths

a	K_F	K_R	K_S	σ_{0x}	σ_{0y}	Δx	Δy	f	t_{GA}	t_{IP}	t_T
mm	MPa $m^{1/2}$	MPa $m^{1/2}$	MPa $m^{1/2}$	MPa	MPa	pix	pix	m	s	s	s
3.47	21.25	0.00	-3.26	-71.47	14.81	56	486	5.64E-09	54.65	5.46	60.11
4.19	23.01	0.00	-3.09	-36.55	2.56	107	484	7.91E-09	55.93	5.29	61.22
4.41	23.50	0.01	-4.03	-78.48	22.89	117	481	6.16E-09	57.13	3.92	61.05
4.59	24.62	0.00	-4.29	-89.93	38.26	129	481	8.34E-09	59.79	4.28	64.07
4.78	25.39	0.00	-1.57	-87.52	92.37	138	481	1.00E-08	56.02	3.25	59.27
5.00	25.96	-0.28	-2.45	-94.19	96.20	154	481	8.26E-09	54.96	6.63	61.59
5.23	26.12	-0.35	-2.96	-103.84	101.64	168	481	9.95E-09	53.89	4.96	58.85
5.47	27.40	0.00	-3.13	-103.17	105.71	188	478	1.38E-08	58.97	4.53	63.50
5.69	28.46	-0.24	-1.78	-103.63	144.95	193	478	2.71E-08	56.43	5.15	61.58
5.91	29.67	-0.07	-2.45	-115.79	150.43	212	478	2.04E-08	56.09	4.07	60.16
6.20	30.28	0.00	-3.18	-117.35	145.47	244	479	1.36E-08	57.65	3.47	61.12
6.49	32.99	-0.40	-3.61	-126.24	155.83	267	477	3.48E-08	53.47	3.87	57.34
6.86	35.51	-0.71	-3.59	-143.19	186.71	288	477	3.18E-08	53.55	3.86	57.41
7.15	36.56	-0.64	-4.18	-151.04	191.65	308	477	3.29E-08	54.28	5.97	60.25
7.32	35.51	-1.22	-5.12	-165.59	196.25	321	476	2.21E-08	57.33	4.11	61.44
7.53	37.40	-1.03	-5.26	-170.33	202.41	336	476	3.06E-08	57.91	3.55	61.46
7.75	38.44	-1.36	-5.38	-180.74	219.86	350	475	2.97E-08	53.75	5.55	59.30
7.97	40.36	-1.58	-5.49	-191.75	240.70	367	475	2.23E-08	58.34	4.15	62.49
8.20	40.34	-1.61	-6.32	-201.62	237.61	385	473	1.49E-08	56.01	4.05	60.06
8.46	42.10	-2.17	-6.73	-223.61	264.21	400	474	3.81E-08	52.74	5.20	57.94
8.73	41.05	-3.09	-7.65	-245.80	279.31	424	472	3.48E-08	55.39	5.71	61.10
9.03	42.47	-2.76	-9.32	-258.56	268.00	447	472	3.60E-08	54.81	5.95	60.76
9.40	47.24	-2.70	-9.16	-281.10	311.15	470	471	2.42E-08	58.42	4.43	62.85

6.2. Validation of the proposed methodology for extending crack tip field models to non-planar surfaces

In this section, results for validating the proposed approach to characterise the crack tip field, considering the curvature effect, are presented and discussed. Two materials with different crack growth shape are analysed, an austenitic stainless steel (304L) and aluminium alloy (2024-T3). First, the plane stress hypothesis was checked via finite element analysis since digital image correlation data provides only surface information and hence, a whole stress tensor cannot be calculated since through-thickness gradients are required. Secondly, an experimental verification is performed by analysing inferred mode I SIFs using Williams' series model and assessing the fitting quality (quantitative and qualitative) via confidence intervals and other fitting quality parameters as the relative function error value. Here, Williams' model was used instead of other

advanced models to avoid the inclusion of other variables related to crack shielding effect to simplify the validation. Subsequently, a comparison in terms of numerically and experimentally obtained stress intensity factors is performed. In last, a comprehensive comparison between numerically and experimentally obtained displacements fields is done by the Image Decomposition technique.

6.2.1. Satisfying the plane stress hypothesis

The first step for validating the proposed approach is to check the plane stress hypothesis over the cylinder surface since original flat crack tip field models are formulated for a plane elasticity problem, either plane stress or plane strain. Thus, according to the adopted coordinate formulation, the out-of-unwrapped-plane direction coincides with the radial direction (expressed in cylindrical coordinates) and it should be zero or almost zero. Figure 40 shows the radial stress along the circumferential direction expressed in terms of the azimuthal angle at different cylinder heights for both aluminium alloy and stainless steel numerical simulations and for different crack lengths. As shown in Figure 40, for both materials and any analysed crack length, there is a high stress and positive value at the crack tip and then descends to negative values, which imply compression surrounding the crack tip and later the radial stress goes to almost zero (residual calculation). These values are due to the singularity at the crack tip, which enhances the stress up to higher values as well as the high out-of-plane contraction due to Poisson's effect, which also is magnified at this area nearest the crack tip. However, it can be established that it exists a plane stress state on the cylinder surface beyond those points and hence, confirming the hypothesis.

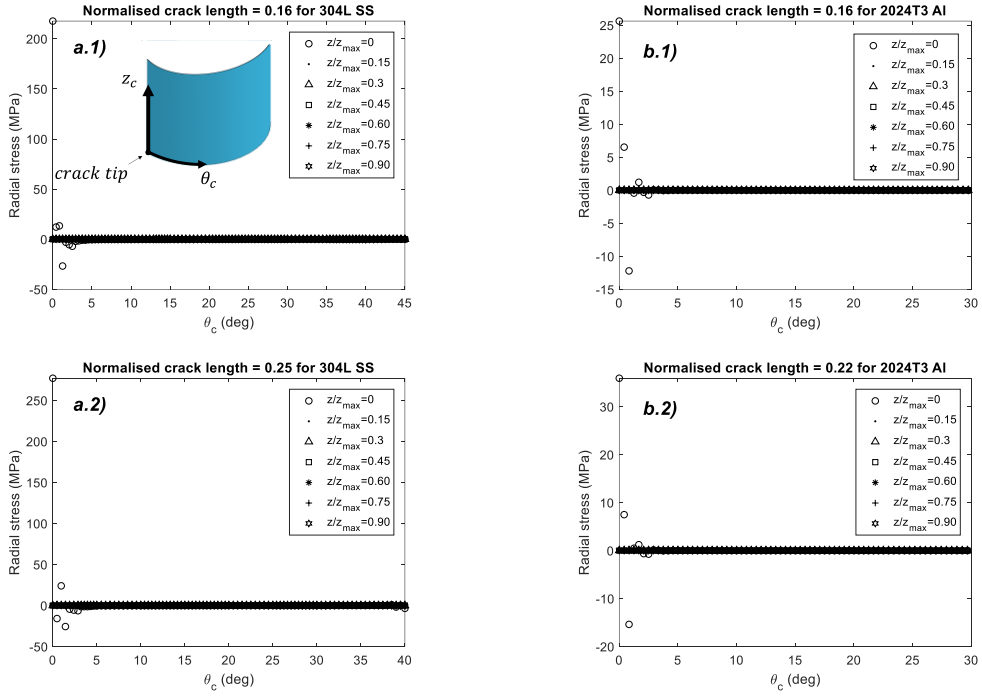

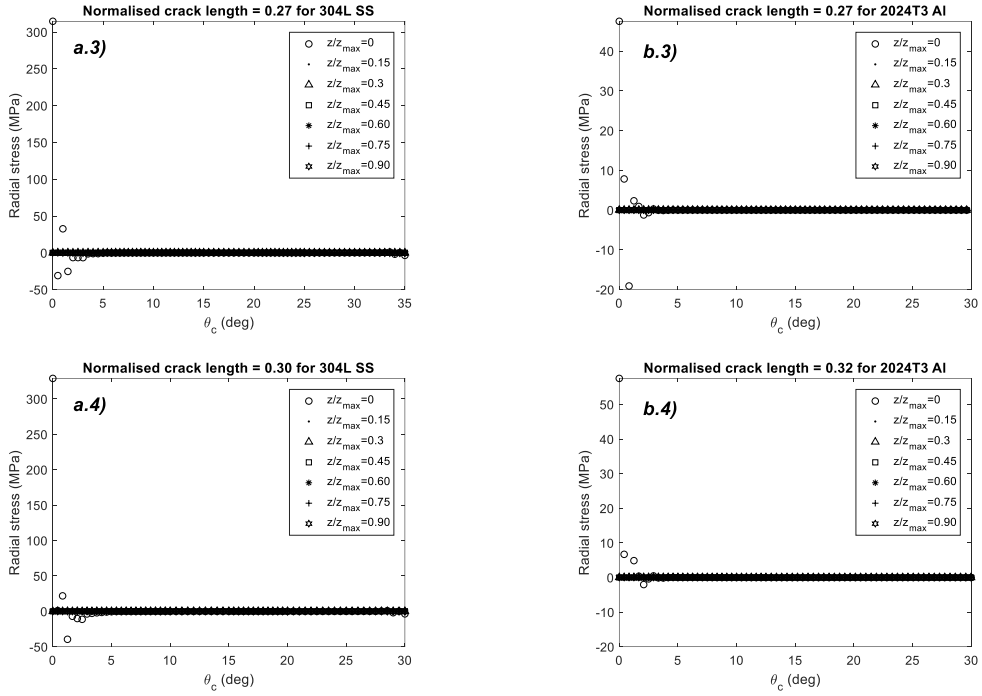

Figure 40: Radial stress profiles along the circumferential direction at different cylinder heights (axial direction) for different crack lengths (1-4) and for different materials (a and b refer to stainless steel and aluminium alloy respectively). Origin at the crack tip.

6.2.2. Experimental validation

Figure 41a shows the computed stress intensity factors on the stainless steel specimen for different crack lengths and employing different terms of Williams' model against the normalised crack length. As shown in this Figure, up to 4 terms were employed due to results for higher order terms do not change regarding the results obtained using 4 terms and hence, the model becomes stable. In fact, the high-order coefficients were negligible (less than 10^{-16}). Hence, this fact shows the great correlation between the experimental data and the theoretical formulation. Regarding the values of the mode I SIFs, all values present a high level of agreement with the theoretical solution. Average errors for mode I SIFs of 6.36%, 5.38% and 4.13% were found for 2, 3 and 4 terms, respectively. For the aluminium alloy (Figure 42a), average errors of 3.18%, 3.74% and 3.78 for 2, 3 and 4 terms, respectively. These small relative errors also shows the results reliability.

These slight differences could be attributed to noise inherent to DIC technique (spatial calibration residuals and image matching residuals) as well as the required derivatives to perform this methodology. Moreover, the employed Young modulus (provided by the manufacturer) is an average value that could vary the results around 1%. Nonetheless, the major differences could be attributed to the crack tip plasticity, which could modify the global elastic field and therefore K values, and it is not explicitly considered in the theoretical correlations.

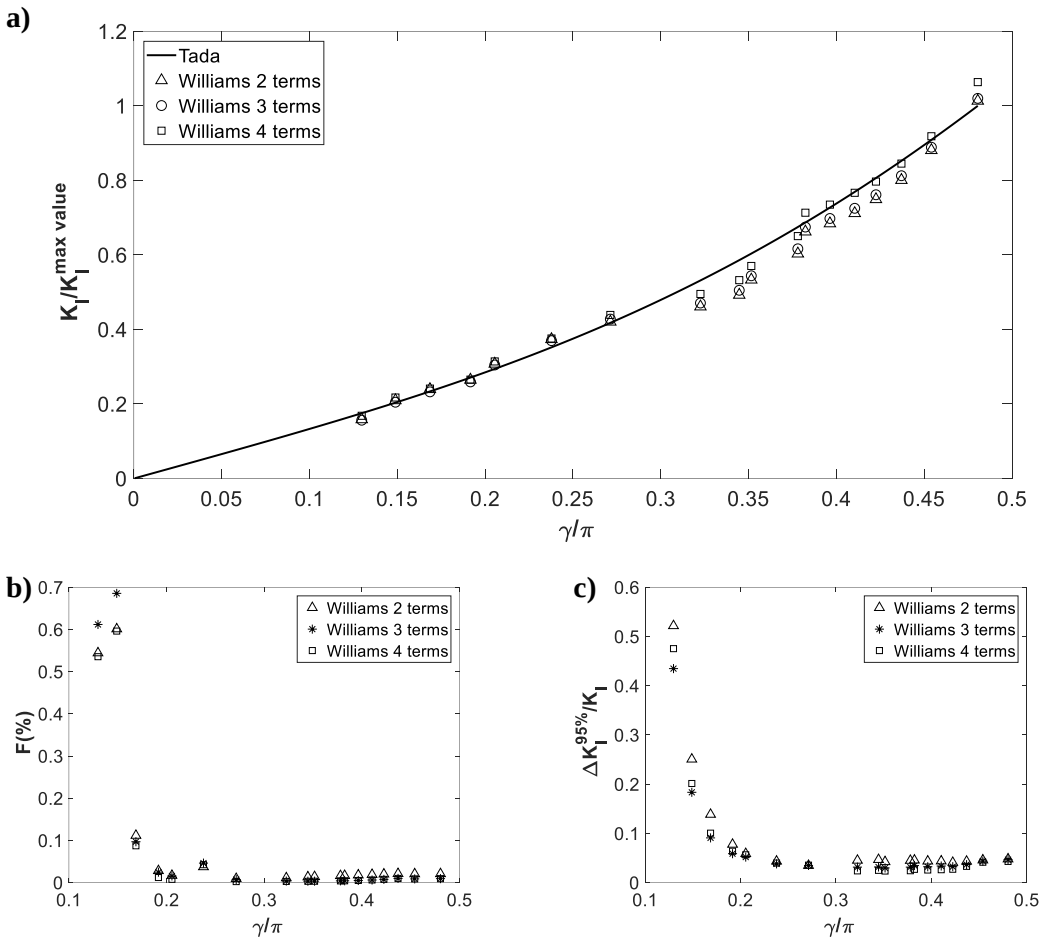

Figure 41: Variation with the normalised crack length and the number of Williams' series terms of a) normalised stress intensity factor, b) relative error function and c) normalised 95% confidence intervals range for the 304L-SS alloy

Figure 41b and c and Figure 42b and c show the relative error function and the normalised 95% confidence intervals range for the SS304Land the AA2024-T3, respectively. As displayed in these Figures, the relative objective function for any case is lower than 0.7% for the stainless steel, and 0.15% for the aluminium alloy. Moreover, the same trend was found in both materials. For shorter crack length, the maximum error is found and then it decreases exponentially until reaching almost constant values of around 0.005%. A similar trend was found for the 95% confidence intervals, which are around 0.5 for the shortest crack length, and then it suddenly descends until values around 0.05. Regarding the influence of the number of terms in Williams' model, a similar trend to the mode I SIF was found since the dispersion decreases as the number of terms increase. These higher dispersions at shorter crack lengths could be attributed to the effect of the residual stresses due to the notch manufacturing process. However, values in terms of SIFs as well as fitting quality parameters present reasonable values and can be considered acceptable. The highest analysed normalised crack length was around 50% and 70% for the stainless steel and the aluminium alloy, respectively. Both values agree with small scale yielding conditions established by ASTM E647 [120] (normalised crack length around 70%). Hence, it can be stated that there

are no limitations in terms of the crack length analysed and the major limitations are due to the effect of the plasticity, which larger values enhance its effect as the uncracked ligament is reduced and then it fully yields.

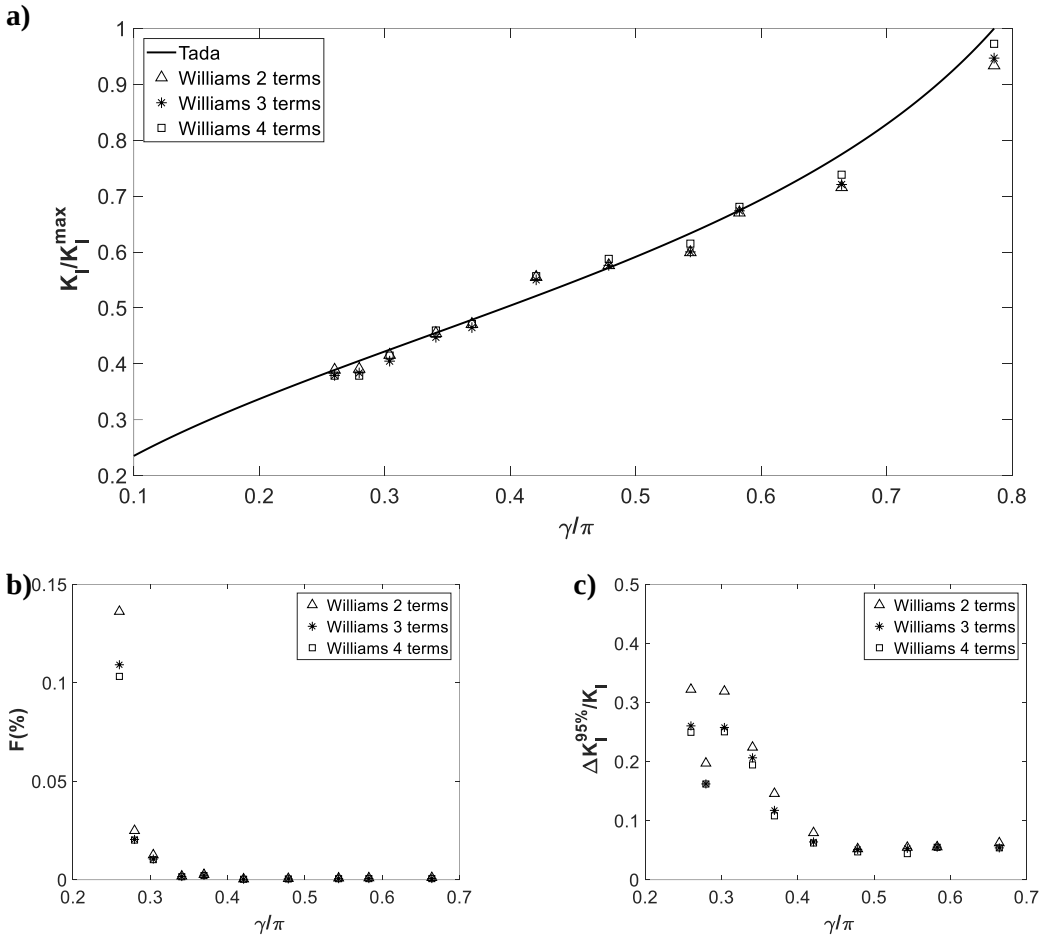

Figure 42: Variation with the normalised crack length and the number of Williams' series terms of a) normalised stress intensity factor, b) relative error function and c) normalised 95% confidence intervals range for the Al 2024-T3 alloy

Beyond the single-parameters comparison, a qualitative and quantitative evaluation of the fitting quality was done by comparing the experimental fields with those theoretically reconstructed using the proposed approach for different crack lengths and Williams' series terms. Figure 43 and Figure 44 clearly illustrate aspect of the proposed approach. Firstly, the number of terms does not have significant influence on the agreement between the experimental and the theoretical displacement maps. Secondly, for short crack lengths, a higher dispersion was found as previously shown and discussed due to the effect of notch residual stresses. Thirdly, a noticeable change was found in the tangential component as the crack grows and it is attributed to the influence of the non-singular stress along this direction (far-field boundary effect) [135,136]. Above exposed results, show how the surrounding crack tip field on a cracked, non-flat and developable surface under plane stress conditions can be perfectly characterised by employing a 2D model taking into account the curvature effect using differential geometry modifications.

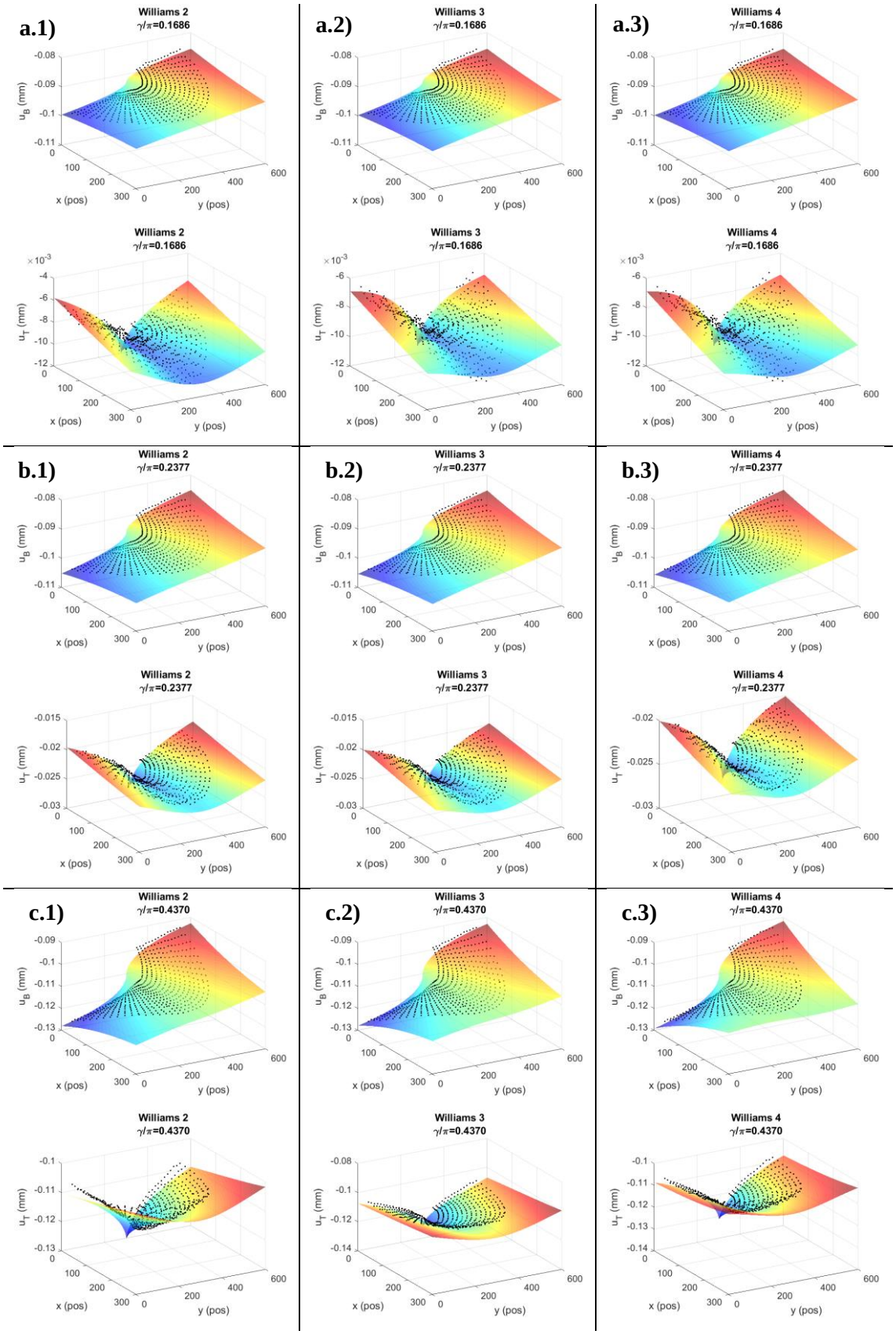

Figure 43: 304L alloy. Comparison between the experimentally measured and the theoretically reconstructed crack tip displacements fields (binormal and tangential) as a function of normalised crack length and the number of Williams' series terms. a, b and c refer to the normalised crack length and 1, 2 and 3 indicate the number of terms employed.

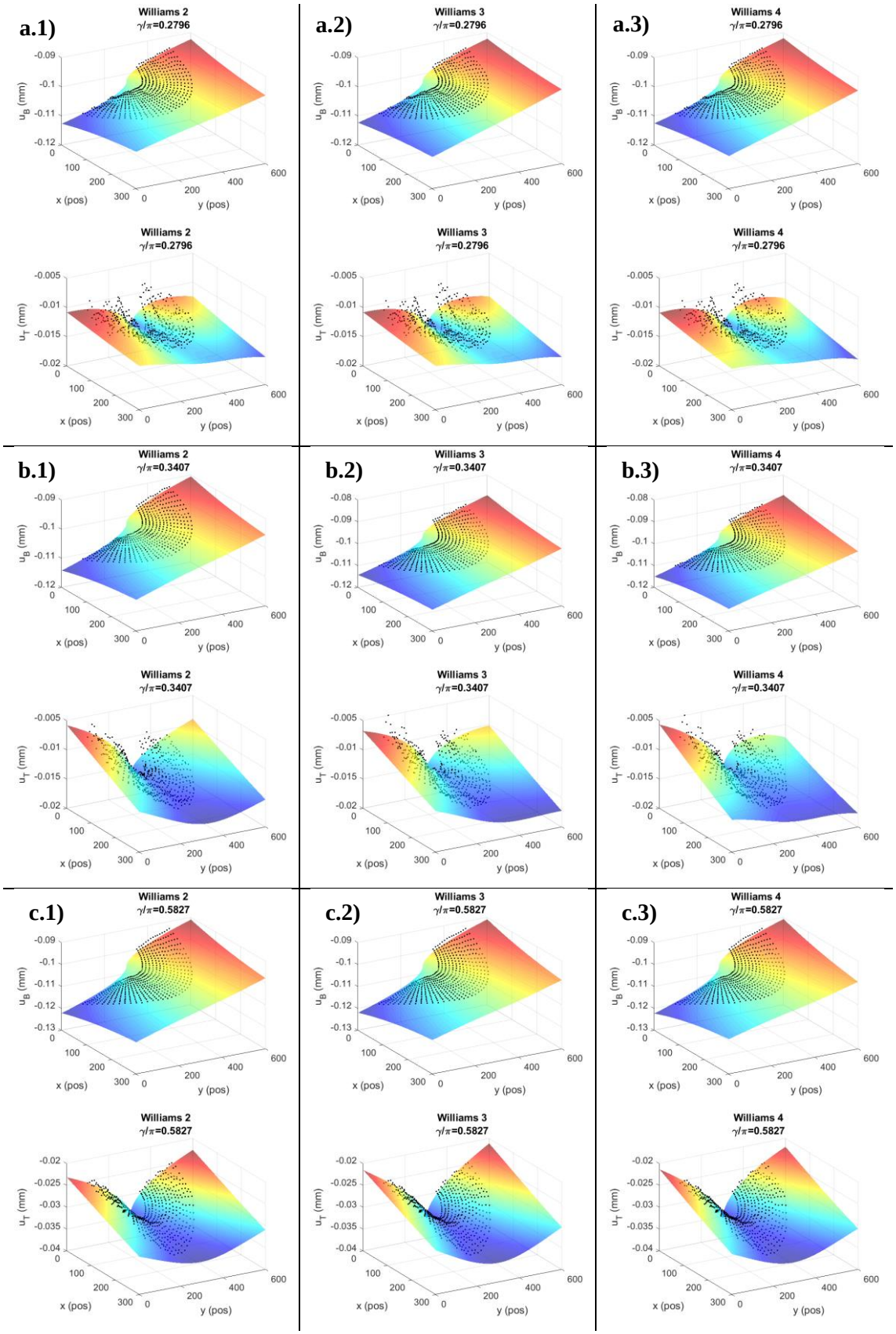

Figure 44: 2024-T3 alloy. Comparison between the experimentally measured and the theoretically reconstructed crack tip displacements fields (binormal and tangential) as a function of normalised crack length and the number of Williams' series terms. a, b and c refer to the normalised crack length and 1, 2 and 3 indicate the number of terms employed.

Table 8 shows some optimised and alternatively determined crack tip locations for different representative crack lengths and Williams' series terms in both alloys. Results in terms of optimised crack tip locations present a high level of agreement with those determined via the alternative displacement-based method. The difference between both optimised and alternatively determined values was quantified through the Euclidean distance between the optimised crack tip coordinate and the alternatively calculated. As shown in this Table, for the case of 4 Williams' terms, the obtained differences were lower than for the other cases as above reported for the opening mode SIFs where lower differences regarding theoretical values were found. Nonetheless, for some cases (normalised crack lengths of 0.27 for SS304L and 0.47 for AA2024-T3), higher differences than for results reported in Table 7 were found in terms of the Euclidean distance for 2 and 3 series terms. These differences when less series terms are used can be attributed to the influence of crack tip plasticity that implies the appearance of high order terms (different to the main $r^{-1/2}$ term governing the elastic singularity). In addition, Williams' series does not explicitly incorporate crack tip shielding effects in contrast to the CJP model (Table 7) and hence, provides less accuracy results in terms of that variable. It is significant to see how optimised SIFs agree well with theoretical values even for less accurate crack tip positions as reported by Vasco-Olmo [105]. In fact, as shown in Figure 45, both stress intensity factors and non-singular stresses hold almost constants during a large number of iterations that also confirms the low sensitive of that model to the crack tip location. Moreover, as the number of terms increase, optimised values reach the stability with a low number of iterations, which support above exposed and explained fact.

Table 8: Comparison between some optimised crack tip positions and those calculated using the alternative displacement-based method

	Williams 2 terms		**Williams 3 terms**		**Williams 4 terms**		**Alternative method**		**Difference in terms of Euclidean distance**		
γ/π	**Δx**	**Δy**	**Δx**	**Δy**	**Δx**	**Δy**	**Δx**	**Δy**	**2 terms**	**3 terms**	**4 terms**
Units in pixels											
SS304L											
0.16	185	382	183	379	182	380	186	379	3.16	3.00	4.12
0.27	376	380	399	381	393	382	386	380	10.00	13.04	7.28
0.33	498	378	499	378	498	379	499	378	1.00	0.00	1.41
AA2024T3											
0.27	87	340	82	340	88	341	87	341	1.00	5.10	1.00
0.36	137	335	135	333	135	334	134	335	3.00	2.24	1.41
0.47	221	323	227	323	237	322	240	324	19.03	13.04	3.61

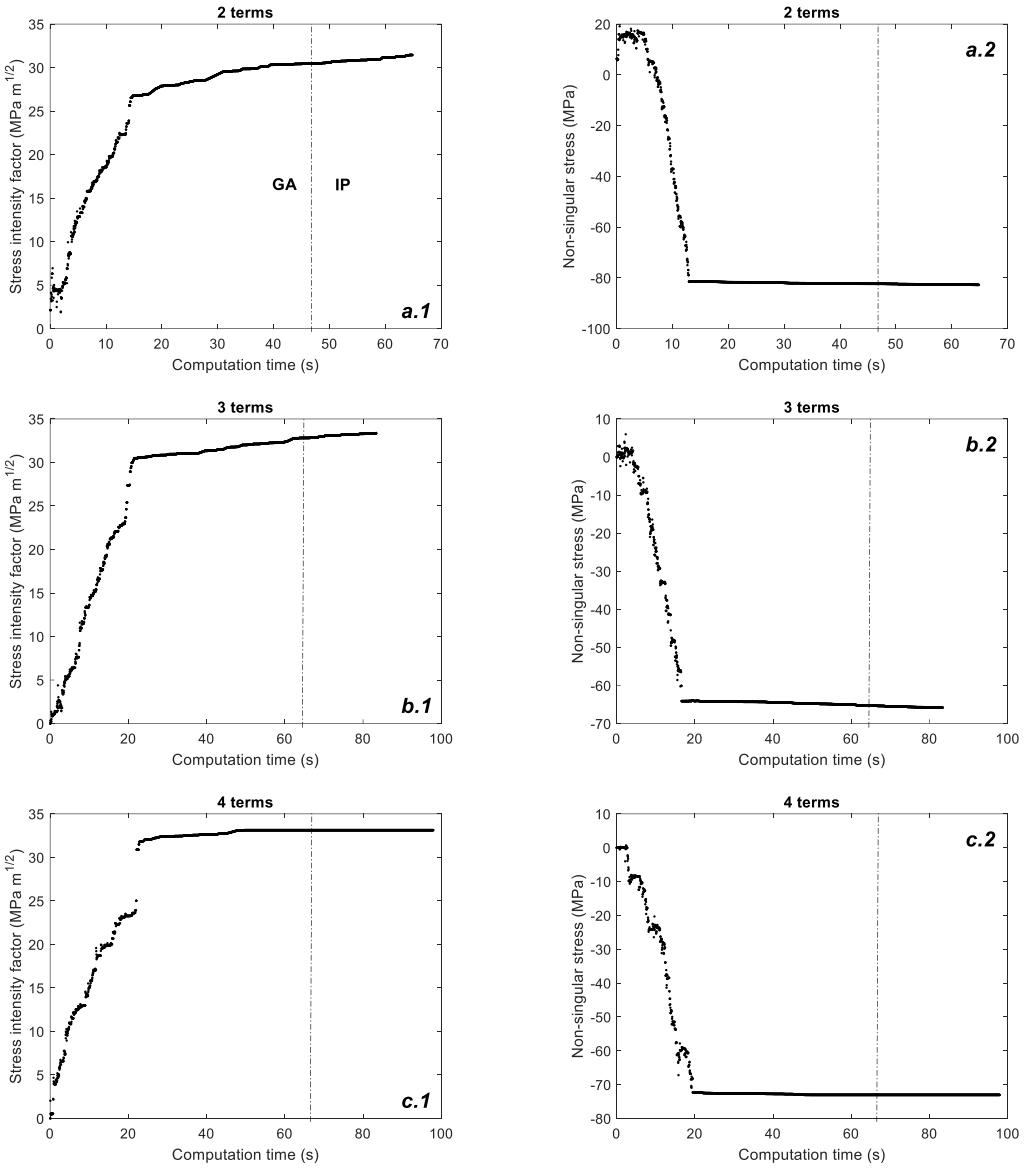

Figure 45: Stress intensity factor (left column) and non-singular stress along the crack growth direction (right column) during the optimisation process for a normalised crack length of 0.33 304L alloy. 1 and 2 refer to stress intensity factor and non-singular stress respectively and a, b and c refer to 2, 3 or 4 series terms, respectively. The dashed line separates GA and IP iterations.

6.2.3. Single-parameter comparison between numerical and experimental data through SIFs

Figure 46 and Figure 47 show the computed SIFs (experimental, numerical and theoretical) for the stainless steel and aluminium alloys, respectively. A good agreement between experimental and numerical SIFs was found. For the stainless steel, average errors of 3.5% and 3% were found for *K* values based on displacements and stress, respectively; whilst for the aluminium alloy, average errors of 3.11% and 3.64% for *K* values based on displacements and stress were obtained, respectively. As shown in Figure 46b, for short crack lengths in the case of the stainless steel alloy, numerical SIFs present slight differences regarding the nominal value (higher than 5%). These differences can be explained through the stress intensity level of the crack as well as the

numerical resolution. At those shorter cracks, the stress intensity is lower and hence, the stresses and displacements distributions were less well defined.

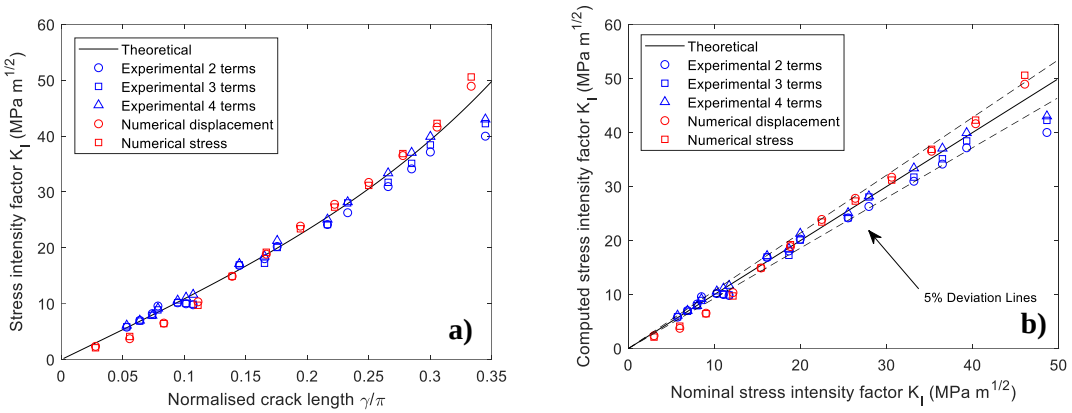

Figure 46: Comparison between experimental, numerical and theoretical stress intensity factors for the 304L alloy. a) Stress intensity factors against the normalised crack length and b) computed stress intensity factors against the theoretical stress intensity factor

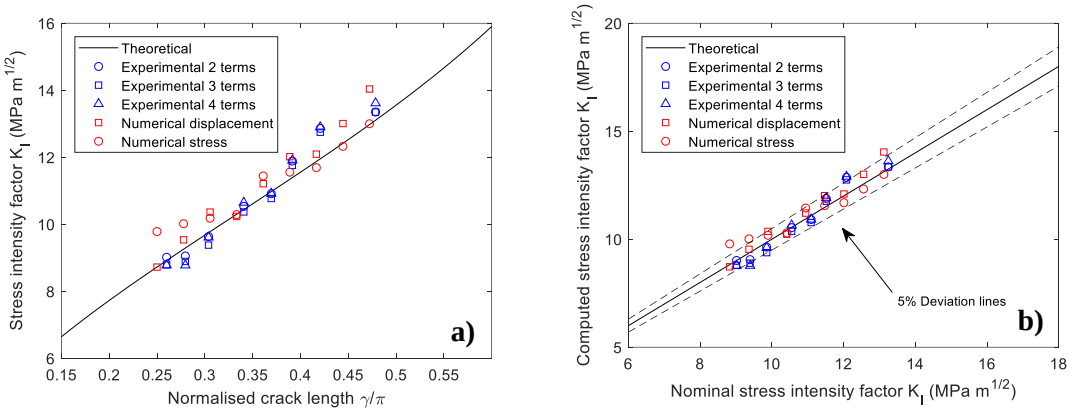

Figure 47: Comparison between experimental, numerical and theoretical stress intensity factors for the Al-2024T3 alloy. a) Stress intensity factors against the normalised crack length and b) computed stress intensity factors against the theoretical stress intensity factor

Fitting quality was assessed via Pearson' correlation coefficient between the theoretical fitted and the numerically obtained data as shown in Figure 48. For displacement data, averages values of 95.4% and 93.7% correlation coefficients were obtained for the aluminium alloy and the stainless steel alloy, respectively; whilst for the axial stress data, averages values of 96.2 and 98.6 were obtained for the aluminium alloy and the stainless steel alloy, respectively. Moreover, as shown in this Figure, both displacement and stress fitted profiles agree well with those numerically obtained and hence, it indicates that numerically obtained values can be considered suitable.

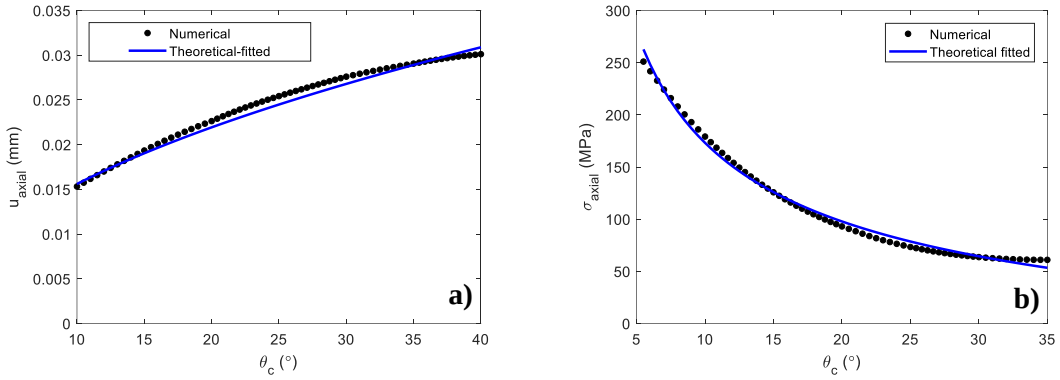

Figure 48: Numerical and theoretical axial displacement and stress profiles a) behind the crack tip and b) ahead of the crack tip, respectively. 304L alloy

6.2.4. Full-field comparison between experimental and numerical data using image comparison

As reported in section 5.4, twenty shape descriptors were employed to describe both numerical and experimental displacement maps since this value provides correlation coefficients higher than 97% for any map and hence, it can be considered suitable for reproducing those maps. To carry out a relevant comparison, for both alloys, three significant crack lengths were chosen. The analysed crack lengths were 0.16, 0.27 and 0.32 for the SS304L and 0.27, 0.36 and 0.47 for the aluminium alloy. Thus, for any normalised crack length, both the binormal and the tangential component were compared (24 decompositions to perform 12 comparisons). Figure 49 and Figure 50 show numerical shape descriptors against experimental shape descriptors for different crack lengths and for the 304L alloy and aluminium alloy, respectively. Thus, the coincidence in a 45º line indicates a perfect agreement between both shape descriptors. As shown in these Figures, a great level of agreement between numerical and experimental maps was found and the minimum value for the correlation coefficient found was 97.4%. Thus, these results confirms the agreement between both experimental and numerical fields beyond the analysis of a single parameter as K_I as done in the previous section.

Moreover, in these Figures, dashed red lines represent the measurement uncertainty bands. As shown, these bands are generally closer to the 45º line and as the crack grows, the bands range decreases since the stress intensity enhances and the inherent measurement noisy disappears.

As shown in these Figures, some shape descriptors are slightly far from the 45 º line, however, these shape descriptors correspond to high order shapes descriptors which are not significant for the map modelling as shown in Figure 51 and Figure 52.

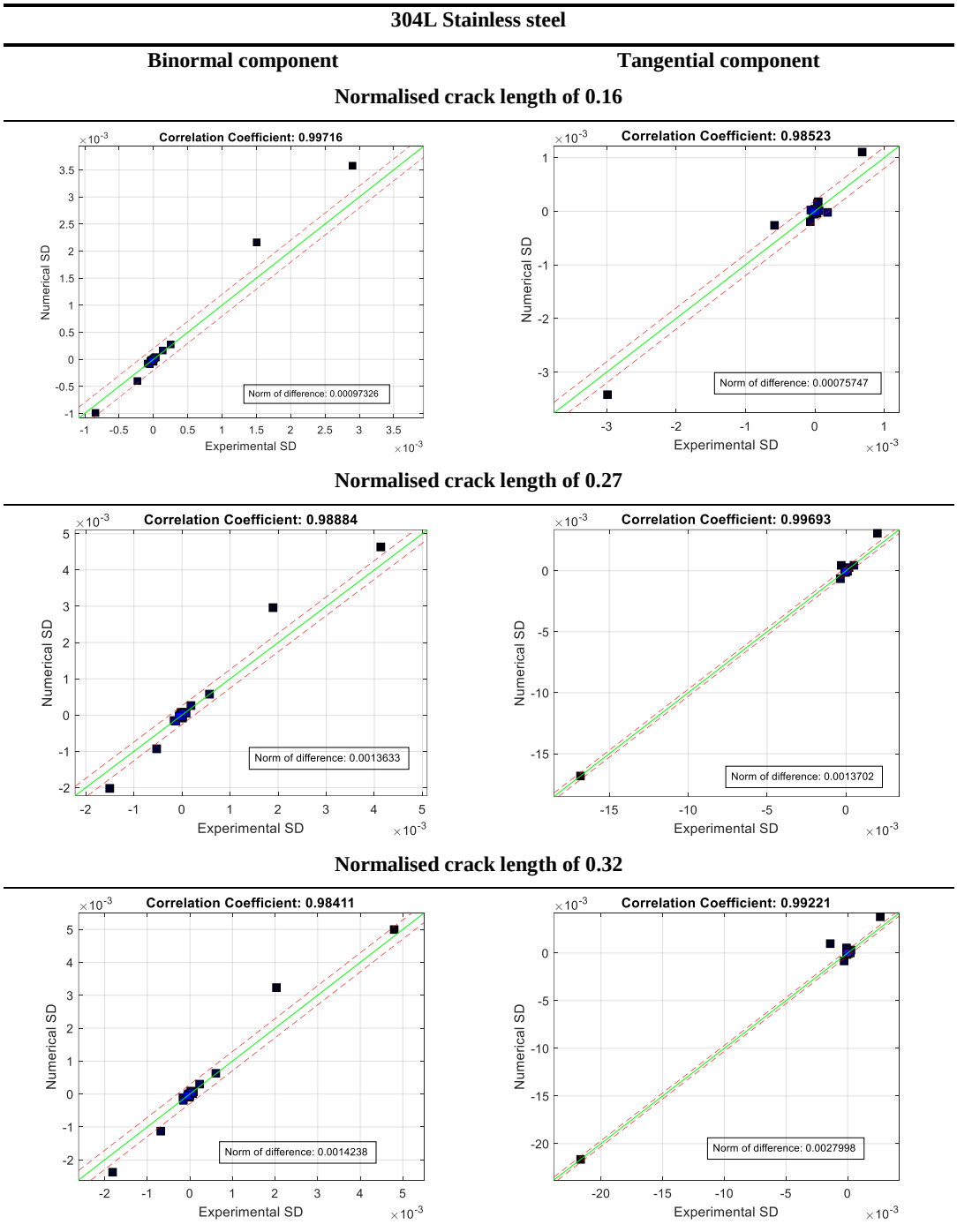

Figure 49: Comparison between numerical and experimental shape descriptors for both tangential and binormal maps and for different crack lengths. 304L alloy

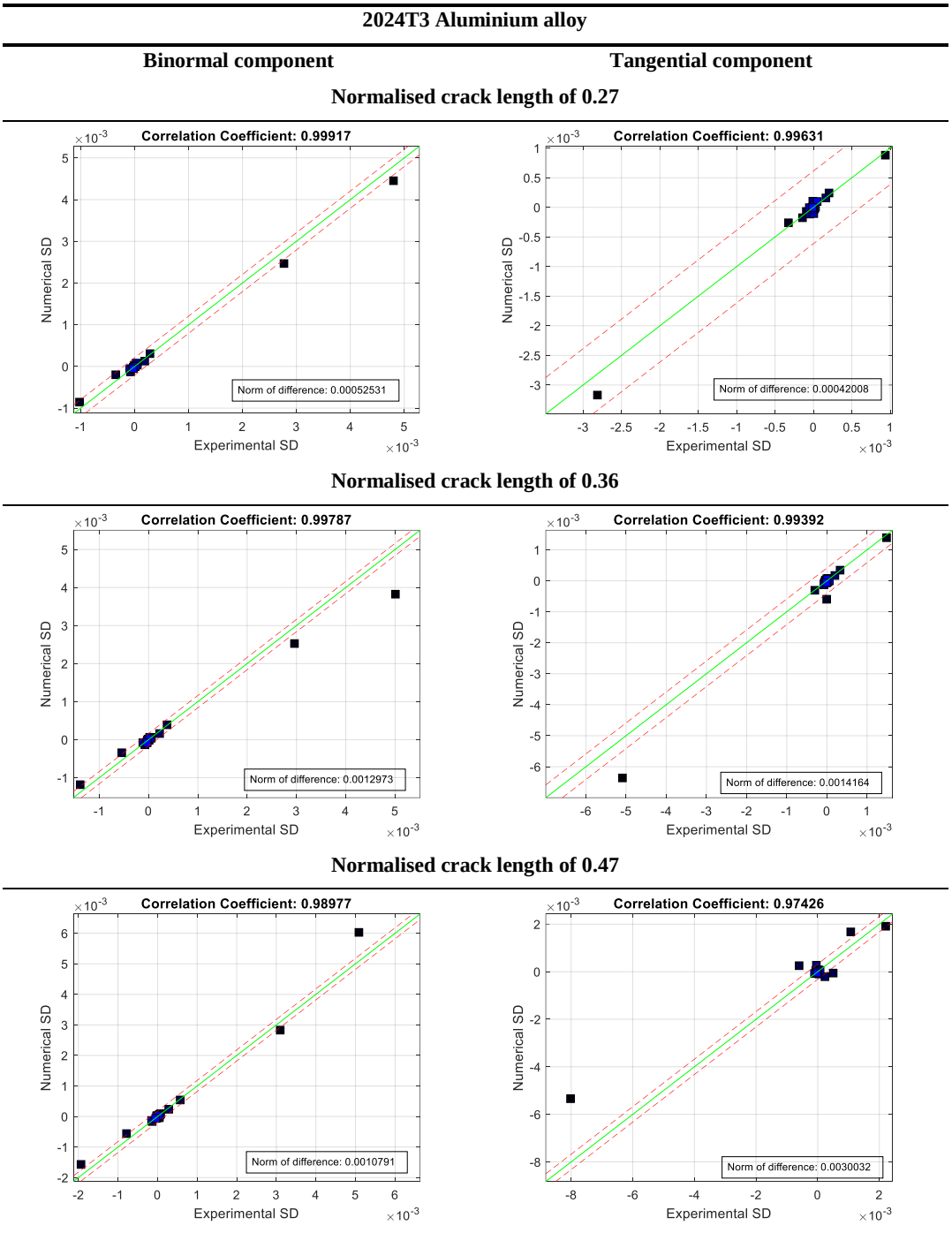

Figure 50: Comparison between numerical and experimental shape descriptors for both tangential and binormal maps and for different crack lengths. 2024T3 alloy

Figure 51 shows a bar plot comparing the numerical and experimental shape descriptors for a map with a normalised crack length of 0.32 for the 304L alloy. As shown in this Figure, governing shape descriptors are commonly the first ten presenting the higher and hence, the most representative values since the others are less than 5% of the first shape descriptor as marked by the red dashed line. In addition, these most representative numerical shape descriptors for both binormal and tangential maps agree well with experimental shape descriptors.

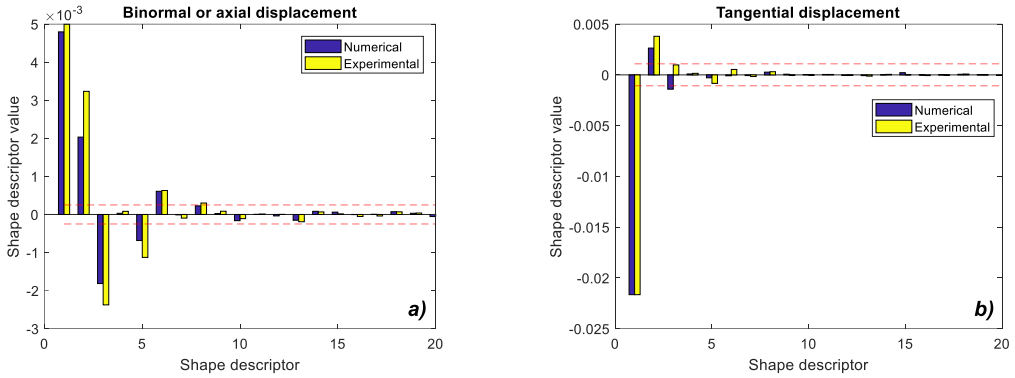

Figure 51: Bar plot comparing numerical and experimental shape descriptors for a normalised crack length of 0.32. 304L alloy. a) binormal or axial displacement and b) tangential displacement.

Figure 52 shows a representative case of the shape descriptors values for the aluminium alloy with a normalised crack length of 0.36. As shown in this Figure, the shape descriptors trend agree with those displayed in Figure 51 for the stainless steel specimen. In addition, numerical and experimental shape descriptors agree.

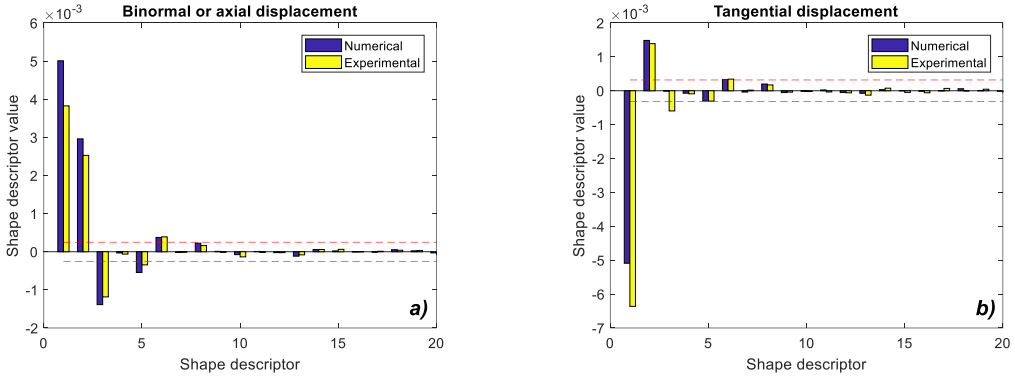

Figure 52: Bar plot comparing numerical and experimental shape descriptors for a normalised crack length of 0.36. 2024T3 aluminium alloy. a) binormal or axial displacement and b) tangential displacement

The great coincident in trend and in value for both numerical and experimental shape descriptors, as shown in Figure 51 and Figure 52, provides a better validation of the results beyond the analysis of a global parameters as correlation coefficients as shown in Figure 49 and Figure 50 since the agreement between each shape descriptor implies that the same physical effect is being quantified.

To conclude the results related to this part, the point-by-point differences between both numerical and experimental maps are quantified through representing a feature vector obtained as the difference between the numerical and experimental feature vectors. Figure 53 shows different maps for both the tangential and the binormal component and for both alloys. It is important to remark that the spatial domain shown in these Figures does not affect to the comparison since as reported in section 5, the Tchebichef decomposition allows decomposing those maps in a non-dimensional domain (which is one of the main advantages of that technique). Thus, for the 304L the experimental domain was chosen and 2024T3 alloy the numerical domain to show the non-dependence of that parameter.

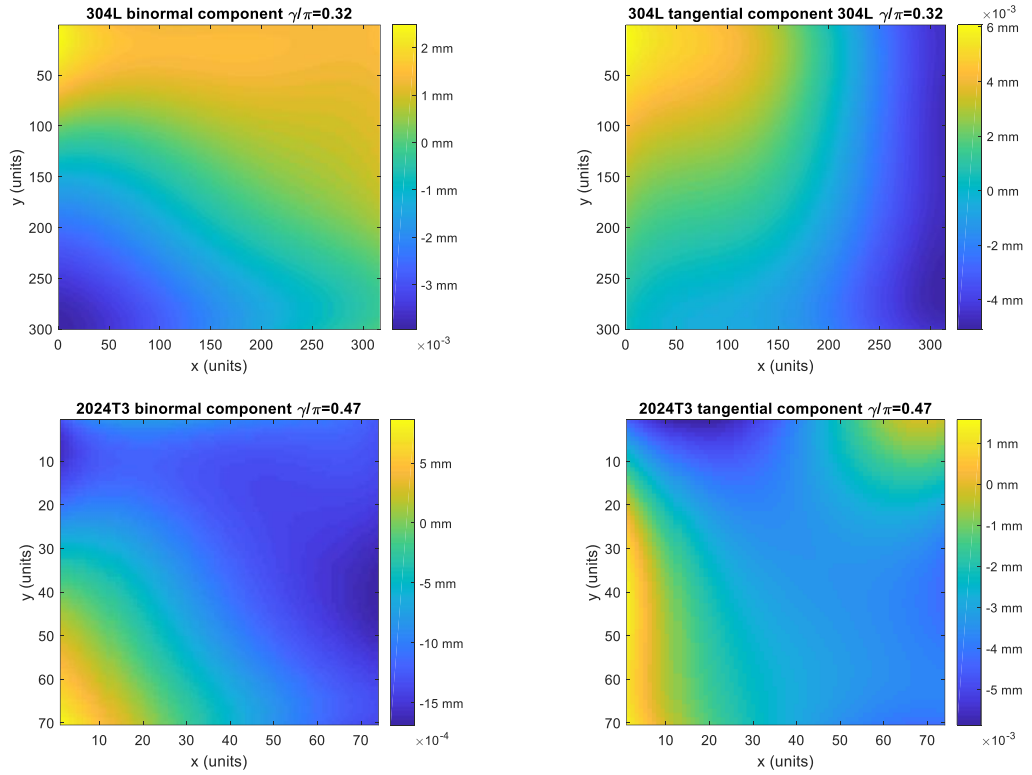

Figure 53: Differences between numerical and experimental binormal maps through differences between features vectors. First row for 304L alloy and second row for 2024T3 alloy. Origin at the crack tip

As displayed in Figure 53, the found highest absolute error is around 6 μm, which is a great value according to the magnitude order of these maps as shown in Figure 28 and Figure 29. This reconfirms the great agreement between the experimental and the numerical fields. In addition, major differences are found in the area surrounding the crack tip. These higher differences at this zone can be attributed to the resolution of both numerically and experimentally fields. First, a proper modelling of the plasticity nearest the crack tip implies the use of highly refined meshes. Secondly, surrounding crack tip experimental data might be affected by edges or tips occurring due to the crack and add noisy to the DIC processing. However, beyond these differences, it can be stated that there is a great agreement between both numerical and experimental fields and hence providing a stronger results validation.

7.Conclusions

In this thesis, a novel methodology for the characterisation of crack tip fields on zero Gaussian curvature non-planar cracked surfaces under plane stress conditions has been experimentally validated and numerically supported. This validation is based on the analysis of single-parameter values as K, as well as a more comprehensive way as the full-field comparison via a Tchebichef polynomials-based image comparison technique. Hollow cylindrical specimens under pure tensile loading have been employed for fatigue crack growth testing and subsequent measurements of crack tip displacement fields via 3D-DIC. Two materials presenting different crack growth shapes (cracks emanating from either only one hole or both holes) have been analysed showing that the methodology is not limited to any specific crack growth morphology. Results in terms of SIFs as well as a comparative study among theoretical, experimental and numerical displacement fields show a high level of agreement reporting low relative errors and a good fitting quality for the parameters values. Moreover, limitations due to the crack length size have not been found since a wide range of normalised crack lengths have been assessed. In fact, the major limitations lies in the existence of plasticity surrounding the crack tip which could limit the use of linear elastic fracture mechanics parameters as K but cannot be attributed to the mathematical basis of the described approach. The methodology has been validated under pure tensile mode loading. However, an extension to mixed mode loading would not require major modifications of the methodology mathematical heart as it will be discussed in the next Chapter.

One of the main advances of the exposed methodology is that allows addressing fatigue and fracture problems in complex geometries which are addressed through pure theoretical expressions (complex differential equations) or numerically via finite element analysis (requiring experimental validations) thus far. The experimental-theoretical nature of this approach allows obtaining results related to the component structural integrity without requiring any additional validation. Thus, this approach represents a breakthrough in the structural integrity analysis of complex geometry mechanical components through experimental optical techniques beyond the identification of critical points in stresses, displacements or strains maps since crack tip

characterising parameters can be estimated and hence, providing a representative parameter on the fatigue or fracture failure.

Perhaps, the plane stress hypothesis might be a limitation, however, thin-wall components, which are very usual in engineering applications, could be perfectly analysed using the developed approach. In addition, for components not satisfying that hypothesis, the methodology could provide a representative value at the surface of the component in order to validate any numerical result as well as to provide an idea about the crack driving force for fatigue advance in the analysed component.

On the other hand, the optimisation-based hybrid methodology for determining the crack tip characterising parameters from experimentally measured fields supposes a great advance in the mathematical performance for the calculation of the crack tip parameters and the crack tip location. As discussed in the above Chapter, that methodology is a necessity rather than an improvement since some advances in the crack tip field models are very sensitive to some required fitting variables (especially the crack tip location) and otherwise, not accurate results could be obtained using another existing method. Results in terms of characterising parameters (stress intensity factors and non-singular stresses) as well as crack tip locations agree very well with those obtained using other methods. An interest application beyond the determination of SIFs and T-stresses is the accurate determination of the crack tip position which is required in other fatigue applications as in singular displacements determination as CTOD, COD or CMOD, for instance. This methodology has been validated using 2D and 3D DIC data on different specimens (compact tension and cylindrical pipes), for different crack tip field models (Westergaard, Williams and CJP) and for different materials (pure titanium, stainless steel and aluminium). Nonetheless, this algorithm can be easily extrapolated to other optical techniques as thermoelastic stress analysis, digital photoelasticity or electronic speckle pattern interferometry, among others. Another special point is the easily automation of this approach since the initial heuristic method avoids including initial solutions, which could be bad-chosen by the user, and depend on the analysed element geometry, the loading conditions and the crack growth shape and size, among others. Thus, the developed methodology can be considered as robust, automatable and easily applicable to any optical technique or cracked element. Although this approach has been developed for opening mode growing fatigue cracks, an extension to mixed mode loading could be simply developed by introducing some changes in the fitness function as well as including some variables into the optimisation problem as it will be discussed in the future work Chapter.

7E. Conclusiones

En la presente tesis, se ha desarrollado y validado de forma experimental y numérica una metodología novedosa para la caracterización de campos en las inmediaciones del vértice de grieta en superficies agrietadas no planas con curvatura Gaussiana nula en condiciones de tensión plana. La validación se ha llevado a cabo utilizando tanto el factor de intensidad de tensiones, pudiéndose considerarse este como un valor único y representativo de la singularidad, así como empleando una comparación de campo completo utilizando la técnica de descomposición de imágenes basada en polinomios de Tchebichef. Para la validación experimental, se han ensayado probetas cilíndricas huecas de pared delgada sometidas a carga axial cíclica para la posterior medición de los campos de desplazamiento circundantes al vértice empleando la técnica de Correlación Digital de Imágenes en su versión tridimensional. Se han analizado dos materiales que han presentado diferentes formas de crecimiento de grieta (creciendo desde un orificio o desde ambos) y mostrando que la metodología expuesta no queda limitada a una morfología concreta de grieta. Los resultados tanto en términos de los factores de intensidad de tensiones como en términos de los campos teóricos, experimental y numéricos muestran un alto nivel de coincidencia reportando errores relativos bajos, así como buenos valores de bondad de ajuste. Asimismo, no puede decirse que se hayan encontrado limitaciones respecto a los valores de longitud de grieta normalizada analizados, ya que se ha analizado un amplio rango. De hecho, las principales limitaciones se deben a la existencia del enclave plástico que rodea al vértice y a la grieta y que limita el uso de parámetros elásticos y lineales como K y no a la formulación matemática empleada. La metodología ha sido validada para una carga uniaxial que induce puramente el modo de apertura (I). No obstante, como será discutido en la siguiente sección, una extensión a modo mixto no requeriría mayores modificaciones de la esencia o base matemática del método.

El mayor avance de la metodología expuesta es que permite abordar problemas de fatiga o fractura en geometrías complejas siendo éstos abordados hasta la fecha de forma teórica (ecuaciones diferenciales complejas) o vía simulación numérica (requiriendo validaciones experimentales).

La naturaleza teórico-experimental del método permite obtener resultados relativos a la integridad estructural de componentes sin requerir de validaciones o resultados adicionales. Por tanto, el método propuesto supone un gran avance en el análisis de integridad estructural de componentes ya que va más allá de la identificación de puntos críticos utilizando mapas de tensión, deformación o desplazamiento, ya que permite estimar parámetros cuantificadores de la singularidad en el vértice y por tanto obtener un valor representativo de asociado al fallo por fatiga o fractura.

Quizá, la hipótesis de tensión plana podría ser una limitación en cuanto a la aplicabilidad. No obstante, existe un amplio rango de componentes industriales bajo estas condiciones tensionales, como los elementos de pared delgada, donde la metodología desarrollada puede aplicarse perfectamente. Además, en componentes donde no se satisfaga completamente esta hipótesis, la metodología podría emplearse para obtener un valor representativo en la superficie del componente y así poder validar resultados numéricos o bien proporcionar una estimación de la fuerza motriz de crecimiento de grieta en dicho componente.

Por otro lado, la metodología híbrida basada en optimización para determinar los parámetros de caracterización del vértice de grieta a partir de campos medidos experimentalmente supone un gran avance en la determinación de éstos, así como en la localización del vértice. Como se ha comentado en el capítulo anterior, esta metodología es una necesidad más que una mejora, ya que algunos más modelos avanzados de caracterización de campos son muy sensibles a algunas variables de ajuste (especialmente la localización del vértice) y, de lo contrario, podrían obtenerse resultados poco precisos utilizando algún otro método existente. Los resultados en cuanto a los parámetros de caracterización (factores de intensidad de tensiones y tensiones no singulares) así como la localización de vértice coinciden en gran medida con los obtenidos mediante otros métodos. Una aplicación interesante más allá de la determinación de los SIFs y las tensiones no singulares es la determinación precisa de la posición del vértice de grieta. Esto se debe a que la posición del vértice es una variable considerablemente importante a la hora de determinar desplazamientos singulares como CTOD, COD o CMOD, los cuales pueden ser utilizados como parámetros caracterizados del crecimiento de grieta por fatiga. Esta metodología ha sido validada utilizando datos de Correlación Digital de Imágenes en 2D y 3D, en diferentes tipos de probetas (probetas CT y del tipo cilíndrico), para diferentes modelos de campo de punta de grieta (Westergaard, Williams y CJP) y para diferentes materiales (titanio puro, acero inoxidable y aluminio). No obstante, este algoritmo es fácilmente extrapolable a otras técnicas ópticas como el análisis termoelastico de tensiones, fotoelasticidad o la interferometría speckle, entre otras. Otro punto especial es la fácil automatización de la metodología, ya que el método heurístico inicial evita incluir soluciones iniciales, que tienen una alta probabilidad de ser mal elegidas, y que dependen de la geometría del elemento analizado, de las condiciones de carga y de la forma y tamaño del crecimiento de la grieta, entre otros. Así, la metodología desarrollada puede

considerarse robusta, automatizable y fácilmente aplicable a cualquier técnica óptica o elemento agrietado. Aunque esta metodología se ha desarrollado para grietas por fatiga en modo de apertura (I), una extensión al análisis de estados multiaxiales y por tanto modo mixto podría desarrollarse de forma simple introduciendo algunos cambios en la función error e incluyendo algunas variables en el problema de optimización, como se discutirá en el capítulo de trabajos futuros.

8.Future works

In this work, uniaxial loading states have been used for simplicity to validate the proposed methodology. A possible extension to mixed-mode crack is potentially considered and it would not require major modifications in the modified crack tip field equations beyond introducing some geometrical transformations on the measured crack tip field. Moreover, a parameter defining the crack growth direction that changes as the crack grows under mixed mode loading should be included in the mathematical fitting problem. Thus, the displacement data orientation should be modified according to the new crack growth direction at each crack increment. Perhaps the major limitation could lie in the fracture mode type since depending on the geometry and the applied load, in-plane shear mode (II), out-of-plane shear mode (III) or a combination (II+III) can be appear together with the opening tensile mode (I). For example, for a cylindrical thin wall pipe as tested in this work, if tensile and torsion loadings are applied, a combined mode (I+II) should be appear since remote axial and shear stresses are contained in the unwrapped plane (axial normal stress and axial-tangential shear stress). A priori, this loading case could be assessed by employing the proposed method without any modification of the equations. However, if the thickness increases, a radial component appears which corresponds to an additional fracture mode III. Thus, thickness influence should be analysed. Moreover, in this case in which a third mode appears, K_{II} appearing in crack tip field models could be a combination between the reals K_{II} and K_{III} governing the crack tip singularity since the axial-tangential remote shear stress generates both modes. Thus, the out-of-plane (mode III) equations should be included into the fitting problem to infer this K_{III} derived from plane models and to establish a comparison between experimentally inferred K_{II} and K_{III} with the real values, which could be obtained using any correlation or finite element analysis.

The differential geometry approach developed on this thesis to extend crack tip field models to the analysis of non-planar surfaces has been validated on a constant curvature geometry element as a hollow cylinder. The next step would be to test the proposed methodology on a thin wall element with single and variable curvature. A potential geometry of this type could be an elliptical

single curvature panel containing either edge or centred cracks. Furthermore, different curvature panels could be assessed to check and test the methodology to this kind of elements.

The double curvature elements are widely employed in engineering structures, as in aircraft structures and the application of the presented method in this work to these structures would provide interest results in terms of structural integrity in mechanical components in order to achieve safety and optimisation requirements. However, in the view of the author, these kind of structures would require a deeply analysis since the most of these structures do not present zero Gaussian curvature and they would not be developable. Thus, an approximate approach would be employed and the influence of Gaussian curvature should be extensively analysed (results variations as the Gaussian curvature increases in absolute value). A possible approach to address this issue would consist of employing the parametrised plane instead of the real physical domain to generate a geometrical situation of the displacement maps. However, this approach obviates the real geometrical situation and hence, it could present problems to define the crack tip singularity.

A potential application not requiring any methodology formulation would be a fatigue crack growth analysis on any curved element within the scope of the current methodology. Thus, a more realistic fatigue crack growth characterisation could be carried out since it is common to employ standards specimens for that purpose and hence, some differences might be found on parameters modelling the respective fatigue crack law. Moreover, advanced models taking into account explicitly the shielding effect during fatigue crack growth (CJP model) could be used and therefore providing a more effective rationalisation on fatigue crack growth rates.

Regarding fatigue crack growth analysis, the extension of the developed methodology to the analysis of thermoelastic data could provide a powerful tool to assess and determine effective fatigue crack driving forces for fatigue advance due to the nature of thermoelastic stress analysis. Beforehand, the analysis of crack tip thermoelastic data via the proposed approach would not require any geometrical transformation for the measured thermoelastic field since the first stress invariant would be measured and hence only requiring the generation of the physical domain (unwrapped plane). However, to digitalise a curved-shape surface, an integration between TSA and DIC would be required and hence needing a more complex experimental set-up as well a very accurate synchronisation between both cameras system. In addition, a correct temperature measurement on the surface during the loading cycle, high-speed cameras would necessary to acquire DIC images for subsequent matching with thermal images (data recording at high frequencies for avoiding addiabaticity problems). Nonetheless, a simplified measurement could be performed without needing high-speed cameras and hence, only using DIC cameras to generate

the physical domain but an error due to the surface motion could affect to the measured temperature data.

8E. Trabajos futuros

En este trabajo, se han ensayado estados de carga uniaxiales (tracción) por simplicidad en la validación de la metodología propuesta. Una posible extensión al análisis de grietas en modo mixto es potencialmente considerada. Esta extensión no requeriría grandes modificaciones en las ecuaciones extendidas de los modelos de caracterización, más allá de introducir algunas transformaciones geométricas en los campos medidos experimentalmente. Además, debería ser incluido en el problema de ajuste matemático un parámetro que definiese la dirección de crecimiento de la grieta ya que esta cambia a medida que la grieta crece bajo una carga en modo mixto. Asimismo, la orientación de los datos de desplazamiento debería modificarse de acuerdo con la nueva dirección de crecimiento de la grieta en cada incremento de la misma. Quizás la mayor limitación podría residir en el modo de fractura, ya que, dependiendo de la geometría y de la carga aplicada, puede aparecer el modo de cizalladura (II), el modo de desgarro (III) o una combinación de ambos (II+III), junto con el modo de apertura (I). Por ejemplo, para un tubo cilíndrico de pared delgada como el ensayado en este trabajo, si se aplican cargas de tracción y torsión, debería aparecer un modo combinado (I+II) ya que las tensiones axiales y tangenciales remotas quedan contenidas en el plano desarrollado (tensión normal axial y tensión tangencial axial-tangencial). A priori, este caso de carga podría evaluarse empleando el método propuesto sin ninguna modificación de las ecuaciones. Sin embargo, si el espesor aumenta, aparece una componente radial que corresponde a un modo adicional de fractura del tipo desgarro (III). Por lo tanto, debería analizarse la influencia del espesor. Además, en este caso en el que aparece un tercer modo, el parámetro K_{II} que aparece en los modelos podría ser una combinación entre los valores reales de K_{II} y K_{III}, ya que la tensión cortante remota axial-tangencial induce ambos modos. Por lo tanto, las ecuaciones de desplazamiento fuera del plano de grieta (modo III) deberían incluirse en el problema de ajuste para estimar el parámetro K_{III} obtenido de los modelos planos y establecer una comparación entre los K_{II} y K_{III} inferidos experimentalmente con los valores reales, que podrían obtenerse utilizando cualquier correlación o análisis de elementos finitos.

El enfoque de geometría diferencial desarrollado en esta tesis para extender el uso de los modelos planos al análisis de superficies no planas ha sido validado en un elemento de curvatura constante como un cilindro hueco. El siguiente paso sería probar la metodología propuesta en un elemento de pared delgada con curvatura única y variable. Una geometría potencial de este tipo podría ser un panel elíptico de curvatura única que contenga grietas de borde o centradas. Además, se podrían evaluar diferentes curvaturas para poner a prueba la metodología en este tipo de elementos.

Los elementos de doble curvatura son empleados frecuentemente en las estructuras de ingeniería, como en las estructuras aeronáuticas, y la aplicación de la metodología presentada a este tipo de estructuras proporcionaría resultados interesantes en términos de integridad estructural para optimizarlos y alcanzar unos requisitos confiables de seguridad. Sin embargo, en opinión del autor, este tipo de estructuras requeriría un análisis profundo ya que la mayoría de estas estructuras no presentan curvatura gaussiana cero y no serían desarrollables. De esta forma, el método se aplicaría de forma aproximada y se debería analizar ampliamente la influencia de la curvatura gaussiana (variaciones de los resultados a medida que la curvatura gaussiana aumenta en valor absoluto). Un posible enfoque para abordar esta cuestión consistiría en emplear el plano parametrizado en lugar del dominio físico real para generar una situación geométrica de los mapas de desplazamiento. Sin embargo, este enfoque obvia la situación geométrica real y, por tanto, podría presentar problemas a la hora de definir la singularidad en el vértice.

Una aplicación potencial que no requiere reformulaciones de la metodología sería un análisis de crecimiento de grieta a fatiga en cualquier elemento curvo dentro del alcance de la metodología propuesta. De este modo, se podría llevar a cabo una caracterización más realista del crecimiento de la grieta por fatiga, ya que es habitual emplear probetas estándar para este fin y, por tanto, se podrían encontrar algunas diferencias en los parámetros que modelizan las leyes de crecimiento de grieta por fatiga. Además, podrían utilizarse modelos avanzados que tuvieran en cuenta explícitamente el efecto de shielding inducido por plasticidad durante el crecimiento de la grieta por fatiga (modelo CJP) y, por tanto, proporcionar valores más realistas en términos de tasa de crecimiento de grieta.

En cuanto al análisis del crecimiento de la grieta por fatiga, la extensión de la metodología desarrollada al análisis de datos termoelásticos podría proporcionar una poderosa herramienta para evaluar y determinar las fuerzas efectivas conductoras durante el crecimiento de grieta por fatiga debido a la naturaleza de esta técnica experimental. De antemano, el análisis de los datos termoelásticos en el vértice empleando el método propuesto no requeriría ninguna transformación geométrica para el campo de temperatura medido experimentalmente, ya que se mediría el primer invariante de tensión y, por lo tanto, sólo se requeriría la generación del dominio físico (plano

desarrollado). Sin embargo, para digitalizar una superficie de forma curvada, se necesitaría una integración entre TSA y DIC y, por tanto, un montaje experimental más complejo, así como una sincronización muy precisa entre ambos sistemas de cámaras. Además, para una correcta medición de la temperatura en la superficie durante el ciclo de carga, serían necesarias cámaras de alta velocidad para adquirir imágenes DIC para su posterior cotejo con las imágenes térmicas (adquisición de datos a altas frecuencias para evitar problemas de adiabaticidad). No obstante, se podría realizar una medición simplificada sin emplear cámaras de alta velocidad y, por tanto, utilizar exclusivamente las cámaras de DIC para generar el dominio físico. Sin embargo, podrían existir errores debido al movimiento de la superficie durante la aplicación de cargas y por tanto podría afectar a los datos de temperatura medidos.

References

[1] Nishida SI. Failure Analysis in Engineering Applications. Elsevier; 1992. https://doi.org/10.1016/c2013-0-06527-9.

[2] Sanford RJ. A critical re-examination of the Westergaard method for solving opening-mode crack problems. Mech Res Commun 1979;6:289–94. https://doi.org/10.1016/0093-6413(79)90033-8.

[3] Nurse AD, Patterson EA. Experimental determination of stress intensity factors for cracks in turbine disks. Fatigue Fract Eng Mater Struct 1993;16:315–25. https://doi.org/10.1111/j.1460-2695.1993.tb00089.x.

[4] Tomlinson RA, Nurse AD, Patterson EA. On determining stress intensity factors for mixed mode cracks from thermoelastic data. Fatigue Fract Eng Mater Struct 1997;20:217–26. https://doi.org/10.1111/j.1460-2695.1997.tb00279.x.

[5] Shterenlikht A, Díaz Garrido FA, Lopez-Crespo P, Withers PJ, Patterson EA. Mixed Mode (KI+KII) Stress Intensity Factor Measurement by Electronic Speckle Pattern Interferometry and Image Correlation. Appl Mech Mater 2004;1–2:107–12. https://doi.org/10.4028/WWW.SCIENTIFIC.NET/AMM.1-2.107.

[6] Christopher CJ, James MN, Patterson EA, Tee KF. Towards a new model of crack tip stress fields. Int J Fract 2007;148:361–71. https://doi.org/10.1007/s10704-008-9209-3.

[7] Christopher CJ, James MN, Patterson EA, Tee KF. A quantitative evaluation of fatigue crack shielding forces using photoelasticity. Eng Fract Mech 2008;75:4190–9. https://doi.org/10.1016/j.engfracmech.2008.03.013.

[8] Vasco-Olmo JM, Diaz FA, Garcia-Collado A, Dorado-Vicente R. Experimental evaluation of crack shielding during fatigue crack growth using digital image correlation. Fatigue Fract Eng Mater Struct 2015;38:223–37. https://doi.org/10.1111/ffe.12136.

[9] Gonzáles GLG, González JAO, de Castro JTP, Freire JL de F. Measuring elastoplastic strain loops in the near crack-tip region using a Stereo Microscope DIC system. Int J Fatigue 2020;133. https://doi.org/10.1016/J.IJFATIGUE.2019.105427.

[10] De Matos PFP, Nowell D. Analytical and numerical modelling of plasticity-induced crack closure in cold-expanded holes. Fatigue Fract Eng Mater Struct 2008;31:488–503. https://doi.org/10.1111/J.1460-2695.2008.01245.X.

[11] Nowell D, Paynter RJH, De Matos PFP. Optical methods for measurement of fatigue crack closure: Moiré interferometry and digital image correlation. Fatigue Fract Eng Mater Struct 2010;33:778–90. https://doi.org/10.1111/j.1460-2695.2010.01447.x.

[12] Gonzales GLG, Gonzalez JAO, Castro JTP, Freire JLF. A J-integral approach using digital image correlation for evaluating stress intensity factors in fatigue cracks with closure effects. Theor Appl Fract Mech 2017;90:14–21. https://doi.org/10.1016/j.tafmec.2017.02.008.

[13] Vasco-Olmo JM, Yang B, James MN, Diaz FA. Investigation of effective stress intensity factors during overload fatigue cycles using photoelastic and DIC techniques. Theor Appl Fract Mech 2018;97:73–86. https://doi.org/10.1016/j.tafmec.2018.07.011.

[14] Vasco-Olmo JM, Diaz FA, James MN, Yang B. Crack tip plastic zone evolution during an overload cycle and the contribution of plasticity-induced shielding to crack growth rate changes. Fatigue Fract Eng Mater Struct 2018;41:2172–86. https://doi.org/10.1111/ffe.12840.

[15] Vasco-Olmo JM, James MN, Christopher CJ, Patterson EA, Diaz FA. Assessment of crack tip plastic zone size and shape and its influence on crack tip shielding. Fatigue Fract Eng Mater Struct 2016;39:969–81. https://doi.org/10.1111/ffe.12436.

[16] Ould Chikh B, Imad A, Benguediab M. Influence of the cyclic plastic zone size on the propagation of the fatigue crack in case of 12NC6 steel. Comput Mater Sci 2008;43:1010–7. https://doi.org/10.1016/J.COMMATSCI.2008.02.019.

[17] Chen J, Huang Y, Dong L, Li Y. A study on evaluation method of crack tip reverse plastic zone size for the center cracked steel plate model under tension–compression cyclic loading. Eng Fract Mech 2015;133:138–51. https://doi.org/10.1016/J.ENGFRACMECH.2014.11.008.

[18] Tong J, Alshammrei S, Lin B, Wigger T, Marrow T. Fatigue crack closure: A myth or a misconception? Fatigue Fract Eng Mater Struct 2019;42:2747–63. https://doi.org/10.1111/FFE.13112.

[19] Borges MF, Antunes F V., Neto DM, Vasco-Olmo JM, Díaz FA, James MN. Validity of small-scale yielding regime in notched-cracked geometries. Int J Fatigue 2022;154:106563. https://doi.org/10.1016/J.IJFATIGUE.2021.106563.

[20] Kujawski D. Discussion and Comments on KOP and ΔKeff. Mater 2020, Vol 13, Page 4959 2020;13:4959. https://doi.org/10.3390/MA13214959.

[21] Borges MF, Neto DM, Antunes F V. Revisiting Classical Issues of Fatigue Crack Growth Using a Non-Linear Approach. Mater 2020, Vol 13, Page 5544 2020;13:5544. https://doi.org/10.3390/MA13235544.

[22] González JAO, de Castro JTP, Meggiolaro MA, Gonzáles GLG, Freire JL de F. Challenging the "ΔKeff is the driving force for fatigue crack growth" hypothesis. Int J Fatigue 2020;136. https://doi.org/10.1016/J.IJFATIGUE.2020.105577.

[23] Pippan R, Hohenwarter A. Fatigue crack closure: a review of the physical phenomena. Fatigue Fract Eng Mater Struct 2017;40:471–95. https://doi.org/10.1111/FFE.12578.

[24] Vormwald M, Hos Y, Freire JLF, Gonzales GLG, Diaz JG. Crack tip displacement fields measured by digital image correlation for evaluating variable mode-mixity during fatigue crack growth. Int J Fatigue 2018;115:53–66. https://doi.org/10.1016/j.ijfatigue.2018.04.030.

[25] Pommier S, Hamam R. Incremental model for fatigue crack growth based on a displacement partitioning hypothesis of mode I elastic-plastic displacement fields. Fatigue Fract Eng Mater Struct 2007;30:582–98. https://doi.org/10.1111/j.1460-2695.2007.01128.x.

[26] Goldberg DE. Genetic algorithms in search, optimization, and machine learning. 1st ed. Boston, MA: Addison-Wesley Longman Publishing Co., Inc.,; 1989. https://doi.org/10.5555/534133.

[27] Waltz RA, Morales JL, Nocedal J, Orban D. An interior algorithm for nonlinear optimization that combines line search and trust region steps. Math Program 2006;107:391–408. https://doi.org/10.1007/s10107-004-0560-5.

[28] Westergaard HM. Bearing pressures and cracks. J Appl Mech 1939;61:49–53.

[29] Irwin GR. Analysis of stresses and strains near the end of a crack traversing plate. J Appl Mech 1957;24:361–70.

[30] Williams ML. On the stress distribution at the base of a stationary crack. J Appl Mech 1957;24:109–14.

[31] James MN, Christopher CJ, Lu YW, Patterson EA. Local crack plasticity and its influences on the global elastic stress field. Int J Fatigue 2013;46:4–15. https://doi.org/10.1016/j.ijfatigue.2012.04.015.

[32] Nurse AD, Patterson EA. Determination of predominantly mode-II stress intensity factors from isochromatic data. Fatigue Fract Eng Mater Struct 1993;16:1339–54. https://doi.org/10.1111/j.1460-2695.1993.tb00743.x.

[33] Muskhelishvili NI. Some Basic Problems of the Mathematical Theory of Elasticity. Springer Netherlands; 1977. https://doi.org/10.1007/978-94-017-3034-1.

[34] Yang B, Vasco-Olmo JM, Díaz FA, James MN. A more effective rationalisation of fatigue crack growth rate data for various specimen geometries and stress ratios using the CJP model. Int J Fatigue 2018;114:189–97. https://doi.org/10.1016/j.ijfatigue.2018.05.027.

[35] Kobayashi S. Differential geometry of curves and surfaces. Singapore: Springer Singapore; 2010. https://doi.org/10.1007/978-981-15-1739-6.

[36] Wright SJ. Primal-Dual Interior-Point Methods. Society for Industrial and Applied Mathematics; 1997. https://doi.org/10.1137/1.9781611971453.

[37] Coleman TF, Li YY. An interior trust region approach for nonlinear minimization subject to bounds. Siam J Optim 1996;6:418–45. https://doi.org/10.1137/0806023.

[38] Byrd RH, Gilbert JC, Nocedal J. A trust region method based on interior point techniques for nonlinear programming. Math Program Ser B 2000;89:149–85. https://doi.org/10.1007/PL00011391.

[39] Byrd RH, Hribar ME, Nocedal J. An interior point algorithm for large-scale nonlinear programming. SIAM J Optim 1999;9:877–900. https://doi.org/10.1137/S1052623497325107.

[40] Nocedal J, Wright SJ. Numerical Optimization. 2006. https://doi.org/10.1007/978-0-387-40065-5.

[41] Dantzig GB. Recent Advances in Linear Programming. Manage Sci 1956;2:131–44. https://doi.org/10.1287/mnsc.2.2.131.

[42] Kuhn HW, Tucker AW. Nonlinear programming. Proc. 2nd Berkeley Symp., 1951, p. 481–92.

[43] Sutton MA, Orteu JJ, Schreier HW. Image Correlation for Shape, Motion and Deformation Measurements. New York: Springer US; 2009. https://doi.org/10.1007/978-0-387-78747-

3.

[44] Peters WH, Ranson WF. Digital Imaging Techniques In Experimental Stress Analysis. Https://DoiOrg/101117/127972925 1982;21:427–31. https://doi.org/10.1117/12.7972925.

[45] Sutton M, Wolters W, Peters W, Ranson W, McNeill S. Determination of displacements using an improved digital correlation method. Image Vis Comput 1983;1:133–9. https://doi.org/10.1016/0262-8856(83)90064-1.

[46] Sutton M, Mingqi C, Peters W, Chao Y, McNeill S. Application of an optimized digital correlation method to planar deformation analysis. Image Vis Comput 1986;4:143–50. https://doi.org/10.1016/0262-8856(86)90057-0.

[47] Chu T, Peters WH, Ranson WF, Sutton MA. Application Of Digital Correlation Methods To Rigid Body Mechanics. Https://DoiOrg/101117/127973231 1983;22:738–42. https://doi.org/10.1117/12.7973231.

[48] Chu TC, Ranson WF, Sutton MA. Applications of digital-image-correlation techniques to experimental mechanics. Exp Mech 1985 253 1985;25:232–44. https://doi.org/10.1007/BF02325092.

[49] www.correlatedsolutions.com n.d.

[50] Pan B, Qian K, Xie H, Asundi A. Two-dimensional digital image correlation for in-plane displacement and strain measurement: A review. Meas Sci Technol 2009;20:062001. https://doi.org/10.1088/0957-0233/20/6/062001.

[51] Sutton MA, Yan JH, Tiwari V, Schreier HW, Orteu JJ. The effect of out-of-plane motion on 2D and 3D digital image correlation measurements. Opt Lasers Eng 2008;46:746–57. https://doi.org/10.1016/J.OPTLASENG.2008.05.005.

[52] Molina-Viedma AJ. Full-field experimental modal analysis using high speed digital image correlation. Universidad de Jaén, 2018.

[53] Suresh S. Fatigue of Materials. Fatigue Mater 1998. https://doi.org/10.1017/CBO9780511806575.

[54] Wells AA. Unstable crack propagation in metals-cleavage and fast fracture. Crack Propag. Symp., Cranfield: Cranfield: College of Aeronautics; 1961.

[55] Williams ML, Ellinger GA. Investigation of Fractured Steel Plates Removed from Welded Ships. 1949.

[56] Paris PC, Gomez MP, Anderson WP. A rational analytic theory of fatigue. Trend Eng

1961;13:9–14.

[57] P. Paris, M. Gomez WA, Paris PC, Gomez MP, Anderson WEP. A Rational Analytic Theory of Fatigue. Trend Eng 1961;13:9–14.

[58] Forman RG, Kearney VE, Engle RM. Numerical Analysis of Crack Propagation in Cyclic-Loaded Structures. J Basic Eng 1967;89:459–63. https://doi.org/10.1115/1.3609637.

[59] Klesnil M, Lukáš P. Influence of strength and stress history on growth and stabilisation of fatigue cracks. Eng Fract Mech 1972;4:77–92. https://doi.org/10.1016/0013-7944(72)90078-1.

[60] Walker K. The Effect of Stress Ratio During Crack Propagation and Fatigue for 2024-T3 and 7075-T6 Aluminum. Eff Environ Complex Load Hist Fatigue Life 2009:1-1–14. https://doi.org/10.1520/STP32032S.

[61] Erdogan F, Ratwani M. Fatigue and fracture of cylindrical shells containing a circumferential crack. Int J Fract Mech 1970 64 1970;6:379–92. https://doi.org/10.1007/BF00182626.

[62] Elber W. Fatigue crack closure under cyclic tension. Eng Fract Mech 1970;2:37–44. https://doi.org/10.1016/0013-7944(70)90028-7.

[63] Elber W. The Significance of Fatigue Crack Closure. ASTM Spec Tech Publ 1971:230–42. https://doi.org/10.1520/STP26680S.

[64] Ritchie RO. Mechanisms of fatigue crack propagation in metals, ceramics and composites: Role of crack tip shielding. Mater Sci Eng A 1988;103:15–28. https://doi.org/10.1016/0025-5416(88)90547-2.

[65] Rice JR. A path independet integral and approximate analysis of strain concentration by notches and cracks. J Appl Mech 1968;35:379–86. https://doi.org/10.1115/1.3601206.

[66] Rozumek D, Macha E. Elastic-plastic fatigue crack growth in 18G2A steel under proportional bending with torsion loading. Fatigue Fract Eng Mater Struct 2006;29:135–44. https://doi.org/10.1111/J.1460-2695.2006.00972.X.

[67] Dowling N, Begley J. Fatigue Crack Growth During Gross Plasticity and the J-Integral. Mech Crack Growth 2009:82-82–22. https://doi.org/10.1520/STP33940S.

[68] Li L, Yang YH, Xu Z, Chen G, Chen X. Fatigue crack growth law of API X80 pipeline steel under various stress ratios based on J-integral. Fatigue Fract Eng Mater Struct 2014;37:1124–35. https://doi.org/10.1111/ffe.12193.

[69] Donahue RJ, H. M-C, Atanmo P, Kumble R, McEvily AJ. Crack opening displacement and the rate of fatigue crack growth. Int J Fract Mech 1972;8:209–19. https://doi.org/https://doi.org/10.1007/BF00703882.

[70] Vasco-Olmo JM, Diaz FA, Antunes F V, James MN. Experimental evaluation of CTOD in constant amplitude fatigue crack growth from crack tip displacement fields. Frat Ed Integrita Strutt 2017:157–65. https://doi.org/10.3221/igf-esis.41.22.

[71] Vasco-Olmo JM, Diaz FA, Antunes F V, James MN. Experimental characterisation of fatigue crack growth based on the CTOD measured from crack tip displacement fields using DIC. Frat Ed Integrita Strutt 2019:658–66. https://doi.org/10.3221/igf-esis.50.56.

[72] Vasco-Olmo JM, Díaz Garrido FA, Antunes FV, James MN. Plastic CTOD as fatigue crack growth characterising parameter in 2024-T3 and 7050-T6 aluminium alloys using DIC. Fatigue Fract Eng Mater Struct 2020;43:1719–30. https://doi.org/10.1111/ffe.13210.

[73] Borges MF, Lopez-Crespo P, Antunes F V., Moreno B, Prates P, Camas D, et al. Fatigue crack propagation analysis in 2024-T351 aluminium alloy using nonlinear parameters. Int J Fatigue 2021;153:106478. https://doi.org/10.1016/J.IJFATIGUE.2021.106478.

[74] Sanford RJ, Dally JW. A general method for determining mixed-mode stress intensity factors from isochromatic fringe patterns. Eng Fract Mech 1979;621:621–33.

[75] Bradley WB, Kobayashi AS. An investigation of propagating cracks by dynamic photoelasticity. Exp Mech 1970;10:106–13. https://doi.org/10.1007/BF02325114.

[76] Schroedl M, Smith C. Local Stresses near Deep Surface Flaws under Cylindrical Bending Fields. ASTM Spec Tech Publ 1973:45–63. https://doi.org/10.1520/STP49636S.

[77] Etheridge JM, Dally JW. A three-parameter method for determining stress intensity factors from isochromatic fringe loops. J Strain Anal Eng Des 1978;13:91–4. https://doi.org/10.1243/03093247V132091.

[78] Chisholm DB, Jones DL. An analytical and experimental stress analysis of a practical mode II fracture test specimen. Exp Mech 1977;17:7–13. https://doi.org/10.1007/BF02324265.

[79] Smith DG, Smith CW. Photoelastic determination of mixed mode stress intensity factors. Eng Fract Mech 1972;4:357–66. https://doi.org/10.1016/0013-7944(72)90050-1.

[80] Brewster D. On the communication of the structure of doubly refracting crystals to glass, muriate of soda, flour spar and other substances by mechanical compression and dilatation. Philos Mag 1816;106:156–78.

[81] Thomson W (Lord K. On the Thermoelastic, Thermomagnetic and Pyro-electric Properties of Matters. Philos Mag 1878;5:4–27.

[82] NURSE AD, PATTERSON EA. Photoelastic determination of fatigue-crack stress intensity factors. In: Valley, MT and DelGrande, NK and Kobayashi A, editor. Nondestruct. Insp. AGING Aircr., vol. 2001, PO BOX 10, BELLINGHAM, WA 98227-0010: SPIE - INT SOC OPTICAL ENGINEERING; 1993, p. 155–62. https://doi.org/10.1117/12.163841.

[83] Diaz FA, Patterson EA, Tomlinson RA, Yates JR. Measuring stress intensity factors during fatigue crack growth using thermoelasticity. Fatigue Fract Eng Mater Struct 2004;27:571–83. https://doi.org/10.1111/j.1460-2695.2004.00782.x.

[84] Diaz FA, Yates JR, Patterson EA. Some improvements in the analysis of fatigue cracks using thermoelasticity. Int J Fatigue 2004;26:365–76. https://doi.org/10.1016/j.ijfatigue.2003.08.018.

[85] Lopez-Crespo P, Shterenlikht A, Patterson EA, Yates JR, Withers PJ. The stress intensity of mixed mode cracks determined by digital image correlation. J Strain Anal Eng Des 2008;43:769–80. https://doi.org/10.1243/03093247jsa419.

[86] Lopez-Crespo P, Shterenlikht A, Yates JR, Patterson EA, Withers PJ. Some experimental observations on crack closure and crack-tip plasticity. Fatigue Fract Eng Mater Struct 2009;32:418–29. https://doi.org/10.1111/J.1460-2695.2009.01345.X.

[87] Du Y, Diaz FA, Burguete RL, Patterson EA. Evaluation Using Digital Image Correlation of Stress Intensity Factors in an Aerospace Panel. Exp Mech 2011;51:45–57. https://doi.org/10.1007/s11340-010-9335-5.

[88] Diaz FA, Vasco-Olmo JM, Lopez-Alba E, Felipe-Sese L, Molina-Viedma AJ, Nowell D. Experimental evaluation of effective stress intensity factor using thermoelastic stress analysis and digital image correlation. Int J Fatigue 2020;135:10. https://doi.org/10.1016/j.ijfatigue.2020.105567.

[89] Ayatollahi MR, Nejati M. An over-deterministic method for calculation of coefficients of crack tip asymptotic field from finite element analysis. Fatigue Fract Eng Mater Struct 2011;34:159–76. https://doi.org/10.1111/j.1460-2695.2010.01504.x.

[90] Lopez-Crespo P, Moreno B, Garcia-Gonzalez A, Zapatero J, Lopez-Moreno A. Study of short cracks under biaxial fatigue. Frat Ed Integrità Strutt 2014;8:244–51. https://doi.org/10.3221/IGF-ESIS.30.31.

[91] Mokhtari M, Lopez-Crespo P, Moreno B, Zanganeh M. Some experimental observations of crack-tip mechanics with displacement data. Frat Ed Integrità Strutt 2015;9:143–50. https://doi.org/10.3221/IGF-ESIS.33.18.

[92] Lopez-Crespo P, Garcia-Gonzalez A, Moreno B, Lopez-Moreno A, Zapatero J. Some observations on short fatigue cracks under biaxial fatigue. Theor Appl Fract Mech 2015;80:96–103. https://doi.org/10.1016/J.TAFMEC.2015.05.004.

[93] Lopez-Crespo P, Moreno B, Lopez-Moreno A, Zapatero J. Study of crack orientation and fatigue life prediction in biaxial fatigue with critical plane models. Eng Fract Mech 2015;136:115–30. https://doi.org/10.1016/J.ENGFRACMECH.2015.01.020.

[94] Mokhtarishirazabad M, Lopez-Crespo P, Moreno B, Lopez-Moreno A, Zanganeh M. Optical and analytical investigation of overloads in biaxial fatigue cracks. Int J Fatigue 2017;100:583–90. https://doi.org/10.1016/j.ijfatigue.2016.12.035.

[95] Nelder JA, Mead R. A simplex-method for function minimization. Comput J 1965;7:308–13. https://doi.org/10.1093/comjnl/7.4.308.

[96] Lagarias JC, Reeds JA, Wright MH, Wright PE. Convergence properties of the Nelder-Mead simplex method in low dimensions. Siam J Optim 1998;9:112–47. https://doi.org/10.1137/s1052623496303470.

[97] Palumbo D, De Finis · R, Di Carolo · F, Vasco-Olmo · J, Diaz · F A, Galietti · U. Influence of Second-Order Effects on Thermoelastic Behaviour in the Proximity of Crack Tips on Titanium. Exp Mech 2021 2021:1–15. https://doi.org/10.1007/S11340-021-00789-4.

[98] Yates JR, Zanganeh M, Tai YH. Quantifying crack tip displacement fields with DIC. Eng Fract Mech 2010;77:2063–76. https://doi.org/10.1016/j.engfracmech.2010.03.025.

[99] Nowell D, Nowell SC. A comparison of recent models for fatigue crack tip deformation. Theor Appl Fract Mech 2019;103:6. https://doi.org/10.1016/j.tafmec.2019.102299.

[100] Yoneyama S, Morimoto Y, Takashi M. Automatic evaluation of mixed-mode stress intensity factors utilizing digital image correlation. Strain 2006;42:21–9. https://doi.org/10.1111/j.1475-1305.2006.00246.x.

[101] Zanganeh M, Lopez-Crespo P, Tai YH, Yates JR. Locating the Crack Tip Using Displacement Field Data: A Comparative Study. Strain 2013;49:102–15. https://doi.org/10.1111/str.12017.

[102] Audet C, Dennis JE. Analysis of Generalized Pattern Searches. Http://DxDoiOrg/101137/S1052623400378742 2006;13:889–903.

https://doi.org/10.1137/S1052623400378742.

[103] Yang B, Wei Z, Díaz FA, Liao Z, James MN. New algorithm for optimised fitting of DIC data to crack tip plastic zone using the CJP model. Theor Appl Fract Mech 2021;113:102950. https://doi.org/10.1016/J.TAFMEC.2021.102950.

[104] Moré JJ. The Levenberg-Marquardt algorithm: Implementation and theory 1978:105–16. https://doi.org/10.1007/BFB0067700.

[105] Vasco-Olmo JM. Experimental evaluation of plasticity induced crack shielding effect using full-field optical techniques for stress and strain measurement. University of Jaén, 2014.

[106] ASTM International. ASTM E606 Standard Test Method for Strain-Controlled Fatigue Testing. West Conshohocken, PA 2008:1–16.

[107] Vasco-Olmo JM, Diaz FA, Patterson EA. Experimental evaluation of shielding effect on growing fatigue cracks under overloads using ESPI. Int J Fatigue 2016;83:117–26. https://doi.org/10.1016/j.ijfatigue.2015.10.003.

[108] Kalnaus S, Fan F, Jiang Y, Vasudevan AK. An experimental investigation of fatigue crack growth of stainless steel 304L. Int J Fatigue 2009;31:840–9. https://doi.org/10.1016/J.IJFATIGUE.2008.11.004.

[109] VOCE, E. The Relationship between Stress and Strain for Homogeneous Deformation. J Inst Met 1948;74:537–62.

[110] Chaboche JL. A review of some plasticity and viscoplasticity constitutive theories. Int J Plast 2008;24:1642–93. https://doi.org/10.1016/J.IJPLAS.2008.03.009.

[111] Antunes F V., Ferreira MSC, Branco R, Prates P, Gardin C, Sarrazin-Baudoux C. Fatigue crack growth versus plastic CTOD in the 304L stainless steel. Eng Fract Mech 2019;214:487–503. https://doi.org/10.1016/j.engfracmech.2019.04.013.

[112] Camas D, Garcia-Manrique J, Antunes F V., Gonzalez-Herrera A. Three-dimensional fatigue crack closure numerical modelling: Crack growth scheme. Theor Appl Fract Mech 2020;108:102623. https://doi.org/10.1016/j.tafmec.2020.102623.

[113] Hwang JH, Kim YJ, Kim JW. Load interaction effect on fatigue crack growth in through-wall cracked pipes under large scale yielding: Experimental and numerical investigation. Int J Mech Sci 2021;211:106761. https://doi.org/10.1016/j.ijmecsci.2021.106761.

[114] Ramberg W, Osgood WR. Description of stress-strain curves by three parameters. 1943.

[115] Dugdale DS. Yielding of steel sheets containing slits. J Mech Phys Solids 1960;8:100–4. https://doi.org/10.1016/0022-5096(60)90013-2.

[116] Irwin GR. Plastic zone near a crack and fracture toghness. Seventh Sagamore Ord Mater Conf 1960;4:63–78.

[117] Fletcher R, Powell MJD. A Rapidly Convergent Descent Method for Minimization. Comput J 1963;6:163–8. https://doi.org/10.1093/comjnl/6.2.163.

[118] Broyden CG. Quasi-Newton Methods and their Application to Function Minimisation. Math Comput 1967;21:368. https://doi.org/10.2307/2003239.

[119] Goldfarb D. A Family of Variable-Metric Methods Derived by Variational Means. Math Comput 1970;24:23. https://doi.org/10.2307/2004873.

[120] ASTM. E 647 - 00: Standard Test Method for Measurement of Fatigue Crack Growth Rates. Annu B ASTM Stand 1103 2000.

[121] Tada H, Paris PC, Irwin GR. The Stress Analysis of Cracks Handbook. 3rd ed. New York: ASME Press; 2000. https://doi.org/10.1115/1.801535.

[122] Sanders JL. Analysis of circular cylindrical-shells. J Appl Mech Asme 1983;50:1165–70. https://doi.org/10.1115/1.3167198.

[123] Sanders JL. Circumferential through-cracks in cylindrical-shells under tension. J Appl Mech Asme 1982;49:103–7. https://doi.org/10.1115/1.3161948.

[124] Mukundan R, Ong SH, Lee PA. Image analysis by Tchebichef moments. IEEE Trans Image Process 2001;10:1357–64. https://doi.org/10.1109/83.941859.

[125] Wang W, Mottershead JE, Ihle A, Siebert T, Schubach HR. Finite element model updating from full-field vibration measurement using digital image correlation. J Sound Vib 2011;330:1599–620. https://doi.org/http://dx.doi.org/10.1016/j.jsv.2010.10.036.

[126] Sebastian C, Hack E, Patterson E. An approach to the validation of computational solid mechanics models for strain analysis. J Strain Anal Eng Des 2012;48:36–47. https://doi.org/10.1177/0309324712453409.

[127] Hack E., Lampeas G., Patterson EA. An evaluation of a protocol for the validation of computational solid mechanics models. J Strain Anal Eng Des 2016;51:5–13. https://doi.org/10.1177/0309324715616017.

[128] Lampeas G, Pasialis V, Lin X, Patterson EA. On the validation of solid mechanics models using optical measurements and data decomposition. Simul Model Pract Theory

2015;52:92–107. https://doi.org/10.1016/j.simpat.2014.12.006.

[129] Burguete RL., Lampeas G., Mottershead JE., Patterson EA., Pipino A., Siebert T., et al. Analysis of displacement fields from a high-speed impact using shape descriptors. J Strain Anal Eng Des 2014;49:212–23. https://doi.org/10.1177/0309324713498074.

[130] Vasco-Olmo JM, Diaz FA, Antunes F V, James MN. Characterisation of fatigue crack growth using digital image correlation measurements of plastic CTOD. Theor Appl Fract Mech 2019;101:332–41. https://doi.org/10.1016/j.tafmec.2019.03.009.

[131] Breitbarth E, Strohmann T, Besel M, Reh S. Determination of Stress Intensity Factors and integral based on Digital Image Correlation. Frat Ed Integrita Strutt 2019:12–25. https://doi.org/10.3221/igf-esis.49.02.

[132] Breitbarth E, Strohmann T, Requena G. High-stress fatigue crack propagation in thin AA2024-T3 sheet material. Fatigue Fract Eng Mater Struct 2020;43:2683–93. https://doi.org/10.1111/FFE.13335.

[133] O'Connor SJ, Nowell D, Dragnevski KI. Measurement of fatigue crack deformation on the macro- and micro-scale: Uniform and non-uniform loading. Int J Fatigue 2016;89:66–76. https://doi.org/10.1016/j.ijfatigue.2016.02.032.

[134] Nowell D, Dragnevski KI, O'Connor SJ. Investigation of fatigue crack models by micro-scale measurement of crack tip deformation. Int J Fatigue 2018;115:20–6. https://doi.org/10.1016/j.ijfatigue.2018.01.015.

[135] Gupta M, Alderliesten RC, Benedictus R. A review of T-stress and its effects in fracture mechanics. Eng Fract Mech 2015;134:218–41. https://doi.org/10.1016/j.engfracmech.2014.10.013.

[136] Shahani AR, Tabatabaei SA. Effect of T-stress on the fracture of a four point bend specimen. Mater Des 2009;30:2630–5. https://doi.org/10.1016/j.matdes.2008.10.031.

Appendix 1: Papers published in JCR indexed journals

Papers attached in the order in which are detailed.

PAPER Nº1

Title: Characterization of non-planar crack tip displacement fields using a differential geometry approach in combination with 3D digital image correlation

Authors: Alonso Camacho-Reyes, Jose Manuel Vasco-Olmo, Malcolm Neil James, Francisco Alberto Diaz

Journal: Fatigue & Fracture of Engineering Materials and Structures

Acceptance date: 16 February 2022

Publication date: 3 March 2022

DOI: 10.1111/ffe.13686

Most recent JCR data

Impact factor: 3.373

Rank by Journal Impact Factor

Category of Engineering, Mechanical: 51/137 (63.14%) Q2

Category of Materials Science, Multidisciplinary: 193/345 (44.05%) Q3

PAPER Nº2

Title: Experimental evaluation of plastic wake on growing fatigue cracks from the analysis of residual displacement fields

Authors: Jose Manuel Vasco-Olmo, Francisco Alberto Diaz, Alonso Camacho-Reyes, Malcolm Neil James, Fernando Ventura Antunes

Journal: Fatigue & Fracture of Engineering Materials and Structures

Acceptance date: 12 February 2022

Publication date: 19 March 2022

DOI: 10.1111/ffe.13681

Most recent JCR data

Impact factor: 3.373

Rank by Journal Impact Factor

Category of Engineering, Mechanical: 51/137 (63.14%) Q2

Category of Materials Science, Multidisciplinary: 193/345 (44.05%) Q3

PAPER Nº3

Title: Towards a new methodology for the characterisation of crack tip fields based on a hybrid computational approach

Authors: Alonso Camacho-Reyes, Jose Manuel Vasco-Olmo, Malcolm Neil James, Francisco Alberto Diaz

Journal: International Journal of Fatigue

Acceptance date: 18 April 2022

Publication date: 22 April 2022

DOI: 10.1016/j.ijfatigue.2022.106942

Most recent JCR data

Impact factor: 5.489

Rank by Journal Impact Factor

Category of Engineering, Mechanical: 16/137 (88.69%) Q1

Category of Materials Science, Multidisciplinary: 114/345 (67.10%) Q2

Received: 17 December 2021 | Revised: 15 February 2022 | Accepted: 16 February 2022

DOI: 10.1111/ffe.13686

SPECIAL ISSUE ARTICLE

FFEMS Fatigue & Fracture of Engineering Materials & Structures WILEY

Characterization of non-planar crack tip displacement fields using a differential geometry approach in combination with 3D digital image correlation

Alonso Camacho-Reyes[1] | **Jose M. Vasco-Olmo**[1] | **M. Neil James**[2,3] | **Francisco A. Diaz**[1]

[1]Departamento de Ingeniería Mecánica y Minera, Universidad de Jaén, Jaén, Spain

[2]School of Engineering, University of Plymouth, Plymouth, UK

[3]Department of Mechanical Engineering, Nelson Mandela Metropolitan University, Port Elizabeth, South Africa

Correspondence
Alonso Camacho-Reyes, Departamento de Ingeniería Mecánica y Minera, Universidad de Jaén, Jaén, Spain.
Email: acreyes@ujaen.es

Funding information
Junta de Andalucía, Grant/Award Number: 1380786

Abstract

This paper describes a novel differential geometry method that is used in combination with 3D digital image correlation (3D-DIC) for crack tip field characterization on non-planar (curved) surfaces. The proposed approach allows any of the two-dimensional crack tip field models currently available in the literature to be extended to the analysis of a 3D developable surface with zero Gaussian curvature. The method was validated by analyzing the crack tip displacement fields on hollow thin-walled cylindrical specimens, manufactured from either 304L or 2024-T3 alloy that contained a central circumferential crack. The proposed approach was checked via a comparison between experimentally measured displacement fields (3D-DIC) and those reconstructed from a modified 2D crack tip model (utilizing either 2, 3, or 4 terms of the William's expansion series) and implementing a 3D geometrical correction. Further validation was provided by comparing model-derived stress intensity factors with values provided by empirical correlations.

KEYWORDS

3D-DIC, crack tip field, curved circumferential crack, differential geometry, non-planar surface

1 | INTRODUCTION

Optimized design of mechanical components requires guarantees of their in-service structural integrity performance over the complete lifetime. This implies associated development of accurate methods of analysis that reduces their behavioral uncertainty. Cracks, or crack-like defects, are endemic in mechanical elements, and their existence can lead to catastrophic failures, particularly from fatigue processes.[1] Evaluation of the severity of a defect or crack is based on characterization of the crack tip stress/strain distributions, and a number of different mathematical models, based on various singular crack tip parameters, are available in the literature.[2–9] Many of the mathematical models, such as Westergaard's classical equations,[2,3] Williams' series expansion,[4] or Muskhelishvili's complex potentials,[6,7] are based on linear elastic fracture mechanics (LEFM). However, there

some other models, for example, those due to Hutchinson[5] or Pommier and Hamman[8] that assume an elastoplastic material behavior. More recently, a mathematical approach based on Muskhelishvili's complex potentials has been developed by Christopher, James, and Patterson, that is referred to in the literature as the CJP model.[9] It considers the potential influences on the surrounding elastic field of the plastic enclave around the tip and flanks of a fatigue crack. This opens up the possibility of directly assessing the influence of shielding mechanisms during fatigue crack growth.[10] The singularity characterization parameters that are given by most models can be successfully determined by combining the mathematical description of the crack tip field with experimental measurements obtained using full-field optical techniques. Descriptions of such techniques are given in Brewster[11] (digital photo-elasticity), Schreier et al[12] (digital image correlation [DIC]), and Thomson[13] (thermoelastic stress analysis [TSA]), and they allow direct analysis of the crack tip fields, and hence evaluation of the driving force for fatigue crack advance,[14,15] or the assessment of crack shielding phenomena.[16–18] All of these models have their origin in the differential equations of the theory of elasticity and simplify the situation to a planar geometry under 2D plane stress or plane strain conditions. The crack tip field is then generally defined by a set of polar coordinates (origin at the crack tip) in the crack plane together with the respective characterization parameters. This limitation of the models to the analysis of flat surfaces, and consequently planar components, is a major restriction in their more general applicability.

Consequently, there is a very limited number of research works in the literature in which such 2D models have been employed for the analysis of non-planar cracked surfaces. In such cases, important assumptions are made to provide an approximation to the real crack tip field at the surface. Mokhtarishirazabad et al[19] employed 2D-DIC with a high magnification lens, to calculate the stress intensity factor (SIF) from the Williams equations in an analysis of a cracked cylindrical surface. This approximate approach was valid when the magnification was sufficiently high over a small analysis zone, that the surface curvature could be neglected. However, the presence of the near crack tip plastic enclave constituted a major limitation on this approach as the authors used a linear elastic crack tip model. In essence, only data from the plastic enclave could be captured at this resolution while any plasticity effects are explicitly excluded when using a linear elastic crack tip model. To rectify this anomaly, the analysis has to be focused on the elastic zone which requires a decrease in the spatial resolution, where the effect of specimen curvature can no longer be neglected. In more recent work, Vormwald et al[20] employed 3D-DIC for the analysis of crack tip displacements; however, they also assumed a hypothetical negligible curvature with very high magnification, in order to infer SIFs using a 2D crack tip model in a thin-walled cylindrical tube under mixed mode loading.

The current work advances the characterization of curved surfaces by outlining a novel experimental approach for crack field quantification based on non-planar bodies in combination with 3D digital image correlation (3D-DIC). The method is based on a modified two-dimensional planar model using a differential geometry formulation to account for the 3D shape of the surface. In this way, a generalized plane stress crack field description for non-flat surfaces can be obtained at the surface of the specimen. The proposed methodology was applied to the analysis of crack tip displacement fields on the surface of hollow cylindrical specimens with a wall thickness of 2.11 mm made from either 304-L stainless steel or 2024-T3 aluminum alloy. Specimens contained starter notches in the form of central circumferential holes on opposite sides of the specimen with crack-like sawn extensions at their equatorial plane (illustrated in Figure 3). The accuracy of the proposed approach was assessed by comparing the displacement field measured using 3D-DIC, with that reconstructed by using a modified 2D Williams' model (with either 2, 3, or 4 terms) with a 3D geometrical correction. The observed average fitting error was lower that 0.15%, highlighting the capability of the approach in characterizing the crack tip field at the surface of a non-planar geometry. SIFs were determined at maximum load for various crack lengths and compared with empirical correlations available in the literature for this geometry.[21–23] Experimental and modeling results showed a high level of agreement, with an average error lower than 5%. Finally, to illustrate the robustness of the proposed methods, the plane stress assumption made at the specimen surface was experimentally demonstrated to be valid from an analysis of displacement components at the specimen surface, again using 3D-DIC.

This technique has significant potential in application areas that include identifying empirical fatigue crack growth relationships and determining the effective driving force for crack growth using advanced crack tip field models that incorporate influences of plasticity-induced shielding. Fatigue and fracture models developed for planar surfaces can now be extended to curved surfaces. There is also potential for application to problems of crack propagation direction, as the analysis presented has been developed for Mode I, but could be extended to include Modes II and III, allowing the likelihood of crack deflections to be predicted from the SIF changes.

2 | FUNDAMENTAL THEORY

2.1 | Williams crack tip field model

The Williams expansion series[4] is widely recognized inside the fatigue and fracture community as a reliable model that approximates the crack tip field on a flat cracked surface. According to this model, the displacement fields around the crack tip under opening mode (tensile) loading can be defined as follows:

$$\begin{Bmatrix} u_x \\ u_y \end{Bmatrix} = \sum_{p=1}^{\infty} \frac{r_2^{\frac{p}{2}}}{2G} a_p \begin{Bmatrix} \left(\kappa + \frac{p}{2} + (-1)^p\right)\cos\frac{p\theta}{2} - \frac{p}{2}\cos\frac{(p-4)\theta}{2} \\ \left(\kappa - \frac{p}{2} - (-1)^p\right)\sin\frac{p\theta}{2} + \frac{p}{2}\sin\frac{(p-4)\theta}{2} \end{Bmatrix} \tag{1}$$

where u_x and u_y are respectively the horizontal and vertical components of the displacement field; r and θ are polar coordinates over an xy plane centered at the crack tip; G is the shear modulus; p is a sum index; κ is a function of Poisson's coefficient, which depends on the stress state (2D or 3D); and a_p is the half crack length for a through-thickness crack. The first coefficient of the sum is related to the Mode I SIF, K_I while the second coefficient is related to the non-singular stress in the x direction (the T-stress), $\sigma_{0x} = 4a_2$. Higher order terms can be neglected if only the singularity zone is being analyzed and no significant plastic deformation at the crack tip occurs. Moreover, if only the first two terms are considered, the Williams' model is equivalent to the Irwin–Westergaard model.[2,3] Under plane stress conditions, the out-of-plane displacement component normal to the crack plane is given by Equation 2.

$$u_z = -2z\frac{G(1+\nu)}{\nu}(\sigma_x + \sigma_y) \tag{2}$$

where z is the out-of-plane coordinate and σ_x and σ_y are the normal stresses in the horizontal and vertical directions. Conventionally, the x-axis is the crack growth direction, and the y-axis is the crack opening direction under tensile loading.

2.2 | Tangential directions and Frenet trihedral

When a non-planar curved surface is under consideration, it can be parametrized as a function of two parameters ξ and η which represent two orthogonal directions. Each point at the surface can be defined by a position vector $\vec{\rho}$ referred to a general Cartesian reference system (x, y, z) as shown in Figure 1. For a particular surface point, Q, three tangent directions can be defined by three orthogonal unity vectors (tangential, $\vec{T}$, binormal, $\vec{B}$, and normal, $\vec{N}$) according to the Frenet–Serret formulation, which gives an innate geometric description of a curve.[24] These three vectors are calculated from the position vector and the parameters ξ and η as shown in Equations 3, 4, and 5.

$$\vec{T} = \frac{\frac{\partial\vec{\rho}}{\partial\xi}}{\left\|\frac{\partial\vec{\rho}}{\partial\xi}\right\|} = \frac{\frac{\partial x}{\partial\xi}\vec{e_x} + \frac{\partial y}{\partial\xi}\vec{e_y} + \frac{\partial z}{\partial\xi}\vec{e_z}}{\sqrt{\left(\frac{\partial x}{\partial\xi}\right)^2 + \left(\frac{\partial y}{\partial\xi}\right)^2 + \left(\frac{\partial z}{\partial\xi}\right)^2}} \tag{3}$$

$$\vec{B} = \frac{\frac{\partial\vec{\rho}}{\partial\eta}}{\left\|\frac{\partial\vec{\rho}}{\partial\eta}\right\|} = \frac{\frac{\partial x}{\partial\eta}\vec{e_x} + \frac{\partial y}{\partial\eta}\vec{e_y} + \frac{\partial z}{\partial\eta}\vec{e_z}}{\sqrt{\left(\frac{\partial x}{\partial\eta}\right)^2 + \left(\frac{\partial y}{\partial\eta}\right)^2 + \left(\frac{\partial z}{\partial\eta}\right)^2}} \tag{4}$$

$$\vec{N} = \frac{\frac{\partial\vec{\rho}}{\partial\xi}}{\left\|\frac{\partial\vec{\rho}}{\partial\xi}\right\|} \times \frac{\frac{\partial\vec{\rho}}{\partial\eta}}{\left\|\frac{\partial\vec{\rho}}{\partial\eta}\right\|} \tag{5}$$

where $\vec{T}$, $\vec{B}$, and $\vec{N}$ are the tangential, binormal, and normal unitary vectors, respectively. Double vertical bars denote the two-norm of the vector (which calculates the distance of the vector coordinate from the origin of the vector space), the operator $\times$ denotes the vector cross-product, and e_x, e_y, and e_z are the components of unit vectors in the Cartesian directions.

The lengths x' and y' over the surface along the parametrization directions, ξ and η, are obtained by integration according to Equations 6 and 7.

$$x' = \int_{\xi_0}^{\xi} \sqrt{\left(\frac{\partial x}{\partial\xi}\right)^2 + \left(\frac{\partial y}{\partial\xi}\right)^2 + \left(\frac{\partial z}{\partial\xi}\right)^2}\, d\xi \tag{6}$$

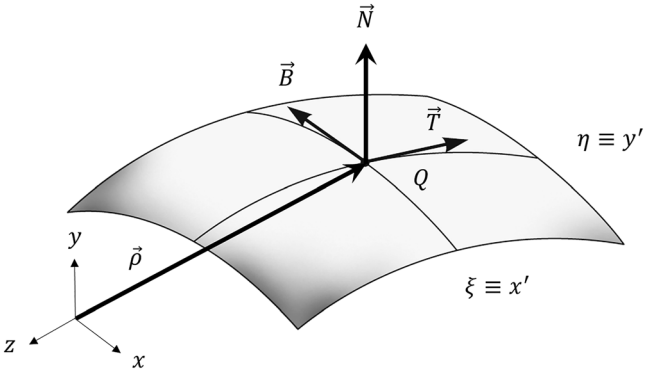

FIGURE 1 Schematic illustration showing the components of the Frenet trihedral for an arbitrary point over a generic non-flat surface[24]

$$y' = \int_{\eta_0}^{\eta} \sqrt{\left(\frac{\partial x}{\partial \eta}\right)^2 + \left(\frac{\partial y}{\partial \eta}\right)^2 + \left(\frac{\partial z}{\partial \eta}\right)^2}\, d\eta \tag{7}$$

where ξ_0 and η_0 are the integration lower limits, respectively.

2.3 | Extended crack tip model for the analysis of curved surfaces

The proposed formulation for the analysis of the crack tip field on curved surfaces assumes plane stress conditions. The objective is to combine the description provided by the curved surface crack tip field model with experimental stress and strain measurements obtained from any suitable optical technique. Thus, considering a developable surface, that is, one that can be flattened onto a plane without distortion, the normal direction given by $\vec{N}$ is the principal direction and the stress value is zero. For simplicity in illustrating the proposed methodology, a cylindrical surface containing a central circumferential crack has been considered (Figure 2A). The parametric ξ and η directions have been chosen to be respectively coincident with the crack growth and opening directions. In addition, the surface can be geometrically unwrapped over a $\xi-\eta$ plane as schematically illustrated in Figure 2B. Hence, as for the case of a two-dimensional flat surface, the Williams model can be reformulated to account for the effect of the curvature in the unwrapped surface (Equations 5 and 6). As indicated in Figure 2, the displacement in the horizontal direction (crack growth direction) is replaced by the displacement in the tangential direction, while the displacement in the vertical direction (crack opening direction) is replaced by the displacement in the binormal direction. Similarly, the rectilinear coordinates of the surface points are replaced by the curvilinear coordinates.

$$\begin{Bmatrix} u_T \\ u_B \end{Bmatrix} = \sum_{p=1}^{\infty} \frac{r'^{\frac{p}{2}}}{2G} a_p \begin{Bmatrix} \left(\kappa + \frac{p}{2} + (-1)^p\right)\cos\frac{p\theta'}{2} - \frac{p}{2}\cos\frac{(p-4)\theta'}{2} \\ \left(\kappa - \frac{p}{2} - (-1)^p\right)\sin\frac{p\theta'}{2} + \frac{p}{2}\sin\frac{(p-4)\theta'}{2} \end{Bmatrix} \tag{8}$$

$$u_N = -2z_n \frac{G(1+\nu)}{\nu}(\sigma_T + \sigma_B) \tag{9}$$

where u_T, u_B, and u_N are the displacement components in the tangential, binormal, and normal directions, respectively. If the surface is unwrapped over a plane, r' and θ' are the polar coordinates of a point Q referred to a Cartesian reference system $x'-y'$ (Figure 2B), z_n is the normal coordinate in the unwrapped plane (out-of-plane direction), and σ_T and σ_B are the normal stresses along tangential and binormal directions, respectively. The displacement components u_T, u_B, and u_N are calculated by projecting the displacement vector $\vec{u}$ at each direction defined by the Frenet trihedral as shown in Equations 10 to 12.

$$\begin{aligned} u_T &= \vec{u}\cdot\vec{T} \\ &= \left(u_x\cdot\vec{e_x} + u_y\cdot\vec{e_y} + u_z\cdot\vec{e_z}\right)\cdot\left(T_x\cdot\vec{e_x} + T_y\cdot\vec{e_y} + T_z\cdot\vec{e_z}\right) \end{aligned} \tag{10}$$

$$\begin{aligned} u_B &= \vec{u}\cdot\vec{B} \\ &= \left(u_x\cdot\vec{e_x} + u_y\cdot\vec{e_y} + u_z\cdot\vec{e_z}\right)\cdot\left(B_x\cdot\vec{e_x} + B_y\cdot\vec{e_y} + B_z\cdot\vec{e_z}\right) \end{aligned} \tag{11}$$

$$\begin{aligned} u_N &= \vec{u}\cdot\vec{N} \\ &= \left(u_x\cdot\vec{e_x} + u_y\cdot\vec{e_y} + u_z\cdot\vec{e_z}\right)\cdot\left(N_x\cdot\vec{e_x} + N_y\cdot\vec{e_y} + N_z\cdot\vec{e_z}\right) \end{aligned} \tag{12}$$

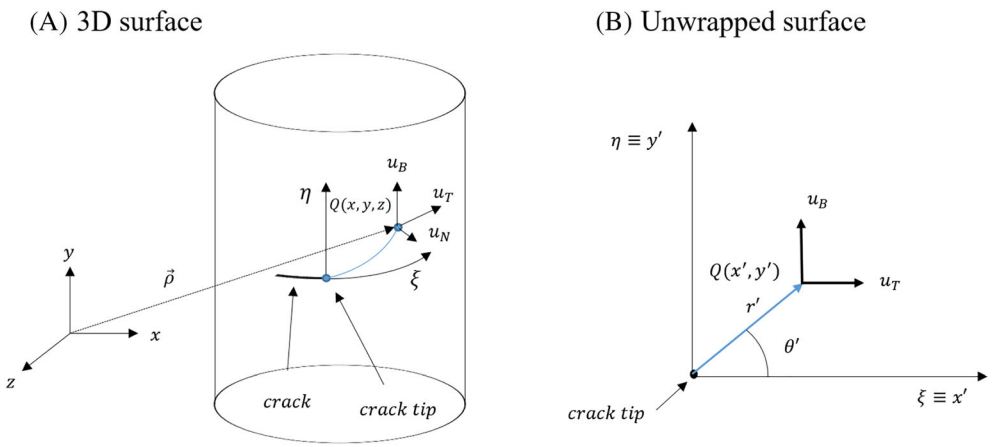

FIGURE 2 Figure to illustrate the analogy with flat models. Cracked surface (A, 3D surface) and the equivalent system on the unwrapped plane (B, unwrapped surface) [Colour figure can be viewed at wileyonlinelibrary.com]

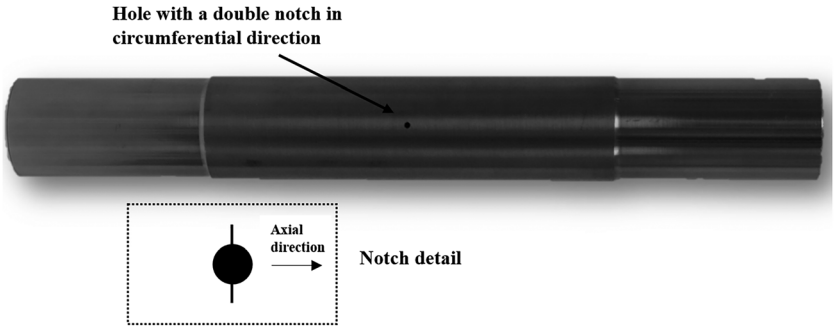

FIGURE 3 304L-SS specimen used during fatigue experiments

TABLE 1 Chemical composition of both alloys (wt %)

304L	0.02 C	0.39 Si	1.37 Mn	0.001 S	0.029 P	8.01 Ni	18.15 Cr	
2024-T3	3.8 Cu	0.1 Cr	0.3 Mn	0.5 Fe	1.2 Mg	0.5 Si	0.15 Ti	0.25 Zn

TABLE 2 Mechanical properties of the alloys

Mechanical property	Units	304L	2024-T3
Young modulus	MPa	197,000	73,100
Poisson ratio	Dimensionless	0.33	0.33
Yield stress	MPa	312	355
Ultimate tensile stress	MPa	646	483
Elongation at failure	%	53	18

3 | EXPERIMENTAL DETAILS

The proposed approach was validated by fatigue crack growth rate testing using cylindrical seamless tubes with centrally introduced notches as shown in Figure 3. Specimens were machined from either 304L austenitic stainless steel or 2024-T3 aluminum alloy. The chemical composition and mechanical properties of the two alloys are given in Tables 1 and 2. The specimens were designed and manufactured according to ASTM standard E-606-92,[25] with a length of 203.2 mm and a thickness of 2.11 mm. To suit the available material, the external diameter of the 304L specimens was 26.8 mm and that of the 2024-T3 specimens was 25.4 mm. The central notch (Figure 3) was machined from an initial drilled through-thickness hole extended with a 0.1-mm sawn slot in the circumferential direction. Crack length was calculated in radians, as the ratio between the circumferential angle subtended by the crack divided by the complete circumference (2π radians). The normalized initial notch length was 0.02 (equivalent to a crack length along the outer circumference of 1.7 mm, or 1.5° expressed in terms of the crack angle) and was chosen to provide a good resolution of the crack tip field even for very short cracks. However, the notch manufacturing process left residual stresses that affected the crack tip field at short crack lengths (in the range of normalized crack lengths from approximately 0.02 to 0.15). A 100-kN servohydraulic testing machine (MTS Landmark 370.10) was used in the fatigue tests with constant amplitude tensile loading at 10 Hz. The stress ratio was 0.525, in order to avoid any influences of crack wake closure in the measured crack tip field.[10,26] The maximum applied load was selected to ensure that SIF values were significantly higher than the threshold range[16,26] for fatigue crack growth. Hence, the maximum applied load was 30% of the yield stress for stainless steel and 20% for the aluminum specimens.

The specimen surface was prepared for the DIC work by spraying it with a stochastic black speckle pattern on a white background. Crack tip displacement fields were recorded using a 3D-DIC technique.[12] 3D-DIC can record the three-dimensional surface displacement field on the specimen, allowing calculation of the experimental SIF at maximum load for a given crack length. Experimental data were acquired with a stereoscopic vision system comprising three 5-megapixel monochrome CCD cameras each fitted with a zoom lens (MLH-10X EO) to increase the spatial resolution around the crack tip. The required depth of field to avoid blurring in the image was set via the lens aperture, with smaller apertures giving greater depth of field. A dual point fiber optic light guide was used to achieve a uniform illumination pattern around the initial notch on both sides of the specimen. The experimental set-up is shown in Figure 4.

A calibration grid (a rectangle comprising 9 × 6 dots with a 2-mm spacing between dots)[27] was used to calibrate the stereoscopic system and calculate the relative position and distance between the cameras and the specimen surface.[12] This calibration process was particularly important when measuring the very small displacements

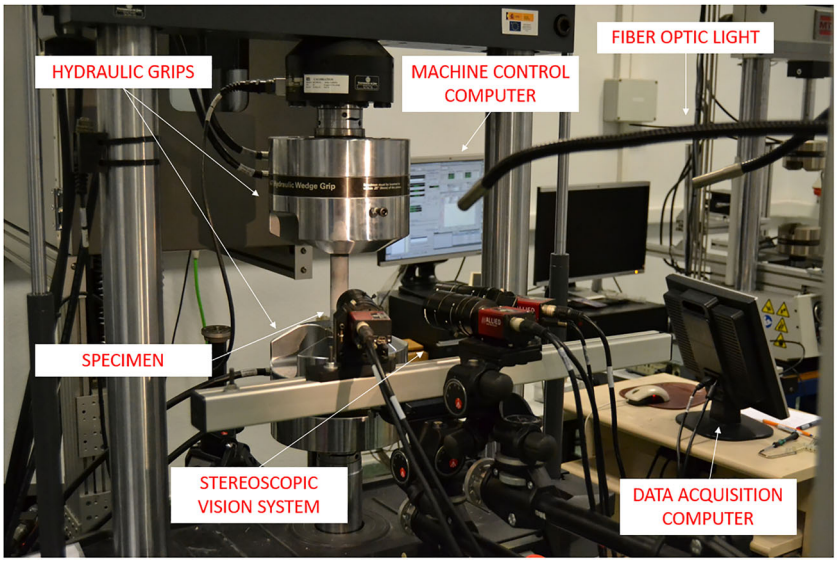

FIGURE 4 Experimental set-up [Colour figure can be viewed at wileyonlinelibrary.com]

associated with small crack lengths, and an average spatial resolution of 0.02 mm/pixel was achieved. That average spatial resolution was computed as the mean value of the distance between the adjacent points in a domain. In order to capture all possible movements of the non-planar specimen surface during a test, it was important to account for any motion of the calibration plate (either rotation or displacements) that might occur during the calibration process. DIC processing used a square subset facet size of 29 pixels with an overlap of one pixel, as this was found to reliably provide the required displacement field information.

4 | DISPLACEMENT FIELD MEASUREMENT

The crack tip displacement field under maximum load at various crack lengths was measured using the previously described 3D-DIC set-up and the commercial software VIC-3D from Correlated Solutions Inc. The measured surface displacement field together with the spatial coordinates of the central point of the facets allowed calculation of the directions of the Frenet trihedral. Figure 5 gives the measured displacement values in the Frenet binormal and tangential directions. Note that normalized crack length in radians has been used in this figure, defined as the ratio of the half angle subtended by the crack γ/π. For the chosen geometry, the crack growth direction corresponded with the circumferential direction while the crack opening direction corresponded with the axial direction since the applied load was perpendicular to the crack plane. Using Equations 3 to 7, the unitary transformation vectors and the coordinates of the unwrapped surface relative to the crack tip were calculated. Note that for the particular case considered, the transformation performed is equivalent to the use of a cylindrical (polar) coordinate system. Circumferential and axial directions were calculated from the relative position between the surface points and the directional derivatives were calculated using a finite difference approach. To reduce the error arising from the discretization process, the first derivative was calculated using a second-order finite difference approach (central derivative). Computation of the distance between points at the specimen surface used a numerical integration approach based on the compound trapezium rule. Hence, the transformation parameters were calculated corresponding to the unwrapped surface of the displacement field. Figure 5 shows tangential and binormal displacement components over the unwrapped plane for a particular crack length of 19.71 mm. Figure 5A.1,B.1 shows both displacement components in a three-dimensional plot while Figure 5A.2,B.2 shows both displacements on a map plot.

In order to extract singularity characterizing parameters from the displacement field, the Multi-Point Over-Deterministic Method (MPODM) developed by Sanford and Dally[28] was used. Mathematical fitting was performed using a mesh of points in an annular region around the crack tip (see Figure 6). This annulus avoided the plastic enclave surrounding the crack tip so that LEFM parameters could be determined. Previous work[10] has shown that the choice of mask shape, that is, rectangular or circular, does not significantly affect the results and a circular mask is easier to implement and define in data collection terms. The inner mesh radius was computed using the Dugdale[29] plastic zone radius approximation. The outer radius value was chosen in order to capture the singularity zone. Thus, according to some

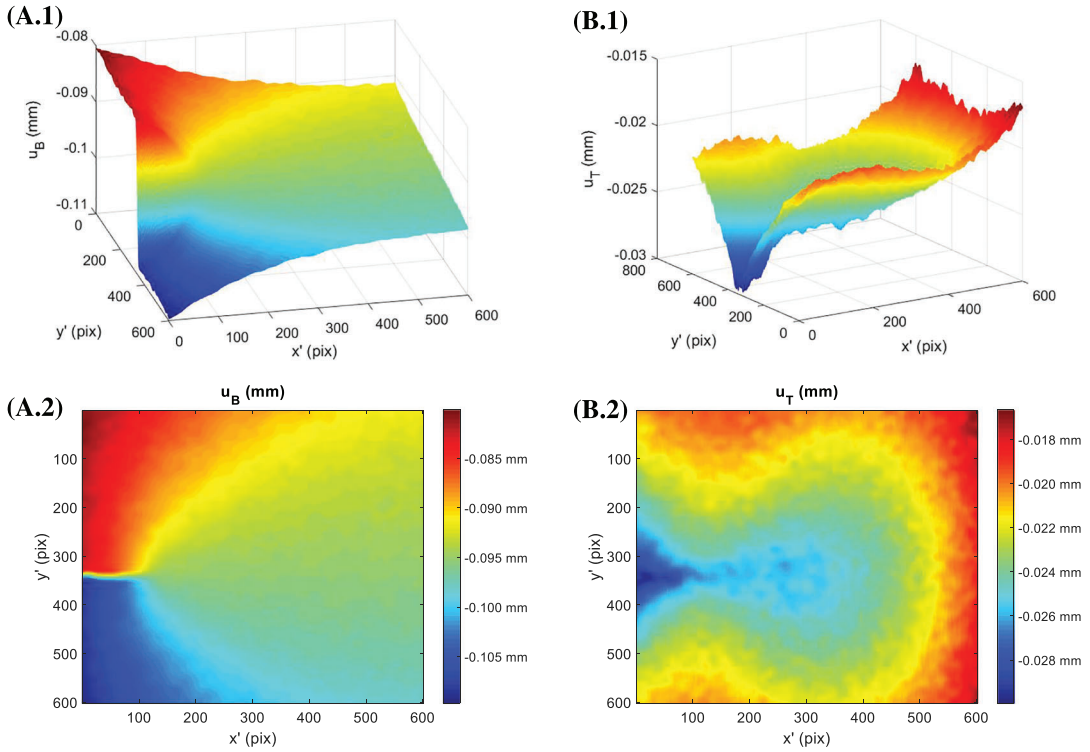

FIGURE 5 Displacement field around the crack tip in terms of binormal and tangential directions at maximum load for a crack length of 19.7 mm (normalized crack length $\gamma/\pi = 0.2377$). (A) Binormal and (B) tangential components. 304L-SS [Colour figure can be viewed at wileyonlinelibrary.com]

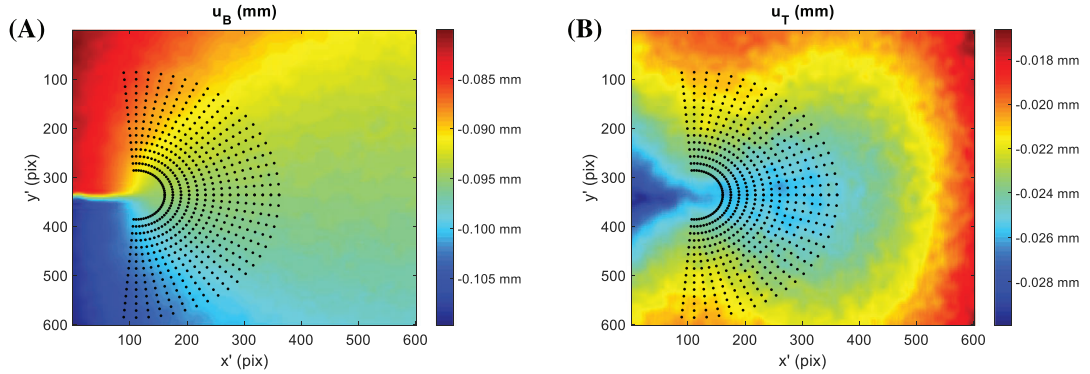

FIGURE 6 Annular mesh for data collection. (A) binormal displacement map and (B) tangential displacement map [Colour figure can be viewed at wileyonlinelibrary.com]

previous works,[6,16] a value around 40% of the crack length was chosen. Mesh points were defined linearly and therefore were equally spaced. Crack tip singularity parameters were then computed by solving a linear system of equations (with a suitable matrix factorization) using the measured surface displacements (u_T and u_B) at selected locations around the crack tip and their relative position in the unwrapped plane (x' and y'). The influence of the number of terms in the crack tip stress equations on the quality of the mathematical fitting and its effect on the calculated SIF was also evaluated. As discussed in Section 2, most crack tip stress/displacement models are formulated assuming that the crack tip is at the origin of the reference coordinate system. In the current analysis, the center of the annular mesh was placed at an initial location estimated from the observation of the measured displacement field. That initial point can be located easily and precisely since the crack path can be recognized in both maps. To locate the precise crack tip position on the unwrapped plane, a search grid was

defined over the plane as shown in Figure 7. For each point of the grid, which are defined by their coordinates x_i' and y_i', an error function F_i was formulated (Equation 13). The model was then fitted to the experimental data at each point of the grid and the minimum value of the error function was used to determine the crack tip location.[30,31] These positions were then used to calculate SIFs. Hence, from the mathematical fitting, coefficients that describe the crack tip fields could be obtained and the opening mode SIF K_I calculated.

$$F = \sqrt{\left\| \frac{u_T^{th} - u_T^e}{u_T^{th}} \right\|^2 + \left\| \frac{u_B^{th} - u_B^e}{u_B^{th}} \right\|^2} \tag{13}$$

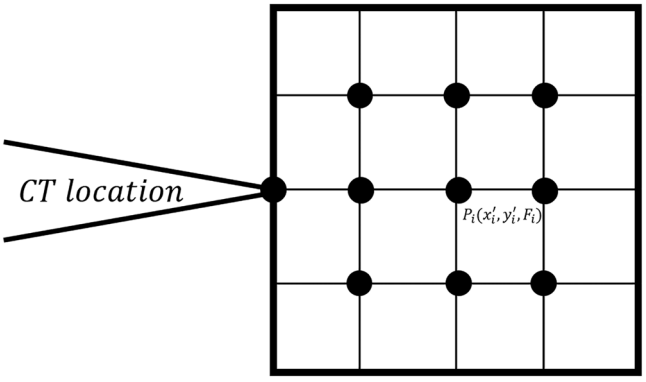

FIGURE 7 Search grid for crack tip localization

where double vertical bars indicate the operator norm and superscripts *e* and *th* refer to experimental and theoretical displacement data, respectively.

To validate the accuracy of the plane stress assumption at the specimen surface, displacement fields in the normal direction were obtained experimentally and theoretically (the latter via mathematical fitting) and compared. Once crack tip parameters were calculated, the displacement field in the normal direction could be calculated (Equation 6) and compared with that measured using 3D-DIC. This comparison was also made for SIFs, where calculated experimental values were compared with values calculated from empirical correlations reported by Tada et al[23] based on Sanders' results.[21,22]

It should be noted that for the stainless steel, the crack grew from the notch on a single side of the specimen, while in the case of the aluminum alloy cracks grew from both notches, as indicated in Figure 8. The crack topology in the two different materials therefore corresponds to different empirical correlations. Tada's correlation[21–23] for a single crack (304L-SS) is given by Equation 14, and for the case of a double crack (2024-T3-Al), Equation 15 is applicable.

$$K_I = \frac{P}{2\pi R t}\sqrt{R}\left(\frac{\sqrt{2}}{\left(\frac{t}{R\sqrt{12(1-\nu^2)}}\right)^{\frac{1}{2}}}\right)^{\frac{1}{2}}\left(\gamma + \frac{1-\gamma\cdot\cos\gamma}{2\cot\gamma + \sqrt{2}\cot\left(\frac{\pi-\gamma}{\sqrt{2}}\right)}\right) \tag{14}$$

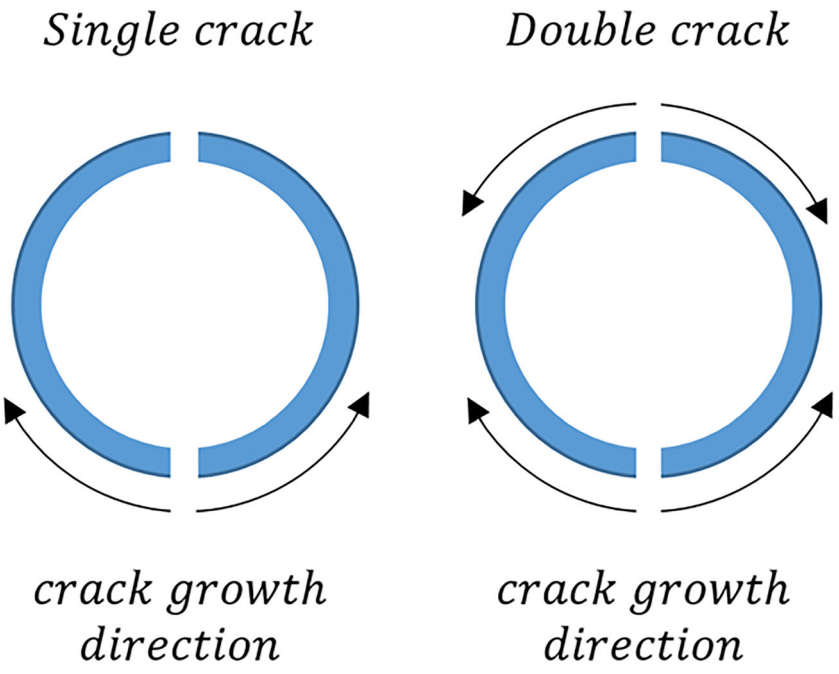

FIGURE 8 Schematic illustration showing how the crack was growing during fatigue test for the two materials tested during fatigue experiments, left) single crack corresponding to 304L-SS and (right) double crack corresponding to 2024-T3-Al [Colour figure can be viewed at wileyonlinelibrary.com]

$$K_I = \sqrt{\frac{\tan\gamma}{\gamma}}\frac{P}{2\pi Rt}\sqrt{\pi R\gamma} \tag{15}$$

In these expressions, P is the axial load, R is the mean radius of the cylindrical specimen, t is the wall thickness, ν is Poisson's ratio, and γ is the subtended half angle of the crack. The crack length was measured as the distance over the specimen surface between the crack tip location and the center of the original starter hole. In addition, the crack angle was calculated as the ratio between the curved surface crack length and the outer radius of the cylinder. To assess the quality of the proposed methodology in describing the crack tip field, a comparison was made between the experimental and theoretically fitted displacement field in terms of the SIF confidence intervals and their relative fitting error.

5 | RESULTS AND DISCUSSION

Experimental data were fitted to the Williams model using the methodology described above while also sequentially increasing the number of terms used in the expansion series. In the present work, beyond four terms, the model output became stable, and the magnitude of higher order terms was negligible (less than 10^{-16}). This is indicative of a high quality correlation between the experimental and the mathematically fitted data. Furthermore, the SIF values obtained using a reduced number of terms did not change significantly as the number of terms was increased. The resultant Mode I SIF values calculated using 2, 3, and 4 terms in the Williams' expansion series as a function of the normalized crack length are shown in Figure 9 for 304L-SS and in Figure 10 for 2024-T3-Al. The reliability of the results was also illustrated via a comparison with the nominal values of K_I calculated according to Equations 14 and 15 (Figures 9 and 10) and showed a high level of agreement, with average errors for the 304L alloy of only 6.36%, 5.38%, and 4.13% using 2, 3, and 4 terms, respectively, and 3.18%, 3.74%, and 3.18% for 2, 3, and 4 terms in the case of the 2024-T3 alloy.

These small differences can be explained by the presence of noise inherent to the DIC stereoscopic calibration residuals and the differentiation process that occurs when implementing the proposed approach. Moreover, the use of average values in the elastic constants could also modify the results by around 1% (the range of Young's modulus provided by the alloy manufacturer).

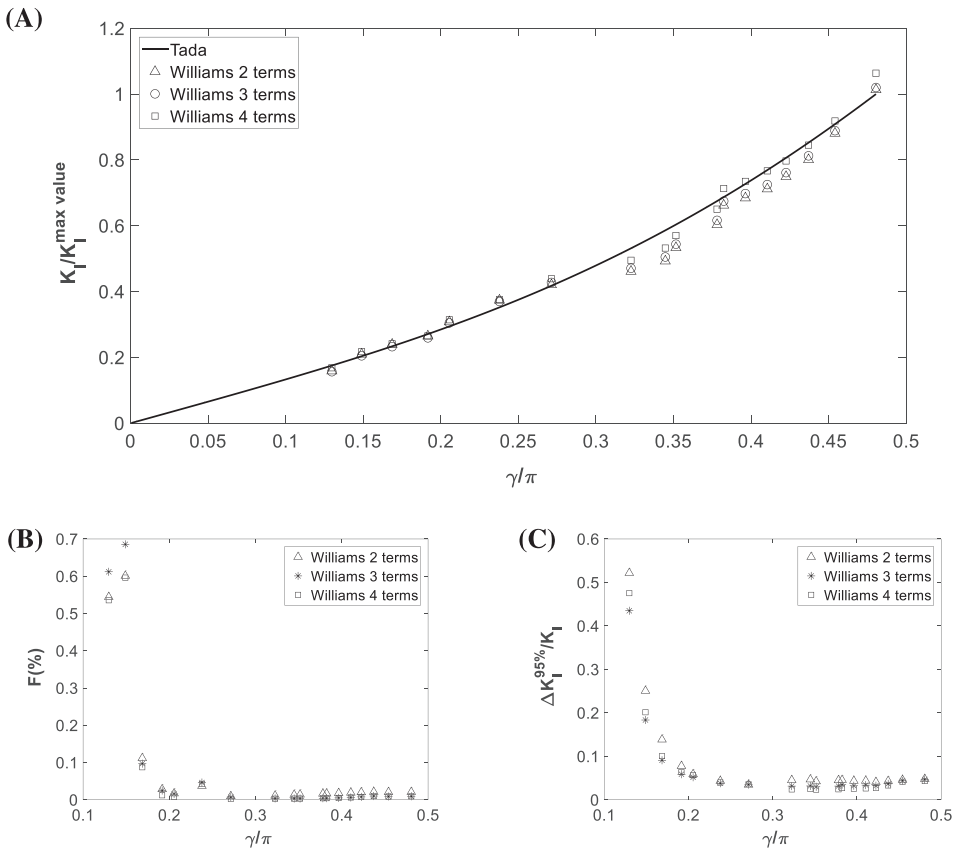

FIGURE 9 Variation with the normalized crack length and the number of terms in the Williams stress series expansion used in the calculations, as a function of (A) the ratio between the calculated and the standard expression stress intensity factors; (B) relative fitting error between the calculated and standard SIF values; and (C) the ratio between the stress intensity factor range within a 95% confidence interval and the standard stress intensity factor values for 304L-SS

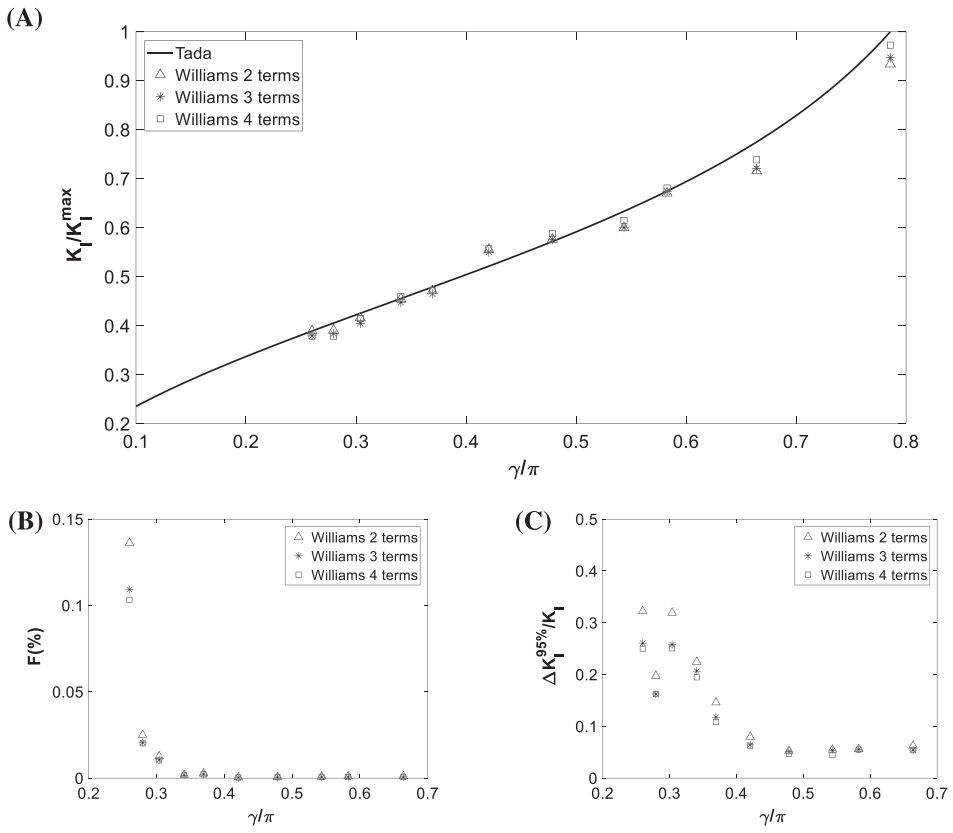

FIGURE 10 Variation with the normalized crack length and the number of terms in the Williams stress series expansion used in the calculations, as a function of (A) the ratio between the calculated and the standard expression stress intensity factors; (B) relative fitting error between the calculated and standard SIF values; and (C) the ratio between the stress intensity factor range within a 95% confidence interval and the standard stress intensity factor values for 2024-T3-Al

Equally, however, standard SIF correlations do not consider any effect of crack tip plasticity during fatigue crack growth and, consequently, their values may differ slightly from the experimental values calculated using the present hypothesis. Nonetheless, the mathematical model developed to perform the stress field fitting is also based on linear elastic fracture mechanics, thus any shielding effect due to crack tip plasticity is not explicitly considered.

The accuracy of the mathematical fitting together with the relative error in the fitting process (given by the error function defined in Equation 13) and the dimensionless range of the 95% confidence intervals around the results are illustrated in Figure 9 and 9C for the 304L alloy and in Figure 10B,C for the 2024-T3 alloy. These parameters in both materials show similar trends with a higher fitting error of between 0.4% and 0.7% at shorter crack lengths, followed by an exponential decrease to a stable lower value of ≈0.005%. It is believed that these initial higher values seen with short cracks (normalized crack lengths between 0.1 and 0.15) reflect the influence on the initial crack tip field of residual stresses generated during notch machining. In all cases, the maximum error was <1%. The upper limit of the model in terms of normalized crack length, as indicated in Figures 9 and 10, is around 0.5 for 304L alloy and 0.7 for the 2024-T3 alloy. This upper limit occurs because the displacement fields at longer crack lengths are not adequately described by the Williams crack field equations, since the specimen ligament was fully plastic. Thus, a limitation on applicability of the proposed model arises from excessive plasticity (large-scale yielding conditions) in the remaining uncracked ligament in the specimen.

However, the results obtained clearly illustrate the ability of the proposed differential geometry method to characterize crack tip fields on non-planar elements through a two-dimensional planar model.

In addition to a quantitative evaluation of the proposed method in terms of the calculation of SIFs, it is useful to show a direct comparison between the displacement values measured at the fitting locations superimposed on the reconstructed 3D surface displacement field obtained using Williams' analytical model with the fitting coefficients obtained at various normalized crack lengths (as shown in Figures 11 and 12). These figures clearly illustrate three aspects of the proposed model (the binormal displacement in the figures A.1 to A.3 and the tangential displacement in figures B.1 to B.3). Firstly, the number of terms used in the Williams stress expansion does not have any significant effect on the observed agreement between the experimental data and the reconstructed displacement field. Secondly, at short crack lengths, data dispersion is higher than seen for longer cracks and, as previously discussed, this is attributed to

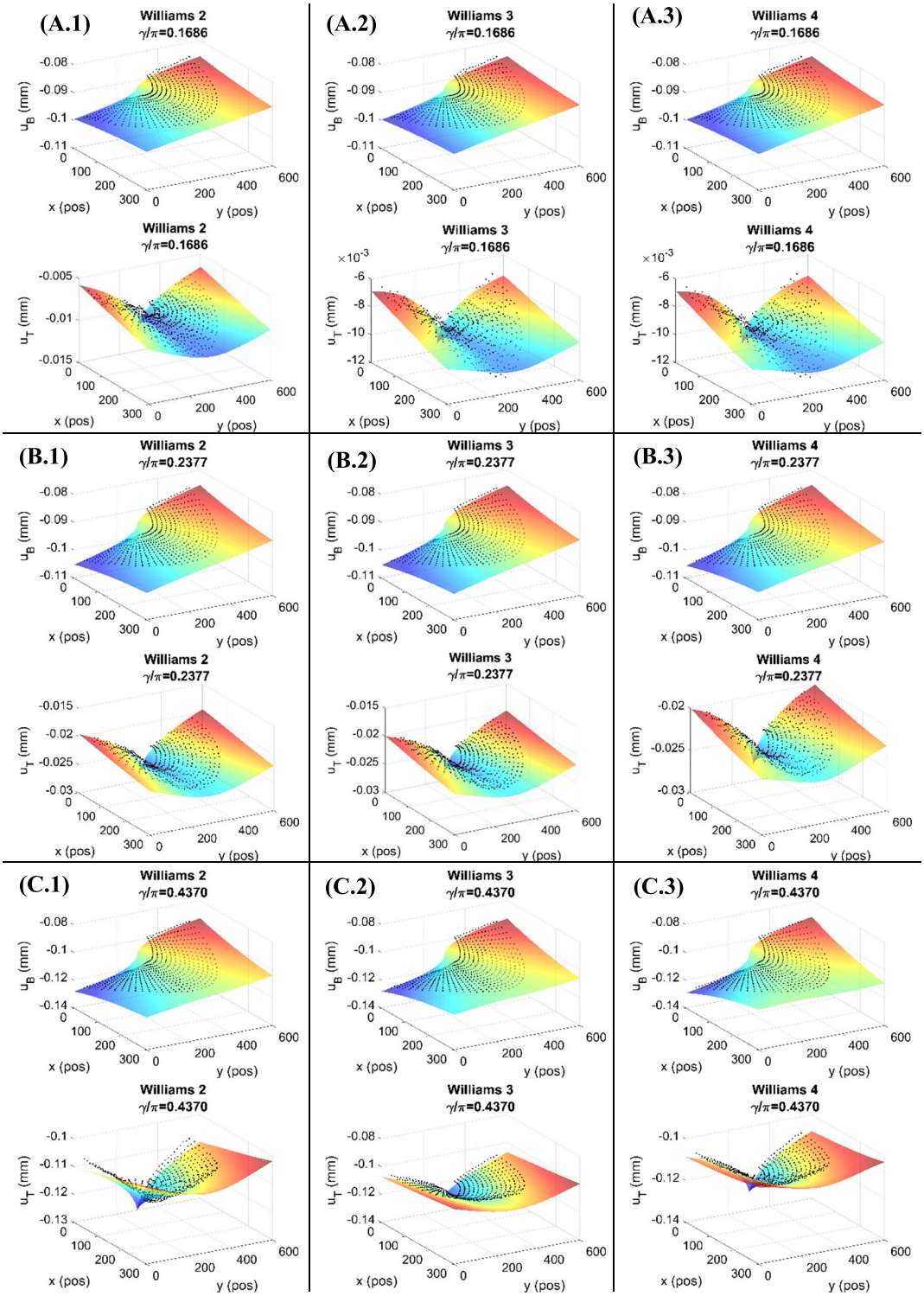

FIGURE 11 304L alloy: Comparison between the experimentally measured and the fitted crack tip displacement fields (tangential and binormal) as a function of normalized crack length and the number of terms used in the mathematical fitting; (A), (B), and (C) refer to normalized crack lengths γ/π, of 0.1686, 0.2377, and 0.4370, while 1, 2, and 3 identify the number of stress expansion terms used, that is, 2, 3, and 4 [Colour figure can be viewed at wileyonlinelibrary.com]

notch-induced residual stresses. Finally, as crack length increases, the tangential component changes more significantly than the binormal component and this is attributed to the influence of *T*-stress, whose value increases as the uncracked ligament is reduced (far-field boundary effect).[32]

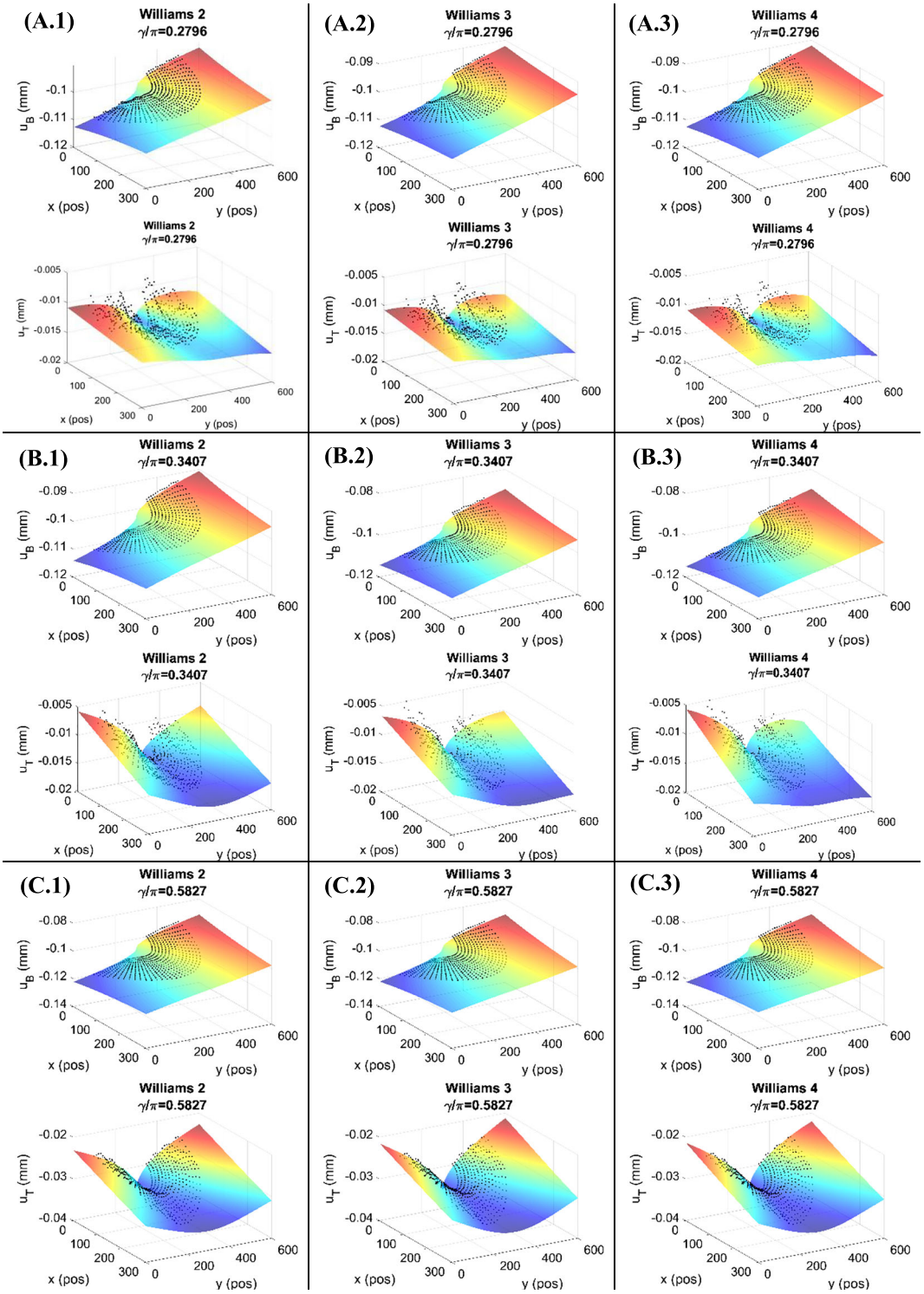

FIGURE 12 2024-T3 alloy: Comparison between the experimentally measured and the fitted crack tip displacement fields (tangential and binormal) as a function of normalized crack length and the number of terms used in the mathematical fitting; (A), (B), and (C) refer to normalized crack lengths γ/π, 0.2796, 0.3407, and 0.5827, while 1, 2, and 3 identify the number of stress expansion terms used, that is, 2, 3, and 4 [Colour figure can be viewed at wileyonlinelibrary.com]

To summarize this work, experimentally measured 3D displacement fields have been compared using a mathematically fitted 2D model, in order to demonstrate that the specimen surface experiences plane stress conditions. Using the fitting coefficients obtained in the process, the tangential and binormal stresses were

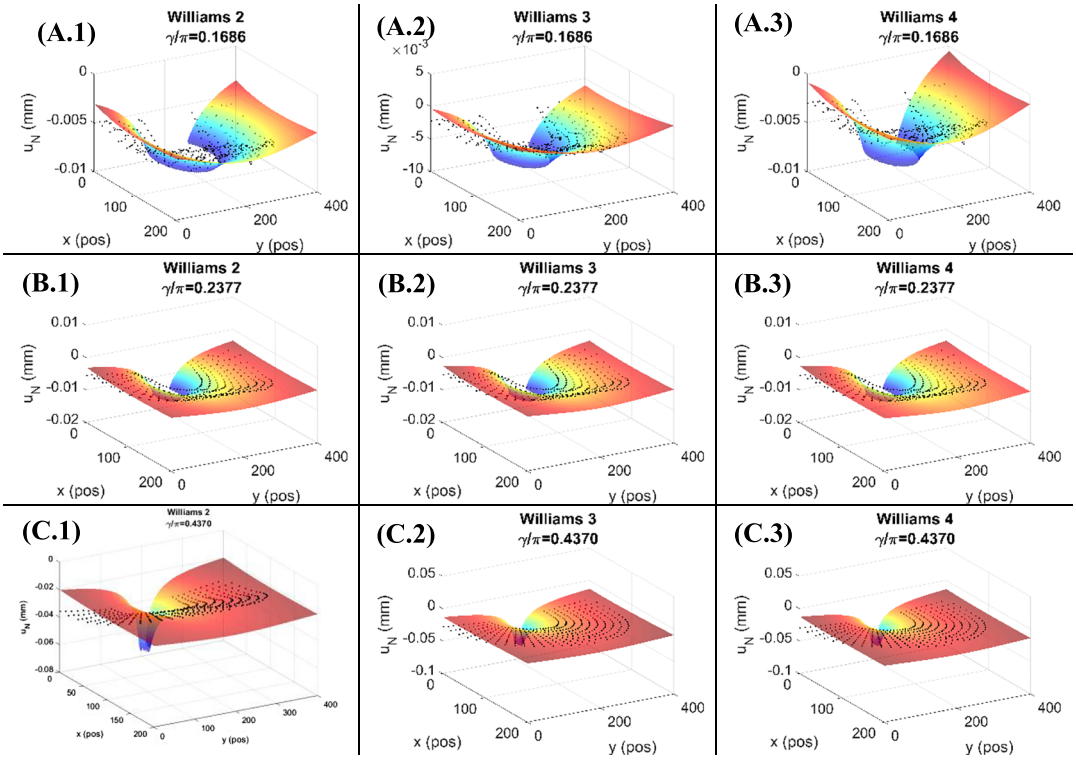

FIGURE 13 304L alloy: Comparison between measured and fitted normal displacements as a function of the normalized crack length and the number of terms used in the mathematical fitting; (A), (B), and (C) refer to normalized crack lengths of 0.1686, 0.2377, and 0.4370, while 1, 2, and 3 identify the number of stress expansion terms used, that is, 2, 3, and 4 [Colour figure can be viewed at wileyonlinelibrary.com]

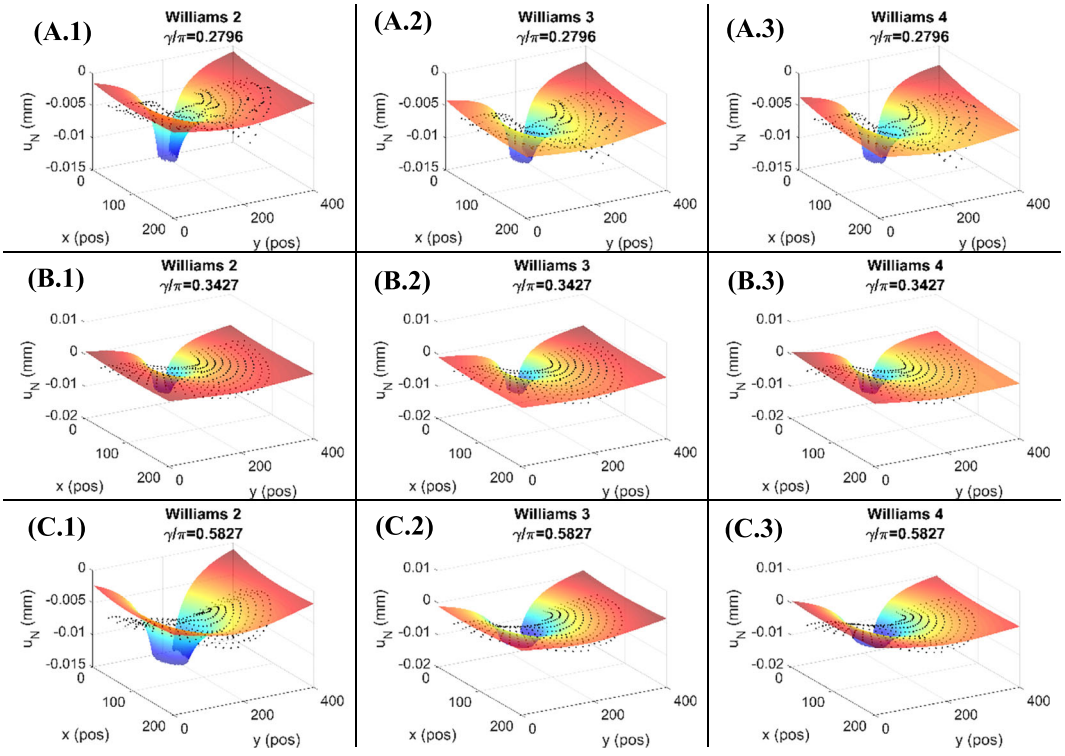

FIGURE 14 Comparison between measured and fitted normal displacements as a function of the normalized crack length and the number of terms used in the mathematical fitting; (A), (B), and (C) refer to normalized crack lengths of 0.2796, 0.3427, and 0.5827, while 1, 2, and 3 identify the number of stress expansion terms used, that is, 2, 3, and 4 [Colour figure can be viewed at wileyonlinelibrary.com]

calculated, and hence, the normal component of the stress could be found (Equation 9). In this case, the variable z_n represents the radial direction (for the particular geometry evaluated, this is the radius of the sample, 13.4 and 12.7 mm for the 304L alloy and the 2024-T3 alloy, respectively). Figures 13 and 14 show a comparison between the measured and calculated displacement field in the radial direction, and similar trends are observed in both materials. The scatter in the experimental data at shorter crack lengths reflects the influence of the residual notch manufacturing stresses, as the magnitude of the measured normal displacements was particularly small for the case of short cracks (values close to 1 μm) which emphasizes the effect of any noise arising during differentiation of the data. For longer cracks, the noise is very significantly reduced as the magnitude of the measured displacements increases. The mean relative fitting error was calculated as 7.45% and 11.25% for the stainless steel and the aluminum alloy, respectively. While these values are significantly higher than the equivalent error found in the binormal and tangential components, they seem reasonable in view of the fact that the order of magnitude of this displacement component is much lower than for the binormal or tangential, and hence, the presence of noise is more significant. Regarding the higher error in the aluminum alloy, scatter was higher due to the lower applied load levels, and in consequence, the lower displacement values.

6 | CONCLUSIONS

A novel technique has been presented in this paper for the characterization of crack tip fields on non-flat and developable surfaces. It combines a two-dimensional crack tip field model with differential geometry, and the results obtained demonstrate that crack tip fields at the surface on non-planar geometries can be accurately characterized via a modified two-dimensional planar model. In terms of SIF, the field shape and relative fitting error results demonstrate a high level of agreement between the measured and fitted displacement fields. The present paper has presented an analysis of the proposed technique under pure Mode I loading. Extending the analysis to mixed mode cracking is an obvious next step but has increased complexity due to such mixed mode phenomena such as load-path dependence, arising from crack tip plasticity. The order in which the loads are applied, as well as whether they are applied in-phase or out-of-phase, therefore influence the crack path. However, the proposed method opens up the possibility of experimentally studying fatigue and fracture problems for curved surfaces that, until now, could only be addressed analytically or numerically. This paper therefore presents a powerful tool in the analysis of cracked non-planar structural components. Although there are some limitations in the plane stress assumption, the proposed technique covers a wide range of thin-walled mechanical elements with curved geometries. One of the main advantages of this method is that the approach does not require any additional experimental validation, in contrast with numerical simulations. The ability to analyze cracked components with complex geometries using full-field optical techniques in conjunction with crack field models represents a significant advance in the subject, as there is a scarcity of experimental-analytical models suitable for addressing this kind of problem.

ACKNOWLEDGMENTS

The authors want to acknowledge the financial support from Junta de Andalucía through the research project "1380786" funded by the program "Proyectos de I + D + i en el Marco del Programa Operativo FEDER Andalucía 2014-2020. Convocatoria 2020."

CONFLICT OF INTEREST

The authors declare that they have no known competing financial interests or personal relationships that could have appeared to influence the work reported in this paper.

DATA AVAILABILITY STATEMENT

The data that support the findings of this study are available from the corresponding author upon reasonable request.

NOMENCLATURE

F	relative error fitting function
G	shear modulus
κ	function of Poisson's coefficient
K_I	Mode I stress intensity factor
p	Williams' model sum index
P	axial loading
r,θ	polar coordinates
r',θ'	polar coordinates over the unwrapped surface
Q	arbitrary 3D surface point
R	mean radius of the cylindrical pipe
t	cylindrical pipe wall thickness
T_i,B_i,N_i	component of the vector along Cartesian i direction. $i=x,y,z$
u_T,u_B,u_N	displacement field components expressed in Frenet–Serret trihedron directions
u_x,u_y,u_z	components of the displacement field
ν	Poisson's coefficient

x,y,z	Cartesian coordinates
x',y'	lengths over a 3D surface
z_n	out-of-plane direction in the unwrapped plane
a_p	coefficients of Williams' model
γ	subtended half angle of the crack
ξ,η	parametrization parameters
ξ_0,η_0	integration lower limits of the integral for computing curve lengths
σ_T,σ_B	normal stresses expressed along Frenet–Serret trihedon directions
σ_{0x}	non-singular stress in the x direction
σ_x,σ_y	normal components of the plane stress tensor
$\vec{e_x},\vec{e_y},\vec{e_z}$	unitary vectors in Cartesian axes
$\vec{\rho}$	position vector
$\vec{T},\vec{B},\vec{N}$	Frenet–Serret trihedon components

ORCID

Alonso Camacho-Reyes https://orcid.org/0000-0002-7524-0039
Jose M. Vasco-Olmo https://orcid.org/0000-0002-2250-2306
Francisco A. Diaz https://orcid.org/0000-0003-0467-542X

REFERENCES

1. Nishida SI. *Failure Analysis in Engineering Applications*. Elsevier; 1992.
2. Westergaard HM. Bearing pressures and cracks. *J Appl Mech*. 1939;61(2):49-53. doi:10.1115/1.4008919
3. Irwin GR. Analysis of stresses and strains near the end of a crack traversing plate. *J Appl Mech*. 1957;24(3):361-370. doi:10.1115/1.4011547
4. Williams ML. On the stress distribution at the base of a stationary crack. *J Appl Mech*. 1957;24(1):109-114. doi:10.1115/1.4011454
5. Hutchinson JW. Crack tip singularity fields in non-linear fracture mechanics. *Adv Fract Res*. 1982;6:2669-2684. doi:10.1016/B978-0-08-025428-9.50015-2
6. Nurse AD, Patterson EA. Determination of predominantly mode-II stress intensity factors from isochromatic data. *Fatigue Fract Eng Mater Struct*. 1993;16(12):1339-1354. doi:10.1111/j.1460-2695.1993.tb00743.x
7. Muskhelishvili NI. *Some Basic Problems of the Mathematical Theory of Elasticity*. Netherlands: Springer; 1977.
8. Pommier S, Hamam R. Incremental model for fatigue crack growth based on a displacement partitioning hypothesis of mode I elastic-plastic displacement fields. *Fatigue Fract Eng Mater Struct*. 2007;30(7):582-598. doi:10.1111/j.1460-2695.2007.01128.x
9. Christopher CJ, James MN, Patterson EA, Tee KF. Towards a new model of crack tip stress fields. *Int J Fract*. 2007;148(4):361-371. doi:10.1007/s10704-008-9209-3
10. Vasco-Olmo JM, Diaz FA, Patterson EA. Experimental evaluation of shielding effect on growing fatigue cracks under overloads using ESPI. *Int J Fatigue*. 2016;83:117-126. doi:10.1016/j.ijfatigue.2015.10.003
11. Brewster D. On the communication of the structure of doubly refracting crystals to glass, muriate of soda, flour spar and other substances by mechanical compression and dilatation. *Philos Mag*. 1816;106:156-178.
12. Schreier H, Orteu JJ, Sutton MA. *Image Correlation for Shape, Motion and Deformation Measurements: Basic Concepts, Theory and Applications*. US: Springer; 2009.
13. Thomson W. On the thermoelastic, thermomagnetic and pyroelectric properties of matters. *Philos Mag*. 1878;5(28):4-27. doi:10.1080/14786447808639378
14. Lopez-Crespo P, Shterenlikht A, Patterson EA, Yates JR, Withers PJ. The stress intensity of mixed mode cracks determined by digital image correlation. *J Strain Anal Eng Des*. 2008;43(8):769-780. doi:10.1243/03093247JSA419
15. Yates JR, Zanganeh M, Tai YH. Quantifying crack tip displacement fields with DIC. *Eng Fract Mech*. 2010;77(11):2063-2076. doi:10.1016/j.engfracmech.2010.03.025
16. Vasco-Olmo JM, Diaz FA, Garcia-Collado A, Dorado-Vicente R. Experimental evaluation of crack shielding during fatigue crack growth using digital image correlation. *Fatigue Fract Eng Mater Struct*. 2015;38(2):223-237. doi:10.1111/ffe.12136
17. Vasco-Olmo JM, James MN, Christopher CJ, Patterson EA, Diaz FA. Assessment of crack tip plastic zone size and shape and its influence on crack tip shielding. *Fatigue Fract Eng Mater Struct*. 2016;39(8):969-981. doi:10.1111/ffe.12436
18. Diaz FA, Vasco-Olmo JM, Lopez-Alba E, Felipe-Sese L, Molina-Viedma AJ, Nowell D. Experimental evaluation of effective stress intensity factor using thermoelastic stress analysis and digital image correlation. *Int J Fatigue*. 2020;135:105567. doi:10.1016/j.ijfatigue.2020.105567
19. Mokhtarishirazabad M, Lopez-Crespo P, Moreno B, Lopez-Moreno A, Zanganeh M. Optical and analytical investigation of overloads in biaxial fatigue cracks. *Int J Fatigue*. 2017;100:583-590. doi:10.1016/j.ijfatigue.2016.12.035
20. Vormwald M, Hos Y, Freire JLF, Gonzales GLG, Diaz JG. Crack tip displacement fields measured by digital image correlation for evaluating variable mode-mixity during fatigue crack growth. *Int J Fatigue*. 2018;115:53-66. doi:10.1016/j.ijfatigue.2018.04.030
21. Sanders JL. Circumferential through-cracks in cylindrical-shells under tension. *J Appl Mech Asme*. 1982;49(1):103-107. doi:10.1115/1.3161948
22. Sanders JL. Analysis of circular cylindrical-shells. *J Appl Mech Asme*. 1983;50(4b):1165-1170. doi:10.1115/1.3167198
23. Tada H, Paris PC, Irwin GR. *The Stress Analysis of Cracks Handbook*. 3rded. New York: ASME Press; 2000.
24. Kobayashi S. *Differential Geometry of Curves and Surfaces*. Singapore: Springer Singapore; 2010.
25. ASTM. E 606-92: standard practice for strain-controlled fatigue testing. In: *Annual Book of ASTM Standards*. ASTM International; 1998 E-606-92.
26. Kalnaus S, Fan F, Jiang Y, Vasudevan AK. An experimental investigation of fatigue crack growth of stainless steel 304L.

Int J Fatigue. 2009;31(5):840-849. doi:10.1016/j.ijfatigue.2008.11.004

27. Correlates Solutions. (n.d.). Correlates solutions. Accessed January 20, 2021. https://www.correlatedsolutions.com/
28. Sanford RJ, Dally JW. A general method for determining mixed-mode stress intensity factors from isochromatic fringe patterns. *Eng Fract Mech*. 1979;621:621-633.
29. Dugdale DS. Yielding of steel sheets containing slits. *J Mech Phys Solids*. 1960;8(2):100-104. doi:10.1016/0022-5096(60)90013-2
30. Yoneyama S, Morimoto Y, Takashi M. Automatic evaluation of mixed-mode stress intensity factors utilizing digital image correlation. *Strain*. 2006;42(1):21-29. doi:10.1111/j.1475-1305.2006.00246.x
31. Zanganeh M, Lopez-Crespo P, Tai YH, Yates JR. Locating the crack tip using displacement field data: a comparative study. *Strain*. 2013;49(2):102-115. doi:10.1111/str.12017
32. Shahani AR, Tabatabaei SA. Effect of T-stress on the fracture of a four point bend specimen. *Mater Des*. 2009;30(7):2630-2635. doi:10.1016/j.matdes.2008.10.031

How to cite this article: Camacho-Reyes A, Vasco-Olmo JM, James MN, Diaz FA. Characterization of non-planar crack tip displacement fields using a differential geometry approach in combination with 3D digital image correlation. *Fatigue Fract Eng Mater Struct*. 2022; 1-16. doi:10.1111/ffe.13686

Received: 17 November 2021 | Revised: 9 February 2022 | Accepted: 12 February 2022

DOI: 10.1111/ffe.13681

SPECIAL ISSUE ARTICLE

FFEMS Fatigue & Fracture of Engineering Materials & Structures WILEY

Experimental evaluation of plastic wake on growing fatigue cracks from the analysis of residual displacement fields

Jose M. Vasco-Olmo[1] | **Francisco A. Díaz**[1] | **Alonso Camacho-Reyes**[1] | **Neil James**[2,3] | **Fernando V. Antunes**[4]

[1]Departamento de Ingeniería Mecánica y Minera, University of Jaén, Jaén, Spain

[2]School of Engineering, Computing and Mathematics, University of Plymouth, Plymouth, UK

[3]Department of Mechanical Engineering, Nelson Mandela Metropolitan University, Port Elizabeth, South Africa

[4]Centre for Mechanical Engineering, Materials and Processes (CEMMPRE), Department of Mechanical Engineering, University of Coimbra, Coimbra, Portugal

Correspondence
Jose M. Vasco-Olmo, Departamento de Ingeniería Mecánica y Minera, University of Jaén, Jaén, Spain.
Email: jvasco@ujaen.es

Funding information
Fundação para a Ciência e a Tecnologia, Grant/Award Number: UIDB/00285/2020; Junta de Andalucía, Grant/Award Number: 1380786

Abstract

A growing fatigue crack gives rise to a plastically deformed wake of material that envelops the crack. In this work, the plastic wake extent during fatigue crack growth is experimentally quantified by analyzing the crack tip displacement fields measured with digital image correlation. A novel technique based on use of a yield criterion is proposed that uses the undamaged state of the specimen as the reference state in the image processing. The plastic wake was identified by differentiation of the residual displacement fields obtained with a near-zero load level to avoid any rigid body motion. The plastic wake extent was then found by assuming that the boundary between the elastic and plastic regions would occur when the equivalent stress was higher than the yield stress of the material. The results presented can contribute to a better understanding of the mechanisms driving fatigue crack propagation.

KEYWORDS

digital image correlation, fatigue crack growth, plastic wake, residual displacement fields, yield criterion

1 | INTRODUCTION

During fatigue crack growth under constant amplitude loading, a cyclic plastic zone is generated at the crack tip and a region of residual tensile deformation is left along the crack surfaces as the crack propagates. This plastically deformed region, known as the plastic wake, shields the crack from the full influence of the elastic stress field that drives fatigue crack growth and induces a reduction in crack opening displacement. These effects give rise to premature contact occurring between the crack flanks during unloading.[1] This premature contact mechanism is known as plasticity-induced crack closure. It was first observed by Elber in early 1970s[2,3] and is a direct consequence of the plastic wake generated during fatigue crack growth. Experiments by Elber demonstrated that crack propagation rates are influenced not only by the conditions ahead of the crack tip but also by the nature (magnitude and position) of the contact between the crack flanks behind the tip.

Subsequent research showed that there are other mechanisms that can lead to premature contact between the crack surfaces: These include roughness-induced crack closure,[4–6] oxide-induced crack closure,[7,8] viscous

fluid-induced crack closure,[9] and phase transformation-induced crack closure.[10] Nonetheless, plasticity-induced crack closure is the most widespread and extensively investigated fatigue crack shielding mechanism. More recent work has proposed that plastic shielding of the crack tip includes influences from a compatibility-induced interfacial shear stress at the elastic–plastic boundary and the effect of crack flank contact.[11] The plastic deformation attendant on fatigue crack propagation generates a residual stress field whose components depend on the applied load history,[12] and this residual stress field also varies with load amplitude. Quantifying the residual stresses generated by a fatigue crack could therefore shed light on the relative contribution from parameters that influence fatigue crack propagation, such as the crack shielding effect, the applied load history or the stress ratio, among others. However, the study of the influence and effects of residual stresses in the plastic enclave that surrounds a fatigue crack is clearly a complex problem. This difficulty associated with experimental characterization of the plastic wake is demonstrated by the fact that, to the authors' knowledge, there is virtually no reported work on the topic. Doubts remain regarding how best to estimate the residual stresses left around a fatigue crack.

The effect of the residual stresses on fatigue crack propagation and their relaxation during fatigue cycling has, however, been investigated by a number of authors through analytical evaluation[13–15] and numerical studies.[16–18] These works concluded that residual stresses have a significant effect on fatigue crack propagation behavior and that aspects such as the applied load history and the stress ratio have a significant influence on the residual stress field. Therefore, a detailed description of the residual stress field must include any wake contact stresses and those generated by compatibility requirements at the boundary between the elastic and plastic regions in the specimen. These arise because Poisson's ratio is different in the two regions, as plastic deformation is a constant volume process. Such an approach is clearly more complex than simply considering a detailed description of the cyclic plastic deformation in front of the crack tip, which is, in itself, very difficult.[12]

There are various methods or techniques that can be used to measure residual stresses.[19] They are commonly grouped as destructive, semidestructive and nondestructive techniques. The most usual destructive and semidestructive techniques are incremental hole drilling[20] and the ring core technique.[21] Among the nondestructive methods, some of the most useful 3D techniques are synchrotron X-ray diffraction (XRD),[22–24] neutron diffraction,[25,26] and the ultrasonic methods. Although some work has been published that has used synchrotron diffraction to measure crack tip residual stress fields and explore the possibility of crack wake contact,[24,27,28] insufficient beam time is generally available in such experiments to quantify, in the required detail, the residual stress field or plasticity-induced wake contact. Nonetheless, a significant body of work has been published that used X-ray and neutron diffraction to identify crack tip deformation fields and residual stresses. Examples include the work by Korsunsky et al.[29] who presented an overview of experimental and modeling studies of fatigue crack growth rates in Ti-6Al-4V alloy, Coules et al.[30] who used neutron diffraction to obtain full-field strain measurements and linked this with finite element analysis to demonstrate that the effect of residual stresses on the crack growth resistance curve in 7475-T751 alloy could be understood using elastic–plastic fracture mechanics, and Salvati et al.[31] who studied the changes in fatigue crack propagation following a single compressive underload using synchrotron XRD and digital image correlation (DIC). Besides the above techniques, other localized techniques capable to evaluate residual stress are high-resolution electron back scatter diffraction (HR-EBSD), focused ion beam–DIC (FIB-DIC),[32] or nanoscale-focused synchroton XRD.[33]

Nowadays, DIC is a well-established optical technique used in research on fracture mechanics and fatigue crack propagation. It allows crack tip displacement fields to be measured with high resolution and accuracy.[34] DIC has been previously used successfully by some authors of the current work in such areas as the estimation of stress intensity factors (SIFs),[35] evaluation of fatigue crack shielding and the effect of overloads on fatigue crack growth,[36,37] characterization of the fatigue crack growth rates,[38] quantification of the size and shape of crack tip plastic zone,[39] or measurement of crack tip opening displacement (CTOD) as a characterizing parameter for fatigue crack propagation.[40]

In the present work, DIC was applied to measuring residual displacement fields for fatigue cracks subject to constant amplitude loading in order to quantify the plastic wake left behind the crack tip. Residual displacements were measured using a novel method that considered the undamaged state of the specimen as the reference state in the image processing. To the author's knowledge, this is the first time that DIC has been used in this way to obtain the residual displacement fields in a fracture problem. The undamaged state image is then correlated with other images acquired at a load level close to zero, for various crack length values. This avoids including any extraneous rigid body motion in the analysis. In addition, the use of the undamaged state of the specimen allows identification of the accumulated damage during fatigue crack propagation. The effects of the applied load history

or load changes during fatigue cycling on fatigue crack growth rates can be deduced from the analysis of the residual displacement fields, which can potentially contribute to an improved understanding of the mechanisms driving fatigue crack propagation.

The technique for identifying the plastic wake applies a yield criterion to the stress fields that are obtained from the strain fields estimated by differentiating the residual displacement fields measured via DIC. The plastic wake extent is identified as that region where the equivalent stress is higher than the yield stress of the material.

2 | EXPERIMENTAL WORK

Two compact tension (CT) specimens (Figure 1A) were manufactured from a sheet of commercially pure Grade 2 titanium with a thickness of 1 mm and tested under constant amplitude fatigue with a maximum load of 750 N at stress ratio values of 0.1 and 0.6. The equivalent values of SIF at maximum load are 19 and 47 MPa·m$^{1/2}$, corresponding with crack lengths of 3 and 9.5 mm, respectively. These crack lengths represent the notch and the longest crack studied, where SIF values are approaching the fracture toughness of the material. The chemical composition for Grade 2 titanium is given in Table 1, and the tensile data are provided in Table 2.

Both sides of the two specimens were prepared so as to allow simultaneous measurements of the displacement fields by DIC on one side and crack length on the other. The side used for DIC was sprayed with a random black speckle pattern over a white background (Figure 1B), while the other side of the specimens was ground and polished to allow tracking of the crack tip position with a macrozoom lens (MLH-10X EO).

An Instron Electropuls E3000 electrodynamic machine was used for fatigue testing at a frequency of 10 Hz. A CCD camera, fitted with a macrozoom lens similar to the one used to track crack tip position, gave increased spatial resolution in the region surrounding the crack tip and was positioned perpendicularly to the side of the specimens. Fatigue cycling was periodically paused to allow data acquisition at different crack lengths and to obtain an image at near-zero loads.

The CCD camera used to view the speckled surface was set up to give a field of view of 17.3 × 13 mm (a resolution of 13.7 μm/pixel) with the crack path located at the center of the image. A fiber optic ring light was placed around the zoom lens to illuminate the specimen surface and in this way capture higher quality images.

3 | EXPERIMENTAL QUANTIFICATION OF PLASTIC WAKE

As noted above, the technique presented in this work is based on applying a yield criterion to the residual displacement data that fatigue crack growth leaves in its wake. Although 2D-DIC was used in this work, any technique that allows displacement fields to be obtained would be applicable. The sequential procedure is described in the following paragraphs.

In the first step, the residual displacement fields that remain around the crack tip at near-zero load are measured, and these incorporate effects of both the applied loads and those induced by plasticity as a consequence of crack propagation. Measuring the displacement fields at a near-zero load level avoids incorporating into the subsequent analysis any rigid body motion that might have arisen during the loading half cycle. In this work, 10 N was the load level used to define the unloaded state of the specimen since it was the lowest load that could be reliably applied with the load cell on the testing machine and represents only 1.3% of the maximum load in the

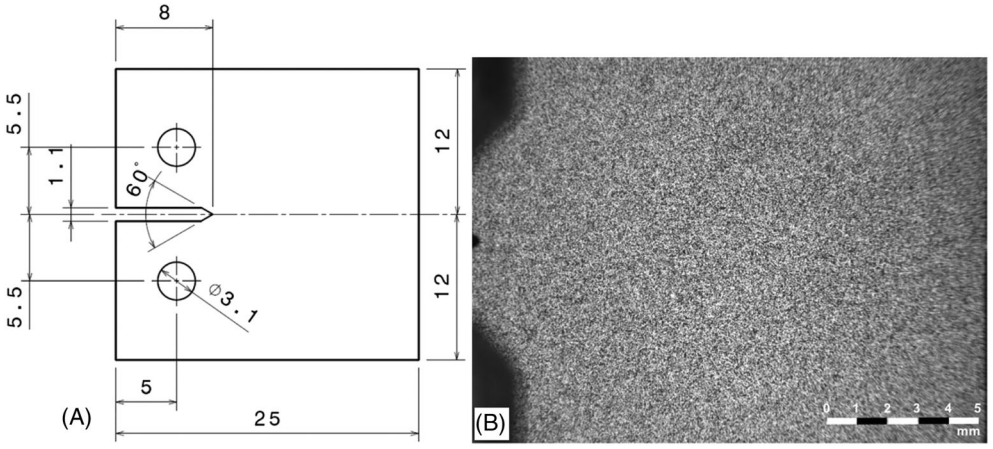

FIGURE 1 (A) Dimensions of the CT specimens (mm). (B) Illustration of the speckle pattern sprayed onto the specimen surface for making DIC measurements

Element (wt%)	N	C	H	Fe	O	Ti
Requirement	≤0.05	≤0.08	≤0.015	<0.20	≤0.20	Balance
Result	<0.01	0.01	0.002	0.10	0.12	Balance

TABLE 1 Chemical composition for commercially pure titanium grade 2

Parameter	E (GPa)	UTS (MPa)	σ_{ys} (MPa)	ε_f (%)	ν
Value	105	448	390	20	0.33

TABLE 2 Measured mechanical properties

fatigue cycle. A particularly innovative aspect of this work is that residual displacement fields at each crack length were obtained by comparison with the unloaded state that was analyzed using the undamaged state of the specimen as a reference. Figure 2 shows an example of the horizontal and vertical residual displacement maps obtained with a crack 9.2 mm long tested at $R = 0.6$.

In the second step, the strain fields at the crack tip are determined by differentiation of the residual displacement fields using the Green–Lagrange strain tensor (pages 88–91 of Mechanics of Solids book[41]) because it considers second-order terms and is hence more accurate than expressions that use only first-order terms. This strain tensor is given as follows:

$$\begin{pmatrix} \varepsilon_{xx} \\ \varepsilon_{yy} \\ \varepsilon_{xy} \end{pmatrix} = \begin{pmatrix} \frac{\partial u}{\partial x} \\ \frac{\partial v}{\partial y} \\ \frac{\partial u}{\partial y} + \frac{\partial v}{\partial x} \end{pmatrix} + \frac{1}{2} \begin{pmatrix} \frac{\partial u}{\partial x} & 0 & \frac{\partial v}{\partial y} & 0 \\ 0 & \frac{\partial u}{\partial y} & 0 & \frac{\partial v}{\partial y} \\ \frac{\partial u}{\partial y} & \frac{\partial u}{\partial x} & \frac{\partial v}{\partial y} & \frac{\partial v}{\partial x} \end{pmatrix} \begin{pmatrix} \frac{\partial u}{\partial x} \\ \frac{\partial u}{\partial y} \\ \frac{\partial v}{\partial x} \\ \frac{\partial v}{\partial y} \end{pmatrix}. \tag{1}$$

Therefore, the Green–Lagrange tensor includes the linear infinitesimal tensor for small strains (first term in Equation 1) and the nonlinear terms for large strains (second term in Equation 2).

Once the residual strains have been obtained, the residual stress fields can be calculated using Hooke's law:

$$\begin{aligned} \sigma_{xx} &= \frac{E}{1-\nu^2}\left(\varepsilon_{xx} + \nu\varepsilon_{yy}\right), \\ \sigma_{yy} &= \frac{E}{1-\nu^2}\left(\varepsilon_{yy} + \nu\varepsilon_{xx}\right), \\ \sigma_{xy} &= 2G\varepsilon_{xy}, \end{aligned} \tag{2}$$

where $G = E/2(1+\nu)$ is the shear modulus and E and ν are the Young's modulus and the Poisson's ratio of the material, respectively.

The equivalent stress is then calculated by applying a suitable yield criterion. In this work, the von Mises criterion was used as it has been shown to be the most appropriate for a ductile material.[42,43] A first-order estimate of the size and shape of the plastic wake can then be obtained by connecting all points where the yield criterion is met, that is, where the equivalent stress is higher than the yield stress of the material. Figure 3A shows this region in a binary black–white image, and this identifies the monotonic plastic wake generated during fatigue propagation that surrounds the crack. A greater than or equal operator (>=) was used to convert the equivalent stress map analyzed to a binary black and white format.

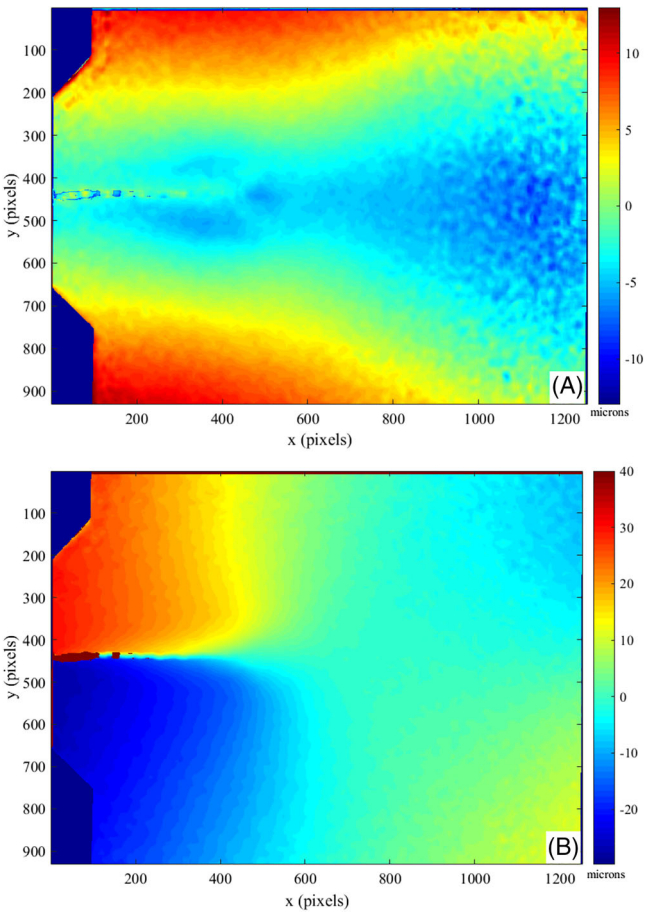

FIGURE 2 Residual displacement maps for a specimen tested at $R = 0.6$ and a crack length of 9.2 mm. (A) Horizontal and (B) vertical [Colour figure can be viewed at wileyonlinelibrary.com]

Thus, the yield stress of the material was used to the right operand to return true if the equivalent stress was greater or equal to the yield stress and false otherwise.

The current work considers the area of the plastic wake as a variable that contains useful information on crack growth, and the method clearly provides an efficient and powerful way for making quantitative measurements of the monotonic plastic wake region. Once this region has been identified, its area can be calculated using the function "bwarea," implemented in Matlab®. This function is used to estimate the area of objects in a black–white binary image. To use this function, the equivalent stress map analyzed must be converted to a binary black–white format before the area of the plastic wake can be estimated. Figure 3B shows the plastic wake region isolated from the rest of the map and on a completely black background to assist in estimation of its area. The area of the plastic wake in this case of a 9.2-mm-long crack grown at $R = 0.6$ is obtained as 13.51 mm^2.

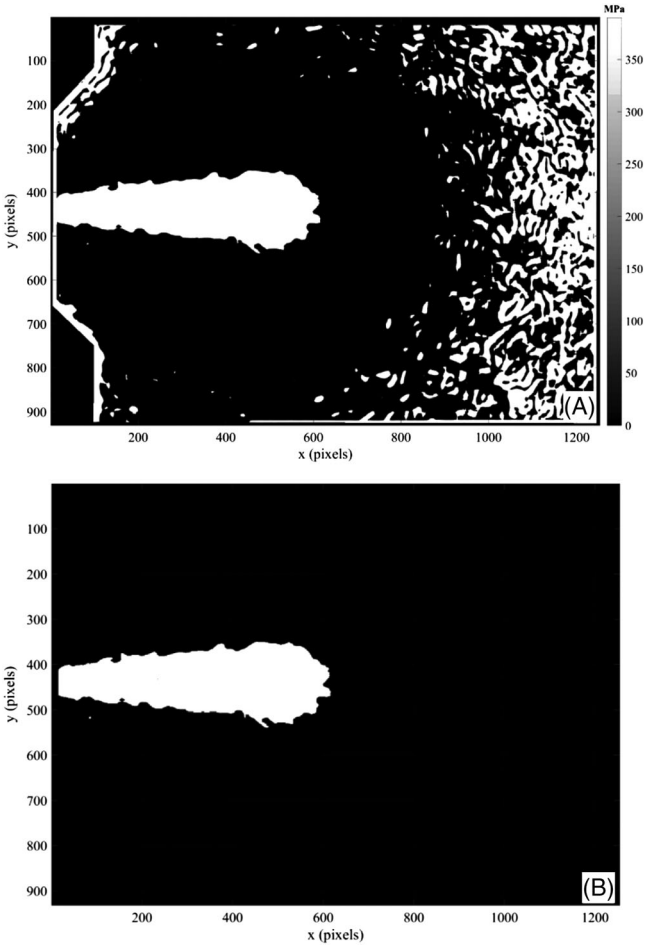

FIGURE 3 Illustrations showing (A) the equivalent stress map for the region where its value exceeds the yield stress for a crack 9.2 mm long tested at $R = 0.6$; (B) the extent of the plastic wake isolated from the rest of the stress map to assist in quantifying its area

4 | EXPERIMENTAL RESULTS

The procedure described above was applied to all the data for the various crack lengths analyzed, and this allowed the evolution of the plastic wake to be followed as the crack grew. Figure 4 shows a plot of crack length as a function of the number of cycles for the two specimens tested at stress ratio values of 0.1 and 0.6. In addition, Table 3 details the specific values of number of cycles and the crack length in both cases. Figure 5 shows plastic wake data corresponding to three different crack lengths for each of the two specimens. The figure shows data for crack lengths of 4.8, 6.9, and 9.4 mm for the specimen tested at $R = 0.1$ and 4.7, 6.9, and 9.2 mm for the specimen tested at $R = 0.6$. The area of the plastic wake obtained in each case is also given.

The plastic wake outline contour can also be found and plotted in a single figure to show the evolution of the plastic wake during fatigue crack propagation as shown in Figure 6. The contours shown for the specimen tested at $R = 0.1$ correspond to those cases of Table 3 between Datapoints 1 (5000 cycles, 3.5 mm crack) and 23 (13,500 cycles, 9.4 mm crack), while for the specimen tested at $R = 0.6$, the contours correspond to the cases between Datapoints 5 (25,000 cycles, 3.4 mm) and 25 (74,000 cycles, 9.2 mm crack). A gradual increase of the plastic wake is observed as the crack propagates that agrees with the gradual development of plasticity and, consequently, the residual stresses, in a growing fatigue crack at constant amplitude loading cycle. These results demonstrate that the plastic wake can be identified and calculated from the analysis of the residual displacement fields generated during fatigue crack growth using DIC. From a direct observation of the contours, it is difficult to establish any differences among them. For this reason, trying to find a possible effect of the stress ratio, the qualitative comparison in Figure 6 can be extended to provide quantitative data through estimating the area of the plastic wake. Figure 7 shows the variation in the plastic wake area with crack length, normalized by the specimen width, for both stress ratios. The trend in the data can be fitted with a quadratic polynomial (fit coefficient of 0.997 in the case of the specimen tested at $R = 0.1$ and 0.999 for the specimen tested at $R = 0.6$), giving the following expressions that relate the plastic wake area with the normalized crack length (a/W):

$$R = 0.1: \quad A = 117.05\left(\frac{a}{W}\right)^2 - 35.73\frac{a}{W} + 3.1903. \qquad (3)$$

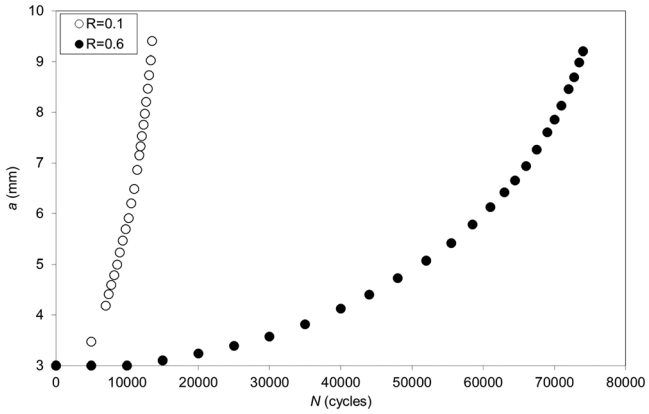

FIGURE 4 Crack length as a function of number of cycles for both specimens tested at stress ratios of 0.1 and 0.6

$$R = 0.6: \quad A = 110.84\left(\frac{a}{W}\right)^2 - 25.108\frac{a}{W} + 1.301. \qquad (4)$$

To the knowledge of the authors, no similar mathematical fitting for other parameters used in quantifying damage based on crack tip plasticity have been published in the literature. There was little difference between the plastic wake area at either stress ratio for normalized crack lengths below 0.25. This is perhaps not surprising, as the maximum stress was the same in both tests and the influence of the stress ratio would be minimized when the plastic wake area is smaller at the shorter crack lengths. A divergence in the data occurs above a/W approximately $\geq$0.30. This is likely to reflect both the

TABLE 3 Data of number of cycles and crack lengths for both tests

$R = 0.6$			$R = 0.1$		
Data	***N* (cycles)**	***a* (mm)**	**Data**	***N* (cycles)**	***a* (mm)**
0	0	3.0	0	0	3.0
1	5000	3.0	1	5000	3.5
2	10,000	3.0	2	7000	4.2
3	15,000	3.1	3	7400	4.4
4	20,000	3.2	4	7800	4.6
5	25,000	3.4	5	8200	4.8
6	30,000	3.6	6	8600	5.0
7	35,000	3.8	7	9000	5.2
8	40,000	4.1	8	9400	5.5
9	44,000	4.4	9	9800	5.7
10	48,000	4.7	10	10,200	5.9
11	52,000	5.1	11	10,600	6.2
12	55,500	5.4	12	11,000	6.5
13	58,500	5.8	13	11,400	6.9
14	61,000	6.1	14	11,700	7.1
15	63,000	6.4	15	11,900	7.3
16	64,500	6.7	16	12,100	7.5
17	66,000	6.9	17	12,300	7.8
18	67,500	7.3	18	12,500	8.0
19	69,000	7.6	19	12,700	8.2
20	70,000	7.9	20	12,900	8.5
21	71,000	8.1	21	13,100	8.7
22	72,000	8.5	22	13,300	9.0
23	72,750	8.7	23	13,500	9.4
24	73,500	9.0			
25	74,000	9.2			

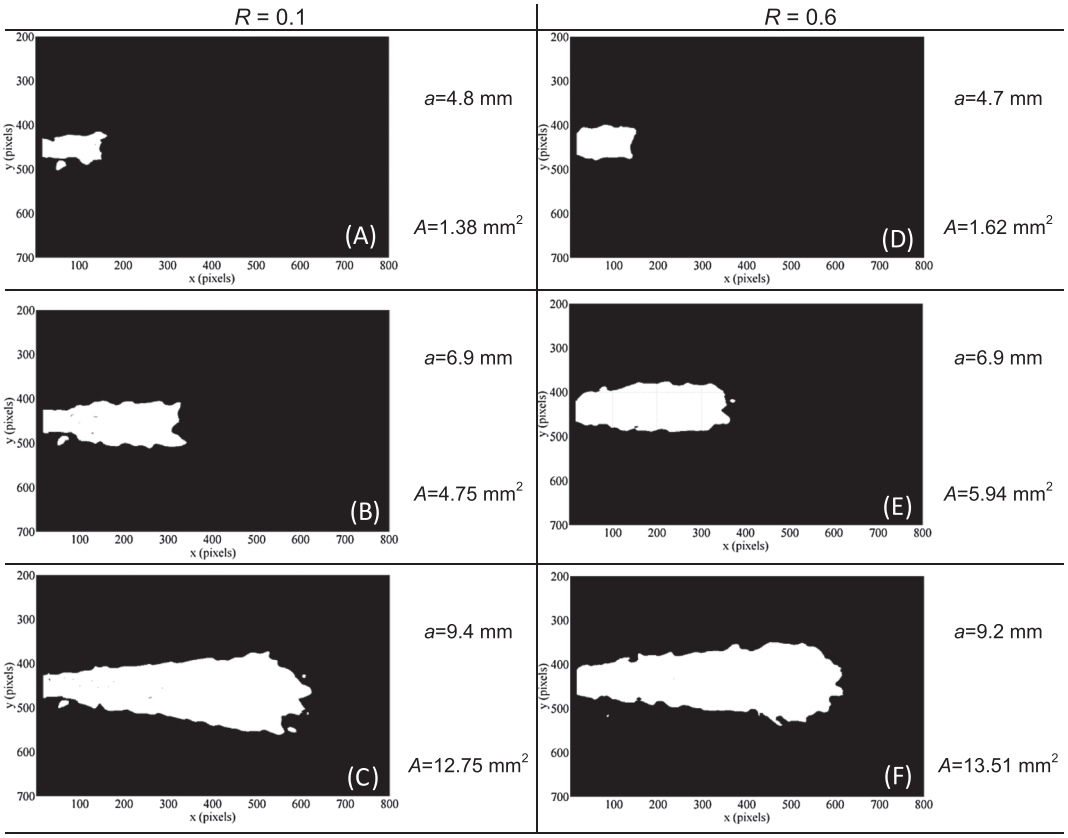

FIGURE 5 Extent of the plastic wake. Left column: data for $R = 0.1$ with crack lengths of (A) 4.8, (B) 6.9, and (C) 9.4 mm long. Right column: data for $R = 0.6$ with crack lengths (D) 4.7, (E) 6.9, and (F) 9.2 mm long

increased amount of reversed plasticity that will occur at $R = 0.1$ during the unloading half cycles and the higher mean stress in cycling at $R = 0.6$ that increases the ratcheting strain with continued cycling. This can be interpreted as leading to a smaller compressive residual stress zone in the specimen tested at $R = 0.6$ a higher residual tensile stress field along the crack path than would be the case for the specimen tested at low R ratio. Hence, the larger compressive residual stress region in the case of the specimen tested at $R = 0.1$ would cause a greater retardation effect on fatigue crack growth than for a specimen tested at R ratio of 0.6, that is, a greater level of plasticity-induced crack tip shielding. This behavior was reported in a previous work[39] where a retardation effect on fatigue propagation was observed in the case of the specimen tested at low R ratio but was not seen for a specimen tested at $R = 0.6$.

Figure 8 compares the trends in the maximum values of the residual vertical displacements (v) as a function of normalized crack length (a/W). It is observed that the values are higher in the test at $R = 0.6$ for $a/W \geq 0.3$. Thereafter, the divergence gradually increases in the results obtained at the two stress ratios. This behavior, observed in Figure 8, links well with that observed in the curves for plastic wake area given in Figure 7, and with the development of higher residual tensile stresses in the case of the specimen tested at the higher R ratio.

The experimental method for obtaining crack wake area, as outlined in this paper, has been based on the uniaxial tensile yield stress and could be further refined through use of the cyclic stress–strain curve since the plastic wake is the region plastically deformed left as a fatigue crack propagates. However, it is important to note that all discussion of results and conclusions drawn, especially on the comparison between the two stress ratios analyzed, would not be affected.

These results support the conclusions drawn by other authors[16,18,44,45] that residual stresses can significantly affect fatigue crack propagation behavior. It seems likely that studying the residual displacement fields could shed additional light on some of the effects of applied load history, or changes in the load amplitude, on fatigue crack growth rate. Further insights could also be gained on the crack wake contact phenomenon since it is, at least in part, a direct consequence of the plastic deformation left in the wake of a propagating crack.[2] Therefore, although the study of the residual displacement fields could contribute to a better understanding on the contact

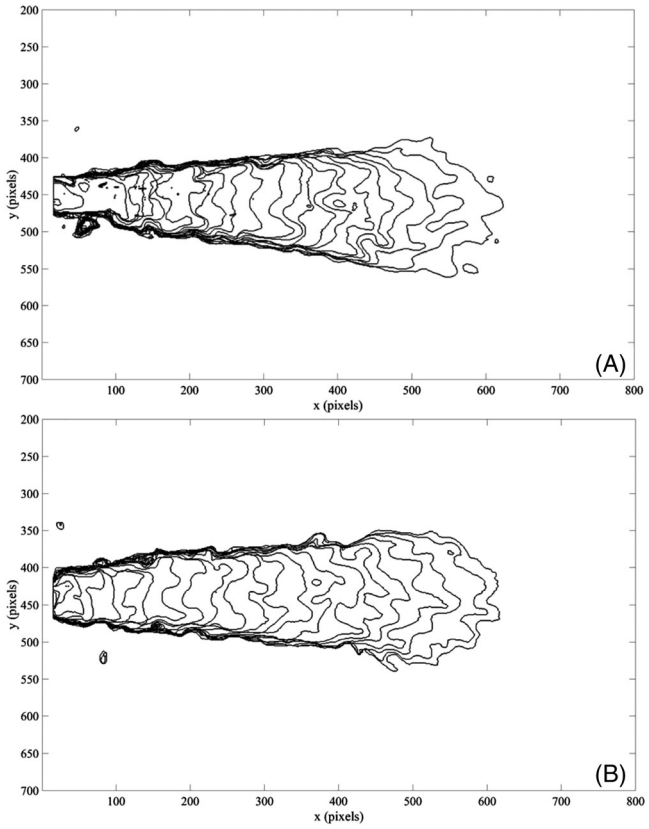

FIGURE 6 Development of the plastic wake as the crack grows for (A) $R = 0.1$ and (B) $R = 0.6$. The plastic wake contours shown, according to the data detailed in Table 3, are the following. $R = 0.1$: from Datapoint 1 (5000 cycles, 3.5 mm crack) until Datapoint 23 (13,500 cycles, 9.4 mm crack); $R = 0.6$: from Datapoint 5 (25,000, 3.4 mm crack) until Datapoint 25 (74,000, 9.2 mm crack)

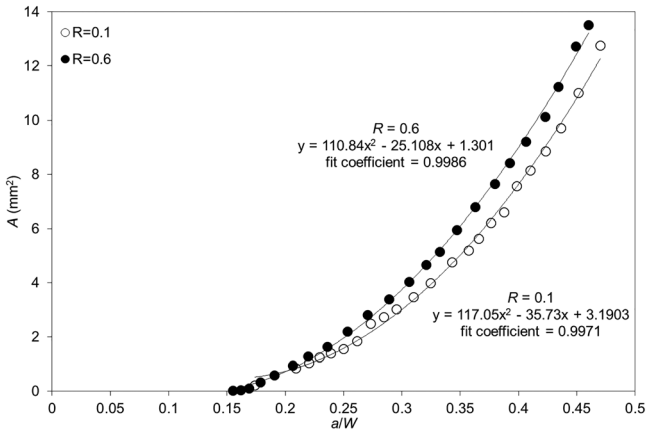

FIGURE 7 Evolution of the plastic wake area as a function of the normalized crack length for stress ratio values of 0.1 and 0.6

phenomenon between the crack flanks, further work must be performed on how the fields can be related with the shielding effect during fatigue crack propagation.

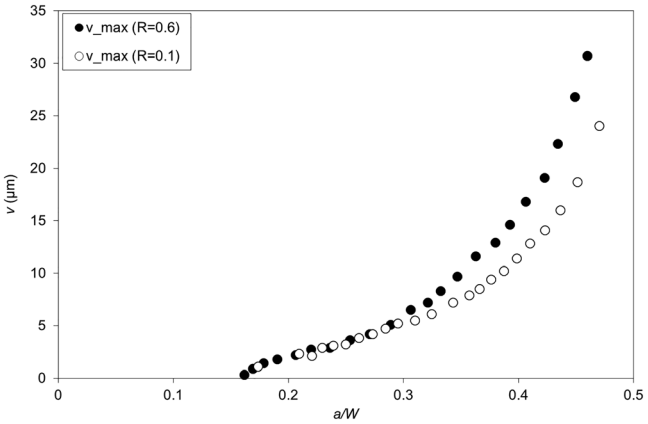

FIGURE 8 Maximum values of residual vertical displacements as a function of the normalized crack length for stress ratio values of 0.1 and 0.6

Thus, future work might explore the relationship between the plastic wake left by a growing fatigue crack and the shielding effect by using the SIFs calculated from the analysis of the residual displacement fields. In this respect, the CJP model can be useful in characterizing crack tip displacement fields due to its demonstrated ability to incorporate the shielding effects of the plastic enclave on a growing fatigue crack.[11] The discussions and conclusions drawn in this work can be extended through such additional work on investigating how the influences of shielding can be linked with the plastic wake left by a propagating fatigue crack. In addition, it is believed that the proposed methodology could be used to explore the effect of an overload on a growing fatigue crack, because the overload effect would be reflected in the residual displacement fields. Much work has been published dealing with overloads. Simpson et al.[46] provide a useful starting point on the topic.

5 | CONCLUSIONS

In this paper, a DIC-based method has been outlined that allows experimental determination of the plastic wake region that is generated by a growing fatigue crack. The area of the plastic wake has been used as a quantifying parameter for residual displacements in the wake. The experimental method was applied on two CT titanium specimens, fatigued at stress ratios of 0.1 and 0.6. For both specimens, a quadratic relationship between the plastic wake area and the normalized crack length a/W was obtained. The plastic wake region was found by differentiating the residual displacement fields obtained for a near-zero load level so as to avoid any rigid body motion that might occur during loading. In this work,

10 N was used as the reference load that defined the unloaded state of the specimen; this represents 1.3% of the maximum applied load. A particularly innovative aspect of the work is the use of the undamaged state of the specimen as the reference for image processing. Applying the von Mises yield criterion then gives the plastic wake area as that region where the equivalent stress is higher than the yield stress of the material. Stress fields were then determined from the strain fields via Hooke's law.

This work has demonstrated that is experimentally possible to measure the residual displacement fields using DIC by taking the undamaged specimen state as the reference image and correlating this field with that obtained for the unloaded state at any particular crack length during fatigue crack propagation. This opens up the possibility that the influence of prior history or changes in load amplitude can be investigated from an analysis of the residual displacement field. The technique outlined in this paper therefore offers strong potential to contribute to a better understanding of the mechanisms driving fatigue crack growth and plasticity-induced shielding.

ACKNOWLEDGMENTS

The authors want to acknowledge the financial support from Junta de Andalucía through the research project "1380786" funded by the program "Proyectos de I+D+i en el Marco del Programa Operativo FEDER Andalucía 2014-2020. Convocatoria 2020." This research is also sponsored by Portuguese national funds by Fundação para a Ciência e a Tecnologia (FCT) under the project UIDB/00285/2020.

AUTHOR CONTRIBUTIONS

The original idea was conceived by F. A. Díaz and N. James and countersigned by F. V. Antunes. J. M. Vasco-Olmo and A. Camacho-Reyes performed the experimental work, composed the fatigue tests, collected the data, and performed the processes to obtain the experimental results. All authors worked on the analysis, interpretation, and discussion of the results, where the most critical feedback was provided by F. A. Díaz, F. V. Antunes, and N. James. J. M. Vasco-Olmo took the lead in writing the original version of the manuscript, and the rest of authors contributed to its final version through their critical comments, editions, and reviews. All authors agree on the order in which their names are listed in the manuscript.

DATA AVAILABILITY STATEMENT

The data that support the findings of this study are available from the corresponding author upon reasonable request.

NOMENCLATURE

a	crack length
A	plastic wake area
CT	compact tension
DIC	digital image correlation
E	Young's modulus
G	shear modulus
N	number of cycles
R	ratio between the minimum and the maximum applied load
u, v	horizontal and vertical components of the displacement field
UTS	ultimate tensile strength
W	width of the specimen
x, y	Cartesian coordinates
ε_f	fracture strain
ε_{xx}, ε_{yy}, ε_{xy}	Cartesian components of the strain field
ν	Poisson's ratio
σ_{eq}	equivalent stress
σ_{xx}, σ_{yy}, σ_{xy}	Cartesian components of the stress field
σ_{ys}	yield stress

ORCID

Jose M. Vasco-Olmo https://orcid.org/0000-0002-2250-2306
Francisco A. Díaz https://orcid.org/0000-0003-0467-542X
Alonso Camacho-Reyes https://orcid.org/0000-0002-7524-0039
Fernando V. Antunes https://orcid.org/0000-0002-0336-4729

REFERENCES

1. Suresh S. *Fatigue of Materials*. Cambridge University Press; 1998, doi:10.1017/CBO9780511806575.
2. Elber W. Fatigue crack closure under cyclic tension. *Eng Fract Mech*. 1970;2(1):37-45. doi:10.1016/0013-7944(70)90028-7.
3. Elber W. The significance of fatigue crack closure. In: Rosenfeld M, ed. *Damage Tolerance in Aircraft Structures, ASTM STP 486*. American Society for Testing and Materials; 1971:230-242.
4. Suresh S, Ritchie RO. A geometric model for fracture surface roughness-induced crack closure during fatigue crack-growth. *J Met*. 1982;34:71.
5. Ritchie RO, Suresh S. Some considerations on fatigue crack closure at near-threshold stress intensities due to fracture surface morphology. *Metall Trans A*. 1982;13(5):937-940. doi:10.1007/BF02642409.
6. Suresh S, Ritchie RO. A geometric model for fatigue crack closure induced by fracture surface roughness. *Metall Trans A*. 1982;13(9):1627-1631. doi:10.1007/BF02644803.

7. Suresh S, White C, Ritchie RO. Oxide-induced crack closure. *J Met*. 1980;32:76.
8. Suresh S, Zamiski GF, Ritchie RO. Oxide-induced crack closure: an explanation for near-threshold corrosion fatigue crack growth behaviour. *Metall Trans A*. 1981;12(8):1435-1443. doi: 10.1007/BF02643688.
9. Endo K, Okada T, Hariya T. Fatigue crack propagation in bearing metals lining of steel plates in lubricating oil. *Bull JSME*. 1972;15(82):439-445. doi:10.1299/jsme1958.15.439.
10. Pineau AG, Pelloux RMN. Influence of strain-induced martensitic transformations on fatigue crack growth rates in stainless steels. *Metall Trans A*. 1974;5(5):1103-1112. doi: 10.1007/BF02644322.
11. James MN, Christopher CJ, Lu Y, Patterson EA. Local crack plasticity and its influences on the global elastic stress field. *Int J Fatigue*. 2013;46:4-15. doi:10.1016/j.ijfatigue.2012.04.015.
12. Pippan R, Hohenwarter A. Fatigue crack closure: a review of the physical phenomena. *Fatigue Fract Eng Mater Struct*. 2017; 40(4):471-495. doi:10.1111/ffe.12578.
13. Lang M. A model for fatigue crack growth, part II: modelling. *Fatigue Fract Eng Mater Struct*. 2000;23(7):603-618. doi: 10.1046/j.1460-2695.2000.00298.x.
14. Zhuang WZ, Halford GR. Investigation of residual stress relaxation under cyclic load. *Int J Fatigue*. 2001;23:S31-S37. doi: 10.1016/S0142-1123(01)00132-3.
15. Noroozi A, Glinka G, Lambert S. Prediction of fatigue crack growth under constant amplitude loading and a single overload based on elasto-plastic crack tip stresses and strains. *Eng Fract Mech*. 2008;75(2):188-206. doi:10.1016/j.engfracmech.2007.03.024.
16. Fischer FD, Davies W, Pippan R, Pointner P. Some comments on surface cracks in rails. *Fatigue Fract Eng Mater Struct*. 2006; 29(11):938-948. doi:10.1111/j.1460-2695.2006.01051.x.
17. González-Herrera A, Zapatero J. Numerical study of the effect of plastic wake on plasticity-induced crack closure. *Fatigue Fract Eng Mater Struct*. 2009;32(3):249-260. doi: 10.1111/j.1460-2695.2009.01335.x.
18. Predan J, Pippan R, Gubeljak N. Fatigue crack propagation in threshold regime under residual stresses. *Int J Fatigue*. 2010; 32(7):1050-1056. doi:10.1016/j.ijfatigue.2009.12.006.
19. Rossini NS, Dassisti M, Benyounis KY, Olabi AG. Methods of measuring residual stresses in components. *Mater Des*. 2012;35: 572-588. doi:10.1016/j.matdes.2011.08.022.
20. Niku-Lari A, Lu J, Flavenot JF. Measurement of residual-stress distribution by the incremental hole-drilling method. *J Mech Work Technol*. 1985;11(2):167-188. doi:10.1016/0378-3804(85)90023-3.
21. Masláková K, Trebuňa F, Frankovský P, Binda M. Applications of the strain gauge for determination of residual stresses using ring-core method. *Procedia Eng*. 2012;48:396-401. doi:10.1016/j.proeng.2012.09.531.
22. James MN, Hughes DJ, Hattingh DG, Bradley GR, Mills G, Webster PJ. Synchrotron diffraction measurement of residual stresses in friction stir welded 5383-H321 aluminium butt joints and their modification by fatigue cycling. *Fatigue Fract Eng Mater Struct*. 2003;27(3):187-202. doi: 10.1111/j.1460-2695.2004.00736.x.
23. James MN, Newby M, Hattingh DG, Steuwer A. Shot peening of steam turbine blades: residual stresses and their modification by fatigue. *Procedia Eng*. 2010;2(1):441-451. doi: 10.1016/j.proeng.2010.03.048.
24. Salvati E, Zhang H, Fong KS, Song X, Korsunsky AM. Separating plasticity-induced closure and residual stress contributions to fatigue crack retardation following an overload. *J Mech Phys Solids*. 2017;98:222-235. doi:10.1016/j.jmps.2016.10.001.
25. Allen AJ, Hutchings MT, Windsor CG, Andreani C. Neutron diffraction methods for the study of residual stress fields. *Adv Phys*. 1985;34(4):445-473. doi:10.1080/00018738500101791.
26. James MN, Ting S-P, Bosi M, Lombard H, Hattingh DG. Residual strain and hardness as predictors of the fatigue ranking of steel welds. *Int J Fatigue*. 2009;31(8-9):1366-1377. doi:10.1016/j.ijfatigue.2009.03.006.
27. James MN, Hattingh DG, Hughes DJ, Wei L-W, Patterson EA, da Fonseca JQ. Synchrotron diffraction investigation of the distribution and influence of residual stresses in fatigue. *Fatigue Fract Eng Mater Struct*. 2004;27(7):609-622. doi: 10.1111/j.1460-2695.2004.00789.x.
28. Thielen M, Schaefer F, Gruenewald P, et al. In situ synchrotron stress mappings to characterize overload effects in fatigue crack growth. *Int J Fatigue*. 2019;121:155-162. doi:10.1016/j.ijfatigue.2018.12.013.
29. Korsunsky AM, Song X, Belnoue J, et al. Crack tip deformation fields and fatigue crack growth rates in Ti-6Al-4V. *Int J Fatigue*. 2009;31(11):1771-1779. doi:10.1016/j.ijfatigue.2009.02.043.
30. Coules HE, Horne GCM, Abburi Venkata K, Pirling T. The effects of residual stress on elastic-plastic fracture propagation. *Mater Des*. 2018;143:131-140. doi:10.1016/j.matdes.2018.01.064.
31. Salvati E, Sui T, Zhang H, et al. Elucidating the mechanism of fatigue crack acceleration following the occurrence of an underload. *Adv Eng Mater*. 2016;18(12):2076-2087. doi: 10.1002/adem.201600069.
32. Salvati E, O'Connor S, Sui T, Nowell D, Korsunsky AM. A study of overload effect on fatigue crack propagation using EBSD, FIB-DIC and FEM methods. *Eng Fract Mech*. 2016;167: 210-223. doi:10.1016/j.engfracmech.2016.04.034.
33. Romano-Brandt L, Salvati E, Le Bourhis E, Moxham T, Dolbnya IP, Korsunsky AM. Nano-scale residual stress depth profiling in Cu/W nano-multilayers as a function of magnetron sputtering pressure. *Surf Coat Technol*. 2020;381:125142 doi: 10.1016/j.surfcoat.2019.125142.
34. Sutton MA, Orteu JJ, Schreier HW. *Image Correlation for Shape, Motion and Deformation Measurements: Basic Concepts, Theory and Applications*. Springer Science+Business Media, LLC; 2009.
35. Du Y, Díaz FA, Burguete RL, Patterson EA. Evaluation using digital image correlation of stress intensity factors in an aerospace panel. *Exp Mech*. 2011;51(1):45-57. doi: 10.1007/s11340-010-9335-5.
36. Vasco-Olmo JM, Díaz FA, García-Collado A, Dorado R. Experimental evaluation of crack shielding during fatigue crack growth using digital image correlation. *Fatigue Fract Eng Mater Struct*. 2015;38(2):223-237. doi:10.1111/ffe.12136.
37. Vasco-Olmo JM, Díaz FA. Experimental evaluation of the effect of overloads on fatigue crack growth by analysing crack tip displacement fields. *Eng Fract Mech*. 2016;166:82-96. doi: 10.1016/j.engfracmech.2016.08.026.
38. Yang B, Vasco-Olmo JM, Díaz FA, James MN. A more effective rationalisation of fatigue crack growth rate data for various

specimen geometries and stress ratios using the CJP model. *Int J Fatigue*. 2018;114:189-197. doi:10.1016/j.ijfatigue.2018.05.027.

39. Vasco-Olmo JM, James MN, Christopher CJ, Patterson EA, Díaz FA. Assessment of crack tip plastic zone size and shape and its influence on crack tip shielding. *Fatigue Fract Eng Mater Struct*. 2016;39(8):969-981. doi:10.1111/ffe.12436.
40. Vasco-Olmo JM, Díaz FA, Antunes FV, James MN. Characterisation of fatigue crack growth using digital image correlation measurements of plastic CTOD. *Theor Appl Fract Mech*. 2019;101:223-341. doi:10.1016/j.tafmec.2019.03.009.
41. Singh AK. *Mechanics of Solids*. Prentice-Hall of India; 2010.
42. Christensen RM. How do Mises and Tresca fit. In *Failure Theory for Materials Science and Engineering*. Oxford University Press; 2021. Accessed on 03/11/2021. http://www.failurecriteria.com/misescriteriontr.html
43. Taylor GI, Quinney H. The plastic distortion of metals. *Philos Trans Royal Soc A*. 1931;230(681-693):323-362. doi:10.1098/rsta.1932.0009.
44. Ritchie RO. Mechanisms of fatigue crack propagation in metals, ceramics and composites: role of crack tip shielding. *Mater Sci Eng A*. 1988;16(1):15-28. doi:10.1016/0025-5416(88)90547-2.
45. Suresh S. Fatigue crack deflection and fracture surface contact: micromechanical models. *Metall Trans A*. 1985;16(2):249-260. doi:10.1007/BF02816051.
46. Simpson CA, Kozuki SC, Lopez-Crespo P, Mostafavi M, Connolley T, Withers PJ. Quantifying fatigue overload retardation mechanisms by energy dispersive X-ray diffraction. *J Mech Phys Solids*. 2019;124:392-410. doi:10.1016/j.jmps.2018.10.020.

How to cite this article: Vasco-Olmo JM, Díaz FA, Camacho-Reyes A, James N, Antunes FV. Experimental evaluation of plastic wake on growing fatigue cracks from the analysis of residual displacement fields. *Fatigue Fract Eng Mater Struct*. 2022;1-11. doi:10.1111/ffe.13681

International Journal of Fatigue 162 (2022) 106942

Contents lists available at ScienceDirect

International Journal of Fatigue

journal homepage: www.elsevier.com/locate/ijfatigue

Towards a new methodology for the characterisation of crack tip fields based on a hybrid computational approach

A. Camacho-Reyes [a], J.M. Vasco-Olmo [a,*], M.N. James [b,c], F.A. Diaz [a]

[a] Departamento de Ingeniería Mecánica y Minera, Universidad de Jaén, Jaén, Spain
[b] School of Engineering, Computing and Mathematics University of Plymouth, Plymouth, England, United Kingdom
[c] Department of Mechanical Engineering, Nelson Mandela Metropolitan University, Port Elizabeth, South Africa

ARTICLE INFO

Keywords:
Crack tip fields
Crack tip characterising parameters
CJP model, hybrid optimisation
Crack tip location, genetic algorithm

ABSTRACT

This work presents a hybrid optimisation technique for the simultaneous calculation of crack tip characterising parameters and its spatial location, which can significantly affect the characterising parameters if the position used is inaccurate. The hybrid technique combines initial use of a genetic algorithm to obtain a well-conditioned set of initial parameter values that is then passed to an interior point optimisation algorithm for subsequent fast optimisation. Use of the hybrid technique is also amenable to easy automation. The capability of the technique is demonstrated using the CJP crack tip field model, with digital image correlation (DIC) being used to measure the 2D crack tip displacement field. This model was chosen, not only for its demonstrated sensitivity to accuracy in crack tip location, but also for its proven utility in providing effective crack growth correlation in the presence of plasticity-induced shielding across a wide range of growth rates. The results obtained from the hybrid technique are shown to be reliable through comparison with results obtained using other established techniques.

1. Introduction

The development of full field optical techniques, such as Digital Image Correlation (DIC) [1], Thermoelastic Stress Analysis (TSA) [2] or Digital Photoelasticity [3], in combination with analytical mathematical models describing crack tip fields, have made it possible to experimentally determine characterising parameters, including the stress intensity factor (SIF) and T-stress, and to better understand their role in the mechanisms driving fatigue crack growth. The Multi-Point Over Deterministic Method (MPODM) developed by Sanford and Dally [4] has underpinned a large body of work aimed at improving understanding of fatigue crack growth where these optical techniques have been combined with various crack tip field models, e.g. the Irwin-Westergaard approach [5,6], Williams' expansion series model [7], complex Fourier analysis [8] the Muskhelishvili approach [9], a displacement partitioning model [10], and the model developed by Christopher James and Patterson (known as CJP model) [11–13]. Depending on what crack tip field (stresses, strains or displacements) is under consideration, as well as which variables and parameters are considered in the fitting process, the mathematical problem can be either linear or nonlinear.

Analytical methods can be used to solve the problem if the mathematical formulation is linear, while numerical methods are necessary to solve cases where the mathematical formulation is nonlinear. Published literature includes a number of studies where displacement data is used in crack tip field research without considering the crack tip location as an initially unknown quantity. For instance, Lopez-Crespo et al [14] employed the mathematical formulation developed by Nurse and Patterson [8] which is based on Muskhelishvili's complex potentials [9], Yates et al [15] used Williams' expansion series [7] and Vasco-Olmo et al [16] compared the Irwin-Westergaard [5,6], Williams' [7], and CJP models [11–13]. All of these studies considered only the crack tip singularity parameters as unknowns in the analytical definition of the crack tip field and hence a system of linear equations was obtained that could be easily solved using direct methods. In addition, in those cases where displacement data and purely elastic models (Westergaard, Williams or Muskhelishvili) are employed, the methodology is robust in terms of the crack tip position chosen for the fitting process, since a crack tip value close to the real one can provide reliable results in terms of singularity characterising parameters.

However, the CJP model is very sensitive to crack tip location [17]. The fitting process of the model to experimental data is therefore more complex than is the case for the other models, since the approach models a novel 'plastic inclusion' that explicitly incorporates the interaction effects at the boundary between the plastic and elastic regions [13]. Including the crack tip location as an unknown in the mathematical

* Corresponding author.
E-mail address: jvasco@ujaen.es (J.M. Vasco-Olmo).

https://doi.org/10.1016/j.ijfatigue.2022.106942
Received 14 January 2022; Received in revised form 25 March 2022; Accepted 18 April 2022
Available online 22 April 2022

Nomenclature

u, v	Displacement field
G	Shear modulus
κ	Poisson's coefficient function
j	Imaginary unit
A, B, C, E, F	CJP model coefficients
$z = x + jy$	Complex variable
K_F, K_R, K_S	CJP model stress intensity factors
T_x, T_y	Non-singular stresses
u_e, v_e	Experimental displacement field
$x_{SD}^{min}, x_{SD}^{max}, y_{SD}^{min}, y_{SD}^{max}$	Search domain bounds
$\Delta x, \Delta y$	Crack tip coordinates
u_0, v_0, R_x, R_y	Rigid body motion coefficients
$\Re$	Complex number real part
$\Im$	Complex number imaginary part
K_N	Nominal stress intensity factor
a	Crack length
W	Specimen width
t	Specimen thickness
d	Euclidean distance between crack tip locations
t_{GA}	GA optimisation time
t_{IP}	IP optimisation time
t_T	Total optimisation time

formulation of the model creates a nonlinear problem. Several techniques can be found in published literature that solve a similar problem. For instance, Yoneyama et al [18] simultaneously determined mixed-mode stress intensity factors, crack-tip location, and higher-order terms in the series expansion of displacement fields and rigid-body displacement components using a nonlinear least squares approach based on the Newton–Raphson method [7]. They used the Newton-Raphson method to solve the problem and the initial solution used values of singularity parameters provided by empirical correlations. Zanganeh et al [19] used the DIC displacement field around a crack tip in work to compare the influence of various methods that they used to locate the crack-tip position, on the values they found for stress intensity factors. They compared two constrained Newton type methods: the trust-region reflective Newton method and the quasi-Newton method; an unconstrained direct search method: the Nelder–Mead Simplex method; a constrained genetic algorithm; and a constrained Pattern Search (PS) method. They showed that the Newton type methods were less accurate compared with the direct search methods studied, while the PS technique was found to be the most accurate. Furthermore, the PS technique was found to be about twice as fast as the Simplex method and ten times faster than a Genetic Algorithm for the same computing hardware and the same input data. Yang et al [20] used the Levenberg-Marquardt algorithm [21] taking as the initial solution those values previously determined through linear fitting.

However, these techniques are not optimum for fitting experimental data to the mathematical formulation of the CJP model due to several factors. The CJP model describes the singularity field in terms of five coefficients that are related to the effect on the global elastic field of the plastic enclave that surrounds the crack. Empirical correlations for these coefficients are not available in the literature and finding suitable initial values for them is not straightforward. Equally, estimating an initial solution by linear fitting is not suitable in the case of the CJP model. A sensitivity analysis to evaluate how the crack tip position could affect the SIF calculation and the quality of the fit was performed by Vasco-Olmo [17] by analysing simulated horizontal and vertical displacement fields. An error of a few pixels in crack tip location was therefore intentionally introduced, leading to the conclusion that the CJP model was rather sensitive to variations in the crack tip position, particularly in the case of the x-coordinate. However, variations in the y-coordinate of the crack tip were not so critical. The ability of the CJP model in accurately characterising the plastic zone and plasticity-induced shielding has been widely demonstrated [16,22–25], and it would be useful to develop a technique that could be easily automated, and that allows an accurate crack tip position and corresponding characterisation of the crack tip fields to be obtained.

This work therefore describes a robust, fast, geometry-independent technique, developed for the CJP model, that calculates crack tip singularity parameters and accurately locates the crack tip position, and that is capable of automation. The proposed methodology addresses the problem through an optimisation approach that combines a stochastically chosen initial solution obtained via a genetic algorithm, with a deterministic gradient-based interior point method. The combination of these two methods provides a powerful tool for accurate calculation of the crack tip singularity parameters (SIFs and T-stresses), as well as correctly determining the crack tip location. The genetic algorithm (GA) generates a well-conditioned initial solution for the nonlinear problem while the interior point (IP) algorithm significantly reduces the high computational time usually associated with GA solutions. A further benefit is that the absence of the requirement for an initial problem solution allows automating the process, which is very useful in the

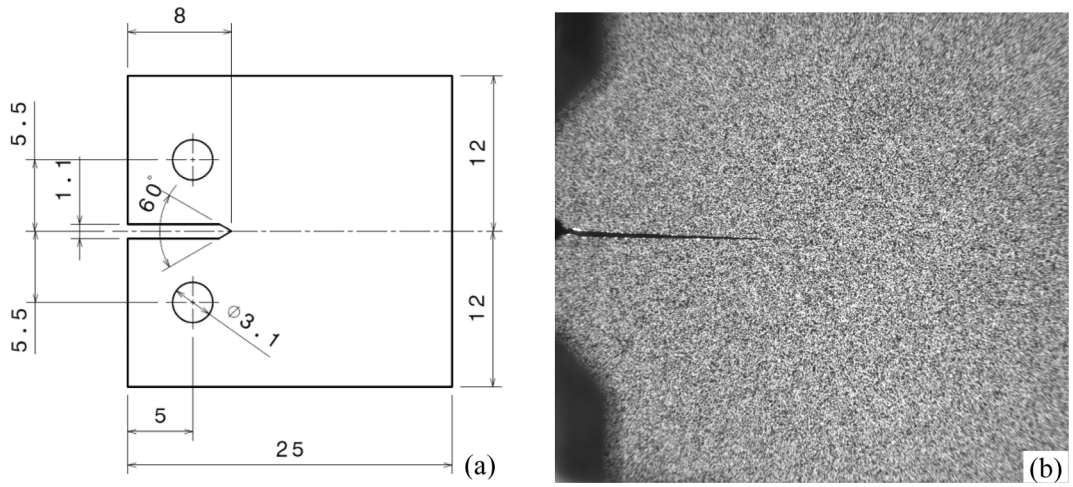

Fig. 1. (a) Dimensions of the CT specimen (mm). (b) Speckle pattern sprayed onto the specimen surface for the DIC work.

Table 1
Chemical composition of commercially pure titanium Grade 2.

Element (wt %)	Fe	C	N	O	H	Ti
Specification	< 0.20	≤ 0.08	≤ 0.05	≤ 0.20	≤ 0.015	Balance
Specimen	0.10	0.01	<0.01	0.12	0.002	Balance

Table 2
Mechanical properties for the commercially pure titanium Grade 2 tested in this work.

Parameter	E (GPa)	UTS (MPa)	σ_{ys} (MPa)	ε_f (%)	ν
Value	105	448	390	20	0.33

analysis of crack tip fields.

2. Theoretical fundamentals

2.1. Mathematical description of crack tip fields in the CJP model

The CJP model [11–13] is a linear elastic mathematical model for describing crack-tip fields based on Muskhelishvili's complex potentials [8,9]. However, the important innovation in the model is that the elastic analysis explicitly incorporates possible influences of the plastic enclave that surrounds the crack on the global elastic field. It does this by solving for any effects of plasticity-induced wake contact [26] and the necessary compatibility-induced strains at the elastic–plastic boundary. These latter strains arise from the change in Poisson's ratio between the elastic and plastic regions. The crack tip displacement fields defined by the CJP model, assuming that $D = -E$, i.e. asymptotic behaviour of the stress along crack flanks, is given by equation (1) [13]:

$$2G(u+vj) = \kappa\left[-2(B+2E)z^{\frac{1}{2}} + 4Ez^{\frac{1}{2}} - 2Ez^{\frac{1}{2}}\ln(z) - \frac{C-F}{4}z\right] - z\left[-(B+2E)\overline{z}^{\frac{-1}{2}} - E\overline{z}^{\frac{-1}{2}}\overline{\ln(z)} - \frac{C-F}{4}\right] - \left[A\overline{z}^{\frac{1}{2}} + E\overline{z}^{\frac{1}{2}}\overline{\ln(z)} - 2E\overline{z}^{\frac{1}{2}} + \frac{C+F}{2}\overline{z}\right] \quad (1)$$

In this equation, G is shear modulus, u and v are the horizontal and vertical field components, respectively, j is $\sqrt{-1}$, κ is a function of Poisson's coefficient that depends on whether the crack experiences plane stress or plain strain conditions [13], z is a complex variable ($x + jy$) and A, B, C, E and F are the coefficients governing the crack tip singularity. The overbar denotes the complex conjugate and ln denotes the natural logarithm operator. Coefficients A, B and E are related to the three stress intensity factors defined by the model. The opening mode stress intensity factor that drives the crack forwards, denoted by K_F, a retardation stress intensity factor that acts against the crack in its plane, denoted by K_R and a shear-induced stress intensity factor denoted by K_S. C and F are the coefficients that determine non-singular stresses along the crack growth (x) and crack opening directions (y), respectively. These crack tip parameters are given by equations (2) to (6) [13].

$$K_F = \sqrt{\frac{\pi}{2}}(A - 3B - 8E) \quad (2)$$

$$K_R = -(2\pi)^{\frac{3}{2}}E \quad (3)$$

$$K_S = \sqrt{\frac{\pi}{2}}(A + B) \quad (4)$$

$$T_x = -C \quad (5)$$

$$T_y = -F \quad (6)$$

2.2. Optimisation algorithms for nonlinear multidimensional problems

2.2.1. Genetic algorithms

Genetic algorithms (GA) [22] as used in mathematical optimisation

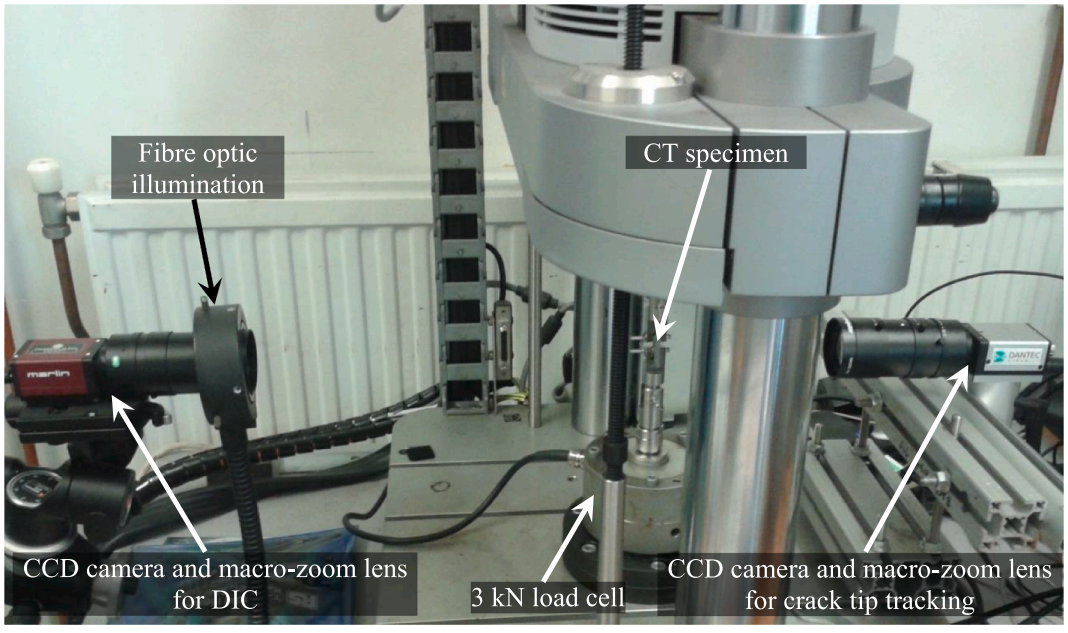

Fig. 2. Experimental set-up used in the fatigue testing and for data acquisition.

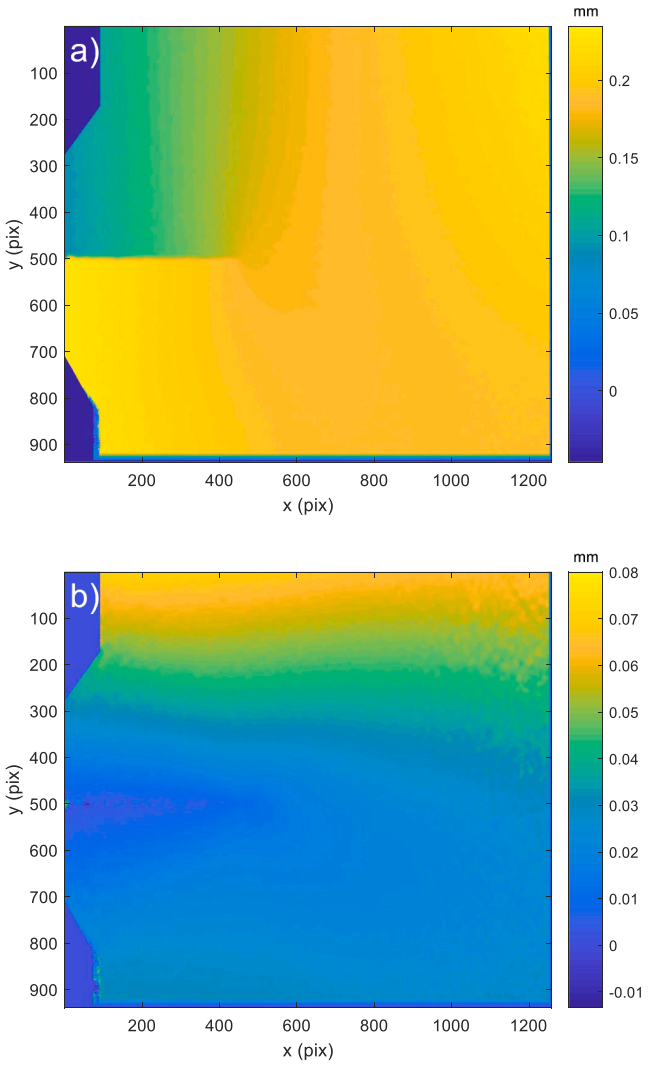

Fig. 3. (a) Vertical and (b) horizontal displacement maps measured with DIC for a 9.40 mm crack at a load of 750 N.

are heuristic, direct search, constrained or unconstrained, and zero order methods based on concepts derived from Darwinian species evolution theory. In a general way, GAs operate as follows. An initial solution population is created stochastically and these "individuals" are evaluated via an objective or fitness function to determine their 'survival' value. According to evolutionary theory, the fittest progenitors must produce the fittest subsequent generation. Thus, the best individuals in the population, according to their fitness value, are selected to create a new and improved generation by replacing the least fit individuals. a better solution is then generated by combining the best progenitors through crossover and mutation operations. This process is repeated through subsequent generations until a solution is found that satisfies the fitness function to the desired accuracy. In mathematical optimisation, GAs are employing in highly nonlinear problems to find global minima. This kind of algorithm is computationally expensive since they usually require a large number of iterations. However, these methods are the only ones that can ensure that a global minimum solution is found. Their advantage is that they do not require accurate initial solutions due to their stochastic and evolutionary nature, compared with other deterministic methods where a well-chosen initial solution is required to achieve a global minimum. GA techniques are often used in conjunction with a second technique to find local minima; this is useful when several global minima have similar values.

2.2.2. *Interior point algorithms*

Interior point (IP) algorithms for nonlinear optimisation [23–27],

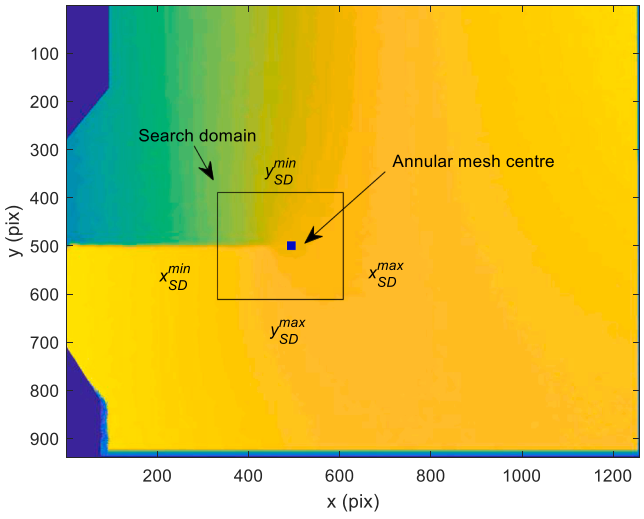

Fig. 5. Search domain in the vertical component of the displacement field.

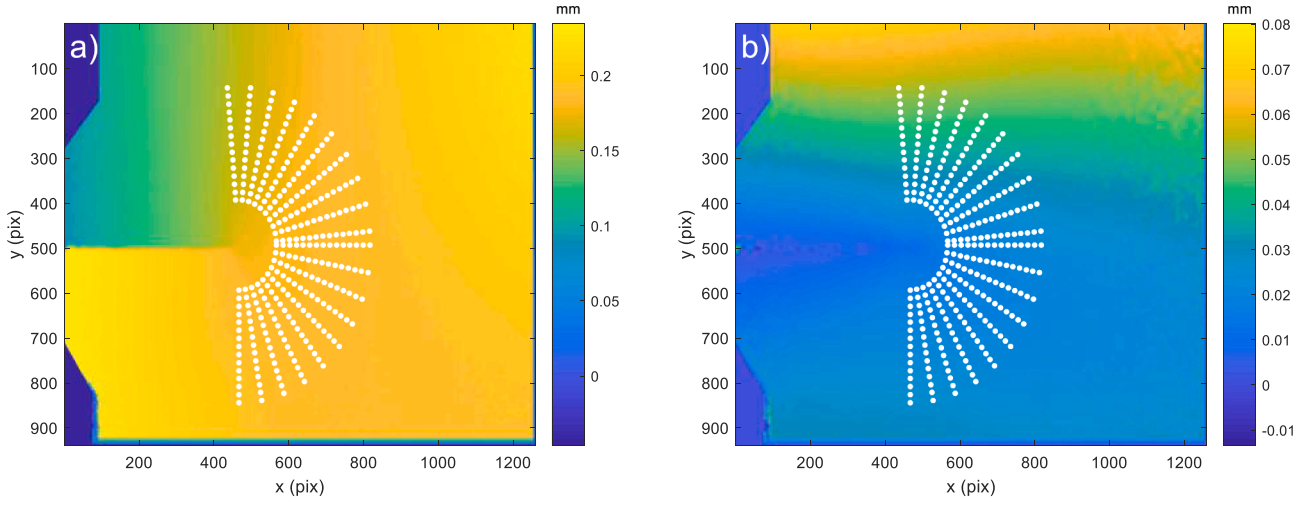

Fig. 4. Annular mesh superimposed on a) vertical and b) horizontal displacement maps for a crack length of 9.4 mm at maximum load.

also known as barrier methods, are deterministic, gradient-based methods for constrained optimisation problems. These methods are considered the most suitable for problems involving large-scale nonlinear optimisation [28]. IP methods were conceived as alternatives to the Dantzig-Simplex method [29] for solving large linear problems. They provide a fast optimisation if the initial solution is well conditioned. The IP algorithm transforms inequality constraints via a barrier logarithmic term that is added to the objective function to include deleted inequality constraints. The problem therefore remains an equality constrained problem whose solution is simpler. Hence, by applying the first order optimality conditions [30] to the barrier problem, together with equality constraints, allows a nonlinear equation system to be obtained which can be addressed using Newton's method. Further detail about how each sub-problem is addressed are given in section 4.1. Additional information about the IP algorithm scheme, as well as the relaxation factors employed in this work, can be found in the paper published by Waltz et al [27].

2.2.3. Hybrid approach: Combining heuristic and deterministic methods

As already mentioned, the most effective way of solving large scale, highly nonlinear optimisation problems, where an initial well-conditioned solution is difficult to find, is via the combination of a genetic algorithm with a second optimisation technique. A hybrid approach is developed in this work that initiates the fitting process with a GA, to avoid the necessity of including an initial well-conditioned solution. After a certain number of iterations, when the GA solution is relatively close to the global minimum, the IP technique is incorporated which uses as its initial solution the one provided by the GA. This approach avoids the disadvantages of the two individual optimisation techniques, as the GA starts with ill-conditioned data and the computation time is reduced by the IP method.

3. Experimental work

A 1 mm thick sheet of commercially pure Grade 2 titanium was used to manufacture a compact tension (CT) specimen (with the geometry shown in Fig. 1a) that was tested in constant amplitude loading at a stress ratio value of 0.6 with a maximum load of 750 N. Table 1 shows the specified chemical composition for Grade 2 titanium, along with the data measured from the specimen sheet; mechanical property data are given in Table 2.

Both surfaces of the specimen were prepared to enable simultaneous measurements of the displacement fields via digital image correlation (DIC) on one side and crack length via a zoom charge-coupled device (CCD) camera on the other. The side of the specimens for the DIC measurements was sprayed with a random black speckle pattern (shown in Fig. 1b) using an airbrush over a white background. In addition, the opposite side of the specimen was ground and polished to enable tracking the crack tip position using a second 1 Mpixel charge-coupled device (CCD) camera (Dantec Dynamics) fitted with a macro-zoom lens (Edmund Optics, model MLH-10X EO) (Fig. 2). In addition, the crack length measurements were used during fatigue testing in order to provide uniform crack increments between DIC measurements of the crack tip displacement field.

Fatigue testing used an Electropuls E3000 electrodynamic machine (Fig. 2) at a loading frequency of 10 Hz. DIC measurements were made with a 1 Mpixel CCD camera (Allied Vision Technology, model Marlin F-146B/C) mounted perpendicular to the specimen surface. The camera system used a macro-zoom lens, similar to the one used in crack tip tracking, to image crack propagation with a resolution of 13.7 μm/pixel (field of view of 17.3 × 13 mm). A fibre optic light ring placed around the macro zoom lens provided illumination of the specimen surface (also shown in Fig. 2).

During fatigue testing, the cyclic loading was periodically paused to acquire a sequence of crack tip displacement images at uniform load increments of 25 N, representing 30 images for both the loading and unloading half-cycles. Image processing used the Vic-2D program from Correlated Solutions with 25 pixels as the subset size and a step value of 1 pixel, to give the maximum resolution for the displacement maps. Fig. 3 shows an example of the horizontal and vertical displacement fields for a crack length of 9.40 mm and a load of 750 N.

4. Data processing

4.1. Displacement data and optimisation procedure

The u_e and v_e data used in the fitting process was obtained from the displacement fields measured ahead of the crack tip outside the high strain plastic zone near the crack tip. In order to do this, an annular data collection region was defined (Fig. 4) via an inner and outer radius, the sweep angle and the mesh centre. The inner radius was calculated by estimating the plastic zone size, so to avoid including the zone of crack tip plasticity. The estimation method described by Vasco-Olmo et al [31] in experimental work on estimation of both size and shape of the plastic zone from displacement field analysis was used for this. The outer radius of the annulus must capture the full crack tip singularity zone. This was ensured using to the criterion described by Vasco-Olmo et al [32], based on the observation of the vertical displacement maps (Fig. 3a), where the singularity dominance zone is recognised via the displacement contours being straight and perpendicular to the crack. As the dominance ceased, these contours start to tilt (see Fig. 3a). Nonetheless, the chosen outer radius size is not a sensitive parameter and an overestimation of the singularity zone value does not significantly affect the results. The mesh sweep angle was chosen as 180 degrees.

If the crack tip location had not been included in the optimization problem, the selected position of the mesh centre would be a critical parameter, as crack tip models generally consider that the crack tip corresponds with the coordinate origin. In the current approach, the mesh centre was simply chosen so as to place the mesh approximately in the singularity zone. During the fitting process, the spatial position of the crack tip changes until an optimum solution is found.

A search domain was defined that enclosed the crack tip location in order to reduce the GA computational time (Fig. 5). The exact crack tip location is not easily determined from displacement field maps; however, a confidence region can be easily established simply from observation of the displacement maps. The search domain was therefore defined by the centre of the annular mesh and an offset value as shown in Fig. 5. A sensitivity analysis of the search domain size was made that demonstrated that increasing its size increased computation times without modifying the computed singularity parameters or the crack tip location. A size of around 10% of the crack length was eventually chosen to give reasonable computation times and allow analysing the crack path during the optimisation process. The inclusion of the search domain into the optimisation problem adds two constraints (upper and lower bounds for x and y) that enclose the crack tip coordinates.

Once fitting data had been extracted from the displacement field maps and the constraints were defined, the optimisation problem was formulated as shown in equation (7):

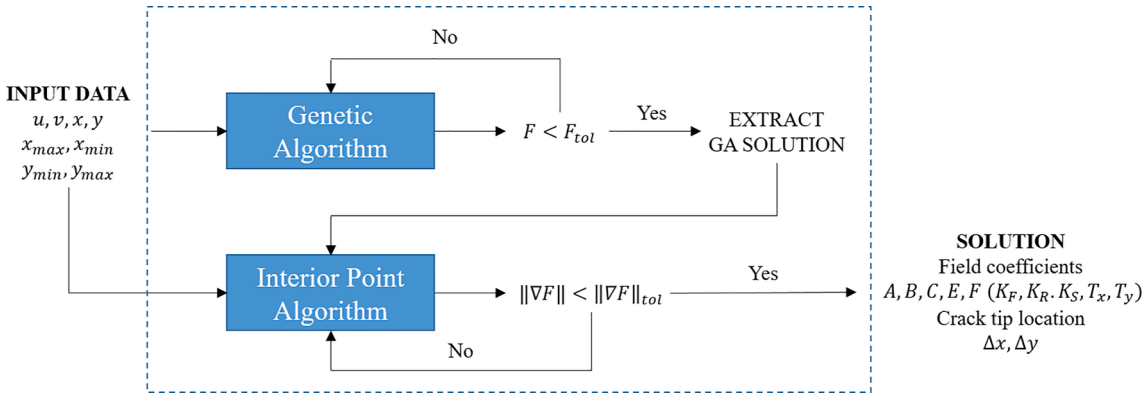

Fig. 6. Hybrid optimisation scheme.

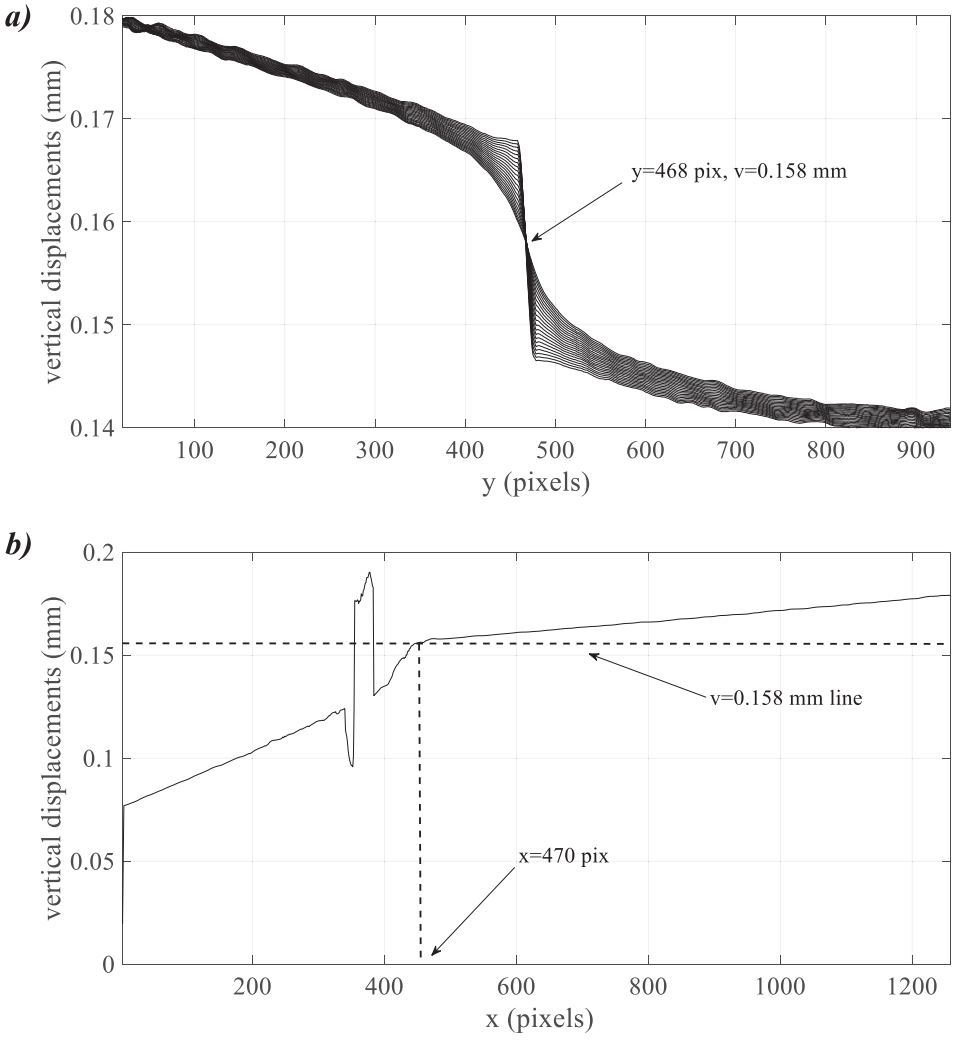

Fig. 7. Plots showing the methodology used to identify the position of the crack tip in the y (a) and $\times$ (b) directions.

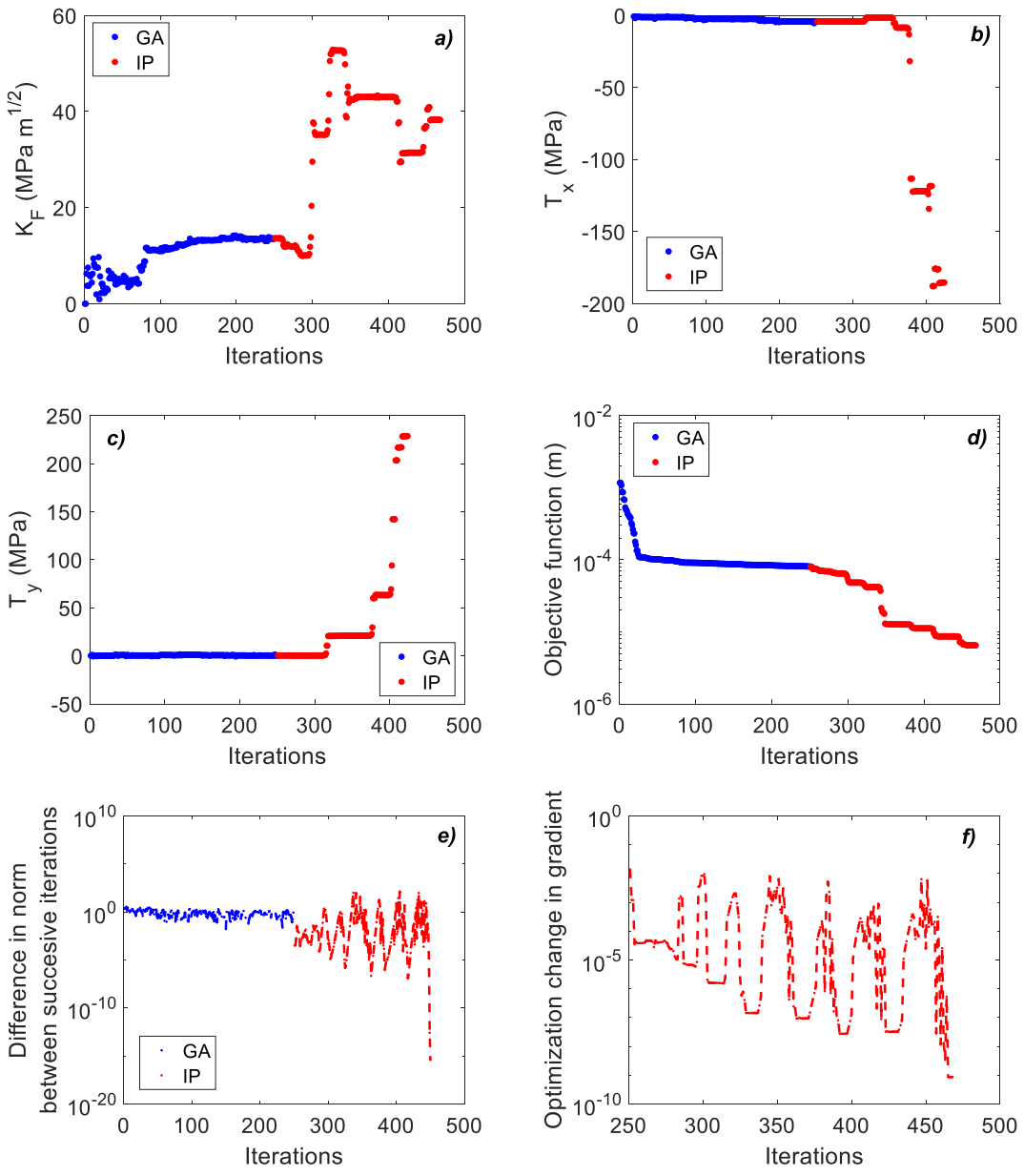

Fig. 8. The changes in specific parameters observed during the optimisation process for a crack length of 7.75 mm. a) CJP opening mode SIF $\boldsymbol{K_F}$, b) and c) Non-singular stresses $\boldsymbol{T_x}$ and $\boldsymbol{T_y}$, d) Objective function e) Difference in norm between successive iterations and f) Optimisation change in gradient (only computed for the gradient-based method).

$$\min_{\substack{A,B,C,E,F\\ \Delta x,\Delta y,u_0,v_0\\ R_x,R_y}} \|2G(u_e+v_e j)-\kappa\left[-2(B+2E)(z-\Delta x-j\Delta y)^{\frac{1}{2}}+4E(z-\Delta x-j\Delta y)^{\frac{1}{2}}-2E(z-\Delta x-j\Delta y)^{\frac{1}{2}}\ln(z-\Delta x-j\Delta y)-\frac{C-F}{4}(z-\Delta x-j\Delta y)\right]$$
$$+(z-\Delta x-j\Delta y)\left[-(B+2E)\overline{(z-\Delta x-j\Delta y)}^{\frac{-1}{2}}-E\overline{(z-\Delta x-j\Delta y)}^{\frac{-1}{2}}\ln(z-\Delta x-j\Delta y)-\frac{C-F}{4}\right]+\left[A\overline{(z-\Delta x-j\Delta y)}^{\frac{1}{2}}+E\overline{(z-\Delta x-j\Delta y)}^{\frac{1}{2}}\ln(z-\Delta x-j\Delta y)\right.$$
$$\left.-2E\overline{(z-\Delta x-j\Delta y)}^{\frac{1}{2}}+\frac{C+F}{2}\overline{(z-\Delta x-j\Delta y)}\right]+2G\big(-u_0-v_0 j-R_x\Im(z-\Delta x-j\Delta y)+jR_y\Re(z-\Delta x-j\Delta y)\big)\|_2 \quad (7)$$

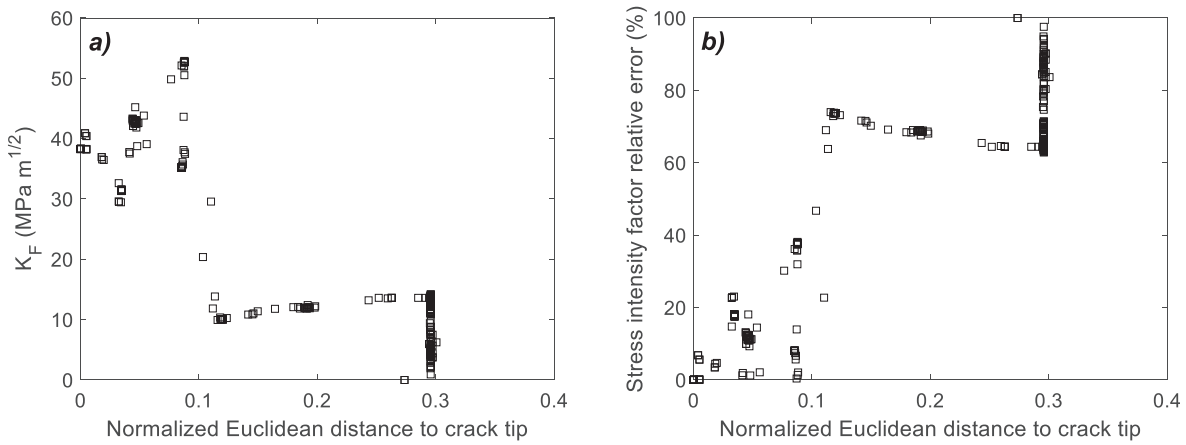

Fig. 9. Variation in opening mode SIF with the normalised Euclidean distance to the crack tip for a crack length of 7.75 mm. Crack tip distance normalised by crack length. a) $\boldsymbol{K_F}$ and b) Relative error in terms of.$\boldsymbol{K_F}$

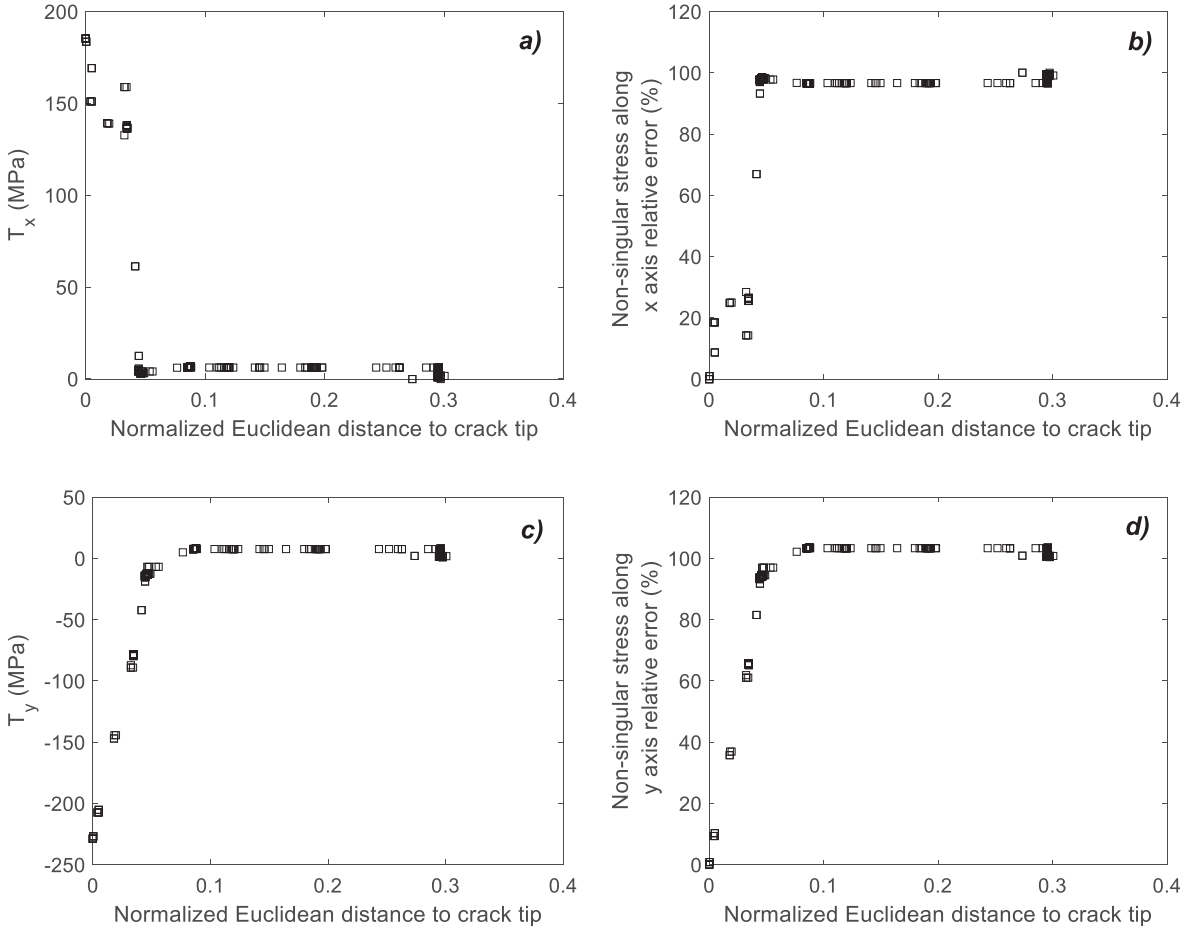

Fig. 10. Variation of non-singular stresses with the normalised Euclidean distance to the crack tip for a crack length of 7.75 mm. Crack tip distance normalised by crack length. a)$\boldsymbol{T_x}$, b) $\boldsymbol{T_x}$ relative error, c) $\boldsymbol{T_y}$ and d) $\boldsymbol{T_y}$ relative error.

$s.t. x_{SD}^{min} < \Delta x < x_{SD}^{max}$

$y_{SD}^{min} < \Delta y < y_{SD}^{max}$

$A, B, C, E, F, \Delta x, \Delta y, u_0, v_0, R_x, R_y notsignconstrained$

In this equation, u_e and v_e are the displacement field components, Δx and Δy are the distances between crack tip position and map origin,u_0, v_0, R_x and R_y are the in-plane rigid body motion coefficients (u_0 and v_0 are horizontal and vertical rigid body translations and $R_x = R_y$ the displacement due to in xy plane rigid body rotation) and x_{SD}^{max}, x_{SD}^{min}, y_{SD}^{max}, y_{SD}^{min} are the bounds of the search domain. Double vertical bars denote the Euclidean norm of the expression. Operator $\Re$ denotes the real part of a complex number and operator $\Im$ denotes the imaginary part of a com-

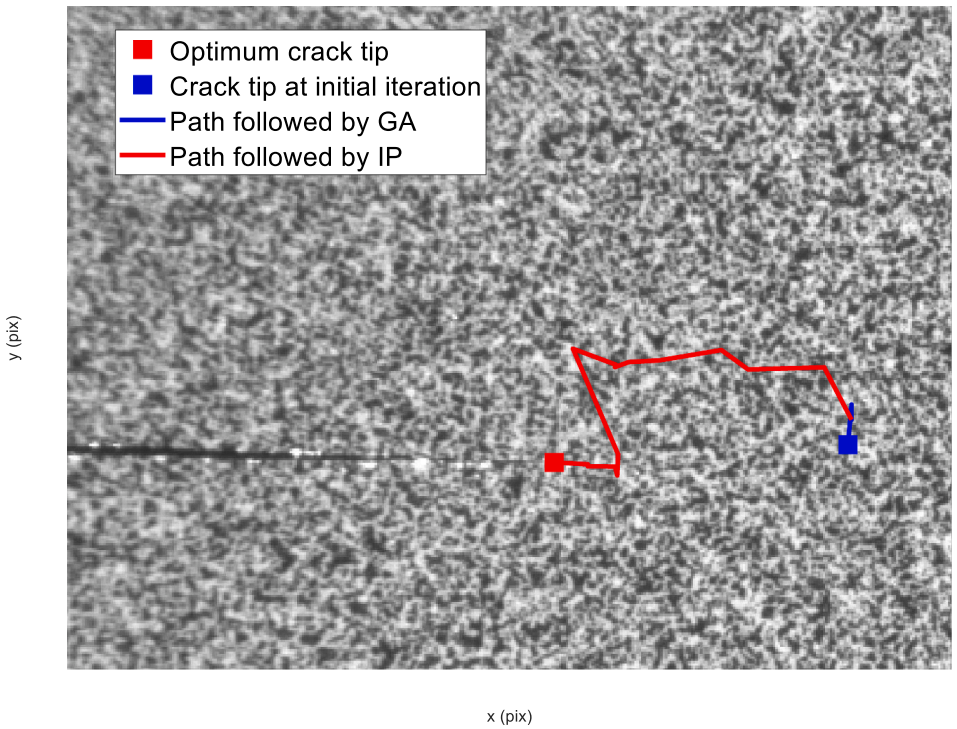

Fig. 11. Illustration of the final optimum crack tip position (red square), the crack tip position at the first iteration (blue square), and paths followed by the optimization algorithms (blue GA and red IP) superimposed on the speckle image. Crack length of 7.75 mm.

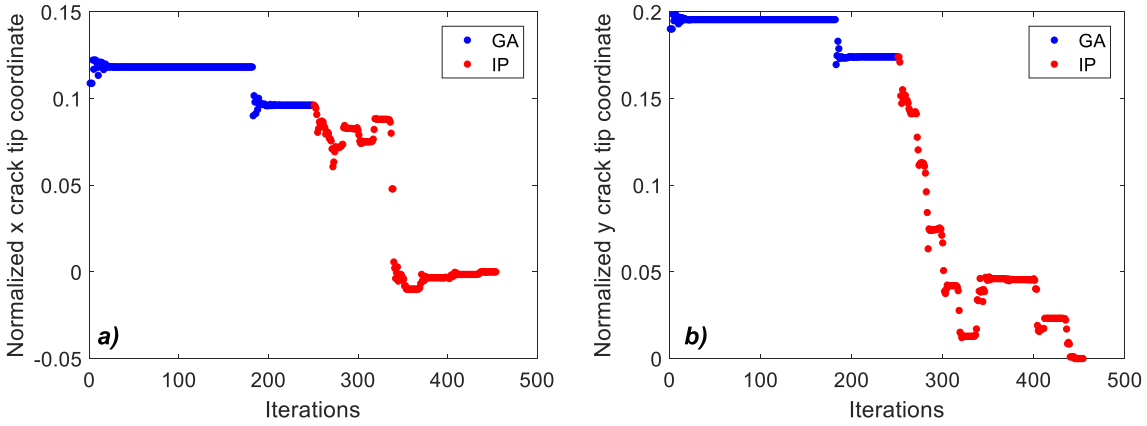

Fig. 12. Changes in the *x* and *y* crack tip coordinates during the iterative process, normalised as the ratio of the distance between their × and y distances and the optimum crack tip position divided by the crack length A value of zero corresponds with the normalised optimum crack tip position during the optimisation process. a) *x*-coordinate and b) *y*-coordinate.

plex number.

The optimisation problem defined in equation (7) remains highly nonlinear and has a large number of variables to optimise. The initial solution chosen for running the algorithm is therefore a critical variable in the fitting problem. A well-conditioned initial solution cannot be easily found since some CJP coefficients are related to nonlinear effects on the elastic field and hence there are no correlations available to estimate these parameters a priori. To avoid defining an initial solution a GA was used to initialise the optimisation problem. When the solution provided by the GA is close to an optimum (determined by checking relative error between theoretical and experimental fields), the IP algorithm starts by taking its initial solution to be the last solution iteration generated by the GA. In this way, potential errors arising from incorrect choice of initial solutions are avoided and computational times are considerably reduced. A schematic of this hybrid approach is shown in Fig. 6.

Fig. 6 illustrates a clear advantage of this approach, in that it is easily automated since only the displacement fields are necessary to calculate the crack tip parameters. In the GA part of the optimisation process, the objective function value was chosen as criterion for stopping further iterations, whilst during the IP optimisation the norm of the objective function gradient was chosen as the criterion for terminating the process. It was observed that in order to achieve a well-conditioned GA solution that is then used to initiate the IP algorithm, the relative value of the error function (quotient between error function and theoretical CJP displacement field) had to be between 15% and 20%. In the GA process a population of 250 individuals was defined and the initial population was generated from a uniform statistical distribution by defining two upper and lower symmetrically bounds. For unconstrained variables a [-10, 10] range was chosen and for constrained variables their defined bounds were used. At the end of each iteration, individuals were sorted using their rank in place of their fitness value since closer

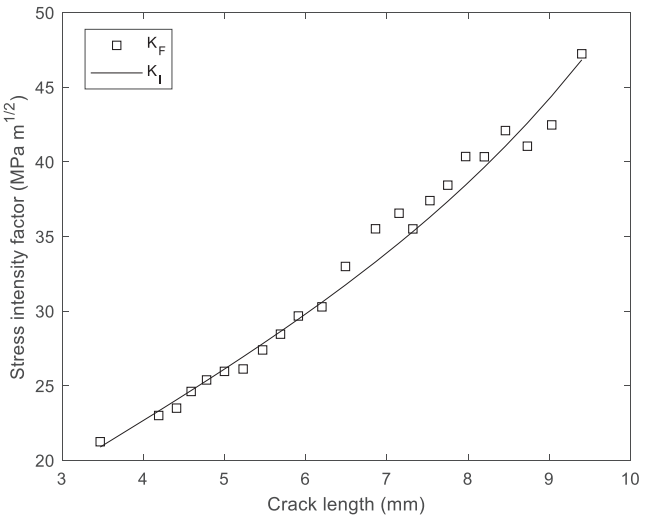

Fig. 13. Experimentally determined CJP driving force, K_F, and standard Mode I stress intensity factor versus crack length at maximum load.

fitness values between individuals can lead to problems during the sorting stage. The fraction of surviving individuals was defined using a 5% elitism level. Separate from the elite individuals, 70% percent of the next generation of data was generated by a crossover technique that used a linear combination between weighted progenitor data according to their fitness values. Finally, mutation was allowed in order to keep the last convergence direction compliant with the defined constraints. In this work, the IP algorithm used a quasi-Newton and trust-region approach [25]. The objective gradient was computed by finite difference using the central derivative to reduce discretisation errors and improve the accuracy of the results. The Hessian matrix was computed using the Broyden-Fletcher-Goldfarb-Shanno (BFGS) algorithm [33–35]. Using a full-Newton approach, convergence could be achieved faster than with a quasi-Newton approach. However, the inclusion of analytical derivatives (either first and second order, or first order and second order by finite difference) into the algorithm increased the computational time and cost. It was noted that the conjugate gradient trust-region approach for solving each sub-problem was very useful in achieving convergence to a global minimum. In contrast, if a line search approach was used, the algorithm could stall in finding a local minimum.

4.2. Results verification

To demonstrate that the proposed methodology provided an accurate calculation of the crack tip location as well as the stress intensity factors, its results were compared with those obtained using the following two procedures.

4.2.1. Crack tip location from the analysis of vertical displacement maps

In this technique, the $\times$ and y coordinates of the crack tip were obtained as follows. Firstly, the y-coordinate is found as the intersection point observed when a set of vertical displacement profiles, plotted perpendicularly to the crack path, cross the crack plane. This convergent behaviour of the profiles at a point on the crack plane can be clearly seen in Fig. 7a. The vertical displacement value (v = 0.158 mm) corresponding to this intersection point is indicated in Fig. 7a because it is used to find the crack tip position in the x-direction (Fig. 7b).

Fig. 7b plots a vertical displacement profile in the x-direction parallel to the crack path and allows identification of the x-coordinate of the crack tip as that point on the displacement profile that has the same value for the vertical displacement identified for the y-coordinate of the crack tip. The $\times$ and y coordinates of the crack tip identified from this procedure were 470 pixels and 468 pixels, respectively, taking the upper left corner of the displacement map (Fig. 3b) as the coordinate origin. This methodology was then applied for all the crack lengths measured during the fatigue testing.

4.2.2. Standard functions for determination of nominal SIF

The second comparison technique used the standard elastic compliance function for a CT specimen provided by the ASTM [36], which is given in equation (8):

$$K_I = \frac{P}{t\sqrt{W}} \frac{2+\frac{a}{W}}{\left(1-\frac{a}{W}\right)^{\frac{3}{2}}} \left[0.886+4.64\left(\frac{a}{W}\right)-13.32\left(\frac{a}{W}\right)^2+14.72\left(\frac{a}{W}\right)^3-5.6\left(\frac{a}{W}\right)^4\right] \quad (8)$$

Table 3
Crack tip locations and opening mode SIFs for different crack lengths. Comparison and differences.

	Optimised Technique		Vertical Displacement Technique							
a	Δx	Δy	Δx	Δy	d	d	d/a	K_F	K_I	SIFs error
mm	pix	pix	pix	Pix	pix	μm	(%)	MPa $m^{1/2}$	MPa $m^{1/2}$	(%)
3.47	56	486	60	482	5.66	73.0	2.24	21.25	20.89	1.71
4.19	107	484	100	481	7.62	99.0	2.48	23.01	23.31	1.29
4.41	117	481	108	481	9.00	117	2.65	23.50	24.06	2.32
4.59	129	481	120	481	9.00	117	2.54	24.62	24.68	0.25
4.78	138	481	130	480	8.06	104	2.17	25.39	25.34	0.19
5.00	154	481	156	480	2.24	29.0	0.52	25.96	26.12	0.59
5.23	168	481	163	477	6.40	83.2	1.49	26.12	26.94	3.03
5.47	188	478	183	477	5.10	66.2	1.18	27.40	27.81	1.49
5.69	193	478	192	479	1.41	18.3	0.22	28.46	28.63	0.61
5.91	212	478	209	479	3.16	41.1	0.65	29.67	29.46	0.71
6.20	244	479	240	477	4.47	58.1	0.83	30.28	30.59	1.00
6.49	267	477	265	477	2.00	26.0	0.40	32.99	31.75	3.90
6.86	288	477	285	475	3.61	46.7	0.75	35.51	33.29	6.67
7.15	308	477	307	475	2.24	29.0	0.36	36.56	34.56	5.79
7.32	321	476	323	474	2.83	36.7	0.53	35.51	35.32	0.52
7.53	336	476	340	475	4.12	53.6	0.69	37.40	36.30	3.04
7.75	350	475	346	474	4.12	53.6	0.67	38.44	37.35	2.90
7.97	367	475	370	473	3.61	46.8	0.65	40.36	38.45	4.96
8.20	385	473	382	474	3.16	41.1	0.47	40.34	39.64	1.77
8.46	400	474	400	474	0.00	0.00	0.00	42.10	41.05	2.54
8.73	424	472	425	474	2.24	29.0	0.29	41.05	42.60	3.63
9.03	447	472	443	473	4.12	53.6	0.57	42.47	44.41	4.37
9.4	470	471	470	470	1.00	13.0	0.13	47.24	46.83	0.87
	Average values				4.14	50				2.35

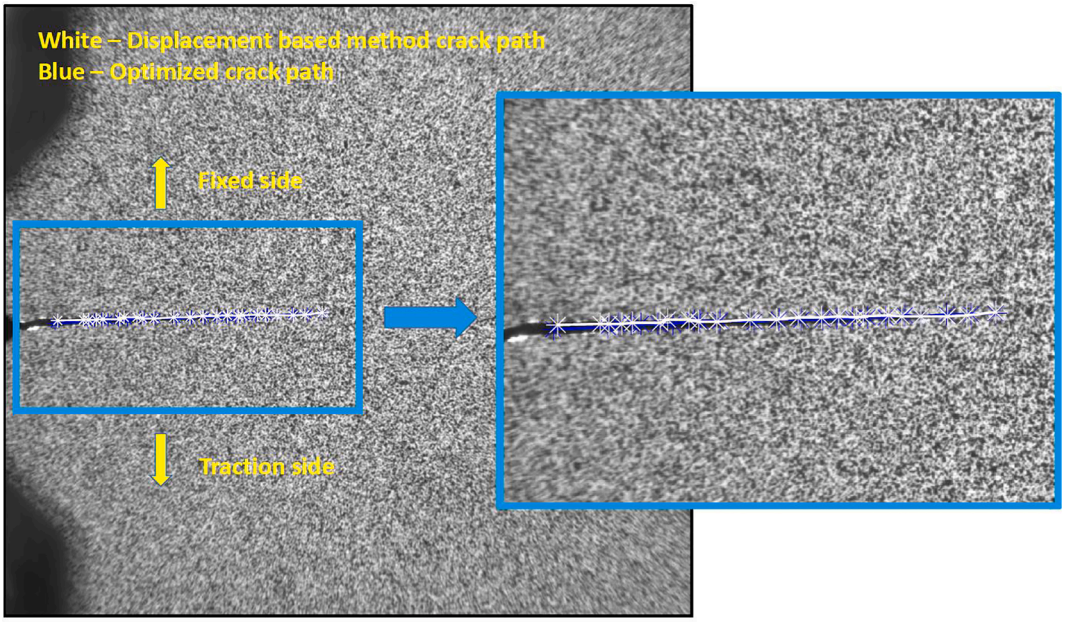

Fig. 14. Crack paths superimposed over the speckle image.

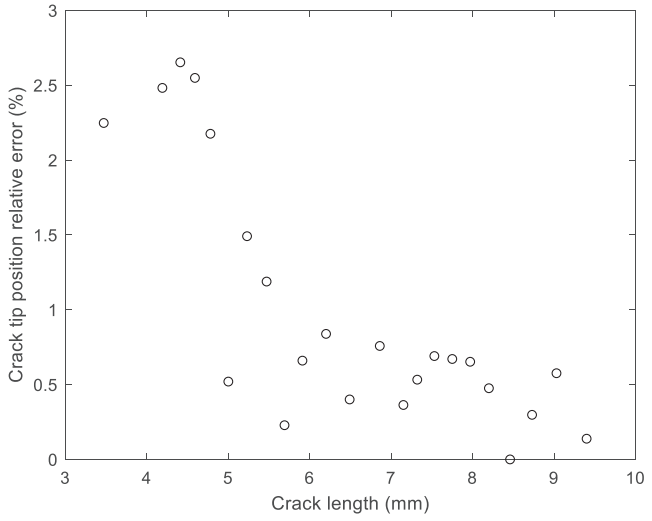

Fig. 15. Relative crack tip position difference between the hybrid optimisation and the displacement intersection methods.

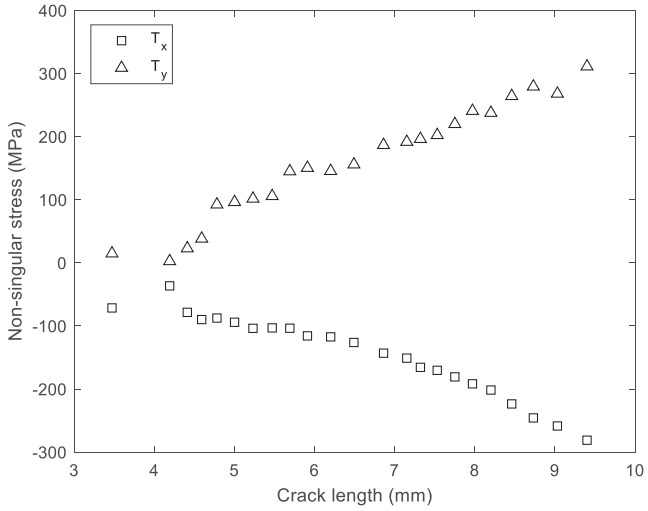

Fig. 16. Non-singular stresses along × and y axes in function of crack length.

where P is the applied load, t and W are the thickness and the width of the specimen, respectively.

5. Results and discussion

5.1. Convergence analysis

Convergence analysis results are presented for an illustrative crack length of 7.75 mm (a/W = 0.38), as typical of the results obtained for any other crack length. The changes in the various parameters observed during the optimisation process are shown in Fig. 8a (change in the opening stress intensity factor K_F), 8b (T-stress in the x-direction, T_x) and 8c (T-stress in the y-direction, T_y). Fig. 8f shows that the optimisation change in gradient while the algorithm is running reaches several successive local minima that are maintained over a number of iterations, before a clear global minimum is achieved. It clearly illustrates the complexity of the optimisation problem. At these local minima, the values found for the crack tip parameters (shown in Fig. 8a, 8b and 8c) do not represent the final solution. For example, in the case of the opening mode SIF K_F (Fig. 8a), either very low or very high values are found. Moreover, the change in the solution value between successive iterations is very significant, as indicated in the values of the non-singular T-stresses (Fig. 8b and 8c); as these parameters remain near zero until the optimisation approaches the global minimum at around 450 iterations. The objective function (Fig. 8d) shows two steep regions of decrease during the optimisation process. The initial decline is observed at the beginning of the GA optimisation over around 50 iterations. This decrease and its subsequent stabilisation are due to the GA generating a well-conditioned initial solution fairly quickly, but then experiencing some difficulty when the solution is refined. The GA can therefore provide a good solution in a short period of time but subsequently requires a substantial time or number of iterations in trying to achieve a global minimum. The second steep decline is observed during the IP optimisation at around 330 iterations, and this coincides with the zone where the crack tip parameters approach their final values. Fig. 8e

Table 4
Results for the CJP characterising parameters, crack tip location, error function and computation times for the various crack lengths.

a mm	K_F MPa $m^{1/2}$	K_R* MPa $m^{1/2}$	K_S MPa $m^{1/2}$	T_x MPa	T_y MPa	Δx pix	Δy pix	F m	t_{GA} s	t_{IP} s	t_T s
3.47	21.25	0.00	−3.26	−71.47	14.81	56	486	5.64E-09	54.65	5.46	60.11
4.19	23.01	0.00	−3.09	−36.55	2.56	107	484	7.91E-09	55.93	5.29	61.22
4.41	23.50	0.01	−4.03	−78.48	22.89	117	481	6.16E-09	57.13	3.92	61.05
4.59	24.62	0.00	−4.29	−89.93	38.26	129	481	8.34E-09	59.79	4.28	64.07
4.78	25.39	0.00	−1.57	−87.52	92.37	138	481	1.00E-08	56.02	3.25	59.27
5.00	25.96	−0.28	−2.45	−94.19	96.20	154	481	8.26E-09	54.96	6.63	61.59
5.23	26.12	−0.35	−2.96	−103.84	101.64	168	481	9.95E-09	53.89	4.96	58.85
5.47	27.40	0.00	−3.13	−103.17	105.71	188	478	1.38E-08	58.97	4.53	63.50
5.69	28.46	−0.24	−1.78	−103.63	144.95	193	478	2.71E-08	56.43	5.15	61.58
5.91	29.67	−0.07	−2.45	−115.79	150.43	212	478	2.04E-08	56.09	4.07	60.16
6.20	30.28	0.00	−3.18	−117.35	145.47	244	479	1.36E-08	57.65	3.47	61.12
6.49	32.99	−0.40	−3.61	−126.24	155.83	267	477	3.48E-08	53.47	3.87	57.34
6.86	35.51	−0.71	−3.59	−143.19	186.71	288	477	3.18E-08	53.55	3.86	57.41
7.15	36.56	−0.64	−4.18	−151.04	191.65	308	477	3.29E-08	54.28	5.97	60.25
7.32	35.51	−1.22	−5.12	−165.59	196.25	321	476	2.21E-08	57.33	4.11	61.44
7.53	37.40	−1.03	−5.26	−170.33	202.41	336	476	3.06E-08	57.91	3.55	61.46
7.75	38.44	−1.36	−5.38	−180.74	219.86	350	475	2.97E-08	53.75	5.55	59.30
7.97	40.36	−1.58	−5.49	−191.75	240.70	367	475	2.23E-08	58.34	4.15	62.49
8.20	40.34	−1.61	−6.32	−201.62	237.61	385	473	1.49E-08	56.01	4.05	60.06
8.46	42.10	−2.17	−6.73	−223.61	264.21	400	474	3.81E-08	52.74	5.20	57.94
8.73	41.05	−3.09	−7.65	−245.80	279.31	424	472	3.48E-08	55.39	5.71	61.10
9.03	42.47	−2.76	−9.32	−258.56	268.00	447	472	3.60E-08	54.81	5.95	60.76
9.40	47.24	−2.70	−9.16	−281.10	311.15	470	471	2.42E-08	58.42	4.43	62.85

* K_R values at the smaller crack lengths are not zero – they are low ($\sim 10^{-3}$) and positive.

shows the difference in the norm observed between successive iterations. This value changes from 10^{-1} to 10^{-16} when the global minimum is found. This observation, along with the associated steep decline in the optimisation change in gradient support the conclusion that an optimum value is achieved using this methodology.

The sensitivity of the crack tip parameters defined by the CJP model to the crack tip position is reflected in Fig. 9. The opening mode SIF K_F varies over a wide range of values (differences around 20%) even when the normalised distance to the computed crack tip location is<5% (0.05). Only when the normalised distance is lower than 2% (0.02) are accurate results obtained (differences lower than 5%). Similar trends are observed in the values of the non-singular T-stresses shown in Fig. 10, although this variable is even more sensitive to crack tip position, as for crack tip normalised distances of approximately to 1% (0.01) the relative error is around 10%. These results deomnstrate the high sensitivity of the CJP model to crack tip position and justify the necessity of using the methodology proposed in the present paper. It also implies that the CJP model is successfully capturing local influences on the overall elastic field.

Fig. 11 shows the path followed by the optimisation algorithm, which has been superimposed on the specimen speckle image. It is particularly significant that the path followed by the algorithm-calculated crack tip position does not reach its final position via a straight line, as the algorithm path searches adjacent points to the crack tip until the coordinates are close to the optimum solution. Fig. 12a and 12b show the changes in the x and y crack tip coordinates during the iterative process, normalised as the ratio of the distance between their × and y distances and the optimum crack tip position divided by the crack length. These normalised values approach zero as the optimum crack tip position is reached. Fig. 12 essentially highlights the optimisation-path distances shown in Fig. 11.

5.2. Crack tip characterising parameters and crack tip location

The crack tip characterising parameters (stress intensity factors and T-stress) and the crack tip location were found for crack lengths between 3.4 mm and 9.4 mm (equivalent to values of normalised crack length of 0.17 and 0.47). As a check of the accuracy of the proposed technique, Fig. 13 plots values of the CJP driving force, K_F and the standard value of Mode I stress intensity factors, K_I, versus crack length. Both sets of data follow a very similar trend line, with an average relative difference between them of 2.63% (Table 3) and are also similar to the results reported by Nowell et al [37].

Although these stress intensity factors appear to be similar, it is important to highlight the significant advantages of the CJP approach, that include the fact that the effective driving force for crack growth, in the presence of plasticity-induced shielding, is directly given by the net driving force K_F - K_R; a geometry-independence of the calculation, at least for some standard specimen types; and a correlation of fatigue crack growth rate over a wider range than the Irwin-Paris value (see reference 23 for details).

An additional check is given in Fig. 14 by comparing the crack path determined by the optimisation technique introduced in the present paper, with the crack path determined by the crack tip displacement intersection method. They are superimposed on the speckle image of the specimen surface for the crack length values given in Table 3. The two crack paths show a very good level of agreement, with an average difference of 50 μm in terms of the Euclidean distance between crack tip positions determined by both techniques (0.98% difference when normalised by the crack length). Fig. 15 shows the relative difference between crack tip positions found by the two techniques as a function of crack length. It can be seen that the difference decreases with increase in crack length. Higher values at short crack lengths are reasonable since the crack tip singularity is less intense than in the case of longer cracks and it is also possible that the manufacturing process of the specimen notch generates residual stresses that may modify the singularity field. As noted earlier, however, the reason for performing this work is because the parameters in the CJP model are rather sensitive to variations of a few pixels in the crack tip position, particularly in the case of the x-coordinate, and 50 μm represents around 4 pixels for the camera system used in this work.

Computed non-singular T-stresses along the × and y directions are plotted in Fig. 16. Both parameters show similar trends and correspond with the expected results, since a negative sign in the crack growth direction corresponds with a lateral contraction of the specimen under axial traction loading, and the positive sign in the case of the crack opening direction also corresponds with traction loading.

Table 4 gives values of the CJP stress intensity parameters, the

optimised crack tip location, the value of the error function at the end of the optimisation process and the time taken by each algorithm. Values of the retardation K_R and shear K_S stress intensity factors agree with those obtained in previous work of the same alloy [31,37,38]. Computation times in all cases are around 1 min, with the GA taking around 92% of the total computation time, which is reasonable compared with values reported in other work [19,20].

6. Conclusions

A novel technique has been outlined in the present work that provides an accurate conjoint determination of the CJP stress intensity factors and the crack tip location. The most important innovation is that the process includes estimation of the precise crack tip location as an additional unknown in the mathematical optimisation. The technique uses a hybrid process that combines an initial optimisation using a genetic algorithm, followed by use of an interior point algorithm. Its utility has been demonstrated through analysis of crack tip displacement fields experimentally measured using 2D-DIC. The value of the proposed technique arises from the known sensitivity of the CJP model to crack tip position where small errors in crack tip location (several pixels) can lead to substantial errors in the crack tip characterising parameters obtained with the model. Although the methodology has been developed specifically for the CJP model and DIC data, the proposed hybrid method can be applied with any model of crack tip fields, any isotropic material and any experimental technique used to measure displacement. An extension of that technique to the analysis of 3D-DIC would require only minor modifications and it would be attractive in analysing out-of-plane crack tip phenomena (i.e. tearing mode singularity parameters). A major advantage of the approach lies in the possibility of easy automation as the crack tip characterisation process sometimes involves large user effort and time. Apart from crack tip field characterisation, the proposed method would be useful in any application that requires a precise crack tip location.

In the light of the demonstrated ability of the CJP model to account for the shielding effects of the plastic enclave that surrounds a growing fatigue crack, future work will explore how the shielding effects during fatigue crack growth can be better evaluated using the proposed methodology. In the view of authors this, combined with a better understanding of the interaction between, and origin of, the five CJP parameters (A - E), will contribute to an increased understanding of the factors contributing to plasticity-induced shielding and the mechanisms involved in variable amplitude load interaction.

Declaration of Competing Interest

The authors declare that they have no known competing financial interests or personal relationships that could have appeared to influence the work reported in this paper.

Acknowledgements

This work has been performed with financial support from the Junta de Andalucía through the research project “1380786” funded by the program “Proyectos de I + D + i en el Marco del Programa Operativo FEDER Andalucía 2014-2020. Convocatoria 2020”.

References

[1] Schreier H, Orteu J-J, Sutton MA, editors. Image Correlation for Shape, Motion and Deformation Measurements. Boston, MA: Springer US; 2009.
[2] Thomson W (Lord K. On the Thermoelastic, Thermomagnetic and Pyro-electric Properties of Matters. Philos Mag 1878;5:4–27.
[3] Brewster D. On the communication of the structure of doubly refracting crystals to glass, muriate of soda, flour spar and other substances by mechanical compression and dilatation. Philos Mag 1816;106:156–78.
[4] Sanford RJ, Dally JW. A general method for determining mixed-mode stress intensity factors from isochromatic fringe patterns. Eng Fract Mech 1979;621:621–33.
[5] Westergaard HM. Bearing pressures and cracks. J Appl Mech 1939;61:49–53.
[6] Irwin GR. Analysis of stresses and strains near the end of a crack traversing plate. J Appl Mech 1957;24:361–70.
[7] Williams ML. On the stress distribution at the base of a stationary crack. J Appl Mech 1957;24:109–14.
[8] Nurse AD, Patterson EA. Determination of predominantly mode-II stress intensity factors from isochromatic data. Fatigue Fract Eng Mater Struct 1993;16(12):1339–54. https://doi.org/10.1111/j.1460-2695.1993.tb00743.x.
[9] Muskhelishvili NI. Some Basic Problems of the Mathematical Theory of Elasticity. Springer Netherlands; 1977. https://doi.org/10.1007/978-94-017-3034-1.
[10] Pommier S, Hamam R. Incremental model for fatigue crack growth based on a displacement partitioning hypothesis of mode I elastic-plastic displacement fields. Fatigue Fract Eng Mater Struct 2007;30:582–98. https://doi.org/10.1111/j.1460-2695.2007.01128.x.
[11] Christopher CJ, James MN, Patterson EA, Tee KF. Towards a new model of crack tip stress fields. Int J Fract 2007;148(4):361–71. https://doi.org/10.1007/s10704-008-9209-3.
[12] Christopher CJ, James MN, Patterson EA, Tee KF. A quantitative evaluation of fatigue crack shielding forces using photoelasticity. Eng Fract Mech 2008;75(14):4190–9. https://doi.org/10.1016/j.engfracmech.2008.03.013.
[13] James MN, Christopher CJ, Lu YW, Patterson EA. Local crack plasticity and its influences on the global elastic stress field. Int J Fatigue 2013;46:4–15. https://doi.org/10.1016/j.ijfatigue.2012.04.015.
[14] Lopez-Crespo P, Shterenlikht A, Patterson EA, Yates JR, Withers PJ. The stress intensity of mixed mode cracks determined by digital image correlation. J Strain Anal Eng Des 2008;43(8):769–80.
[15] Yates JR, Zanganeh M, Tai YH. Quantifying crack tip displacement fields with DIC. Eng Fract Mech 2010;77(11):2063–76. https://doi.org/10.1016/j.engfracmech.2010.03.025.
[16] Vasco-Olmo JM, Diaz FA, Garcia-Collado A, Dorado-Vicente R. Experimental evaluation of crack shielding during fatigue crack growth using digital image correlation. Fatigue Fract Eng Mater Struct 2015;38:223–37. https://doi.org/10.1111/ffe.12136.
[17] Vasco-Olmo JM. Evaluación experimental del fenómeno de crack shielding inducido por plasticidad empleando técnicas ópticas de campo completo para la medida de tensiones y deformaciones. Universidad de Jaén 2014.
[18] Yoneyama S, Morimoto Y, Takashi M. Automatic evaluation of mixed-mode stress intensity factors utilizing digital image correlation. Strain 2006;42:21–9. https://doi.org/10.1111/j.1475-1305.2006.00246.x.
[19] Zanganeh M, Lopez-Crespo P, Tai YH, Yates JR. Locating the Crack Tip Using Displacement Field Data: A Comparative Study. Strain 2013;49:102–15. https://doi.org/10.1111/str.12017.
[20] Yang B, Wei Z, Díaz FA, Liao Z, James MN. New algorithm for optimised fitting of DIC data to crack tip plastic zone using the CJP model. Theor Appl Fract Mech 2021;113:102950. https://doi.org/10.1016/j.tafmec.2021.102950.
[21] Moré JJ. The Levenberg-Marquardt algorithm: Implementation and theory 1978:105–16. https://doi.org/10.1007/BFB0067700.
[22] Goldberg DE. Genetic algorithms in search, optimization, and machine learning. 1st ed. Boston, MA: Addison-Wesley Longman Publishing Co., Inc.,; 1989. https://doi.org/10.5555/534133.
[23] Wright SJ. Primal-Dual Interior-Point Methods. Soc Ind Appl Mathematics 1997. https://doi.org/10.1137/1.9781611971453.
[24] Coleman TF, Li Y. An interior trust region approach for nonlinear minimization subject to bounds. Siam J Optim 1996;6(2):418–45. https://doi.org/10.1137/0806023.
[25] Byrd RH, Gilbert JC, Nocedal J. A trust region method based on interior point techniques for nonlinear programming. Math Program Ser B 2000;89(1):149–85. https://doi.org/10.1007/PL00011391.
[26] Byrd RH, Hribar ME, Nocedal J. An interior point algorithm for large-scale nonlinear programming. SIAM J Optim 1999;9(4):877–900. https://doi.org/10.1137/S1052623497325107.

[27] Waltz RA, Morales JL, Nocedal J, Orban D. An interior algorithm for nonlinear optimization that combines line search and trust region steps. Math Program 2006; 107(3):391–408. https://doi.org/10.1007/s10107-004-0560-5.
[28] Nocedal J, Wright SJ. Numerical Optimization 2006. https://doi.org/10.1007/978-0-387-40065-5.
[29] Dantzig GB. Recent Advances in Linear Programming. Manage Sci 1956;2(2): 131–44. https://doi.org/10.1287/mnsc.2.2.131.
[30] Kuhn HW, Tucker AW. Nonlinear programming. Proc 2nd Berkeley Symp 1951: 481–92.
[31] Vasco-Olmo JM, James MN, Christopher CJ, Patterson EA, Diaz FA. Assessment of crack tip plastic zone size and shape and its influence on crack tip shielding. Fatigue Fract Eng Mater Struct 2016;39:969–81. https://doi.org/10.1111/ffe.12436.
[32] Vasco-Olmo JM, Diaz FA, Patterson EA. Experimental evaluation of shielding effect on growing fatigue cracks under overloads using ESPI. Int J Fatigue 2016;83: 117–26. https://doi.org/10.1016/j.ijfatigue.2015.10.003.
[33] Fletcher R, Powell MJD. A Rapidly Convergent Descent Method for Minimization. Comput J 1963;6(2):163–8. https://doi.org/10.1093/comjnl/6.2.163.
[34] Broyden CG. Quasi-Newton Methods and their Application to Function Minimisation. Math Comput 1967;21(99):368. https://doi.org/10.2307/2003239.
[35] Goldfarb D. A Family of Variable-Metric Methods Derived by Variational Means. Math Comput 1970;24(109):23. https://doi.org/10.2307/2004873.
[36] ASTM. E 647 - 00: Standard Test Method for Measurement of Fatigue Crack Growth Rates. Annu B ASTM Stand 1103 2000.
[37] Nowell D, Nowell SC. A comparison of recent models for fatigue crack tip deformation. Theor Appl Fract Mech 2019;103:6. https://doi.org/10.1016/j.tafmec.2019.102299.
[38] Yang B, Vasco-Olmo JM, Díaz FA, James MN. A more effective rationalisation of fatigue crack growth rate data for various specimen geometries and stress ratios using the CJP model. Int J Fatigue 2018;114:189–97. https://doi.org/10.1016/j.ijfatigue.2018.05.027.